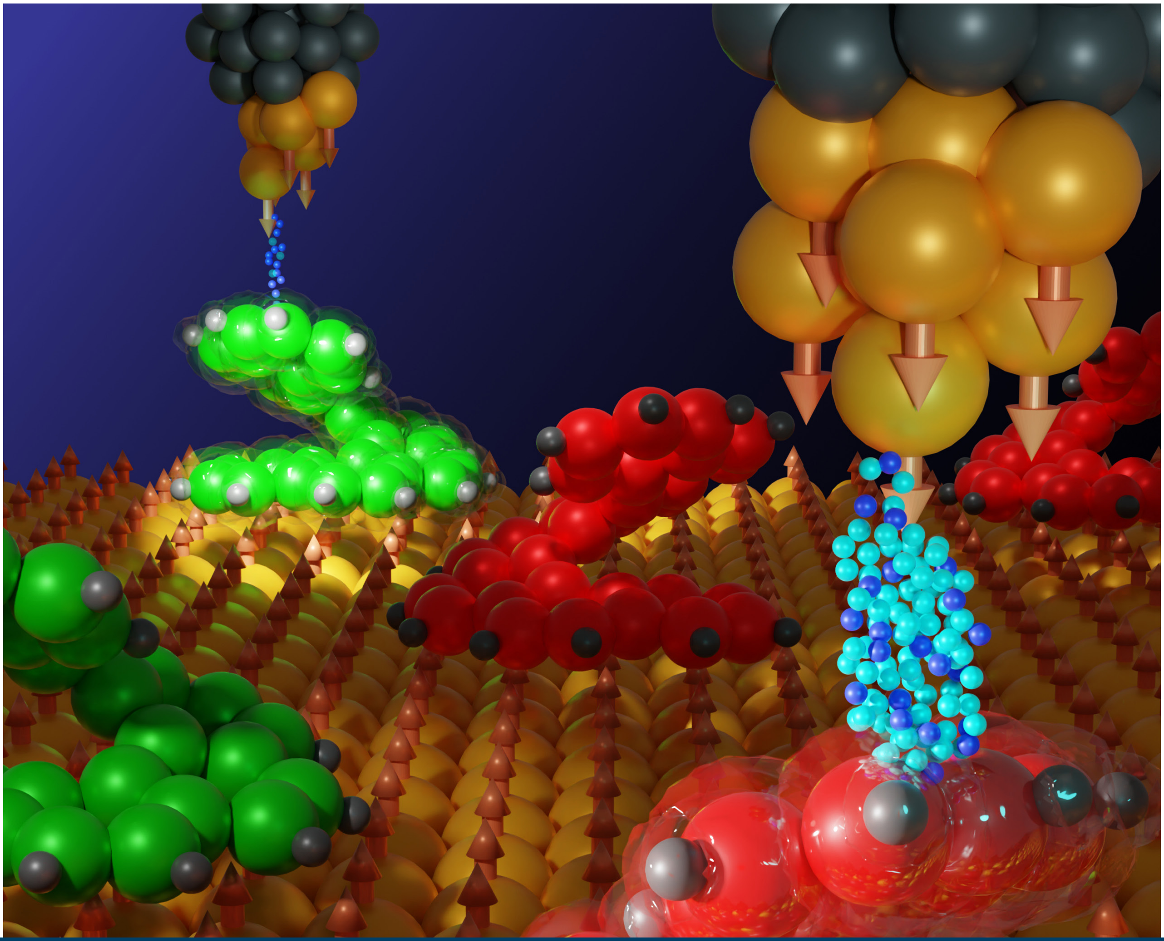

Spin selectivity of chiral molecules on surfaces

Mohammad Reza Safari

Information
Band / Volume 108
ISBN 978-3-95806-810-0

Mitglied der Helmholtz-Gemeinschaft

JÜLICH
Forschungszentrum

Schriften des Forschungszentrums Jülich
Reihe Information / Information Band / Volume 108

Forschungszentrum Jülich GmbH
Peter Grünberg Institut (PGI)
Elektronische Eigenschaften (PGI-6)

Spin selectivity of chiral molecules on surfaces

Mohammad Reza Safari

Schriften des Forschungszentrums Jülich
Reihe Information / Information Band / Volume 108

ISSN 1866-1777 ISBN 978-3-95806-810-0

Bibliografische Information der Deutschen Nationalbibliothek.
Die Deutsche Nationalbibliothek verzeichnet diese Publikation in der
Deutschen Nationalbibliografie; detaillierte Bibliografische Daten
sind im Internet über http://dnb.d-nb.de abrufbar.

Herausgeber und Vertrieb: Forschungszentrum Jülich GmbH
Zentralbibliothek, Verlag
52425 Jülich
Tel.: +49 2461 61-5368
Fax: +49 2461 61-6103
zb-publikation@fz-juelich.de
www.fz-juelich.de/zb

Umschlaggestaltung: Grafische Medien, Forschungszentrum Jülich GmbH

Druck: Grafische Medien, Forschungszentrum Jülich GmbH

Schriften des Forschungszentrums Jülich
Reihe Information / Information, Band / Volume 108

D 38 (Diss. Köln, Univ., 2024)

ISSN 1866-1777
ISBN 978-3-95806-810-0

Abstract

The purpose of this thesis is to investigate the spin selectivity of chiral molecules adsorbed on magnetic substrates, with the aim of improving our understanding of the complex interactions between chirality and magnetism. This research centers on the chirality-induced spin selectivity (CISS) effect, an emerging phenomenon that has captured the interest of the scientific community due to its potential applications in spintronics, efficient quantum computing, enantioseparation, and selective chemical processes. Since the initial identification of the CISS effect, extensive research on various molecules and substrates has yielded significant outcomes. Observations have been made that electrons transmitted through chiral molecules at room temperature exhibit spin polarizations exceeding several tens of percent. The findings also include the enantiospecific adsorption of chiral molecules on perpendicularly magnetized ferromagnetic substrates.

This area of research, which explores both theoretical and experimental aspects of the CISS effect, remains a topic of scientific interest. Despite substantial experimental evidence supporting CISS, a comprehensive theoretical understanding remains elusive. Present theoretical approaches often fail to bridge the gap between the magnitudes of experimental results and theoretical predictions, such as spin polarization values or enantiospecific adsorption energies.

A significant challenge in bridging experimental and theoretical studies stems from the complexity of real-world experiments. Often, these involve molecular ensembles and yield data that reflect averages of various configurations, such as adsorption sites and pathways of electric current. Additionally, experimental conditions may necessitate modifications like protective coatings to prevent oxidation (e.g., Au coating on ferromagnetic substrates) and can introduce other variables such as water from ambient humidity. Meanwhile, theoretical models typically overlook these complexities. In response, this PhD research project is designed to thoroughly investigate the CISS effect under ultra-high vacuum (UHV) conditions, with precise control over geometric configurations at the atomic scale. This approach could facilitate a closer alignment between experimental observations and theoretical calculations.

This thesis investigates chiral heptahelicene (7[H]) molecules adsorbed on various single-crystalline substrates, ranging from the noble metal Cu(111) to more reactive substrates like ferromagnetic Co bilayer nanoislands on Cu(111) and Fe bilayers on W(110). Low-temperature spin-polarized scanning tunneling microscopy (SP-STM) and spectroscopy (SP-STS) are employed to examine molecules that have been deposited on these surfaces through sublimation under UHV conditions.

The molecules remain structurally intact after deposition, with the proximal phenanthrene group aligned parallel to the substrate surface. The high-resolution STM topography data provide a precise method for accurately determining the chirality of individual heptahelicene molecules on these crystalline substrates. Additionally, detailed SP-STS measurements from individual molecules indicate distinct adsorption properties: molecules undergo physisorption on Cu(111) and chemisorption on Co and Fe bilayers. Notably, both Co and Fe bilayers maintain their ferromagnetic properties and exhibit out-of-plane (OOP) magnetization.

Building on our preliminary observations, our investigation delved deeper into the interactions between chiral molecules and magnetic substrates, focusing on two principal aspects.

First, we explored the enantiospecific adsorption of [7]H molecules onto OOP magnetized cobalt nanoislands, using both racemic and enantiopure samples. Our investigations revealed a magnetization-dependent enantiomeric excess upon deposition of these molecules. In the experiment using a racemic mixture, a detailed statistical analysis of over 740 molecules across 110 islands revealed an enantiomeric excess ratio of 0.7. This ratio, when expressed by a Boltzmann factor, corresponds to an energy difference of approximately $10 \pm 2\,\mathrm{meV}$. Further experiments revealed that this energy difference is not related to differences in adsorption energy. This finding was further supported by subsequent experiments with more than 2100 molecules on 225 islands, using enantiopure molecules, demonstrating a consistent picture of enantioselectivity.

The results of our experiment were then compared with state-of-the-art density functional theory (DFT) calculations performed by our colleagues at the Peter Grünberg Institute (PGI-1), Jülich Research Center. Interestingly, these advanced spin-resolved *ab initio* simulations showed no significant differences in enantio-dependent chemisorption energies. This discrepancy between the experimental results and the simulations, along with further experimental findings that molecular mobility decreases significantly when reaching the chemisorbed state on the cobalt islands, led us to hypothesize that enantioselection primarily occurs during an earlier, physisorbed state. These observations suggest that van der Waals interactions, which are critical for molecular magnetochiral processes, should also take spin fluctuations into account.

Secondly, spin-selective electron transport through chiral [7]H molecules at a low temperature of 5 K is investigated using a spin-sensitive STM tip. These molecules are deposited on two distinct types of ferromagnetic bilayer substrates: racemic mixtures are deposited on Co/Cu(111), while enantiopure molecules are deposited on Fe/W(110). This experimental approach enables the direct measurement of tunnelling currents through individual molecules under precisely controlled conditions. In this setup, the magnetization direction of either the STM tip or the substrate can be systematically reversed, and the chirality of the molecules can be selectively chosen, especially in experiments involving racemic mixtures.

This methodology enables accurate assessments of magnetochiral conductance asymmetry (MChA) by comparing the tunneling current measured through two different enantiomers deposited on the same magnetic domain. Additionally, it allows for the evaluation of enantiospecific magnetic conductance asymmetry (EMA) by comparing the tunneling current measured through molecules of the same handedness on two magnetic domains with opposing OOP magnetization. As a result, there is significant conductance asymmetry for [7]H molecules across both types of magnetic substrates, with EMA values on Co islands reaching as high as 50%. This detailed investigation also allows us to effectively exclude ensemble effects and electron-phonon coupling as primary contributing factors, thereby taking a significant step forward in clarifying the underlying mechanisms influencing spin-selective transport through chiral molecules.

Deutsche Kurzzusammenfassung *(German abstract)*

Ziel dieser Arbeit ist es, die Spin-Selektivität chiraler Moleküle zu untersuchen, die auf magnetischen Substraten adsorbiert sind, um unser Verständnis der komplexen Interaktionen zwischen Chiralität und Magnetismus zu vertiefen. Diese Forschung konzentriert sich auf den Effekt der "chirality-induced spin selectivity"(CISS), ein neuartiges Phänomen, das aufgrund seiner potenziellen Anwendungen in der Spintronik, im effizienten Quantencomputing, in der Enantioseparation und in selektiven chemischen Prozessen das Interesse der wissenschaftlichen Gemeinschaft geweckt hat. Seit der ersten Entdeckung des CISS-Effekts haben umfangreiche Forschungsarbeiten an verschiedenen Molekülen und Substraten zu bedeutenden Ergebnissen geführt. Es wurde festgestellt, dass Elektronen, die bei Raumtemperatur durch chirale Moleküle übertragen werden, Spinpolarisationen von mehr als einigen zehn Prozent aufweisen. Zu den Ergebnissen gehört auch die enantiospezifische Adsorption chiraler Moleküle auf senkrecht magnetisierten ferromagnetischen Substraten. Dieses Forschungsgebiet, das sowohl theoretische als auch experimentelle Aspekte des CISS-Effekts untersucht, bleibt ein Thema von wissenschaftlichem Interesse. Trotz umfangreicher experimenteller Belege für den CISS-Effekt fehlt nach wie vor ein umfassendes theoretisches Verständnis. Aktuelle theoretische Ansätze scheitern oft daran, die Diskrepanzen zwischen den Größenordnungen der experimentellen Ergebnisse und den theoretischen Vorhersagen, wie Spinpolarisationswerte oder enantiospezifische Adsorptionsenergien, zu überbrücken.

Eine große Herausforderung bei der Zusammenführung experimenteller und theoretischer Studien ergibt sich aus der Komplexität realer Experimente. Häufig handelt es sich um molekulare Ensembles, deren Daten Mittelwerte verschiedener Konfigurationen, z. B. Adsorptionsstellen und Strompfade, widerspiegeln. Darüber hinaus können die experimentellen Bedingungen Modifikationen wie Schutzbeschichtungen zur Verhinderung von Oxidation (z. B. Au-Beschichtung auf ferromagnetischen Substraten) erfordern und andere Variablen wie Wasser aus der Umgebungsfeuchtigkeit einführen. Theoretische Modelle berücksichtigen diese komplexen Zusammenhänge in der Regel nicht. Daher soll in die-

sem Forschungsprojekt der CISS-Effekt unter Ultrahochvakuumbedingungen (UHV), bei denen die geometrischen Konfigurationen auf atomarer Ebene genau kontrolliert werden können, im Detail untersucht werden. Dieser Ansatz könnte eine bessere Übereinstimmung zwischen experimentellen Beobachtungen und theoretischen Kalkulationen ermöglichen.

In dieser Arbeit werden chiralen Heptahelicen (7[H])-Moleküle untersucht, die auf verschiedenen einkristallinen Substraten adsorbiert sind, vom Edelmetall Cu(111) bis zu reaktiveren Substraten wie ferromagnetischen Co-Doppelschicht-Nanoinseln auf Cu(111) und Fe-Doppelschichten auf W(110). Tieftemperatur-Rastertunnelmikroskopie (SP-STM) und -spektroskopie (SP-STS) werden eingesetzt, um Moleküle zu untersuchen, die durch Sublimation unter UHV-Bedingungen auf diesen Oberflächen abgeschieden wurden.

Die Moleküle bleiben nach der Abscheidung strukturell intakt, wobei die proximale Phenanthrengruppe parallel zur Substratoberfläche ausgerichtet ist. Die hochauflösenden STM-Topographiedaten bieten eine präzise Methode zur genauen Bestimmung der Chiralität einzelner Heptahelicen-Moleküle auf diesen kristallinen Substraten. Darüber hinaus zeigen detaillierte SP-STM Messungen einzelner Moleküle unterschiedliche Adsorptionseigenschaften: Die Moleküle unterliegen einer Physisorption auf Cu(111) und einer Chemisorption auf Co- und Fe-Doppelschichten. Bemerkenswerterweise behalten sowohl Co- als auch Fe-Doppelschichten ihre ferromagnetischen Eigenschaften und zeigen eine out-of-plane (OOP) Magnetisierung.

Aufbauend auf unseren ersten Erkenntnissen haben wir die Wechselwirkungen zwischen chiralen Molekülen und magnetischen Substraten genauer untersucht und uns dabei auf zwei Hauptaspekte konzentriert.

Zunächst wurde die enantiospezifische Adsorption von [7]H-Molekülen an OOP-magnetisierten Kobalt-Nanoinseln untersucht, wobei sowohl racemische als auch enantioreine Moleküle verwendet wurden. Unsere Untersuchungen zeigten einen Enantiomerenüberschuss bei der Abscheidung dieser Moleküle, der von der Magnetisierung abhängig war. Im Experiment mit einer racemischen Mischung ergab eine detaillierte statistische Analyse von über 740 Molekülen auf 110 Inseln ein Enantiomerenüberschussverhältnis von 0,7. Dieses Verhältnis, ausgedrückt durch einen Boltzmann-Faktor, entspricht einem Energieunterschied von etwa $10 \pm 2\,\mathrm{meV}$. Weitere Experimente haben gezeigt, dass dieser Energieunterschied nicht mit Unterschieden in der Adsorptionsenergie zusammenhängt. Dieses Ergebnis wurde durch nachfolgende Experimente mit mehr als 2100 Molekülen auf 225 Inseln unter Verwendung enantioreiner Moleküle weiter untermauert, die ein konsistentes Bild der Enantioselektivität zeigten.

Die Ergebnisse unseres Experiments wurden dann mit state-of-the-art Dichtefunktionaltheorie (DFT)-Berechnungen verglichen, die von unseren Kollegen am Peter Grün-

berg Institute (PGI-1), Forschungszentrum Jülich, durchgeführt wurden. Interessanterweise zeigten diese fortgeschrittenen spinaufgelosten *ab initio*-Simulationen keine signifikanten Unterschiede in den enantioabhängigen Chemisorptionsenergien. Diese Diskrepanz zwischen experimentellen Ergebnissen und Simulationen, zusammen mit weiteren experimentellen Befunden, dass die molekulare Mobilität signifikant abnimmt, sobald ein chemisorbierter Zustand auf den Kobaltinseln erreicht wird, führte uns zu der Hypothese, dass die Enantioselektion hauptsächlich während eines früheren, physisorbierten Zustandes auftritt. Diese Beobachtungen legen nahe, dass van-der-Waals-Wechselwirkungen, die für molekulare magnetochirale Prozesse entscheidend sind, auch Spinfluktuationen berücksichtigen sollten.

Zweitens wird der spinselektive Elektronentransport durch chirale [7]H-Moleküle bei einer tiefen Temperatur von 5 K mit einer spinempfindlichen STM-Spitze untersucht. Diese Moleküle werden auf zwei verschiedenen Arten von ferromagnetischen Doppelschichtsubstraten abgeschieden: Racemische Mischungen werden auf Co/Cu(111) abgeschieden, während enantioreine Moleküle auf Fe/W(110) abgeschieden werden. Dieser experimentelle Ansatz erlaubt die direkte Messung von Tunnelströmen durch einzelne Moleküle unter genau kontrollierten Bedingungen. In dieser Konfiguration kann die Magnetisierungsrichtung entweder der STM-Spitze oder des Substrats systematisch umgekehrt werden, und die Chiralität der Moleküle kann selektiv gewählt werden, insbesondere in Experimenten mit racemischen Mischungen.

Diese Methode erleichtert die genaue Bestimmung der magnetochiralen Leitfähigkeitsasymmetrie (MChA), wenn zwei Enantiomere auf der gleichen magnetischen Domäne vorliegen (für racemische Mischungen auf Co-Inseln), und der enantiospezifischen magnetischen Leitfähigkeitsasymmetrie (EMA), wenn Moleküle der gleichen Chiralität auf zwei magnetischen Domänen mit entgegengesetzter OOP-Magnetisierung verglichen werden. Demzufolge gibt es eine signifikante Leitfähigkeitsasymmetrie für [7]H-Moleküle über beide Arten von magnetischen Substraten, wobei die EMA-Werte auf Co-Inseln bis zu 50% erreichen. Diese detaillierte Untersuchung erlaubt es uns auch, Ensemble-Effekte und Elektron-Phonon-Kopplung als primäre beitragende Faktoren effektiv auszuschließen, und stellt damit einen wichtigen Fortschritt bei der Aufklärung der zugrundeliegenden Mechanismen dar, die den spinselektiven Transport durch chirale Moleküle beeinflussen.

Frequently used acronyms and abbreviations

CISS - chirality-induced spin selectivity
UHV - ultrahigh vacuum
[7]H - heptahelicene
SP-STM - spin polarized scanning tunneling microscopy
SP-STS - spin polarized scanning tunneling spectroscopy
OOP - out-of-plane
MChA - magnetochiral conductance asymmetry
EMA - enantiospecific magnetic conductance asymmetry
RT - room temperature
ML - monolayer
cw - clockwise
ccw - counterclockwise
SAM - self-assembled monolayer
CP-AFM - conductive probe atomic force microscopy
GMR - giant magnetoresistance
TMR - tunnel magnetoresistance
SEM - scanning electron microscope
SOC - spin–orbit coupling

Contents

Abstract **iii**

Deutsche Kurzzusammenfassung *(German abstract)* **vii**

Frequently used acronyms and abbreviations **xi**

1 Introduction **1**
- 1.1 Chirality 1
- 1.2 Chirality-induced spin selectivity (CISS) 3
- 1.3 An overview of experimental studies on CISS 4
  - 1.3.1 CISS in electron transmission 4
  - 1.3.2 CISS in electron transport 10
  - 1.3.3 Magnetoresistance in CISS-based planar junctions 15
  - 1.3.4 Enantioseparation of chiral molecules based on the CISS effect . . . 19
- 1.4 Theoretical models 23
- 1.5 Filling the gap 31

2 Experimental methods and materials **33**
- 2.1 Vacuum system 33
- 2.2 Scanning tunneling microscopy and spectroscopy 35
  - 2.2.1 Tunneling through one-dimensional barrier 36
  - 2.2.2 Bardeen perturbation theory 38
  - 2.2.3 Spin polarized tunneling 42
  - 2.2.4 Constant current mode 46
  - 2.2.5 Constant height mode 47
  - 2.2.6 $I - V$ characteristics 47
  - 2.2.7 dI/dV spectroscopy 48
- 2.3 Materials 50

3 Experimental results **53**
3.1 Manuscript 1: Deposition of chiral heptahelicene molecules on ferromagnetic Co and Fe thin-film substrates 53
3.2 Manuscript 2: Enantioselective adsorption on magnetic surfaces 73
3.3 Enantioselective adsorption of enantiopure *(M)*-[7]H molecules on magnetic Co nanoislands 102
3.4 Manuscript 3: Spin-selective electron transport through single chiral molecules 109
3.5 Enantiospecific magnetic conductance asymmetries through single chiral molecules 128

4 Summary and Outlook **137**

A Appendix A **142**

B Appendix B **148**

Bibliography **151**

Acknowledgements **161**

Erklärung zur Dissertation **163**

Lebenslauf *(Curriculum Vitae)* **165**

CHAPTER 1

Introduction

1.1 Chirality

Chirality is a property of certain objects that refers to their lack of mirror symmetry. The term originates from the Greek word "kheir," which means hand, and it was first defined by Lord Kelvin in the following manner [1]:

> "I call any geometrical figure, or group of points, chiral, and say it has chirality, if its image in a plane mirror, ideally realized, cannot be brought to coincide with itself."

In other words, a chiral object cannot be superimposed on its mirror image, no matter how it is rotated, or translated.

Chiral objects are prevalent across a wide range of scales, from cosmic structures such as spiral galaxies to small-scale objects like human bodies and even down to the microscopic level of single molecules. The concept of chirality in molecules was first uncovered through observations of the optical activity of natural tartaric acid, a compound produced during the process of wine fermentation. These observations were made by Pasteur as part of a comprehensive investigation into the interactions between light and matter [2]. Chirality was later discovered to be present in other molecules involved in organic life, such as DNA, which forms a right-handed double helix in living organisms, and the left-handed amino acids that make up proteins in living cells. This discovery has led to the concept of enantioselectivity in nature, which refers to the preference for one enantiomer over the other in biological systems. The term enantiomer is derived from the Greek words $\epsilon\nu\alpha\nu\tau\iota o\sigma$ (enantios) and $\mu\epsilon\rho o\sigma$ (meros), meaning 'opposite' and 'part' and it is used in chemistry to describe the two different handednesses of a chiral molecule, as illustrated in Figure 1.1.

For instance, L- and D-alanine[1] are two different enantiomers of a molecule with the same chemical components, but they can have different biological effects. Specifically, L-alanine is the active form found in human proteins, while D-alanine is more commonly found in bacterial cell walls and some antibiotics [3].

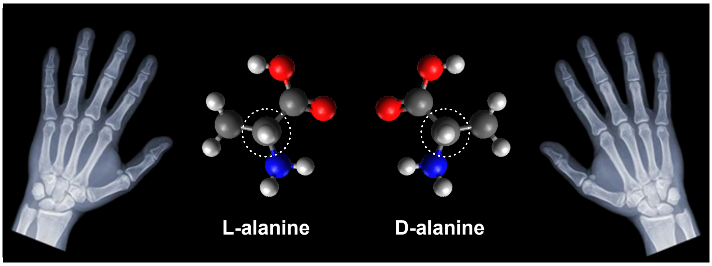

Figure 1.1: The chirality of two asymmetric alanine enantiomers is illustrated as a lack of mirror symmetry. Like our hands, the two mirror images cannot be superimposed. The alanine molecule's chiral center is shown by the dotted circles.

The dotted circles in Figure 1.1 indicate the carbon atom to which four different substituents are attached and is referred to as a chiral center. However, chirality can also be present in molecules that lack a chiral center, as a result of their inherent three-dimensional chiral geometry [4]. One type of inherent chirality is helicity, which occurs in helical molecules with a screw-shaped molecular structure. A well-known example of such chiral structures is DNA, which typically adopts a right-handed helical pattern. Heptaphelicene, the molecule of interest in this study, is another example which exhibits chirality due to the seven ortho-fused benzene rings that do not lie in a single plane, as shown in Figure 1.2. The left- and right-handed [7]H enantiomers are designated *(M)*-[7]H and *(P)*-[7]H, respectively, with M and P representing 'minus' and 'plus' helicity.

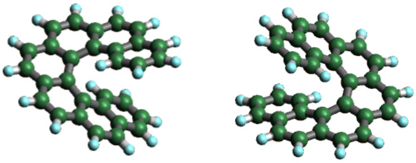

Figure 1.2: Schematic representation of the *(M)*-[7]H (left side of the figure) and *(P)*-[7]H (right side of the figure) molecules.

---

[1] L and D stand for Latin laevus (left) and dexter (right).

1.2 Chirality-induced spin selectivity (CISS)

Chirality was believed to be a purely spatial characteristic for a long time. However, a groundbreaking experiment published in 1999 challenged this belief by demonstrating asymmetrical scattering of electrons with opposite spin polarizations when propogating through chiral organic molecules [5]. In this experiment, circularly polarized light was used to emit spin-polarized photoelectrons from a gold substrate. These electrons were then transmitted through sandwiches composed of five ordered monolayers (MLs) of homochiral stearoyl lysine molecules, which were deposited on the gold surface. The asymmetry in the scattering probability of these spin-polarized electrons upon their transmission through the chiral molecules was then calculated using the following formula [5]:

$$A = \frac{I(+) - I(-)}{I(+) + I(-)}. \tag{1.1}$$

In this equation, $I(+)$ and $I(-)$ represent the intensities of electron beams with positive and negative helicities, respectively. Given the fixed propagation direction of the electrons (from the gold substrate towards the molecule) in this experimental setup, the electron beam intensity with opposite electron helicity can be simplified to the electron beam intensity with opposite electron spin. The calculated asymmetry, with a magnitude of approximately $|A| \approx 0.12$, was three orders of magnitude higher than what has been previously reported in experiments, which studied the asymmetric scattering of electrons with opposite helicity after passing through chiral molecules in their gaseous phase [6, 7]. The phenomenon attracted the attention of scientists after another experiment was published in 2011. Where it was demonstrated that electrons passing through a ML of right-handed double-stranded DNA (dsDNA) exhibited spin polarization exceeding 60% at room temperature (RT) [8]. A detailed explanation outlining the process of calculating this spin polarization will be provided in Section 1.3.1.

Naaman and Waldeck later introduced the concept of the Chirality-Induced Spin Selectivity (CISS) effect, stating that chiral organic molecules on surfaces can act as electron spin filters at RT. Specifically, when electrons are transmitted through chiral molecules, one spin alignment is preferred over the other, and the preferred spin alignment is determined by the molecular chirality and the electron propagation direction [9]. Since then, the CISS effect has been the subject of numerous scientific investigations, exploring a wide range of molecules, substrates, and techniques. These studies have not only deepened our understanding of the CISS effect, but also demonstrated its successful implementation across various experiments, thereby sparking curiosity and enthusiasm among scientists from diverse disciplines. This growing collection of successful experimental results, including the achievement of 99% spin polarization at RT [10], continues to motivate this enthusiasm. Moreover, the CISS effect is not only promising for applications in fields such as spintronics, chemical sensing, enantioseparation, and enantioselective chemical and biological processes [11–14], but it also demonstrates potential to address critical technological needs in human society. These include developing efficient photovoltaic cells based on chiral organic-inorganic devices [15], promoting clean energy harvest through enhanced electrocatalytic oxygen evolution [16], and exploring potential uses for quantum computing technology [17]. Consequently, there is an increasing demand to comprehend the fundamental physical principles underlying this phenomenon and to offer a quantitative understanding of it. The following sections will focus on experimental and theoretical works that contribute towards a more detailed understanding of the CISS effect and help us to become familiar with its promising potential in future applications.

1.3 An overview of experimental studies on CISS

Inspired by the initial reports on this phenomenon, numerous experimental studies have been conducted to further understand the CISS effect [9, 11, 13, 14, 18, 19]. A summary of these experimental efforts will be provided in this section, with the experiments being categorized into four different groups based on the methods used.

- CISS in electron transmission
- CISS in electron transport
- Magnetoresistance in CISS-based planar junctions
- enantioseparation of chiral molecules based on the CISS effect

1.3.1 CISS in electron transmission

Historically, the CISS-related transmission study began with photoemission experiments using an Au substrate, capable of emitting spin-polarized photoelectrons when illuminated by circularly polarized light. This illumination was achieved using a laser beam with an energy of about 5 eV, enough to excite electrons beyond their work function [20]. The handedness of the circularly polarized light, whether clockwise (cw) or counterclockwise (ccw), determines the sign of the spin polarization. Specifically, cw and ccw laser beams created electrons with negative and positive spin polarization, respectively [8] (see Figure

1.4(b)). After creating these spin-polarized electrons, they were then propagated through ML(s) of chiral molecules such as stearoyl lysine, polyalanine, single-stranded DNA and dsDNA, all coated on Au substrates [5, 20–22]. The intensity of transmitted electrons through these molecular layers was then measured using a time-of-flight (TOF) electron spectrometer. By comparing these intensities, it was concluded that different spin polarizations correspond to different transmission probabilities through chiral molecules. A schematic representation of such an experimental setup is shown in Figure 1.3(a).

Figure 1.3(b) displays the energy distribution of spin-polarized electrons following transmission through a right-handed dsDNA ML deposited on an Au substrate. A notable difference in intensity is observed between the electrons initially emitted by ccw polarized light and those created by cw polarized light. This difference is quantified as transmission selectivity (S) using the formula [20]:

$$S = \frac{I_{\mathrm{ccw}} - I_{\mathrm{cw}}}{I_{\mathrm{ccw}} + I_{\mathrm{cw}}}. \tag{1.2}$$

In this equation, I_{ccw} and I_{cw} represent the intensities of electrons originally polarized by ccw and cw light, respectively, after their transmission through the chiral molecules. According to Figure 1.3(b), these data show a selectivity of $8 \pm 2\,\%$. Taking into account an estimated initial spin polarization of 15% for the photoelectrons emitted from the gold substrate, the observed data demonstrates that the chiral dsDNA layer exhibits a minimum spin selectivity of 50% [20].

Although initial studies successfully illustrated spin-dependent electron transmission through chiral molecular layers, these explorations were constrained by a dependence on indirect analysis for determining spin selectivity. They required first examining the difference in intensities of the transmitted electrons, followed by consideration of the initial spin polarization from the photoemission process. To address this challenge, Göhler *et al.* in 2011, proposed using a Mott polarimeter to directly measure the spin polarization of electrons post-transmission through chiral molecules [8].

Figure 1.4(a) shows a Mott electron polarimeter setup, employed to measure spin polarization of the electrons after transmission through the chiral molecular layer. The functioning of the Mott polarimeter is based on the concept of spin-orbit interaction (SOC)[2]. Spin-polarized electrons, shown as green solid line, are directed towards a thin target made of a high atomic number (Z) material, such as gold foil. The polarization of the incoming

---

[2] Detailed descriptions of the working principle and technical information of the Mott polarimiter can be found in Ref. [23]

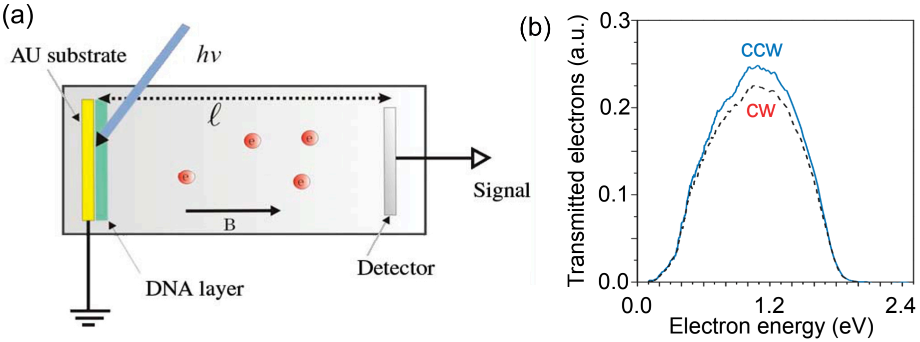

Figure 1.3: (a) The experimental setup in which a circularly polarized laser is used to emit photoelectrons from a gold substrate coated with an ordered ML of dsDNA oligomers. (b) The energy distribution of the transmitted photoelectrons through a ML made from dsDNA oligomers. The electrons are emitted from the gold with clockwise (cw, dotted line) or counterclockwise (ccw, solid line) circularly polarized laser ligth. Figures partially adapted from Ref. [20]

electrons (denoted as $\mathrm{P} = (\mathrm{N}_\uparrow - \mathrm{N}_\downarrow)/(\mathrm{N}_\uparrow + \mathrm{N}_\downarrow)$, where $\mathrm{N}_\uparrow$ ($\mathrm{N}_\downarrow$) is the number of spin-up (spin-down) electrons, relative to the scattering plane) is assumed to be perpendicular to the scattering plane. As a result of spin-orbit interaction, spin-dependent scattering occurs, leading to an asymmetry in intensity (A) between the left and right scattered electrons at set scattering angles $\pm\theta$ [8]. This asymmetry can be expressed as:

$$A = \frac{N_l - N_r}{N_l + N_r}. \tag{1.3}$$

Here, N_l and N_r indicate the number of electrons scattered to the left and right, correspondingly. The transverse polarization (P) of the incident electron beam (represented by a green solid line) is then determined using the relation $A = S_{\text{eff}}P$. S_{eff} is a term that denotes the effective Sherman function. It's a characteristic of the specific experimental setup and can be calibrated by measuring the asymmetry of an electron beam with a known spin polarization. For this particular setup, S_{eff} has been determined to be $-(0.229 \pm 0.011)$ [8].

Figure 1.4(b) displays the measured spin polarization of electrons emitted from a bare Au(111) single crystal using three types of polarized light: cw, ccw, and linear. For circularly polarized light, an intensity asymmetry of $\mathrm{A}{=}\pm(5.03 \pm 1.1)\%$ was reported. Once corrected by S_{eff}, this asymmetry represents a spin polarization of ±22%. However, in

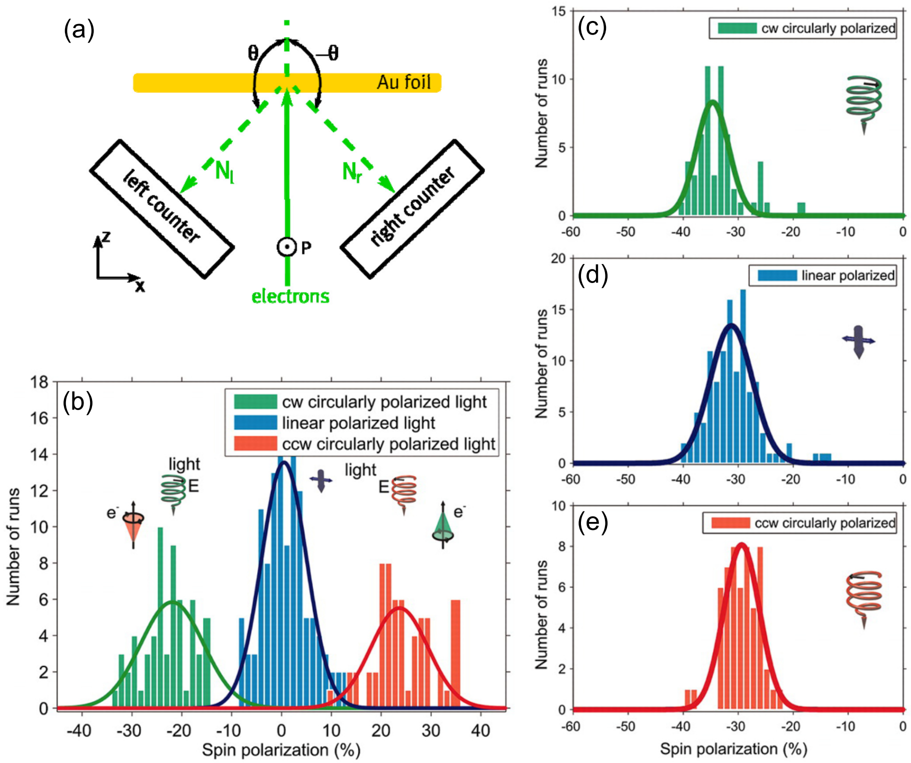

Figure 1.4: (a) Schematic sketch of a Mott electron polarimeter setup. (b) Spin polarization measured for electrons emitted from bare Au(111) with clockwise (cw) (green) and counterclockwise (ccw) (red) circularly polarized light, and with linearly polarized light (blue). The polarization is −22, +22, and 0%, respectively. The longitudinal spin polarization is measured; the spin is oriented parallel (green) or antiparallel (red) to the direction of propagation of the electron. (c-e) Spin polarization of electrons transmitted through 50-bp dsDNA/Au(111). The polarizations were −35, −31, and −29% for light polarized cw circularly [(c), green], linearly [(d), blue], and ccw circularly [(e), red], respectively. Figures adapted from Ref. [8]

the case of linearly polarized light, the measured spin polarization was 0%.

In a subsequent experiment, a self-assembled monolayer (SAM) of 50-base pair[3] (bp) long right-handed dsDNA was deposited on the Au(111) surface. The same set of light polarizations was then used to determine dsDNA molecules' spin selectivity at RT. The

---

[3] Base pairs in DNA consist of two nitrogen-containing nucleotides that come together to form the DNA structure. The four bases in DNA are adenine (A), cytosine (C), guanine (G), and thymine (T), and they form specific pairs: A pairs with T, and G pairs with C. The term 'base pair' (bp) is also a unit used to measure the length of DNA sequences [24]

spin polarization of electrons, after transmission through the molecular layer, is depicted in Figures 1.4(c-e). The results indicate a spin polarization of $-29 \pm 3\%$ for electrons generated by linearly polarized light, and $-35 \pm 3\%$ and $-31 \pm 4\%$ for those generated by cw and ccw circularly polarized light, respectively [8]. Interestingly, even the electrons generated by linearly polarized light, which do not possess an initial spin polarization, become spin-polarized after their transmission through the chiral molecules. These results indicate that the spin polarization of the post-transmission electrons shows a weak dependence on the initial spin polarization of photoelectrons emitted from the Au substrate.

Additionally, three different lengths of dsDNA molecules were deposited on polycrystalline Au substrates - with lengths of 40, 50, and 78 bp - to investigate the impact of the chiral molecules' length on the degree of spin polarization. Notably, although the initial spin polarization of the photoelectrons emitted from the polycrystalline gold substrate was negligible for all three employed light polarizations (cw, ccw, and linear), the measured spin polarization of the electrons after their transmission through the molecules showed a significant effect. For ccw polarized light, the initial spin polarization of $-4.1 \pm 6.3\%$ improved significantly to $-40.1 \pm 5.5\%$, $-38.8 \pm 5.9\%$, and $-60.8 \pm 5.8\%$ after transmission through 40, 50, and 78 bp dsDNA respectively [8]. Demonstrating that nearly spin-balanced electrons become highly spin-polarized, exceeding 60%, after propagation through the ML of 78 bp dsDNA molecules at RT.

Numerous studies have since built upon the initial findings, broadening our comprehension of the CISS mechanism by analyzing the spin polarization of transmitted electrons through a variety of molecules deposited on different substrates. One particular study used long oligopeptides, deposited on Au substrates. This experiment involved a systematic investigation into the dependence of spin polarization on molecular length. The results demonstrated a clear trend: as the molecular length increased from 2.2, to 2.5, and finally to 2.8 nm, the spin polarization of transmitted electrons correspondingly increased, with respective values of -11%, -15%, and -18% [25]. This correlation is consistent with Göhler *et al.*'s description of the dependence between molecular length and spin polarization degree, thereby justifying their interpretation. The investigation then focused on the impact of substrate characteristics on the CISS effect, using long bacterorhodopsin molecules with a length of 49 Å deposited on Au and Al [26]. Interestingly, it was observed that changing the substrate from Au - a heavy metal with high SOC, to Al - a lighter metal with weaker SOC, only resulted in a minor alteration in the spin polarization of the electrons after propagating through the molecules. Under illumination with a cw polarized light beam, spin polarization changed from $17 \pm 5\%$ on Au to $15 \pm 4\%$ on Al.

As the investigation progressed, another twist was added by switching the type of chiral molecules. A double layer of DPED[4] molecules, which are very short (0.25 Å), lack a helical structure, but possess a chiral center, was deposited on a single crystalline Co substrate. The observation of a 5% spin polarization served as a key indication that spin selectivity is not exclusively a feature of long helical molecules; it can be detected even in very short molecules with a chiral center [27].

Furthermore, a detailed study was conducted to explore the spin polarization of electrons transmitted through both enantiomeric forms of the [7]H molecules (shown in Figure 1.2). These molecules, which are of interest to this PhD research, were deposited on three single crystalline substrates: Cu(332), Ag(110), and Au(111) [28]. Although the [7]H molecule is relatively small, possessing a single helical turn, the experiment outcomes were quite promising. When the *(P)*-[7]H molecules were deposited on the Cu(332) substrate, spin polarizations of $+5.5\pm0.6$, $+6.1\pm0.6$, and $+4.4\pm0.6$ were recorded for linear, cw, and ccw light polarizations, respectively. On the other hand, for the *(M)*-[7]H molecules deposited on the same substrate, the measured spin polarizations were -6.7 ± 0.6, -6.0 ± 0.6, and -6.3 ± 0.6. In fact, it was the first experimental evidence, in an electron transmission study, demonstrating that the spin of the preferentially transmitted electron depends on the handedness of the chiral molecule. Interestingly, the same pattern was observed even when the substrate was switched from Cu(332) to Ag(110) and Au(111). Additionally, it was noted that changing the substrate from the heavy metal Au to lighter elements like Ag or Cu had a minimal effect on the amplitude of spin polarization, which is consistent with previously reported experimental observations [28].

To summarize, the experiments provided robust evidence for the validity of the CISS effect for a wide variety of chiral molecules. Ranging from complex, lengthy structures such as DNA and oligopeptides to smaller and simpler molecules such as helicene. These studies demonstrated a link between the handedness of the chiral molecule and the preferential spin orientation of transmitted electrons. Different light polarizations have been employed, establishing that the effect is largely independent of the incident light beam polarization. Furthermore, it was noted that the effect amplifies with an increase in molecules length. This observation aligns with theoretical models that analyze electron spin polarization in CISS effect as a function of chiral molecules' length [29–31]. By exploring the CISS effect on a range of substrates - from heavy metals with strong SOC to lighter metals with weaker SOC - it's been validated that the effect is primarily attributed to the molecular geometry and not the substrate. This interpretation contradicts some

---

[4] 1,2-diphenyl-1,2-ethanediol (C6H5-CHOH-CHOH-C6H5)

theoretical studies [32, 33] that propose substrate-mediated SOC as a key factor in the effective spin selectivity of chiral molecules, a topic that will be further discussed in Section 1.4.

Having reviewed CISS experiments conducted in electron transmission studies, we have deepened our understanding of this remarkable effect. This leads us to the next step, in which we will discuss other experimental approaches that aimed to expand the potential applications of the CISS effect. In the next section, our focus will shift to the study of CISS within the framework of transport experiments, which are more relevant for potential applications of CISS, especially in the field of spintronics.

1.3.2 CISS in electron transport

In CISS-related transport experiments, charge carriers are constrained to move within chiral electrostatic potentials, which may involve hopping or tunneling mechanisms. The method involves placing chiral molecules between conductive leads and applying a bias voltage between the two leads to measure conductance through chiral molecules. The fabrication process of these organic-metal contacts requires precision, given the critical need to control transport at the interface between the molecule and the leads, as well as ensuring the intactness of the organic molecule [18, 34].

Prior to the introduction of CISS experiments, preliminary investigation had already established that by positioning dsDNA molecules between two metallic leads - the tip of a conductive probe atomic force microscope (CP-AFM) and a gold substrate - and applying a bias voltage, it is possible to measure the conductance through these molecules [35]. Building on this foundation, Xie *et al.* later conducted a follow-up experiment. In their study, the gold substrate was replaced with an out-of-plane magnetized ferromagnetic nickel. They measured the transported current as a function of the applied bias voltage through dsDNA molecules of three different lengths (26, 40, and 50 bp) which led to the observation of spin-selective conduction in right-handed dsDNA molecules [36]. A schematic representation of the experimental setup is shown in Figure 1.5(a).

The ferromagnetic Ni substrate was placed above a permanent magnet in order to align its out-of-plane magnetization direction, either parallel or antiparallel to the substrate's surface normal. Single-stranded DNA (ssDNA) molecules were applied to the Ni substrate, while the complementary ssDNA strand was attached to a gold nanoparticle. Only when both strands came together and hybridized into a dsDNA structure was a conductive connection established. The gold nanoparticle was used to establish a proper contact point

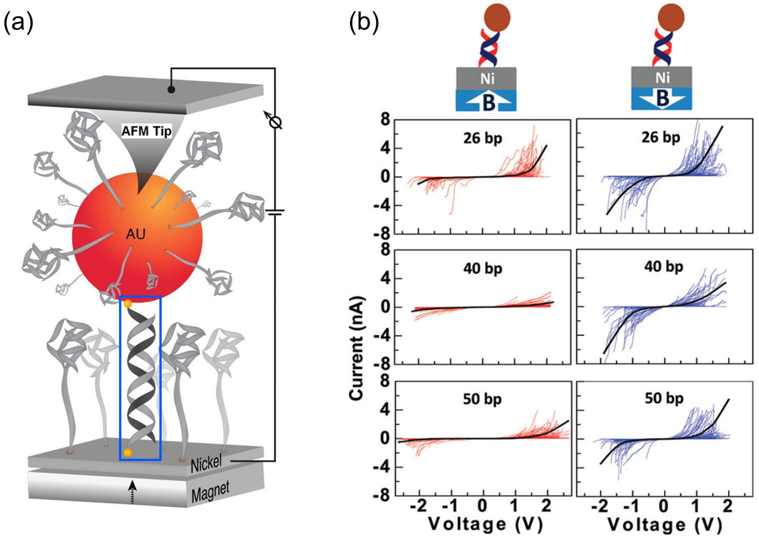

Figure 1.5: (a) Schematic representation of the experimental setup that measures current through a dsDNA molecule (enclosed by a blue rectangle) deposited on a magnetic Ni substrate using a CP-AFM device. Gold nanoparticles were employed to ensure effective electrical contact between the DNA molecules and the AFM tip. (b) Represents the measurement of the current transported through dsDNA oligomers of different lengths (26, 40, and 50 bp) versus the applied bias voltage when the substrate's magnetization was either parallel (upward) or antiparallel (downward) to the surface normal of the substrate. Figures adapted from Ref. [36]

with the tip of the AFM device. After approaching the AFM tip to the gold nanoparticle and establishing contact, the transported current through the molecular junctions was measured as a function of the applied bias voltage and the magnetization alignment of the Ni substrate.

Figure 1.5(b) displays the I-V curves, measured through right-handed dsDNA oligomers of three different lengths. The left panels show red curves representing the measured I-V curves when the substrate magnetization was parallel to the surface normal. The right panels show blue curves depicting the obtained I-V curves when the substrate magnetization was switched from parallel to antiparallel alignment.

To mitigate fluctuations in the obtained I-V curves, which could arise from imperfect contact points or different numbers of molecules contributing to each measured I-V curve, averaged curves were calculated and represented by thick black curves. Upon comparison of these averaged curves for each molecule length, it can be observed that the magnitude of the measured current was influenced by the magnetization direction of the Ni substrate. A higher current magnitude was detected when the magnetization of the substrate was oriented antiparallel to the surface normal (shown by the downward alignment in Figure 1.5(b)). Based on this observation, the authors concluded that spin-down electrons are preferentially transported through right-handed dsDNA molecules when the electrons are flowing away from the Ni substrate, while the opposite spin will dominate the measured current when electrons are flowing from the non-magnetic tip to the magnetic substrate [36]. Therefore, chirality-induced spin selectivity is not only dependent on the handedness of chiral molecules and electron spins, but also on the electron's propagation direction [18, 37].

Despite the complexity of deducing a consistent correlation between amplitude of the measured current, degree of spin selectivity, and length of dsDNA oligomers from this data, the authors have settled for a qualitative explanation, namely that spin selectivity of currents transported through dsDNA molecules is significantly higher for oligomers of 40 and 50 bp, but much less for oligomers of 26 bp.

Following this experimental report, several research groups used the CP-AFM measurement technique to study a variety of molecules. The aim was to determine the impact of the length and type of different enantiomers on the degree of spin polarization in chiral molecules, and to build upon the findings of initial study [25, 38–42]. A number of these studies selected long oligopeptides as the basis for molecular selection [25, 40, 41]. For instance, Tassinari *et al.* used oligopeptides of different handedness, *L*- and *D*-oligopeptides, deposited on Au-coated ferromagnetic Ni substrates. Using a non-magnetic AFM tip, it was shown that when electrons move away from a magnetic substrate, which has been magnetized parallel to the substrate's normal vector, the *L*-oligopeptides (right-handed helix) exhibit higher conductivity than the *D*-oligopeptides (left-handed helix). Conversely, when the magnetization alignment of the substrate is reversed from parallel to antiparallel, *D*-oligopeptides exhibit higher conductivity than *L*-oligopeptides [41].

In another study, a SAM of two different oligopeptides, AL5 and AL7[5], with different lengths but the same handedness, was deposited on a gold substrate. Using a magnetic AFM tip, the transported current through the molecules has been measured and it was reported that the degree of spin selectivity increases with the length of the molecule [40]. The research scope expanded to incorporate other types of molecules. These ranged from longer molecules like cysteine (2.2 nm) [38] and proline (1.5 nm) [42] - comparable in length to the previously discussed oligopeptides - to smaller ones like cationic

---

[5] Al5:SH–(CH2)2NH–(Ala-Aib)5–COOH; Al7:SH–(CH2)2NH–(Ala-Aib)7–COOH

[4]helicene [39], which consists of a single helical turn. Interestingly, all of these diverse molecules demonstrated the CISS effect, illustrating its potential applicability across a wide range of molecules. Among the above mentioned molecules, the cationic [4]helicene (See Figure 1.6a) deserves special attention due to its structural similarities to heptahelicene (the molecule under study in this PhD work). Therefore, an in-depth review of the experimental study involving this molecule will offer valuable insights. In addition, it will serve as a benchmark for comparing the results of our transport experiments obtained from single [7]H molecules, which will be presented in Chapter 3.

Kiran and coworkers deposited enantiopure cationic [4]helicene molecules with *P-(M-)* chirality on a highly oriented pyrolytic graphite (HOPG) substrate and used a CP-AFM setup (shown in Figure 1.6a) to compare the spin-dependent conduction through the different enantiomers with respect to the magnetic alignment of the Fe tip [39]. As shown in Figures 1.6(b) and (c), a number of I-V curves were measured above the *M-1a* helicene molecules for tip magnetization up and down (parallel and antiparallel to the substrate's surface normal), respectively, and an average of these curves is shown in Figure 1.6(d). Another set of experiments was conducted with the *P-1a* helicene molecules, and the averaged I-V curves for the two orientations of the magnetic tip are presented in Figure 1.6(e). The spin polarization (SP) was calculated based on the measured curves using the following equation[6]:

$$SP = \frac{I_{\text{Down}} - I_{\text{Up}}}{I_{\text{Down}} + I_{\text{Up}}}. \tag{1.4}$$

In this context, I_{Up} represents the measured current when the magnetic alignment of the tip is parallel to the substrate's surface normal. Conversely, I_{Down} corresponds to the measured current when the magnetization is in an antiparallel alignment. Figure 1.6(f) presents the spin polarization. When a bias voltage of 1.0 V is applied, the spin polarization for the P- and M-enantiomers were measured to be $49 \pm 3\%$ and $-45 \pm 3\%$, respectively [39]. Remarkably, high spin polarization was achieved using relatively short molecules, possessing only a single helical turn. This noteworthy finding further supports the idea behind our focus on [7]H molecules. Given the inherent simplicity and similar short length of both [7]H molecules and cationic [4]helicene (approximately one helical turn), the [7]H molecules serve as promising model systems, potentially enabling comprehensive theoretical exploration and analysis of the CISS effect.

---

[6] Although 'spin polarization' is often used in the literature, it technically refers to the product of the SP generated in the molecule and that of the FM detector electrode (see Eqs. 2.19 and 2.20). The SP of

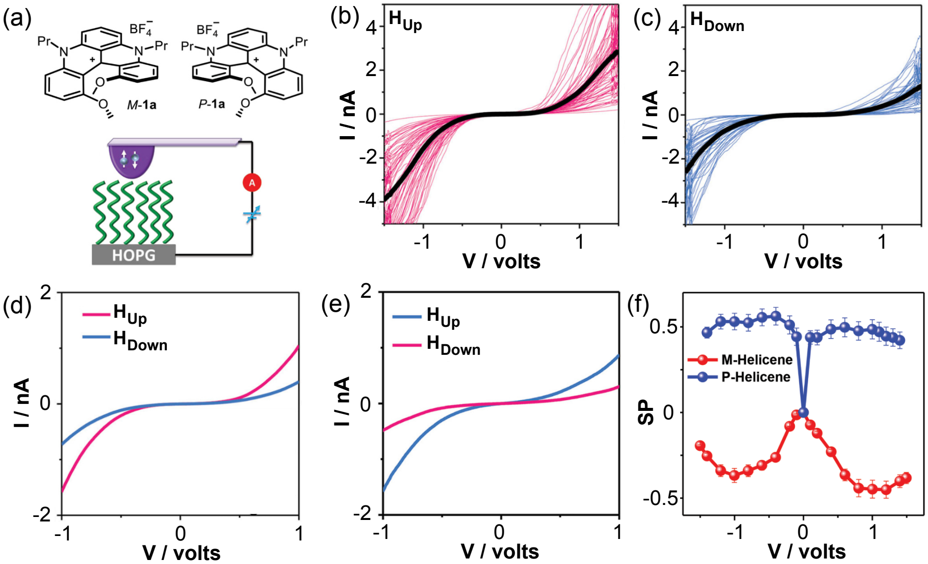

Figure 1.6: (a) Chemical structures of *M-1a* and *P-1a* cationic [4]helicene molecules and diagram of CP-AFM measurements performed with the ferromagnetic Fe tip. (b) and (c) Number of *I-V* curves are plotted from various *M-1a* helicene molecules for tip magnetization in the up and down directions, respectively. (d) Depicts the averaged *I–V* curves extracted from (b) and (c). (e) Shows the averaged *I–V* curves extracted from the various *I-V* measurements above *P-1a* helicene molecules for tip magnetization in the up and down directions. (f) Spin polarization as a function of applied bias voltage for *P*- and *M-1a* helicene molecules adsorbed on HOPG. Figure adapted from Ref. [39]

While the majority of transport experiments have employed the CP-AFM measurement technique, there have been alternative methodologies applied to measure transport of spin-polarized electrons in chiral molecules. One such method, reported by Al-Bustami *et al.*, steps beyond the conventional conductive probe technique to demonstrate the CISS effect. An application-oriented direction was pursued through the fabrication of a nano-scale (30 nm) triple junction device, which incorporated alpha-helix polyalanine molecules. This construction allowed for the measurement of the spin-dependent conductivity of these molecules, marking a significant step towards the potential fabrication of a miniaturized, chiral molecule-based memristor-like logic gate [43].

In another type of examination, precise manipulation of the scanning tunneling microscope (STM) assists performing detailed investigation of the spin polarization property

---

the FM electrode represents the electrode's spin detection efficiency, similar to the Sherman function in a Mott detector.

of chiral molecules [44, 45]. An STM break-junction, comprised of peptide molecules with specific chirality, is bridged between a magnetized STM nickel tip and a gold substrate and the conductivity of the two enantiomers was compared by adjusting the experimental variables, such as the magnetization orientation of the Ni tip, the handedness of the chiral molecules and the sign of the applied bias voltage [44]. The experiment's outcomes reveal that under one specific orientation of the tip magnetization (antiparallel to the substrate's surface normal), the *D*-peptide exhibits higher conductivity than the *L*-peptide, irrespective of the electron propagation direction (whether from the tip to the substrate or vice versa). Conversely, when the tip magnetization direction is reversed, the *L*-peptide displays higher conductivity for both electron propagation directions. Compared to the aforementioned studies [25, 36, 38–43, 45], where the applied bias voltages were in the range of a few volts, the bias voltage in this transport experiment was decreased by two orders of magnitude ($\pm 50\,\mathrm{mV}$). In comparison to previous reports, this study focused on a narrower energy interval around the Fermi level which makes it easier to compare the results with theoretical models.

To summarize, transport experiments have demonstrated the presence of the CISS effect by measuring the propagated currents through various molecules on different substrates. Additionally, it has been reported that the CISS effect becomes more pronounced as the length of the molecules increases [36, 40] which aligns with the conclusions presented in Section 1.3.1.

Transport experiments using scanning probe microscopy provide a solid foundation for investigating the CISS effect and deepening our understanding of it, but they remain a primarily fundamental approach. To bring the CISS effect closer to real-world applications, the design and development of devices utilizing the CISS effect will be explored in the following section.

1.3.3 Magnetoresistance in CISS-based planar junctions

In a typical giant magnetoresistance (GMR) [46, 47] or tunnel magnetoresistance (TMR) [48, 49] spin valve, a device is constructed with two layers of ferromagnetic material separated by a thin layer of non-magnetic metal or an insulator, respectively. The ferromagnetic layer which serves as a reference, known as the pinned layer, has a fixed magnetization, typically obtained through exchange coupling with an adjacent antiferromagnetic layer. This layer functions as a spin polarizer. The other ferromagnetic layer, known as the free layer, adapts its magnetization direction when an external magnetic field is applied, acting as a spin analyzer. By applying a current through the device, the resistance of the GMR(TMR) sensor changes depending on the relative alignment of the magnetization of the free layer with that of the pinned layer.

In contrast to conventional GMR(TMR) spin valves, a CISS-based spin valve utilizes a different approach by replacing the ferromagnetic reference layer and the non-magnetic metal(insulator) interlayer with a chiral tunneling barrier [50] as shown in Figure 1.7.

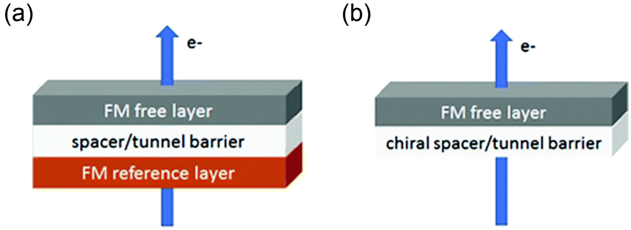

Figure 1.7: Schematic representation of a conventional GMR spin valve (a) and a CISS-based spin valve. The blue arrow indicates the direction of electron propagation when an electrical current is applied. Figure adapted from Ref. [50]

To determine the magnetoresistance of a CISS-based spin valve, a constant current is applied through the system while measuring the voltage drop between the leads in the presence of an external magnetic field. The magnetoresistance is the change in the electrical resistance of the device as the magnetic field is altered. Accordingly, the external magnetic field is swept from a direction parallel to the current flow, known as (H+), to a direction that is antiparallel to the current flow, known as (H-). Consequently, the magnetoresistance of the device can be calculated by using the following equation:

$$\mathrm{MR(H)} = \frac{\mathrm{R(H)} - \mathrm{R(0)}}{\mathrm{R(0)}}, \tag{1.5}$$

where R(0) stands for the resistance of the device in the absence of an external magnetic field and R(H) indicates the resistance when an external magnetic field is applied, which can be either in the H+ or H- direction[7].

In 2014, Mathew *et al.* conducted a noteworthy study in which they proposed an alternative approach for the design of spin valve magnetoresistance devices utilizing chiral

---

[7] This definition of MR is commonly used in spintronics for GMR and TMR measurements, typically performed under constant current conditions. In contrast, CISS-related measurements are performed under voltage control, where CISS-MR is defined as the ratio of the difference to the sum of currents measured when the magnetic field is oriented in the H- and H+ directions, as described in Eq. 1.4.

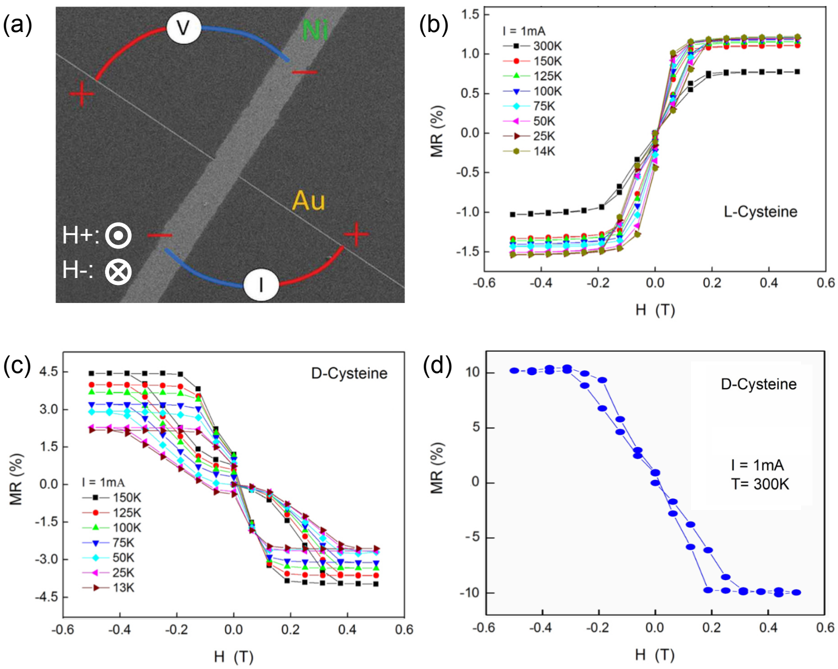

Figure 1.8: (a) SEM image, obtained from a top-view perspective, illustrates a device featuring a thin gold trace (1 μm wide) and a wide nickel trace (50 μm wide) arranged perpendicularly. By passing a constant current (notated as 'I') between the Au and Ni electrodes of the spin valve device, the consequent voltage drop (indicated as 'V') across this device can be measured. The graph in (b) illustrates the magnetoresistance of the device when a constant current of 1 mA is passed through it, for *L*-cysteine at different temperatures. Similarly, (c) and (d) depict the magnetoresistance of a *D*-cysteine device at different temperatures and at a temperature of 300 K, respectively. Figures adapted from Ref. [51]

molecules [51]. A SAM of chiral molecules was deposited on top of a gold electrode to replace the magnetic reference layer with a non-magnetic, organic/inorganic chiral tunneling barrier. This was achieved by depositing a thin polycrystalline layer (1.5 - 2 nm) of Al_2O_3 on top of the chiral molecules, which induced chiral properties in the Al_2O_3 film [52]. The final structure was completed by depositing 150 nm Ni layer on top as a magnetic free layer. A scanning electron microscope (SEM) image (top view) of the fabricated device is shown in Figure 1.8(a).

The magnetoresistance of the device was characterized by measuring the resistance of the tunneling barrier under a constant current of 1 mA while varying the applied magnetic field at different temperatures. The results, presented in Figures 1.8(b) and (c) show the magnetoresistance as a function of the applied magnetic field for *L*- and *D*-cysteine molecules at different temperatures, respectively. Figure 1.8(b) displays a decreasing behavior in the magnetoresistance of a device utilizing the *L*-cysteine molecule by increasing temperature. In contrast, when *D*-cysteine is used, the magnetoresistance value increases with temperature as can be seen in Figure 1.8(c). It reaches maximum magnetoresistance of approximately ±10% at 300 K, as shown in Figure 1.8(d). The authors did not offer a definitive explanation for the temperature dependence of magnetoresistance, speculating that it may result from contamination, which underscores the sensitivity of this dependence to the system's properties. Similar results demonstrating the dependence of magnetoresistance on temperature changes have been reported by [50, 53]. However, another study claims that the magnetoresistance value is not affected by temperature changes and considers the magnetoresistance in a device containing supramolecular chiral molecules to be independent of controlled temperature variations [54]. This implies that there isn't a general behavior for the dependency of magnetoresistance on temperature across different molecules. Apart from the different temperature-dependent reactions of *D*- and *L*-cysteine enantiomers, it's interesting to note that *D*-cysteine usually has a more pronounced magnetoresistance signal compared to the *L*-cysteine under equivalent experimental conditions. Additionally, the overall shapes of the magnetoresistance curves reveal that *D*-cysteine molecules exhibit positive magnetoresistance values when the external magnetic field is oriented in the H- direction and negative values when the field direction changes to H+. In contrast, *L*-cysteine molecules display the opposite pattern. This behavior is consistent with the CISS effect, where the chiral molecules cause the electric current passing through them to become spin-polarized. This spin polarization is then detected by the ferromagnetic Ni layer. Because *D*- and *L*-cysteine induce opposite spin polarizations, they result in magnetoresistance values of opposite signs under the same magnetic field conditions.

In subsequent studies, similar investigations have been conducted using a variety of chiral molecules, ranging from long conductive polymers and CdSe quantum dots to short helicene molecules [38, 39, 53]. These studies aimed to establish the practicality of chiral molecules in spin valve devices. However, the magnetoresistance values reported were significantly smaller (for instance, only ±1% for cationic [4]helicene [39]) than conventional spin valve devices used in real-world applications.

1.3.4 Enantioseparation of chiral molecules based on the CISS effect

Chiral molecules are ubiquitous building blocks of the molecules of life. Despite identical chemical composition and physical properties under achiral conditions, enantiomers behave differently in chiral biological and physiological environments, where they often exhibit disparate pharmacological and toxicological responses [55]. Therefore, separating chiral molecules into their enantiopure forms has been a significant focus in various scientific disciplines such as medicine, pharmacy, and chemistry.

It's worth noting that more than half of the currently used drugs are chiral molecules [56]. This emphasizes the necessity for developing robust and simple techniques for enantiomer separation, a field with a long history. More than a century ago, Pasteur initiated this investigation when he attempted to induce a preferential molecular handedness using an external magnetic field, hoping to shed light on his groundbreaking discovery of homochirality in life's molecules [57,58]. However, many attempts to break chiral symmetry using only a magnetic field, including Pasteur's own efforts, were unsuccessful [59]. As a result, most of today's chiral separation techniques rely on spatial aspects like stereometric matching. These methods utilize various types of chromatography, electrophoresis, and their combinations [60]. However, recent experimental reports have brought Pasteur's original hypothesis back into focus. These reports demonstrate that chiral molecules of different handedness selectively adsorb onto perpendicularly magnetized substrates [45,61–63]. This suggests that substrate magnetization might play the role initially attributed to the magnetic field in Pasteur's original hypothesis.

Enantioseparation of chiral molecules based on their enantiospecific interaction with a ferromagnetic substrate is a relatively novel approach in CISS-related investigations that Banerjee-Ghosh *et al.* introduced in 2018 [61]. In order to avoid oxidation, they coated a ferromagnetic Co substrate with 5 nm gold and adjusted the substrate magnetization alignment by applying an external magnetic field parallel to the surface normal *(H+)* or antiparallel *(H-)*. For the molecules, two enantiopure samples of thiolated polyalanine (PAL) molecules were selected, which form a covalent bond with the gold substrate. After incubating the substrate with $L(D)$-PAL molecules functionalized by SiO_2 nanoparticles for a short period (2 s), the density of adsorbed SiO_2 nanoparticles relative to substrate magnetization alignment was determined with the help of SEM images.

Figure 1.9(a) shows the assessed density of adsorbed nanoparticles (attached to PAL molecules) after incubation with and without a ferromagnetic substrate. It was observed that L-PAL molecules preferentially adsorbed on a ferromagnetic substrate with *(H+)*

magnetization alignment, while *D*-PAL molecules primarily bound to a substrate with *(H-)* magnetization orientation. In contrast, when the ferromagnetic substrate was substituted with a bare Au substrate, no difference in the number of adsorbed *L*- or *D*-PAL molecules was observed, regardless of the presence of an external magnetic field.

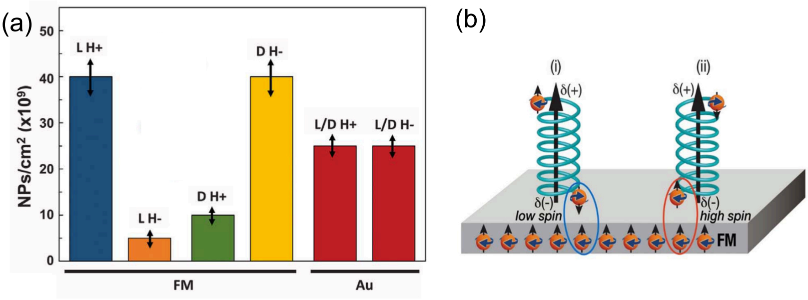

Figure 1.9: (a) The average adsorption densities of nanoparticles on ferromagnetic and Au substrates in the presence of an external magnetic field are presented with an error bar based on statistical analysis of 100 measurements. (b) Schematic representation of the spin alignment of chiral molecules on the ferromagnetic surface. The blue (red) ellipse indicates an antiparallel (parallel) spin alignment between the bottom of the enantiomer and the ferromagnetic substrate, leading to an adsorption configuration that is favorable (unfavorable). Figure adapted from Ref. [61]

In light of these results, it was concluded that the effect was not related to the magnetic dipole interaction of the applied external magnetic field with chiral molecules, but rather the magnetic exchange interaction between spin-polarized molecules and the magnetized substrate. The model illustrated in Figure 1.9(b) explains the enantioseparation of chiral molecules based on their interaction with a ferromagnetic substrate through the phenomenon of chirality-induced spin polarization. When molecules are adsorbed onto a ferromagnetic substrate, the electric field of the substrate induces charge dipole moments across the molecules. Due to the CISS effect in the chiral molecules, this charge polarization leads to different spin accumulations at the bottom of the molecules for left- and right-handed enantiomers. The exchange interaction between spin accumulation at the bottom of the molecule and the spins of the ferromagnetic substrate results in two possible configurations. Antiparallel spin alignment between the molecule and substrate (depicted in the blue ellipse in Figure 1.9(b)) stabilizes the substrate-molecule interaction in the first configuration. In contrast, parallel alignment (shown in the red ellipse in Figure 1.9(b)) weakens the substrate-molecule interactions, leading to an unfavorable adsorption mechanism in the second configuration.

To the best of my knowledge, only a few experimental studies have addressed the enantiospecific adsorption of chiral molecules on ferromagnetic substrates, which will be discussed briefly in the following.

Tassinari *et al.* observed that the adsorption of chiral amino acids on a Au-coated prependicularly magnetized ferromagnetic substrate led to different crystallization rates [62]. It has been reported that the incubation of the Au-coated Ni substrate in the saturated solution of a racemic mixture of Asparagine (Asn) molecules results in enhanced crystallization of *D*-Asn enantiomers on the part of the substrate with magnetization aligned parallel to the surface normal (H+). Conversely, the *L*-Asn enantiomers demonstrated a preference for adsorption on the substrate area where the magnetization was aligned in the opposite direction (H-). A similar procedure was conducted with Glutamic acid hydrochloride (Glu), revealing that the *L*-Glu molecules primarily crystallized on areas where the substrate magnetization was aligned in the H+ direction. In contrast, the *D*-Glu molecules preferred regions with opposite magnetization [62].

Interestingly, the observed selectivity between Asn and Glu was reversed; while the *D*-Asn enantiomer favored the H+ magnetization alignment and *L*-Asn the H-, the opposite preference was found for Glu chiral molecules. Despite the enantiospecific adsorption exhibited by these two chiral molecules, no ground state energy difference between the two enantiomers on a specific magnetic alignment of the substrate could be determined.

To elucidate these results, density functional theory (DFT) calculations were performed for individual Asn and Glu molecules adsorbed on a gold substrate. These revealed that Asparagine mainly interacts with the substrate through its amide moiety ($CONH_2$ group), whereas Glutamic acid interacts primarily through its non-amino acid carboxylic group. The authors suggested that the variations in enantiospecific interactions of these two different chiral molecules with the ferromagnetic substrate could be attributed to differences in the type of binding of the molecules to the substrate [62].

In another line of investigation, Lu *et al.* employed the electrochemical quartz crystal microbalance (EQCM) technique to determine if the enantiospecific interaction between chiral cysteine molecules and a ferromagnetic substrate is kinetically or thermodynamically controlled [63]. The quartz crystal was coated with a 100 nm ferromagnetic Ni layer and to prevent the oxidation of Ni, an additional protective layer of Au, 10 nm thick, was deposited on top. The coated crystal was immersed in a solution containing enantiopure *L*- or *D*-cysteine molecules and exposed to an external magnetic field. This magnetic field could alter the substrate's magnetization alignment from being parallel to the surface normal (H+) to an antiparallel alignment (H-).

In the first experiment, they measured the quantity of *D(L)*-cysteine molecules adsorbed onto the coated quartz crystal exposed to an external magnetic field. A constant voltage was applied [8], and the system was allowed to equilibrate for an additional hour, ensuring the establishment of thermodynamic equilibrium. Their observations revealed no significant variation in the number of adsorbed molecules, irrespective of the magnetization alignment of the substrate or the handedness of the molecules [63].

In the subsequent steps, the substrate was subjected to an alternating rectangular voltage pulse in order to facilitate time-dependent adsorption and desorption processes. Notably, the time scale for these processes was set to only five seconds to ensure the system remained far from thermodynamic equilibrium. Their observations revealed that D-cysteine molecules displayed higher adsorption rates when the substrate magnetization was in the H+ direction, whereas L-cysteine had higher adsorption rates when the magnetization was aligned oppositely.

Although the desorption rates showed a weak dependency on the substrate's magnetization direction, attributing clear variations in the desorption rates to either the applied magnetic field or the molecule's handedness proved to be more challenging. This complexity was primarily due to the experiment's time resolution limitations, as acknowledged by the authors [63]. The comparison of the thermodynamic equilibrium and non-equilibrium experimental conditions revealed that chiral cysteine molecules interact enantiospecifically with an out-of-plane magnetized ferromagnetic substrate under kinetic control. This subject will be explored in more detail in Sections 3.2 and 3.3, where our experimental findings on the enantiospecific adsorption of chiral [7]H molecules on perpendicularly magnetized Co nanoislands will be presented.

Nguyen *et al.* later utilized STM measurements in ambient conditions to examine the enantiospecific adsorption of polyalanine molecules on a perpendicularly magnetized Co film, coated with 5 nm Au. Following the incubation of the substrate in a solution of enantiopure molecules, they measured STM topographic data under ambient conditions. The findings indicated that under identical incubation conditions, *L*-polyalanine molecules were predominantly adsorbed on the substrate with magnetization antiparallel to the substrate surface normal. After reversing the substrate magnetization, the amount of adsorbed *L*-polyalanine molecules significantly decreased. While the authors didn't provide

---

[8] Typically, an EQCM device consists of two parts: an electrochemical cell and a QCM sensor. The electrochemical cell features two electrodes - a working electrode (here is the QCM sensor) and a counter electrode. By applying a bias voltage with a specific polarity between these two electrodes, the direction of ion movement within the electrochemical cell can be controlled. In this instance, the direction was adjusted to drive the ions towards the QCM electrode, leading to molecular adsorption.

a quantitative comparison of molecule adsorption relative to the substrate's magnetization alignment, a qualitative analysis of both adsorption rate and adsorbed molecule coverage confirmed that the adsorption density of polyalanine enantiomers on Au-coated ferromagnetic Co films was strongly influenced by the alignment of the substrate magnetization. Furthermore, they conclude that their observation indicates the CISS effect is a cooperative effect initiated by the interaction of multiple molecules [45].

Despite the fact that the experimental reports discussed in this section provide convincing proof of the concept of enantiomeric resolution using the CISS mechanism, there are several complexities to consider. The deposition of molecules from solution under ambient conditions onto ferromagnetic substrates has potential disadvantages, such as the need for a protective coating layer to prevent oxidation, or additional adsorbates being introduced from the solution. Moreover, the provided evidence for enantiospecificity is typically obtained from large ensembles of adsorbed molecules, complicated phenomena that are difficult to include in theoretical models.

To accurately evaluate the potential of this separation mechanism and to provide an appropriate foundation for theoretical investigations, a deeper understanding of the principles behind enantiospecific interaction of chiral molecules with magnetic substrates is necessary. Therefore, studies conducted under well-controlled vacuum conditions at the single-molecule scale, preferably at an atomic level, are highly desirable. As a result of this need for a more detailed understanding, our research, presented in Chapter 3, investigates the enantiospecific adsorption of [7]H molecules on perpendicularly magnetized Co substrates at the single molecule level.

1.4 Theoretical models

In addition to the experimental investigations presented in the previous section, the scientific community has also devoted considerable effort in developing theoretical models to elucidate the underlying mechanisms responsible for the CISS phenomenon. Following the first experimental observations of this effect, theoreticians have started forming theories that could account for the spin selectivity observed in chiral molecules. The interplay between molecular chirality, previously considered as a purely spatial characteristic, and electron spin naturally suggests spin-orbit coupling (SOC) as a fundamental mechanism for explaining the CISS effect. Therefore, SOC has been considered as a key component within these proposed theoretical frameworks [64–67].

SOC is a relativistic effect that originates from the interaction between electron motion in an electric field and its intrinsic spin. In the electron's rest frame, the charges that create the electric field appear to move with respect to the electron. This movement corresponds to electric currents that generate magnetic fields via the Ampère's law. Formally the Lorentz transformation, converts the electric field into an effective magnetic field (Equation 1.6), which is experienced by the electron as it traverses the electric field [68,69].

$$\mathbf{B} = -\frac{1}{c^2}\mathbf{v} \times \mathbf{E} \tag{1.6}$$

In the above equation, $\mathbf{v}$ represents the velocity of the electron, and $\mathbf{E}$ denotes the electric field through which it moves. The electron with a magnetic dipole moment of $\boldsymbol{\mu} = \gamma\mathbf{S}$, where γ is the gyromagnetic ratio and $\mathbf{S}$ is the electron spin, experiences corresponding Hamiltonian when placed in a magnetic field. According to the quantum mechanical derivation of H_{SOC} which results as a perturbative term when considering relativistic effects, this Hamiltonian can be written as [68]:

$$\mathrm{H_{SOC}} = -\boldsymbol{\mu} \cdot \mathbf{B} = \frac{\gamma}{c^2}\mathbf{S} \cdot (\mathbf{v} \times \mathbf{E}). \tag{1.7}$$

By substituting $\gamma = e/2m$, $\mathbf{v} = \mathbf{p}/m$ and $\mathbf{S} = \hbar\boldsymbol{\sigma}/2$, where $\boldsymbol{\sigma}$ is a vector whose components are the Pauli matrices, the Hamiltonian can be written as:

$$\mathrm{H_{SOC}} = \lambda\boldsymbol{\sigma} \cdot (\mathbf{p} \times \mathbf{E}), \tag{1.8}$$

where $\lambda = e\hbar/4m^2c^2$. This concept applies to an electron travelling through any electric field, including the electric field resulting from the chiral potential of a chiral molecule.
When an electron moves through a chiral potential created by a chiral molecule (shown in Figure 1.10(a)), it experiences an electric field that confines it within the potential. This electric filed generates a centripetal force on the electron, which keeps the electron inside the chiral potential. As mentioned above, the interplay between the effective magnetic field generated by the electric field according to the Lorentz transformation and the electron's magnetic moment leads to spin-orbit coupling [19]. As a result, when an electron passes through a chiral potential, the interaction of the magnetic field and electron spin stabilizes one spin direction while destabilizing the other. For further elaboration, an energy diagram illustrating the preference of electron spin direction when passing through a helix (chiral potential) is presented in Figure 1.10(b).
The motion of a freely propagating electron can be described using four quantum states:

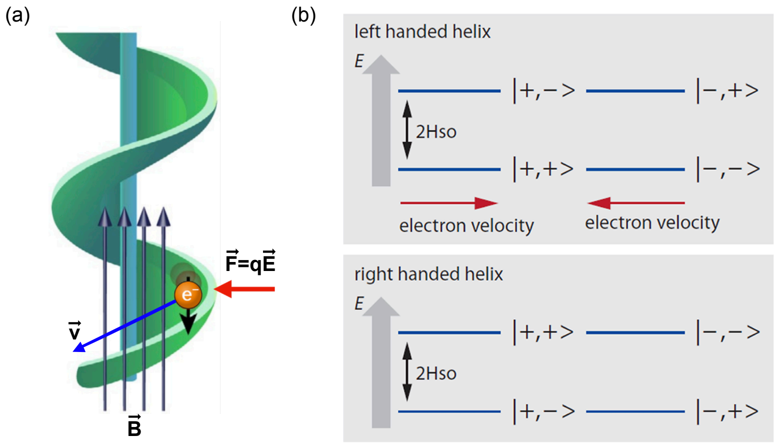

Figure 1.10: (a) Schematic representation of electron's transmission through a chiral potential. The electron is represented by a sphere, and its spin is indicated by an arrow. As the electron with a velocity of $\vec{\mathbf{v}}$ moves within the potential, a constant force ($\vec{\mathbf{F}}$) acts on the electron, which is similar to the classical centripetal force, shown by the red arrow. (b) The energy scheme illustrates the momentum-spin states of an electron as it moves within a chiral potential. The alignment of electron spin changes depending on the handedness of the helix. Figures adapted from Refs. [19] and [9].

$|+,+>$, $|-,->$, $|+,->$, and $|-,+>$ where the first quantum number corresponds to the propagation direction and the second stands for spin alignment. When an electron moves in the positive (+) direction through a left-handed helix, its up spin (+) is favored over its down spin (−). This means that $|+,+>$ is the ground state and $|+,->$ is at a higher energy level with a gap equivalent to $2\mathrm{H}_{\mathrm{SOC}}$. Thus, one state is stabilized by the spin-orbit energy, while the other is destabilized by the same energy, resulting in a difference of twice the $\mathrm{H}_{\mathrm{SOC}}$ value between the two states. Additionally, the ground state $|+,+>$ and the state $|-,->$, which corresponds to an electron moving in the opposite direction with the opposite spin, are degenerate. The state $|+,->$, which lies at a higher energy, and the state $|-,+>$ are also degenerate. When the right-handed enantiomer is chosen, the ground states become $|+,->$ and $|-,+>$, and the higher energy states become $|+,+>$ and $|-,->$ respectively [9]. If an electron undergoes elastic back-scattering within a chiral molecule, the state will change from $|+,+>$ to $|-,->$ or from $|+,->$ to $|-,+>$. This implies a simultaneous alteration in both the electron's spin and linear momentum. According to conservation laws, we must account for the conservation of both the electron's linear momentum and spin separately.

To further clarify this concept, we can examine Equation 1.8. It implies that to maintain the SOC constant (assuming a fixed molecular handedness and thus a constant electric field), if the electron's linear momentum or spin is reversed, spin-orbit coupling requires the simultaneous inversion of the other component. Therefore, for such a simultaneous flip to occur, the system would have to interact with several degrees of freedom in the environment, which is less likely to happen. Accordingly, chiral molecules facilitate an effective transport mechanism for electrons with the appropriate spin alignment by excluding the electron back-scattering possibility.

While theoretical hypotheses that employ the SOC effect [64–67] could qualitatively explain the underlying mechanism of the CISS effect, they faced a significant challenge in reproducing the clearly larger experimentally reported values. The typical value of $\mathrm{H_{SOC}}$ is around 20 meV results in significantly smaller CISS effects (i.e. spin polarization or CISS-MR) than reported by experiments. For a more intuitive understanding of the differences between experimentally reported and theoretically calculated sizes of the CISS effects, let us look again at the transport experiment conducted by Xie *et al.* on the dsDNA molecule which was previously discussed in Section 1.3.2.

Similar to Figure 1.5(b), Figure 1.11(a) shows I-V curves for three different lengths of dsDNA molecules. These curves were derived from a SAM of dsDNA molecules on a Ni substrate. During the measurement, an external magnetic field was applied, which was aligned either parallel (depicted by the red I-V curves) or antiparallel (shown in the blue I-V curves) to the surface normal of the Ni substrate. Figure 1.11(b) illustrates corresponding calculated dI/dV curves, which show an approximation of the density of states for the system. From these dI/dV curves, an "effective barrier" was defined, represented by the gap in the dI/dV curv. This barrier depends on both the length of the molecule and the direction of the applied magnetic field. Interestingly, although the absolute value of the gap increases with the length of the molecule, the difference between the gaps (corresponding to curves obtained from the same molecules under two different magnetic alignments of the substrate) remains constant and independent of length. The determined effective barriers for all three different lengths of molecules are shown in Figure 1.11(c).

Additionally, the authors highlighted that the observed difference in effective barrier energies arises from two different spin orientations. In other words, the "unfavorable spin" in the electron transport mechanism through the chiral molecule is associated with an elevated energy level, estimated to be about 1 eV higher. This energy difference can be related to twice the value of $\mathrm{H_{SOC}}$, as discussed earlier in this section. Consequently, to explain the spin-selective conductance in dsDNA molecules shown in Figure 1.11(a), a $\mathrm{H_{SOC}}$ strength of approximately 0.5 eV is required.

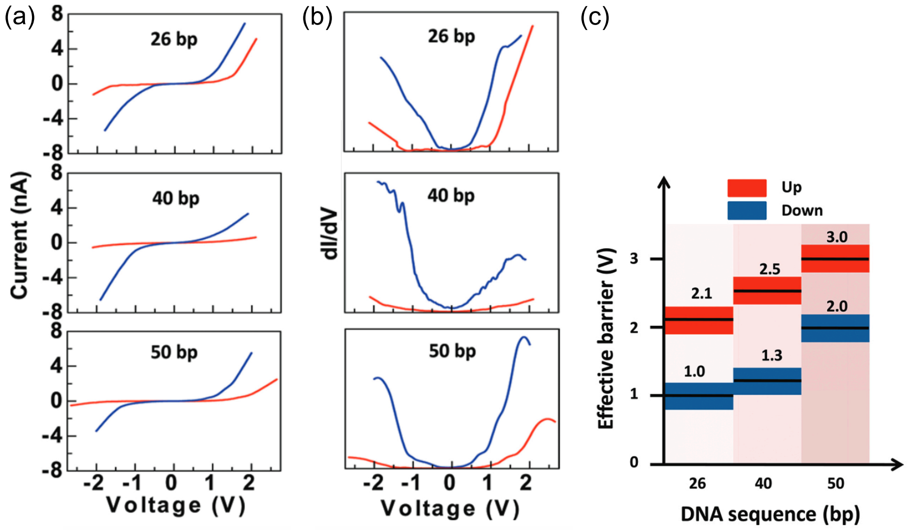

Figure 1.11: (a) Displays the I-V curves obtained from dsDNA oligomers of three different lengths (26, 40, and 50 bp). Measurements were taken with the substrate's magnetization either in a parallel (represented by red I-V curves) or antiparallel (indicated by blue I-V curves) orientation to the substrate's surface normal. (b) Presents the differentiated dI/dV curves based on the I-V curves shown in (a). (c) Depicts the effective barriers derived from the dI/dV graphs in (b) for the three dsDNA oligomer lengths. Comparisons are made when the substrate's magnetization is parallel (illustrated in red) and antiparallel (illustrated in blue) to the surface normal. Figures are adapted from Ref. [36].

In order to address this discrepancy, further theoretical investigations have been carried out. These studies aimed to identify potential mechanisms that could explain the enhanced spin selectivity in electron propagation through chiral molecules, with a particular emphasis on examining the type of experiment from which the spin selectivity was obtained.

Several research groups have explored the theoretical aspects of the photoemission experiments using scattering theory in various models [64, 67, 70–72]. Initially, Yeganeh *et al.* addressed this issue by enhancing the SOC strength through modifying the electron's effective mass [64]. This adjustment resulted in non-negligible spin polarization values, despite still being inconsistent with experimental results. Subsequently, the consideration shifted towards the cumulative effect of atomic SOC from each atom within a chiral molecule, accounting for multiple electron scattering events during transmission [67,70,72]. Even after these modifications, the estimated spin polarization values did not agree with experimental findings. Additionally, a number of theoretical studies have utilized SOC-adjusted Hamiltonians to examine the transport properties of electrons through chiral molecules, with a particular emphasis on DNA oligomers [65, 73, 74], proteins [75], and [13]helicene molecules [76]. While some of these studies specifically investigated these molecules, others took a broader approach by examining electron transport in the presence of a general chiral potential [66,77]. Despite these efforts, the spin polarization values estimated through these theoretical models were 1-2 orders of magnitude smaller than the experimental values previously reported for electron propagation through these types of molecules.

The above mentioned significant gap between theoretical and experimental values suggests that SOC alone might not fully explain the observed spin-selective electron conductance through chiral molecules [78]. Therefore, further theoretical investigations have been conducted to identify other potential mechanisms that could support effective spin selectivity in electron transport through chiral molecules.

In one such approach, Gersten *et al.* proposed that the strong SOC does not originate from the chiral molecules themselves but from the substrate upon which the molecules are adsorbed [32]. Specifically, they attempted to take advantage of the strong SOC of the Au substrate, commonly used in early photoemission experiments. By doing so, they calculated spin polarization values in line with those reported in experimental studies. Building upon this theory, Alwan and Dubi further suggested that the CISS effect is, in fact, an interface-induced phenomenon, stemming primarily from the pronounced SOC in the electrodes (substrates) [33]. However, as mentioned in section 1.3.1, experimental findings demonstrate that the CISS effect is not dependent on the substrate. This is evident from the high spin polarization values obtained from chiral molecules placed on substrates with relatively low atomic numbers like Al and Cu, which do not possess strong SOC.

Another interesting approach was proposed by Michaeli and Naaman [79], considering the amplification of a weak SOC through a secondary mechanism. Their hypothesis postulates that when molecules adsorb onto a substrate, the substrate's surface electric field induces a charge dipole across the molecule due to its polarisability. Even small SOC, which acts on the displacement current during the formation of the electric dipole, leads to opposite spin accumulation at the poles. For further elaboration of this concept, one can refer to the model suggested by Ghosh *et al.* This model, based on Michaeli's hypothesis, presents a slightly different scenario where the chiral molecule is sandwiched between two metallic leads and subjected to an externally applied electric field [80].

Figure 1.12 illustrates a schematic representation of this model. Due to the externally

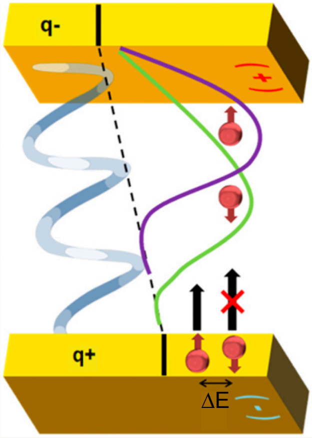

Figure 1.12: Schematic representation of a qualitative model showing the formation of a charge dipole on the molecule upon applying an external electric field, leading to different energy barriers for electrons with different spin orientations, up and down, as they attempt to tunnel through the molecule. Figure adapted from Ref. [80].

applied electric field, charge separation occurs within the sandwiched molecules. This charge separation can also lead to spin separation as a consequence of the CISS effect, which is illustrated by two curves depicting the density of states for spin-down (green curve) and spin-up (purple curve) electrons. As shown in the figure, electron densities shift towards the positive pole. However, the CISS effect results in a different response between the two spin states. The spin-up electron, aligned favorably with the molecule's handedness, progresses further towards the positive pole, while the spin-down electron is left behind.

When a subsequent electron, driven by the external electric field, attempts to move through the molecule from the negative to the positive pole, its propagation is influenced by its spin alignment. If the electron possesses a spin-down orientation, the Pauli exclusion principle hinders its forward movement. Conversely, for a spin-up electron, the Pauli exclusion principle permits its movement. This distinction in electron movement is explained by Pauli's spin repulsion. The difference in these scenarios translates to different energy barriers for electron propagation within the chiral molecule according to their spin characteristic, denoted as ΔE. This model represents a combination of a small SOC with an amplifying spin-blockade-like scenario. The resulting amplification effect is comparable to tunneling through a magnetic barrier, where a minimal energy splitting gets magnified by an exponential term in the tunneling regime [80]. In a basic calculation, we can express the difference in energy barriers as $\Delta E = \Delta P \cdot E_{ST}$, where ΔP represents the spin polarization and E_{ST} denotes the energy splitting between singlet and triplet states due to Pauli repulsion. Assuming that the usual energy splitting between singlet and triplet states, which can also be referred to the exchange interaction responsible for spin blockade in hydrocarbons, is about 1 eV. Thus, a small initial SOC-driven spin polarization of 3% would result in an energy splitting of 30 meV [80]. As we can conclude, taking into account a secondary process that amplifies the small SOC effect to explain the significant CISS effect was a valuable qualitative approach.

In other theoretical approaches, scientists have considered various effects and parameters that could help us progress towards understanding the CISS effect. While a detailed explanation of these theories is beyond the scope of this work, a brief overview of some notable ones is beneficial.

One of the parameters influencing spin polarization achieved through electron propagation within chiral molecules is molecular length. While the CISS effect has been observed in various molecules of different lengths, as discussed in Sections 1.3.1 and 1.3.2, experimental findings indicate a correlation between molecular length and the resulting spin polarization values. This correlation can also be verified theoretically [29–31]. Theoretical calculations suggest that the estimated spin polarization value for electrons propagating through a chiral molecule generally increases with the length of the molecule or the chiral potential.

As part of a different approach, Fransson *et al.* provided an alternative point of view. They noted that although most experimental work was performed at room temperature, many proposed theories did not consider lattice and molecular vibrations. Therfore, they proposed a theoretical model that includes the vibrational contribution to the spin-orbit coupling, capturing all observations and yielding spin polarization values consistent with experimental results [31, 81].

Alternatively, Liu *et al.* suggested a completely novel approach by asserting that SOC in the chiral molecule is too small to account for the CISS effect. They introduced an orbital polarization model with SOC from the electrode to explain CISS in transport. In this model, as electrons pass through the chiral molecule, they become orbital-polarized, and the orbital polarization is converted to spin polarization by the SOC in the electrodes [82]. While this model offers a plausible explanation for CISS-related magnetoresistance, it cannot be universally applied to other findings, such as those from photoemission experiments or enantiospecific adsorption.

In summary, it should be emphasized that the theoretical investigations that have been explored so far primarily focus on describing the CISS effect in terms of transmission, transport, and magnetoresistance phenomena. Nevertheless, as highlighted earlier in Section 1.3.4, the field of enantiospecific adsorption of chiral molecules on ferromagnetic substrates is still in its early stages. Only a handful of experimental reports have been published on this topic. Therefore, the theoretical framework surrounding this area remains underdeveloped [34].

Despite considerable progress has been made over the past decade, a comprehensive model that quantitatively accounts for all experimental findings has yet to be established. Consequently, the CISS effect remains a fascinating and significant research area, engaging the curiosity of scientists who aim to deepen our knowledge of its underlying mechanisms and implications.

1.5 Filling the gap

It has been stated in previous chapters that, although the CISS effect is evident in a wide range of experimental results, the theoretical framework to fully elucidate the mechanism remains underdeveloped. Various scientific investigations over the years have attempted to provide a theoretical foundation for the pronounced spin selectivity of chiral molecules. However, a conclusive and universally accepted theory that can comprehensively address experimental observations has yet to emerge.

One of the primary challenges is to bridge the gap between experimentally studied real systems and theoretically modeled idealized systems. Experimental research generally involves molecular ensembles, yielding information that is averaged across various configurations, such as absorption sites, geometries, or paths of electric current. Additionally, the majority of experiments take place under ambient conditions that require protective measures, like a gold coating layer on ferromagnetic substrates, or lead to the presence of extra adsorbates, such as water due to atmospheric humidity, factors that are typically not considered in theoretical models. Thus, the need for a well-defined experimental system that can be carefully investigated is crucial for closing this gap, allowing for a deeper understanding of the CISS effect and its underlying mechanisms [83]. This is essential not only for advancing our knowledge of the phenomenon but also for developing new technologies and applications that rely on it.

In this doctoral project, we adopt a surface-science approach to investigate the CISS effect in chiral heptahelicene molecules, a member of the chiral helicene family. These molecules have been theoretically [76, 83, 84] and experimentally [28, 39] studied for the

CISS effect. We deposit a racemic mixture on clean, perpendicularly magnetized single-crystalline ferromagnetic surfaces under UHV conditions, preferring this over depositing from solutions. Using high-resolution spin-polarized scanning tunneling microscopy and spectroscopy (SP-STM/STS), we analyze molecular adsorption geometries and identify the handedness of the individual molecules. This enables us to focus on discrete molecules with unique adsorption positions on substrates, thus avoiding the need to average over ensemble of molecules. Such precision facilitates an in-depth analysis of spin selectivity across different enantiomers under otherwise identical conditions.

Ultimately, our goal is to develop an experimental model system that aligns more accurately with theoretical frameworks in order to enhance our understanding of the CISS effect and by bridge the gap between experimental observations and theoretical interpretations.

CHAPTER 2

Experimental methods and materials

2.1 Vacuum system

In this PhD project, all experimental procedures were conducted in the UHV cluster instrument discussed in this section. This setup, known as the Nano Spintronics Cluster Tool (NSCT), consists of five interconnected UHV chambers, as shown in Figure 2.1. Each chamber is capable of independent pumping and sealing, allowing for in-situ sample preparation and analysis under UHV conditions. For the sake of brevity, this description focuses only on those equipment components directly relevant to this study.

1. Preparation chamber
   The preparation chamber can be used to fabricate and analyze a variety of sample systems. The chamber is equipped with a number of techniques, such as argon sputtering, high-temperature heating and flashing stage (particularly for tungsten crystals), electron beam evaporators for ultra-thin film deposition, low energy electron diffraction (LEED) analysis, Auger electron spectroscopy and X-ray photoelectron spectroscopy. A motorized manipulator is available for moving the sample within the preparation chamber and to the STM chamber. The manipulator is equipped with a sample holder stage that can be heated or cooled separately. The preparation chamber base pressure can achieve approximately 2.0×10^{-10} mbar.

2. LT-STM chamber
   All scanning tunneling microscopy (STM) and spectroscopy (STS) measurements were performed using an Omicron low-temperature STM (LT-STM). This STM head is cooled using two bath cryostats: both can be filled with liquid nitrogen to reach a temperature of approximately 78 K, or alternatively, the outer cryostat

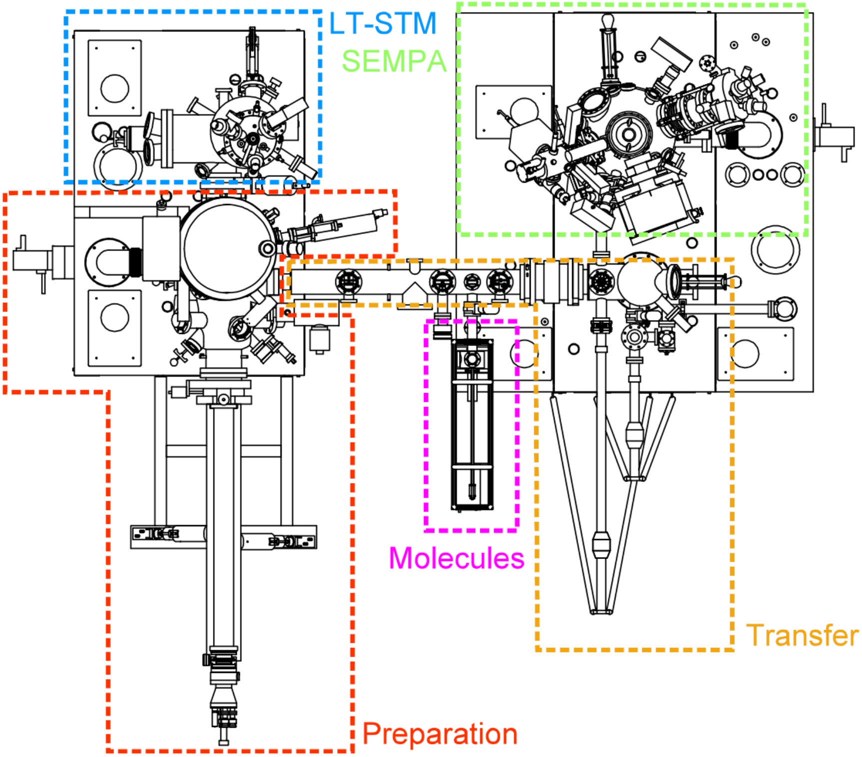

Figure 2.1: Schematic drawing of the Nano Spintronics Cluster Tool. Figure adopted from Ref. [85]

can be filled with liquid nitrogen and the inner one with liquid helium, thereby achieving temperatures as low as $\sim 5\,\mathrm{K}$. Thanks to the reduced drift and enhanced thermal stability at such low temperatures, the LT-STM is exceptionally suitable for single-molecule microscopy and spectroscopy studies. Under standard conditions, the LT-STM chamber can maintain a pressure of approximately 5.0×10^{-11} mbar.

3. Molecular chamber
   The chamber is equipped with a custom-designed Knudsen-cell type evaporator, a pressure gauge and a temperature sensor, which enables the determination of optimal sublimation conditions for precise molecular deposition at the sub-monolayer level. In addition, it can be baked separately, allowing faster molecules exchange

and preventing contamination of other chambers. The vacuum pressure remained below 2.0×10^{-9} mbar during the sublimation of molecules.

4. Load lock and transfer chamber
   To introduce samples, molecules, or STM tips into the UHV system, they are initially placed inside the load lock chamber. Subsequently, the chamber is pumped to the desired vacuum level (approximately 1.0×10^{-7} mbar) utilizing a combination of a roughing pump and a turbo-molecular pump. Once the desired pressure is achieved, the gate valve is briefly opened to allow the transfer of samples into the transfer chamber. There is a rail system within the transfer chamber that facilitates the movement of samples to other chambers within NSCT at a lower pressure of $\sim 5.0 \times 10^{-10}$ mbar.

5. Scanning electron microscope (SEM)
   This chamber is equipped with a scanning electron microscope with polarization analysis (SEMPA) and a focused ion beam (FIB) for the precise fabrication of nanostructures. Although this chamber has many functionalities, it was not used in the current PhD project, so further discussion of its features will not be included. For more information, please refer to References [86, 87].

2.2 Scanning tunneling microscopy and spectroscopy

The scanning tunneling microscope is a technological revolution that has greatly impacted the fields of nanoscience, surface analysis, and material science. Binnig and Rohrer invented a device that takes advantage of the quantum tunneling effect to overcome the resolution limitations of conventional optical microscopes [88–91]. This advancement not only allows researchers to visualize and examine the physical properties of nanostructures, molecules, and even single atoms on surfaces with sub-angstrom resolution, but it also enables the manipulation of individual atoms and molecules [92, 93].

A typical STM operates by placing a sharp metal tip, assisted by a piezoelectric crystal, extremely close to the sample surface at a distance of just a few Ångström. At this proximity, the electron wave functions of the tip and sample overlap, leading to the quantum tunneling phenomenon. This allows electrons from the tip to traverse the tiny vacuum gap to the surface or vice versa. When a bias voltage is applied between the sample and the tip under these tunneling conditions, a net electric current starts flowing, providing information on the sample's surface characteristics. The tip, guided by high-precision

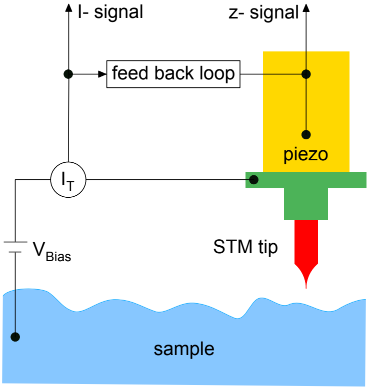

Figure 2.2: A typical STM setup is schematically illustrated with an atomically sharp metallic tip mounted on a piezoelectric element capable of moving the tip in x, y, and z directions with atomic precision. The tip is brought close to the surface, and when the distance between the tip and the conducting sample is within a few Ångström, a tunneling current (I_T) is generated due to the applied bias voltage (V_{Bias}). The STM probes the sample surface by measuring this tunneling current.

piezo elements, explores the sample surface by monitoring the tunneling current as it scans the surface [94,95]. The working principle of STM is shown schematically in Figure 2.2.

The essential concept underlying scanning tunneling microscopy is the tunneling effect, enabling electrons to pass through classically impenetrable potential barriers. To develop a solid understanding and insight, it is helpful to study the theory of STM, starting with the most basic example of tunneling: a one-dimensional rectangular barrier.

2.2.1 Tunneling through one-dimensional barrier

The fundamental concept of the tunneling process can be explained using the one-dimensional rectangular barrier model depicted in Figure 2.3. An electron with energy E is characterized by the wave function $\psi(z)$, which fulfills the time-independent Schrödinger equation.

$$-\frac{\hbar^2}{2m}\frac{d^2}{dz^2}\psi(z) + V(z)\psi(z) = E\psi(z), \tag{2.1}$$

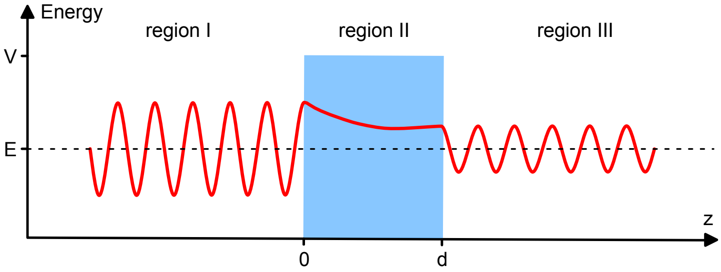

Figure 2.3: Energy diagram of a particle tunneling through a rectangular barrier.

where $\hbar$ is the reduced Planck constant and m is the electron mass. The energy diagram is divided into three distinct regions by the rectangular potential barrier:

$$V(z) = \begin{cases} V, & 0 < z < d \\ 0, & \text{otherwise.} \end{cases} \tag{2.2}$$

As shown in the diagram, regions I and III represent classically permitted zones where $E > V(z)$. In contrast, region II is a classically restricted area where a classical particle with energy $E < V$ cannot overcome the barrier. Due to the wave nature of electrons, quantum mechanics allows electrons to penetrate through the barrier and to pass from the first region to the third. The Schrödinger equation's solution can be expressed as [96]:

$$\begin{aligned} \psi_{\text{I}}(z) &= Ae^{ikz} + Be^{-ikz} \\ \psi_{\text{II}}(z) &= Ce^{-\kappa z} \\ \psi_{\text{III}}(z) &= De^{ikz} + Ee^{-ikz}, \end{aligned} \tag{2.3}$$

with

$$k = \frac{\sqrt{2mE}}{\hbar} \quad \text{and} \quad \kappa = \frac{\sqrt{2m(V-E)}}{\hbar}. \tag{2.4}$$

Since there is a non-zero probability of detecting the electron in region II, the electron can penetrate the rectangular barrier. To analyze the electron's transmission dependence on the barrier, we apply continuity conditions to the wave functions and their first derivatives, obtaining the coefficients and defining the transmission coefficient as the ratio of the incoming and transmitted wave amplitudes. The transmission coefficient T, which represents the electron's ability to tunnel through the barrier, is defined as:

$$T = \left|\frac{D}{A}\right|^2 = \frac{1}{1 + \frac{(k^2+\kappa^2)^2}{4k^2\kappa^2} \cdot \sinh^2(\kappa d)}. \tag{2.5}$$

Considering a thick and high barrier with strong attenuation ($\kappa d \gg 1$), which aligns with typical STM operating conditions, the transmission coefficient can be approximated as:

$$T \approx \frac{16k^2\kappa^2}{(k^2+\kappa^2)^2} \cdot e^{-2\kappa d}. \tag{2.6}$$

Therefore, electron transmission across a barrier is exponentially associated with its width, which corresponds to the distance between the tip and the sample, as well as the square root of the effective barrier height ($\kappa = \sqrt{2m(V-E)}/\hbar$), which is approximated as the average work function of the tip and sample[1]. This exponential dependence of the transmission on the tip-sample distance and average work function of the tip and sample provides a foundational insight. It is, however, necessary to develop a more detailed theoretical framework in order to fully understand the underlying quantum mechanics behind tunneling. This leads us to Bardeen's perturbation theory, which adds to our understanding of tunneling phenomena.

2.2.2 Bardeen perturbation theory

Bardeen initially proposed a theoretical model for metal-insulator-metal tunnel junctions using perturbation theory [97]. In this approach, the combined system is divided into subsystems, and the electronic states of these subsystems can be determined by solving their respective stationary Schrödinger equations. Bardeen demonstrated that when the interaction between the two electrodes is weak, the tunneling probability between the two unperturbed electronic states, ψ_μ and ψ_ν, is determined by the overlap of their wave functions. In STM context, ψ_μ and ψ_ν represent the tip and sample states, respectively.

---

[1] Work function measures the energy needed to remove an electron from a material's surface to a point in the vacuum outside the surface. In STM, both the tip and sample have associated work functions. The average of these work functions determines the effective barrier height an electron has to overcome to tunnel from the tip to the sample or vice versa.

Utilizing Bardeen's framework, a first-order time-dependent perturbation theory can be employed to derive the subsequent expression for the tunneling current I [98]:

$$I = \frac{2\pi e}{\hbar} \sum_{\mu,\nu} f(E_\mu)[1 - f(E_\nu + eV)] \left|M_{\mu\nu}\right|^2 \delta(E_\nu - E_\mu). \tag{2.7}$$

In this formulation, $f(E)$ stands for the Fermi function, while V refers to the applied sample bias voltage. The tunneling matrix element between the unperturbed electronic states ψ_μ of the tip and ψ_ν of the sample surface is represented by $M_{\mu\nu}$. Additionally, the energy of the state ψ_μ is given by E_μ, and the energy of the state ψ_ν is denoted by E_ν, both in the absence of tunneling. The δ function serves to express the conservation of energy in cases of elastic tunneling. In this approach the tunnel matrix element is expressed as:

$$M_{\mu\nu} = -\frac{\hbar^2}{2m} \int d\mathbf{S} \cdot \left(\psi_\mu^* \boldsymbol{\nabla} \psi_\nu - \psi_\nu \boldsymbol{\nabla} \psi_\mu^*\right). \tag{2.8}$$

Integration is carried out over a surface that separates the two electrodes. To determine the tunneling current, we need to consider all possible initial and final states and multiply them by the transition probability. In the case of low temperatures and small bias voltages, the elastic tunneling current at a given bias voltage V can be obtained by integrating all relevant states. Since the precise expressions for ψ_μ and ψ_ν are typically not available, Tersoff and Hamann developed a tunneling model based on an atomically sharp tip, where only the last atom, specifically the one nearest to the surface, contributes to the tunneling process. Their model featured a spherical apex geometry (see Figure 2.4), with the tip's curvature determined by radius R. In their approximation of the tunnel matrix elements, they took into account only s-like wave functions for the tip and disregarded contributions from wave functions with angular dependence [98, 99]. Moreover, they included a work function ϕ (effective barrier height between tip and sample) and an inverse decay length of $\kappa = \sqrt{2m\phi}/\hbar$. Thus, the electronic state of the tip can be represented by:

$$\psi_\mu = \frac{1}{R} e^{-\kappa R}. \tag{2.9}$$

Additionally, they assumed a constant density of states within the energy range of interest and accounted for only elastic tunneling processes, implying energy conservation during tunneling. With these simplifications in place, the tunneling current can be expressed as [100]:

$$I = \frac{2\pi e}{\hbar} V \sum_{\mu,\nu} |M_{\mu\nu}|^2 \, \delta(E_\nu - E_F)\delta(E_\mu - E_F), \tag{2.10}$$

where E_F is the Fermi energy, and E_μ and E_ν are the electron's energy in tip and sample states, respectively. Utilizing the simplified approximation of the tip state presented in Eq. 2.9, we can derive the subsequent expression for the tunneling current:

$$I \propto V \, e^{2\kappa R} \rho_t \left(E_F\right) \sum_{\nu} |\psi_\nu \left(\mathbf{r}_0\right))|^2 \, \delta(E_\nu - E_F), \tag{2.11}$$

where the term $\rho_t(E_F)$ represents the density of states at the Fermi level for the tip. We can also write down:

$$\rho_s \left(E_F{,}\mathbf{r}_0\right) = \sum_{\nu} |\psi_\nu \left(\mathbf{r}_0\right)|^2 \, \delta(E_\nu - E_F), \tag{2.12}$$

which indicates the local density of states (LDOS) for the sample at the Fermi level, calculated at the central point of the spherical tip apex. The sample wave functions exhibit an exponential decay in the z direction (toward the vacuum), such that:

$$|\psi_\nu \left(\mathbf{r}\right)| \propto e^{-\kappa z} \tag{2.13}$$

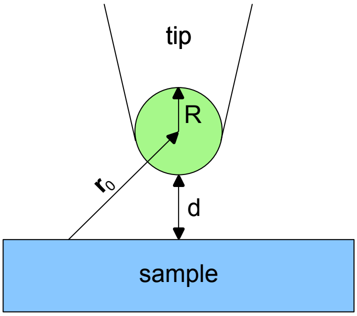

Figure 2.4: Schematic sketch of Tersoff and Hamann's simplified tip-sample geometry. The tip apex is approximated by the spherical form of radius R.

and

$$|\psi_\nu(\mathbf{r}_0)|^2 \propto e^{-2\kappa(d+R)}, \tag{2.14}$$

where d is the thickness of the tunneling barrier. Thus, we can write:

$$\rho_s(E_F,\mathbf{r}_0) \approx \rho_s(E_F)\, e^{-2\kappa(d+R)}, \tag{2.15}$$

by including this expression into Eq. 2.11, we can derive a new equation that explicitly reveals that the tunneling current exhibits an exponential dependence on the distance between the tip and the sample, as well as a linear dependence on the applied bias voltage and the local density of states (LDOS) of both the tip and the sample at the Fermi energy,

$$I \propto V\, \rho_t(E_F)\rho_s(E_F)e^{-2\kappa d}. \tag{2.16}$$

So far, our discussion has been limited to the case of small bias voltages. However, to present a more practical situation, we must remove the restriction of small applied bias voltage. By extending the Tersoff and Hamann model to include a finite bias voltage window V, and assuming that the wave functions and corresponding energy eigenvalues are invariant under the application of this bias voltage, we get:

$$I \propto \frac{2\pi e}{\hbar} \int_0^{eV} \rho_t(E - eV)\, \rho_s(E)\, e^{-2\kappa_{eff}(E,V)d}\, dE, \tag{2.17}$$

where $\kappa_{eff} = \sqrt{2m\,\phi_{eff}(E,V)}/\hbar$ and $\phi_{eff}(E,V) = \frac{\phi_t+\phi_s+eV}{2} - E$. The exponential component in the above equation is commonly referred to as the transmission coefficient $T(E,V)$. Thus, the above equation can be reformulated as:

$$I \propto \frac{2\pi e}{\hbar} \int_0^{eV} \rho_t(E - eV)\, \rho_s(E)\; T(E,V)\; dE. \tag{2.18}$$

Figure 2.5 displays a diagram of a tunneling junction with bias voltage V and the DOS for both tip and sample. When a positive bias voltage is applied to the sample, the tunneling electrons move from the tip's occupied states to the sample's unoccupied states. Conversely, with a negative sample bias, the opposite takes place. By appropriately selecting the bias voltage, we can identify the electronic states contributing to the tunneling cur-

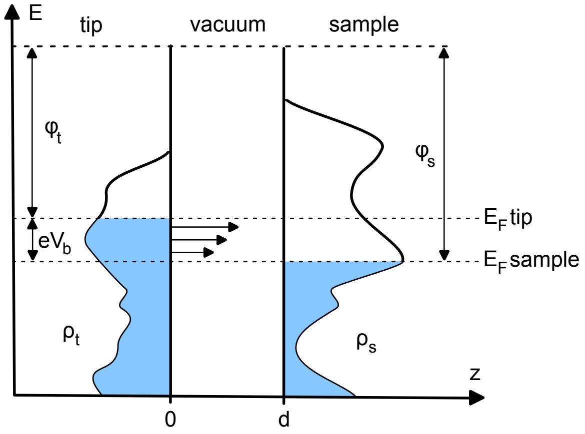

Figure 2.5: Schematic representation of a tunneling junction between a tip and sample, featuring arbitrary DOS, demonstrates that when a positive voltage V is applied to the sample with respect to the tip, electrons from occupied tip states (on the left) tunnel into unoccupied sample states (on the right). Varying lengths of arrows indicate that electrons closer to the Fermi level of the tip have a higher probability of tunneling.

rent, and ideally, measure the local density of states in the sample. However, it should be noted that tunneling currents do not directly correlate with LDOS. Rather, it is related to the convolution of the LDOS of both the tip and sample over the eV energy range. In addition, since the transmission coefficient $T(E, V)$ is a function of energy and bias voltage, electrons near the Fermi level of the negatively biased electrode have a higher probability of tunneling. This is due to the fact that they encounter a lower effective barrier height. Therefore, these electrons make the most significant contribution to the tunneling current as indicated in Figure 2.5.

2.2.3 Spin polarized tunneling

So far, the spin of the electrons contributing to tunneling processes has not been taken into account. However, as this study focuses on magnetic substrates and the unique spin-selective characteristics of chiral molecules, the role of electron spin in the tunneling process becomes extremely important.

The theoretical basis of spin-polarized (SP)-STM can be explained by the Stoner model, a framework that elucidates the behavior of ferromagnetic materials featuring itinerant magnetism. Based on the Stoner model, electron exchange interaction favors parallel spin alignment. This alignment results in distinct densities of states for spin-up and spin-down electrons, which results in a shift in energy between them. This shift results in a spin polarization $\boldsymbol{P}$ that can be expressed as follows [101]:

$$\boldsymbol{P} = \frac{\rho_\uparrow - \rho_\downarrow}{\rho_\uparrow + \rho_\downarrow} \cdot \boldsymbol{e}_z, \quad P = \begin{cases} \text{positive}: & \rho_\uparrow - \rho_\downarrow > 0 \\ \text{negative}: & \rho_\uparrow - \rho_\downarrow < 0, \end{cases} \tag{2.19}$$

here, $\rho_\uparrow$ ($\rho_\downarrow$) represents the DOS for spin-up (spin-down) electrons.

Obtaining spin-polarized STM data necessitates not only a magnetic substrate but also a magnetic tip, essentially creating a tunnel junction between two ferromagnetic materials. In such a configuration, it has been demonstrated that the tunneling conductance depends on the relative alignment of the magnetization direction of the two electrodes [102–104]. This phenomenon, known as tunneling magnetoresistance (TMR), arises from electron spins and serves as the basic principle underlying spin-polarized STM. Under the conditions of low temperatures, small bias voltages, and assuming elastic tunneling process, the spin-polarized tunneling current can be expressed as follows:

$$I_{sp} = I_0(1 + P_t P_s \cos\theta), \tag{2.20}$$

where the tunneling current for the nonmagnetic case is denoted by I_0, P_t and P_s represent the spin polarization of the tip and sample and the angle between the magnetization directions of both electrodes is denoted as θ. It is noteworthy that magnetic information can only be obtained from differential measurements, which eliminate the non-spin-dependent current contributions. There are three cases of particular interest:

$$I = \begin{cases} I_0(1 + P_t P_s), & \theta = 0^\circ \\ I_0, & \theta = 90^\circ \\ I_0(1 - P_t P_s), & \theta = 180^\circ. \end{cases} \tag{2.21}$$

In the case where $\theta = 0^\circ$, the magnetization alignment of the tip and sample is parallel, leading to the highest tunneling current. Figure 2.6a illustrates this situation, displaying the tunneling process between two magnetic materials (tip and sample) with parallel magnetization alignment. The DOS for spin-down electrons at the Fermi level in both electrodes is considerably larger than for spin-up electrons. As a result, many initial and final states are available for transport, generating a high current of spin-down electrons. When spin-flip events are excluded, spin-down electrons from the tip will consistently tunnel into the spin-down states of the sample. Conversely, the DOS at the Fermi level for spin-up electrons in both electrodes is low, with only a few initial and final states accessible for transport. This causes spin-up electrons to contribute significantly less to the total tunneling current.

In contrast, the antiparallel alignment case with $\theta = 180°$ exhibits a high DOS for spin-down electrons in the first electrode but a low DOS in the second electrode, as shown in Figure 2.6b. Despite the availability of many initial states in the tip, the limited number of final states in the sample restricts the tunnelling current. For spin-up electrons, the DOS in the tip is low, while it is high in the sample, resulting in a small number of initial states and large numbers of final states. This condition leads to a reduced tunneling current in both channels, and as a result, the junction's overall conductivity is low.

In the case of orthogonal alignment between the magnetization direction of the tip and the sample, the spin-polarized component of Eq. 2.21 will disappear, and the tunneling current will be the same as in a non-polarized tunneling process ($I_{sp} = I_0$). Thus, to achieve a spin-polarized STM measurement, it is crucial to align the magnetization direction of the tip and the sample along the same axis, or at least have a common magnetization direction component. For instance, a tip with only in-plane components would be unable to investigate the out-of-plane magnetic features of a sample.

While the discussions up to this point clarifies the fundamental mechanism driving spin-polarized tunneling between two ferromagnetic materials, it is essential to expand the model to account for specific aspects of the STM junction in order to gain further insight into the tunneling current's dependence on local properties like the sample's LDOS. This was accomplished by Wortmann *et al.* [105], when they extended the Tersoff and Hamann model to spin-polarized STM. In this context, the density of states for the tip is assumed to be constant ($\rho_{t,\uparrow}, \rho_{t,\downarrow} =$ const.), yet different for both spin directions ($\rho_{t,\uparrow} \neq \rho_{t,\downarrow}$), which accounts for the magnetization of the tip $\mathbf{m}_t = (\rho_{t,\uparrow} - \rho_{t,\downarrow}) \cdot \mathbf{e}_M$. In addition, unlike the tip's DOS, the sample's density of states exhibits a dependence on spatial position as well as energy. The terms $\overline{\rho_s(\mathbf{r}_0,V)}$ and $\overline{\mathbf{m}_s(\mathbf{r}_0,V)}$ denote the energy-integrated LDOS and the energy-integrated local magnetization of the sample, respectively, within the range $[E_F; E_F + eV]$. In the case of finite bias voltages and low temperatures the tunneling current can be described by the following expression [101, 105]:

$$\begin{aligned} I(\mathbf{r}_0,V,\theta) &= I_0(\mathbf{r}_0,V) + I_{sp}(\mathbf{r}_0,V,\theta) \\ I(\mathbf{r}_0,V,\theta) &\propto \rho_t\overline{\rho_s(\mathbf{r}_0,V)} + m_t\overline{m_s(\mathbf{r}_0,V)}\cos\theta. \end{aligned} \tag{2.22}$$

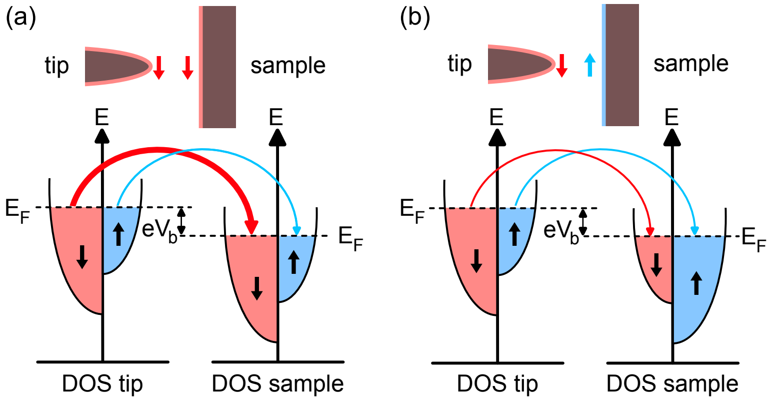

Figure 2.6: Schematic representation of the spin-polarized tunneling process between a magnetic tip and a magnetic sample. By applying a bias voltage V between the tip and sample, a spin-polarized current is generated. (a) When the magnetization directions of the tip and sample are aligned parallel, spin-down electrons from the occupied tip state tunnel into the unoccupied spin-down states of the sample, contributing significantly to the total tunneling current, as marked by the thick red arrow. In contrast, the limited availability of initial states in the tip and final states in the sample for spin-up electrons results in a smaller contribution to the tunneling process, as represented by the thin blue arrow. (b) In the case of anti-parallel alignment of the magnetization directions, spin-down electrons from the occupied state of the tip tunnel into the unoccupied spin-down states of the sample. However, due to the restricted availability of final states in the sample, the number of electrons participating in the tunneling process is limited, as indicated by the thin red arrow. For spin-up electrons, despite the fact that there are many unoccupied majority spin states in the sample's DOS, there are not enough spin-up electrons in the energy interval between E and $E_F - eV$ to contribute to the tunneling process, as shown by the thin blue arrow. In general, the anti-parallel alignment results in a lower tunneling current compared to the parallel configuration.

Utilizing the definition of the $\mathbf{m}_t$, along with the definition of polarization in Eq. 2.19, the tunneling current can be expressed as follows:

$$I(\mathbf{r}_0,V,\theta) \propto I_0 \left[1 + \overline{P_t P_s(\mathbf{r}_0,E_F + eV)} \cos\theta\right]. \tag{2.23}$$

However, as seen from the equation above, it is especially challenging to directly extract magnetic information from the tunneling current, considering that the spin-polarized tunneling current relies on the energy-integrated local magnetization of the sample ($\mathbf{m}_s = (\rho_{s,\uparrow} - \rho_{s,\downarrow}) \cdot \mathbf{e}_M$). This problem occurs because the unpolarized term, I_0, constantly increases as the bias voltage V rises, whereas the spin-dependent component, I_{sp}, may remain constant or even diminish due to variations of the spin polarization within the analyzed energy interval. As a result, the tunneling current I is typically dominated by I_0. Nevertheless, these challenges can be addressed by examining the differential conductance dI/dV, which will be covered in detail in Section 2.2.7.

To ensure the accuracy and reliability of spin-resolved measurements, precise calibration of the magnetic tip is crucial. This calibration is typically conducted using well-characterized magnetic structures, such as bilayer cobalt islands or the domain structure of bilayer Fe/W(110). The significance of this calibration process is further outlined in Chapter 3, where these substrates are employed to calibrate our magnetic tips before performing spin-polarized magnetic measurements.

In addition to exploring the theoretical principles of STM, it is important to acknowledge the different ways in which this technique can be employed. In the following sections, the operational modes used in this study will be described in order to provide a better understanding of STM's potential and its significance to this research.

2.2.4 Constant current mode

The constant current mode is the most frequently used method in STM experiments. In this mode, a feedback loop maintains a constant tunneling current by adjusting the height of the tip above the sample surface. The feedback loop, through the control of a piezoelectric driver and high precision piezo elements retract the tip from or bring it closer to the surface if the current exceeds or falls below the set point value (I_T), respectively, due to sample topography or changes in LDOS [106]. As outlined in Eq. 2.16, the tunneling current depends not only on the exponential distance between the tip and sample but also on the sample's LDOS. When analyzing constant current images, it is essential to realize that they can only be regarded as topographic representations if the tunneling current is mainly influenced by geometric structures. Such examples, however, are rare in typical STM measurements at atomic scales, so constant current images should be interpreted as a representation of both sample apparent height and LDOS. Thus, the tip scans an isosurface of constant integrated LDOS of the sample integrated over the energy window given by $E_F \leq E \leq E_F + eV$. Both the bias voltage and the set point tunneling current are independent parameters in the experiment and the polarity of bias voltage determines whether occupied ($V < 0$) or unoccupied states ($V < 0$) in the sample are detected.

As the STM tip scans the surface laterally, guided by a raster scan generator, the feedback loop continuously adjusts the tip's vertical position (z) based on changes in lateral

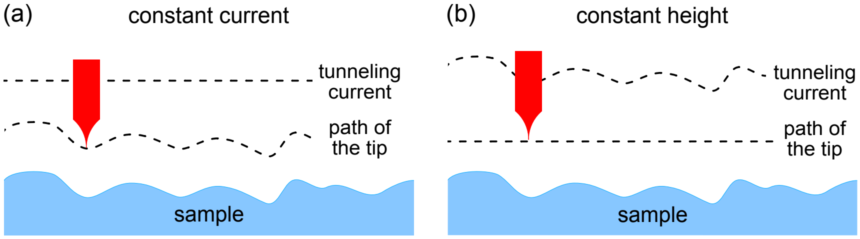

Figure 2.7: (a) The constant current mode in STM topography involves adjusting the tip height to maintain a constant tunneling current while scanning the sample surface. Therefore, the tip height will track the surface topography to a good approximation, providing a visual representation of the surface. (b) In constant height mode, the tip height regulation is switched off while the sample surface is scanned, and the tunneling current is measured. As a result, variations in the tunneling current correspond to the surface topography. The tunneling current decreases with increasing tip-sample distance, whereas tunneling current increases with decreasing the distance, providing a visual representation of the surface topography.

positions (x, y). In this mode, the height of the tip presents a comprehensive visualization of the sample surface, as shown in Figure 2.7a.

2.2.5 Constant height mode

The constant height mode of STM maintains a fixed height of the tip above the sample surface by switching off the feedback loop while the tunneling current varies during scanning. In this mode, changes in the surface topography or LDOS will be reflected in variations in the tunneling current, and by detecting these changes, the surface can be mapped as shown in Figure 2.7b.

The constant height mode is an appropriate method for imaging atomically flat surfaces, can encounter difficulties when applied to surfaces with considerable topographical variations, such as atomic step edges. For example, performing a constant height scan with the feedback loop deactivated, particularly when the tip is in close proximity to the sample surface, can be quite challenging. This may result in high tunneling currents and potential damage to both the tip and the sample [106].

2.2.6 $I - V$ characteristics

The $I - V$ curve mode is a key technique for probing the electronic properties of surfaces at the atomic level in STM measurements. Measuring the tunneling current (I) as a function of applied bias (V) between the STM tip and sample provides insight into the material's LDOS, energy gaps, and potential barriers [95].

To obtain an $I-V$ curve, the STM tip is positioned at a fixed location. The bias voltage is systematically varied while the corresponding tunneling current is recorded. The resulting curve is highly sensitive to the electronic structure of the sample. For example, metallic samples typically exhibit a linear $I-V$ relationship, indicating a continuous density of states, while semiconductors or insulators often exhibit nonlinear behavior due to energy gaps.

In practical applications, once the STM tip is stabilized at the desired location above the sample, the feedback loop is deactivated to maintain a constant tip height and the bias voltage is swept over a specified range.

The $I-V$ curve measurement mode has been an integral part of this dissertation, offering valuable insights into the interactions between chiral molecules and magnetic substrates at the single-molecule level. These interactions, which are relevant to spin selective electron transport, will be further explored in Sections 3.4 and 3.5.

2.2.7 dI/dV spectroscopy

One of the remarkable features of STM is its ability to determine the sample LDOS with atomic precision in specific energy intervals. The tunneling current as a function of bias voltage, provides information about the integrated density of states within the range $[E_F; E_F + eV]$, as explained in Section 2.2.3. To directly access the electronic states within a specific energy interval, differentiating Eq. 2.18 with respect to V reveals the relationship between the differential conductivity (dI/dV) and the sample's LDOS.

$$\begin{aligned}\frac{dI}{dV} \propto \rho_t(0)\rho_s(eV)T(E,eV) + \int_0^{eV} \frac{d(\rho_t\,(E-eV))}{dV}\rho_s\,(E)\,T(E,eV)\,dE \\ + \int_0^{eV} \rho_t\,(E-eV)\,\rho_s\,(E)\,\frac{d(T(E,eV))}{dV}\,dE.\end{aligned} \tag{2.24}$$

In the above equation, the second and third terms account for potential changes in the DOS of the tip and the tunneling transmission probability as the bias voltage varies. However, these contributions are often negligible in practice[2] [107]. Thus, in the first

---

[2] This simplification is based on two key assumptions. First, it is assumed that the DOS of the STM tip, $\rho_t(E)$, remains relatively constant over the small range of bias voltages typically used in STS. Consequently, $\frac{d\rho_t}{dV} \approx 0$, allowing the second term to be ignored. Second, the tunneling transmission probability, $T(E, eV)$, is considered to change only slightly with the applied voltage, rendering the third term negligible.

approximation, the dI/dV signal is proportional to the sample's LDOS, i.e.; $\rho_s(eV)$. Additionally, in a fixed location, the transmission factor $T(E, eV)$ exhibits a monotonic increase with V, creating a smooth background signal where spectroscopic details are superimposed. Since this increase is both steady and monotonic, any structure observed in dI/dV as a function of V can generally be attributed to changes in the density of state through the first term. As a result, it is possible to determine the LDOS of the sample as an energy function at any specific point on the surface [108]. However, the tunneling current is often too noisy to acquire reliable data solely through numerical differentiation of the acquired $I - V$ curve. To address this issue, the lock-in technique is employed to improve the signal-to-noise ratio and extract precise information about the LDOS of the sample.

The lock-in technique works by adding a small high-frequency AC modulation (V_{mod}) to the bias voltage and subsequently detecting the tunneling current's response synchronized with the same modulation frequency. By using a narrow bandwidth around the modulation frequency, the lock-in amplifier filters out noise and enhances the measured signal quality.

By employing a Taylor series for the tunneling current, the following equation can be formulated [106]:

$$I(V + V_{\text{mod}} cos(\omega t)) = I(V) + \frac{dI(V)}{dV} V_{\text{mod}} cos(\omega t) + \frac{d^2 I(V)}{2dV^2} V_{\text{mod}}^2 cos(\omega t)^2 + \dots, \quad (2.25)$$

where V_{mod} and $f_{\text{mod}} = \omega/2\pi$ represent the amplitude and frequency of the applied modulation voltage, respectively. The dI/dV signal is obtained by using a lock-in amplifier to detect the first harmonic.

The spectroscopic dI/dV data presented in this work were obtained using two different methods:

- Maps of differential conductance
- Point spectroscopy

Differential conductance (dI/dV) maps were obtained simultaneously with the acquisition of a constant-current topographic image while the feedback loop was closed. The dI/dV signal was extracted by superimposing the DC bias voltage V_{bias} with a small sinusoidal modulation having an rms amplitude of $V_{\text{mod}} = 20$ or 10 mV and a frequency of $f_{\text{mod}} = 752$ or 875 Hz. The tunneling current's modulation at f_{mod} is detected using a lock-in amplifier and recorded as a function of the lateral tip position during a scan in a second data channel. The dI/dV maps, to a large extent, depict the spatial variations of the LDOS above the sample at the energy interval of $[E_F + eV_{\text{bias}} - eV_{\text{mod}} : E_F + eV_{\text{bias}} + eV_{\text{mod}}]$. In the present study, dI/dV maps were acquired using magnetic tips, which enabled the investigation of magnetic properties and the magnetic domain structures of ferromagnetic substrates of interest.

In the context of dI/dV spectra, the STS technique plays a crucial role in examining the local electronic properties of a sample surface. During the STS curve acquisition process, the tip is carefully positioned over a chosen sample location and stabilized at specific bias voltage and tunneling current values. Once the tip is stabilized, the feedback loop is deactivated to ensure that the tip-sample distance remains constant throughout the measurement. Subsequently, the bias voltage is swept within a predetermined interval to probe various energy levels of the LDOS. As the bias voltage is swept, the lock-in amplifier detects and records the dI/dV signal. In this PhD project, dI/dV point spectra were collected usually for adsorbed molecules, illustrating the different impact of various substrates on the LDOS of the molecules. The amplitude and frequency of the applied modulated voltage are the same as those mentioned for the dI/dV maps.

The manuscript presented in Section 3.1 provides a more elaborate information of the dI/dV maps of the investigated ferromagnetic substrates and the point spectra of the adsorbed molecules.

2.3 Materials

As highlighted in Section 1.5, this study aims to establish an experimental model system for studying individual chiral molecules deposited on ferromagnetic substrates in order to enhance our understanding of the CISS effect. In pursuit of this goal, we selected heptahelicene, a simple chiral molecule, characterized by the helical arrangement of its seven ortho-fused benzene rings that do not lie in the same plane (See Figure 1.2). Due to its relatively simple structure, [7]H molecule stands out as an excellent candidate for precise theoretical modeling and simulations, compared to the more complex and lengthy molecules used in most of the previous experimental investigations.

Additionally, several studies have been conducted on this particular molecule, mainly emphasizing the self-assembly and crystallization processes that occur when the molecule is physisorbed on different substrates [109–114]. The [7]H molecule also belongs to a family of helical molecules whose spin selectivity has been studied previously [28, 39].

Considering the availability of precise modeling and the extensive scientific studies on the adsorption and geometrical configuration of this molecule at the atomic scale, this molecule was likely to be a suitable choice for our single-molecule studies.

For the selection of substrate, we decided for well-established single-crystalline ferromagnetic substrates: the Fe bilayer thin films on W(110) and bilayer Co nanoislands on Cu(111), for which the formation, atomic structure, electronic, and magnetic properties have been extensively investigated and are well established [115–126]. Both substrates exhibit OOP magnetization. In the STM geometry, this OOP magnetization leads to electrons tunneling with either positive or negative helicity, i.e. with a parallel or antiparallel projection of the spin onto the momentum vector. This feature is a prerequisite for investigating the CISS effect as an interplay between the molecule's chirality and the spin of the electron.

In order to prevent unnecessary repetition, the explanations regarding sample preparation and characterization, which covers substrate cleaning, deposition of ultra thin layers of ferromagnetic materials, and the sublimation process of [7]H molecules, will be omitted here. The manuscript presented in 3.1 elaborately discusses these topics.

CHAPTER 3

Experimental results

In this chapter, the experimental results of this PhD study will be presented. Most of the obtained experimental results have already been incorporated into three individual scientific publications, therefore the published manuscripts for these publications will be directly integrated into this chapter. Furthermore, the remaining data, which have not yet been drafted into scientific articles, will be presented and discussed in the following.

3.1 Manuscript 1: Deposition of chiral heptahelicene molecules on ferromagnetic Co and Fe thin-film substrates

This section consists entirely of the above-named manuscript, providing a comprehensive overview of the technical procedures involved in the preparation of ultra-thin ferromagnetic substrates. The manuscript focuses on the characterization of these substrates' atomic structure and magnetic properties. Following this detailed characterization, we investigated the deposition of [7]H molecules from a racemic mixture onto three distinct single-crystalline substrates: non-magnetic Cu(111), OOP magnetized bilayer Fe films on W(110), and OOP magnetized bilayer Co nanoislands on Cu(111). Utilizing high-resolution topographical and spin-polarized STM images, we examined the handedness and in-plane adsorption orientation of several hundred individual chiral molecules, as well as the magnetization of the underlying substrates (in the case of Fe and Co).
Our investigation revealed the persistence of OOP magnetization in the substrates following molecular deposition, a factor that is critical for our subsequent investigations. This persistence is especially significant when examining the CISS effect, which involves the interplay between electron spin and the handedness of chiral molecules.

Beyond the topographical STM data, we conducted point spectroscopy, which revealed that [7]H molecules undergo physisorption on Cu(111) surfaces, while chemisorption takes place on Co(111) and Fe(110) bilayers.
This manuscript is published in Nanomaterials and is available as [127].

> *Mohammad Reza Safari and Frank Matthes conducted the sample preparations and the STM/STS experiments. Karl-Heinz Ernst synthesized and provided the molecules. Mohammad Reza Safari, Frank Matthes and Daniel E. Bürgler conducted the data analysis. Mohammad Reza Safari wrote the manuscript in close collaboration with Daniel E. Bürgler and Frank Matthes and with contributions from Karl-Heinz Ernst and Claus M. Schneider.*

nanomaterials

Article

Deposition of Chiral Heptahelicene Molecules on Ferromagnetic Co and Fe Thin-Film Substrates

Mohammad Reza Safari [1,2,*], Frank Matthes [1,2], Karl-Heinz Ernst [3,4], Daniel E. Bürgler [1,2,*] and Claus M. Schneider [1,2,5]

[1] Peter Grünberg Institute, Electronic Properties (PGI-6), Forschungszentrum Jülich, 52428 Jülich, Germany
[2] Jülich Aachen Research Alliance (JARA), Fundamentals of Future Information Technology, 52425 Jülich, Germany
[3] Molecular Surface Science Group, Empa, Swiss Federal Laboratories for Materials Science and Technology, 8600 Dübendorf, Switzerland
[4] Nanosurf Laboratory, Institute of Physics, The Czech Academy of Sciences, 16200 Prague, Czech Republic
[5] Fakultät für Physik, Universität Duisburg-Essen, 47057 Duisburg, Germany
* Correspondence: m.safari@fz-juelich.de (M.R.S.); d.buergler@fz-juelich.de (D.E.B.)

Abstract: The discovery of chirality-induced spin selectivity (CISS), resulting from an interaction between the electron spin and handedness of chiral molecules, has sparked interest in surface-adsorbed chiral molecules due to potential applications in spintronics, enantioseparation, and enantioselective chemical or biological processes. We study the deposition of chiral heptahelicene by sublimation under ultra-high vacuum onto bare Cu(111), Co bilayer nanoislands on Cu(111), and Fe bilayers on W(110) by low-temperature spin-polarized scanning tunneling microscopy/spectroscopy (STM/STS). In all cases, the molecules remain intact and adsorb with the proximal phenanthrene group aligned parallel to the surface. Three degenerate in-plane orientations on Cu(111) and Co(111), reflecting substrate symmetry, and only two on Fe(110), i.e., fewer than symmetry permits, indicate a specific adsorption site for each substrate. Heptahelicene physisorbs on Cu(111) but chemisorbs on Co(111) and Fe(110) bilayers, which nevertheless remain for the sub-monolayer coverage ferromagnetic and magnetized out-of-plane. We are able to determine the handedness of individual molecules chemisorbed on Fe(110) and Co(111), as previously reported for less reactive Cu(111). The demonstrated deposition control and STM/STS imaging capabilities for heptahelicene on Co/Cu(111) and Fe/W(110) substrate systems lay the foundation for studying CISS in ultra-high vacuum and on the microscopic level of single molecules in controlled atomic configurations.

Keywords: chiral molecules; molecular deposition; ferromagnetic surfaces; adsorption geometry; STM

check for updates

Citation: Safari, M.R.; Matthes, F.; Ernst, K.-H.; Bürgler, D.E.; Schneider, C.M. Deposition of Chiral Heptahelicene Molecules on Ferromagnetic Co and Fe Thin-Film Substrates. *Nanomaterials* **2022**, *12*, 3281. https://doi.org/10.3390/nano12193281

Academic Editors: Gabriele Giancane and Simona Bettini

Received: 11 August 2022
Accepted: 14 September 2022
Published: 21 September 2022

1. Introduction

The discovery of the chirality-induced spin selectivity (CISS) effect [1,2] as an interplay between electron spin and the handedness of chiral molecules has attracted much interest in recent years [3,4] and is expected to lead to a chirality-based quantum leap in quantum sciences [5]. The highly efficient spin-dependent electron transmission through non-conductive chiral molecules also makes the CISS effect a promising approach for future applications in spintronics, chemical sensing, enantioseparation, and enantioselective chemical and biological processes [6,7]. Several experimental approaches have been used to demonstrate the CISS effect for diverse chiral molecules and materials and have led to the following exemplary but certainly not exhaustively listed–findings:

- Spin-selective transmission of charge carriers through various chiral molecules ranging from long DNA strands [8] and polymers [9] to helical molecules (e.g., helicene molecules) with down to a single winding [10] yielded substantial spin polarization values, for instance, exceeding 60% for photo-emitted electrons passing through monolayers (ML) of double-stranded DNA [11] or 80% for the hole current through chiral methylbenzylammonium molecules within a layered organic–inorganic metal–halide hybrid semiconductor framework [12], both at room temperature (RT). This opens perspectives for the realization of a versatile, low-cost and energy-efficient carbon-based spintronics with reduced device size, operating at RT and not requiring ferromagnetic metals [2].

- The enantiospecific adsorption of various chiral molecules on ferromagnetic, perpendicularly magnetized substrates demonstrated a distinct approach to enantiomeric separations by providing a potentially generic, efficient, and cost-effective chromatographic method for enantioseparation, which does not require a specific separating column [7,13].
- Adsorbing a self-assembled ML of chiral molecules can switch the local magnetization of a ferromagnetic layer with perpendicular magnetic anisotropy without the need to apply an electrical current or an external magnetic field [14].

Despite the extensive experimental data on the CISS effect, its theoretical background has not yet been sufficiently clarified; thus, it is still an open question of whether there is a predictive, unifying, and experimentally tractable model of spin-dependent electron transport through a chiral molecule [5]. Most theoretical models still have some shortcomings in filling the large gap between the experimental and theoretically calculated effect size, e.g., spin polarization values or enantiospecific adsorption energies on ferromagnetic surfaces [2,15–20]. A major difficulty is the discrepancy between the experimentally studied *real systems* and the *idealized model systems* accessible to theoretical descriptions. Most experimental work involves molecular ensembles and therefore provides information averaged over many different configurations (e.g., absorption sites and geometries or electric current paths). In addition, most experiments are performed under environmental conditions that require protective coatings to prevent oxidation (e.g., Au coating of ferromagnetic substrates) or result in additional adsorbates (e.g., water due to air humidity), neither of which are accounted for in theoretical models. Therefore, single-molecule scale studies performed under well-defined vacuum conditions and in controlled geometric configurations, ideally on the atomic level, are highly desirable to gain deeper insight into the fundamentals of the CISS effect [20].

Here, we lay the foundation for such experiments by reporting the deposition of the racemic mixture of chiral heptahelicene molecules on different single-crystalline surfaces by sublimation under ultra-high vacuum (UHV, pressure lower than 10^{-7} Pa) conditions, where the substrate materials include the noble metal Cu and the more reactive ferromagnets Fe and Co. Heptahelicene belongs to the family of chiral helicene molecules for which the CISS effect has been demonstrated experimentally [10,21] and intensively studied theoretically [19,20,22]. We use low-temperature scanning tunneling microscopy (LT-STM) to characterize the molecular adsorption geometries and determine the handedness of individually adsorbed molecules. The latter is a prerequisite for heptahelicene on Cu(111), Co(111), or Fe(110) surfaces to be used as model systems for future experiments on the CISS effect at the single-molecule level.

2. Materials and Methods

Heptahelicene $C_{30}H_{18}$ ([7]H) is chiral due to seven ortho-fused benzene rings that do not fit into a plane, thus leading to a helical shape; see Figure 1. For monolayers of heptahelicene molecules on surfaces of the coinage metals Cu, Ag and Au, the CISS effect was demonstrated in photoemission experiments and resulted in 6 to 8% spin polarization [10]. The adsorption of [7]H and film growth in the ML and sub-ML regime on surfaces of the same coinage metals have been extensively studied in the context of self-assembly and crystallization [23–27]. However, to our knowledge, there is only one STM study on the deposition of [7]H on a ferromagnetic and more reactive surface, namely Ni(111) [28], where STM images revealed randomly oriented molecules at low coverage and a hexagonally closed-packed ML with an intermolecular distance consistent with the van der Waals radius of [7]H.

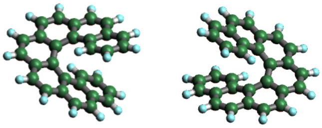

Figure 1. Schematic representation of the helical left-handed (*M*)-[7]H and right-handed (*P*)-[7]H.

Here, we report the adsorption of [7]H molecules in the sub-ML regime on two ferromagnetic thin-film substrate systems with out-of-plane magnetization that are well-known in the magnetism community, namely Co(111) bilayer (BL) nanoislands on Cu(111) and 2 ML Fe(110) thin films on W(110). The out-of-plane magnetization leads in the STM geometry to tunneling electrons with positive or negative helicity (defined as the projection of the spin on the momentum vector), which is a prerequisite for studying the CISS effect and the interplay of spin-polarized currents with chiral molecules. The partly filled 3*d* shell of Co and Fe renders these surfaces more reactive than those of coinage metals. The adsorption of [7]H on the less reactive Cu(111) single-crystal surface between the Co nanoislands is used for comparison with the ferromagnetic surfaces as well as with previous literature. The heptahelicene molecules used in this study were synthesized at Empa, the Swiss Federal Laboratories for Materials Science and Technology, in the form of a racemic powder.

2.1. Sample Preparation

All experiments in this work were performed under UHV conditions in a multi-functional UHV cluster tool with a base pressure of less than 10^{-8} Pa, which is equipped with an LT-STM (Omicron Scienta), a preparation chamber for substrate preparation, thin-film growth and analysis, and a molecule deposition chamber. All chambers are separately pumped and can be sealed from each other.

The [7]H powder was filled without further treatment into a quartz crucible of a Knudsen cell located in the molecule deposition chamber. The sublimation of [7]H molecules sets in at a crucible temperature of about 400 K. Any contamination of the freshly prepared Co and Fe thin-film substrates due to degassing of the heater filament of the Knudsen cell during the slow and careful heat-up is detrimental to the surface magnetism and may impede spin-polarized STM imaging [29]. Therefore, in order to avoid contamination, the substrate was introduced to the molecular chamber only after reaching the sublimation temperature and was immediately exposed to the molecular vapor. The vacuum pressure during molecule sublimation did not exceed 10^{-7} Pa. After molecule deposition, the samples were transferred within 5 min to the STM chamber, where they were cooled to 5 K at a vacuum pressure in the mid 10^{-9} Pa range. We performed numerous cycles of molecular deposition, which proved the reliability and reproducibility of the deposition procedures and allowed repeated STM/STS measurements with both newly fabricated samples and modified (newly functionalized) STM tips.

In the following, we describe the procedures for preparing the three different molecule–substrate systems.

2.1.1. Heptahelicene on Cu(111)

The single-crystal Cu(111) substrate was cleaned by repeated cycles of Ar^+ sputtering and post-annealing at 1070 K according to the procedure described in [30]. After annealing, the cooling was performed with a controlled temperature gradient to promote the formation of wide atomic terraces. The sample cleanness was checked by Auger electron spectroscopy (AES) and LT-STM measurements. Heptahelicene molecules were then sublimated as described above onto the Cu(111) surface, which was at room temperature (RT).

2.1.2. Heptahelicene on Co/Cu(111)

For the preparation of the [7]H/Co/Cu(111) sample, triangular Co BL nanoislands are grown on the cleaned Cu(111) crystal at RT. Co is deposited by electron-beam evaporation (triple evaporator from Scienta Omicron) with a deposition rate of 0.2 ML/min according to [31]. The result of each deposition is verified by topographic and spin-polarized STM measurements to confirm the cleanness of the surface, the density and shape of the Co nanoislands, and their well-developed magnetization perpendicular to the surface. Only when all requirements are met, heptahelicene molecules are deposited on the Co/Cu(111) substrates as described above, whereby it warms up again to RT in the molecule deposition chamber.

2.1.3. Heptahelicene on Fe/W(110)

The single-crystal W(110) substrate was cleaned by repeated cycles of oxygen annealing ($1000 < T < 2000$ K) and high-temperature flashing ($T > 2300$ K) as described in [32]. Subsequently, 1.7 ML Fe was deposited with a growth rate of 0.6 ML/min by electron-beam evaporation onto the substrate, which was at RT. Post-annealing at 570 K results in a completely filled 1st Fe ML and a partially filled 2nd Fe layer. As for the Co/Cu(111) substrate system, the Fe/W(110) film growth quality and the magnetic properties, in particular the presence of out-of-plane magnetized domains in areas covered with 2 ML Fe, were checked by topographic and spin-polarized STM measurements. The deposition of heptahelicene molecules, again with the substrate at RT, followed the procedure described above.

2.2. STM Measurements

All STM measurements were performed using a W tip fabricated by the electrochemical etching of a polycrystalline W wire in 5 M NaOH solution. In order to obtain spin-polarized data, we functionalized the W tip by intentionally driving it into mechanical contact with the ferromagnetic substrate remote from the region of interest and applying short voltage pulses to the tip to pick up atoms from the substrate. Lacking the possibility to apply an external magnetic field to the STM setup, we also use this procedure to modify the direction of the tip magnetization and thus the direction of its magnetic sensitivity, i.e., out-of-plane up to out-of-plane down or to in-plane sensitivity. Although this procedure is somewhat random and unpredictable, it allows us to investigate the same surface area with the tip being sensitive to different magnetization directions.

We present three types of STM data. (i) Topographic STM images were taken in constant-current mode. (ii) Differential conductivity (dI/dV) maps were taken simultaneously with constant-current topographic images (closed feedback loop). dI/dV maps represent, to a good approximation, the local density of states (LDOS) as a function of the lateral position and at the energy eV_{bias}, where $V_{\text{bias}} = 0$ corresponds to the Fermi energy (E_F). (iii) Scanning tunneling spectroscopy (STS) point spectra were acquired at a fixed lateral and vertical tip position (open feedback loop) by sweeping V_{bias}. dI/dV point spectra represent, to a good approximation, the LDOS as a function of the energy eV_{bias} at a fixed tip position. The dI/dV signal for the conductivity maps and point spectra was obtained by superimposing V_{bias} with a small sinusoidal modulation (rms amplitude $V_{\text{mod}} = 10$ or 20 mV; frequency $f_{\text{mod}} = 875$ or 752 Hz) and detecting the resulting modulation of the tunneling current using a lock-in amplifier. In the present case, we employ topographic images (STM data type (i)) to address the quality of the substrates as well as the integrity, adsorption geometry, adsorption position and chirality of the deposited molecules. dI/dV maps (STM data type (ii)) obtained with magnetic tips reveal the ferromagnetism and magnetic domain structure of the Co and Fe substrates. dI/dV point spectra (STM data type (iii)) measured on adsorbed molecules show the different impact of the Cu, Co and Fe substrates on the LDOS of the physisorbed and chemisorbed [7]H molecules, respectively.

3. Results

3.1. Heptahelicene on Cu(111)

Figure 2a shows a constant-current topographic image of a sub-ML coverage of the Cu(111) surface with [7]H molecules. A Cu(111) monatomic step is visible on the right side of the image, which is densely decorated with molecules. The STM data reveal a clean deposition of intact [7]H molecules, since fragments of molecules and other adsorbates are barely visible. The molecules mostly form dimers with only a few trimers and monomers present as reported by Ernst et al. [25], who investigated the structure and binding of the dimers in detail. Both the dense step edge decoration and the almost complete dimer formation indicate the high surface mobility of the molecules at RT. Note that the equilibrium configuration of the molecules on the surface is reached during and immediately after the deposition at RT, and the STM images show a frozen state after cooling the sample to 5 K.

Figure 2b shows a submolecularly resolved image of three dimers. Each molecule appears as a radially asymmetric gray halo with a bright spot that is offset from the center of the halo. The cross-section along the red line in Figure 2b, displayed in Figure 2d, reveals an apparent height of the bright spots of 240 pm, which indicates an adsorption geometry of the [7]H molecule with its helix axis perpendicular to the surface. This is in agreement with an X-ray photoelectron diffraction study of Cu(111) covered with 1/3 ML [7]H [23].

These data agree very well with a previous report [25] on the deposition of a racemic mixture of [7]H molecules on Cu(111). The authors related the off-centered maximum and the radially asymmetric, hence helical, gray halo of the apparent height profile to the handedness of the [7]H molecules and found that the dimers are heterochiral; i.e., each dimer consists of one (*M*)-[7]H and one (*P*)-[7]H molecule. Similar to Ernst et al. [25], we apply a Gaussian high-pass filter to the topographic STM image in Figure 2b and obtain a better visualization of the molecules' handedness in Figure 2c, where the handedness can be directly determined, as indicated by the dashed blue and red circular arrows. Technical information about the Gaussian high-pass filter is detailed in Appendix A. In the following, we will use dashed blue and red circular arrows to label right-handed (*P*)-[7]H and left-handed (*M*)-[7]H molecules, respectively. The arrows are drawn to start adjacent to the proximal phenanthrene group close to the surface and with the arrowheads adjacent to the distal end (see scheme in Figure 2e).

In order to improve the statistics, we applied the Gaussian high-pass filter to high-resolution data of a larger area marked by a red square in Figure 2a. The result is shown in Figure 2f. For molecules not marked with a dashed arrow, the assignment of absorption orientation and handedness was not possible. This can be caused by adsorption on a defect of the substrate or by aggregation with more than one other molecule. Evidently, the heterochiral nature of the dimers is clearly confirmed. In addition, we find only three rotational orientations of the adsorbed molecules, which occur with approximately equal probability (see Table 1): The bright spot is offset from the halo center in the $[\bar{1}\,1\,0]$, $[1\,0\,\bar{1}]$, or $[0\,\bar{1}\,1]$ direction of the Cu(111) surface. The observation of three distinct adsorption orientations is in agreement with the above-mentioned photoelectron diffraction study of [7]H on Cu(111) [23]. In Appendix B, we present a larger data set for which we have performed a so-called mosaic measurement that includes a set of high-resolution topography images. By merging these images, we have data from a more extended area of the sample surface with sufficient resolution for analysis. The evaluation of 593 [7]H molecules again yields an even distribution on the three adsorption orientations specified in Figure 2e (see 1st row in Table 1).

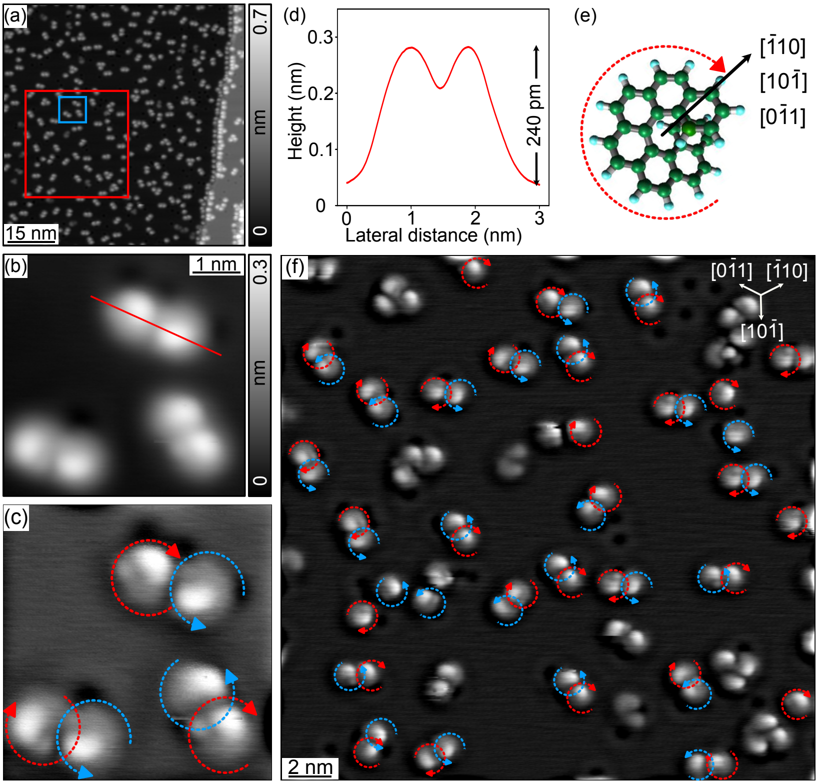

Figure 2. (**a**) Constant-current topographic image of [7]H molecules on the Cu(111) surface ($V_{\text{bias}} = 500$ mV, $I_t = 100$ pA). (**b**) Zoom view of the blue marked area in (**a**) showing [7]H molecules with submolecular resolution ($V_{\text{bias}} = 500$ mV, $I_t = 200$ pA). (**c**) High-pass filtered data of (**b**). (**d**) Cross-section (averaged over a line width of 10 pixels) along the red line in (**b**) showing the apparent height profile of a (*M*)-[7]H–(*P*)-[7]H dimer. (**e**) Schematic representation of the position of a [7]H molecule's topmost C hexagon and the dashed arrow marking the handedness and in-plane adsorption orientation (black arrow), which points on the Cu(111) surface along the $[\bar{1}\,1\,0]$, $[1\,0\,\bar{1}]$, or $[0\,\bar{1}\,1]$ direction. (**f**) High-resolution image of the red marked area in (**a**) after applying the Gaussian high-pass filter ($V_{\text{bias}} = 500$ mV, $I_t = 100$ pA). Dashed blue and red circular arrows mark right-handed (*P*)-[7]H and left-handed (*M*)-[7]H molecules, respectively. All STM data were measured at 5 K with a W tip.

In summary, the [7]H molecules adsorb on Cu(111) in a configuration, in which the molecule spirals away from the surface and forms in the sub-ML regime mostly heterochiral dimers. Within dimers, the [7]H molecules adsorb at a well-defined adsorption site in three orientations with respect to the substrate, which result from the three-fold symmetry of the (111) surface of the face-centered cubic (fcc) Cu crystal, making them energetically degenerate and evenly occupied.

3.2. Heptahelicene on Bilayer Co Nanoislands

The formation, atomic structure, electronic and magnetic properties of Co BL nanoislands on Cu(111) have been extensively studied and are well established [31,33–37]. Figure 3a shows the result of depositing a sub-ML amount of Co on Cu(111) at RT. Triangular islands are formed with a typical size of 10 nm and an apparent height of 370 pm, corresponding to an island height of 2 ML (see blue cross-section in Figure 3b taken along the blue line in Figure 3a). The two different island orientations, which are rotated by 60° with respect to each other, result because the first layer's Co atoms can adsorb on Cu(111) to fcc or hexagonal-closed-packed (hcp) sites, leading to so-called "unfaulted" and "faulted" islands, respectively [31,35]. On both island types, the second-layer Co atoms can also adsorb to either fcc or hcp sites. In all four cases, the atomic structure of the island surfaces is three-fold symmetric. Islands with throughout fcc or hcp stacking have the same symmetry-equivalent in-plane directions as the Cu(111) surface below, while on islands with mixed stacking, all in-plane directions are inverted.

Figure 3c shows the differential conductivity (dI/dV) map at $-600\,\mathrm{mV}$ recorded simultaneously with the topographic image in Figure 3a and using a Co-functionalized W tip. The Co nanoislands can be divided into two groups with distinctly different differential conductivity, i.e., LDOS at $-600\,\mathrm{meV}$. Figure 3d shows another dI/dV map at $-600\,\mathrm{mV}$ taken in the same sample area as Figure 3a,c but after intentional modification of the Co-functionalized W tip on a remote Co nanoisland as described in Section 2.2. Evidently, the differential conductivity of all islands has changed from low to high or vice versa. An exception is the nanoisland in the red frame in Figure 3a, which, however, is 3 instead of 2 ML high (see red line profile in Figure 3b) and is therefore not of further interest here, since Co films on Cu(111) thicker than 2 ML are in-plane magnetized [38]. Consistent with previous reports [33,34,36,37,39], the different dI/dV contrast of the islands and its inversion in Figures 3c and d arise from spin-polarized tunneling between the out-of-plane magnetized Co nanoislands [33] and the Co-functionalized W tip. The islands appear light or dark in the dI/dV maps if the magnetization of the tip is parallel or antiparallel to the island magnetization, respectively. The contrast reversal from Figure 3c,d is due to a reversal of the tip magnetization caused by the intentional modification of the tip. Thus, the Co/Cu substrate system provides oppositely out-of-plane magnetized, single-domain Co nanoislands with bare Cu(111) regions in between within an area of less than $200 \times 200\,\mathrm{nm}^2$.

Table 1. Statistics of the [7]H adsorption orientations on Cu(111), Co/Cu(111), and Fe/W(110). On Cu(111), [7]H absorbs in three equally populated and thus degenerate orientations. Co BL nanoislands on Cu(111) occur in four different stacking sequences that can be assigned to two orientations of the Co lattice with respect to the Cu substrate. The plus sign in, for example, $\pm[\bar{1}10]$ refers to the Co lattice aligned to the Cu lattice, and the minus sign refers to the inverted Co lattice. Hence, [7]H adsorbs uniformly distributed in three orientations with respect to the atomic lattice of the Co BL nanoislands. On Fe/W(110), [7]H adsorbs with equal probability in only two orientations. The error margins are the statistical errors of the counts.

Substrate (Data)	Analyzed Molecules	Orientation 1	Orientation 2	Orientation 3
Cu(111) (Figure 2f)	56	$[\bar{1}10]$: 20 ± 4	$[10\bar{1}]$: 21 ± 5	$[0\bar{1}1]$: 15 ± 4
Cu(111) (Figure A2)	593	$[\bar{1}10]$: 205 ± 14	$[10\bar{1}]$: 202 ± 14	$[0\bar{1}1]$: 186 ± 14
Co/Cu(111) (Figure 4a)	152	$\pm[1\bar{1}0]$: 50 ± 7	$\pm[\bar{1}01]$: 45 ± 7	$\pm[01\bar{1}]$: 57 ± 8
Fe/W(110) (Figure 6e)	87	$[001]$: 44 ± 7	$[\bar{1}10]$: 43 ± 7	-

The result of depositing a sub-ML amount of [7]H molecules on the Co/Cu substrate system at RT is shown in Figure 4. The constant-current topographic image in Figure 4a shows that all molecules are adsorbed on the Co nanoislands, and not a single molecule is found on the Cu surface. The apparent height (about 250 pm) and shape of the molecules are similar to those in Figure 2, implying an adsorption geometry on Co(111) in which the lower phenanthrene group is also aligned parallel to the surface. The high surface mobility of the [7]H molecules on the Cu surface at RT allows them to diffuse to Co nanoislands, where they accumulate in the thermal equilibrium due to the much stronger binding to the more reactive Co [40]. The numerous adsorption along the island edges is due to the enhanced interaction at step edges and with the Co rim states [34]. The dI/dV map in Figure 4b recorded simultaneously with Figure 4a reveals the magnetic contrast of the Co nanoislands in the presence of [7]H molecules. Note that in contrast to Figure 3c,d, we used a color scale with multiple color transitions to visualize both the different LDOS due to the oppositely out-of-plane magnetized islands (dark and red) and the enhanced LDOS above the [7]H molecules and the rim state (green-blue). These data indicates a clean molecule sublimation process that does not affect the magnetism of the Co nanoislands.

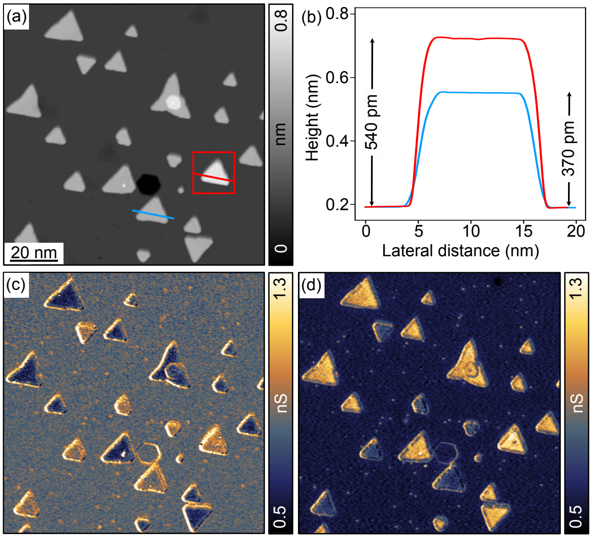

Figure 3. (**a**) Constant-current topographic image of Co nanoislands on Cu(111). (**b**) Line profiles (averaged over a line width of 10 pixels) along the blue and red lines in (**a**). (**c**) dI/dV map at $-600\,\mathrm{mV}$ measured simultaneously with the topographic image in (**a**). (**d**) dI/dV map at $-600\,\mathrm{mV}$ of the same area as in (**a**,**c**) after reversing the tip magnetization. All data are measured with $V_{\mathrm{bias}} = -600$ mV, $I_{\mathrm{t}} = 1$ nA, $V_{\mathrm{mod}} = 10$ mV, $f_{\mathrm{mod}} = 875$ Hz and at 5 K using a Co-functionalized W tip.

Figure 4c shows a high-resolution topographic image of the area marked in red in Figure 4a, to which we have applied the Gaussian high-pass filter. Similar to the case of [7]H on Cu(111) in Section 3.1, the filtered data show submolecular features that allow determining the molecules' handedness and adsorption orientation, as indicated by the blue and red circular arrows. We observe only three adsorption orientations, which are exactly opposite to those found for [7]H on Cu(111): $-[\bar{1}\,1\,0]$, $-[1\,0\,\bar{1}]$, and $-[0\,\bar{1}\,1]$, where the Miller indices always refer to the lattice of the Cu substrate. We performed the same analysis for all Co nanoislands in Figure 4a and found for each island, that there are only three absorption orientations. For some islands, they coincide with those of [7]H on Cu(111) (i.e., $[\bar{1}\,1\,0]$, $[1\,0\,\bar{1}]$, and $[0\,\bar{1}\,1]$, see Figure 2) and for the others with those in Figure 4c (i.e., $-[\bar{1}\,1\,0]$, $-[1\,0\,\bar{1}]$, and $-[0\,\bar{1}\,1]$). Both groups include both faulted and unfaulted islands. These observations, in combination with the different stacking sequences of the four island types, lead to the conclusion that there are only three adsorption orientations of the [7]H molecule with respect to the atomic lattice of the Co BL nanoislands. Two exactly opposite adsorption orientations with respect to the Cu substrate (e.g., $[\bar{1}\,1\,0]$ and $-[\bar{1}\,1\,0]$) that we find on different islands correspond to the same orientation with respect to the respective Co lattice. In the 3rd row of Table 1, we summarize the analysis of 152 molecules on all islands in Figure 4a and report the totals for the three orientations with respect to the Co lattice, which we have labeled $\pm[\bar{1}\,1\,0]$, $\pm[1\,0\,\bar{1}]$, and $\pm[0\,\bar{1}\,1]$. Similar to adsorption on Cu(111), we find a uniform distribution within the limits of statistics.

In summary, the [7]H molecules adsorb on Co nanoislands on Cu(111) in a configuration with the helix axis perpendicular to the surface and occur in the sub-ML regime as monomers with a preference to occupy the island edges. The molecules adsorb at a well-defined adsorption site in three in-plane orientations with respect to the Co lattice that coincide with those found in Section 3.1 for [7]H on Cu(111). The uniform distribution of the three orientations indicates their energetic degeneracy resulting from the three-fold symmetry of the atomic lattice of the Co nanoislands. Sub-ML coverage with [7]H molecules does not affect the magnetism of the Co nanoislands, which remain in a single-domain state and magnetized out-of-plane.

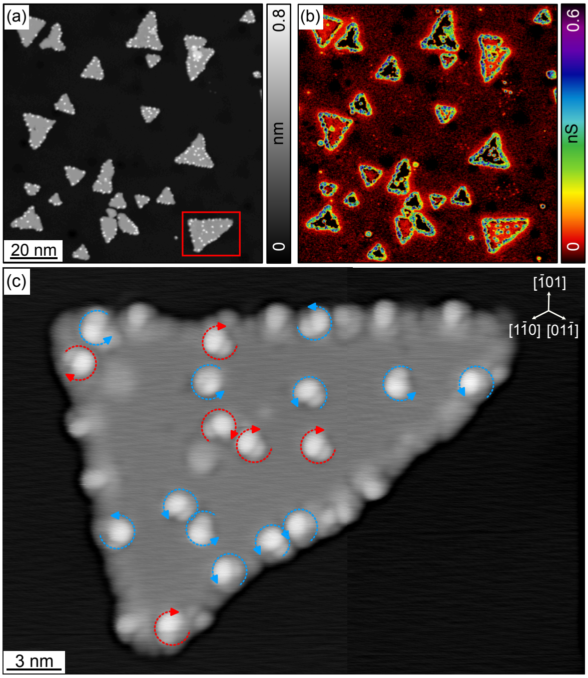

Figure 4. (**a**) Constant-current topographic image of [7]H molecules on Co nanoislands on Cu(111). (**b**) Simultaneously with (**a**) measured dI/dV map at $-600\,\text{mV}$ (V_{bias} =-600 mV, I_{t} = 900 pA, $V_{\text{mod}} = 20\,\text{mV}$, $f_{\text{mod}} = 752$ Hz, 5 K, Co-functionalized W tip). (**c**) High-resolution topographic image of the red marked area in (**a**) after subsequent Gaussian high-pass filtering. Dashed blue and red circular arrows indicate the handedness and in-plane adsorption orientation of the [7]H molecules ($V_{\text{bias}} = 1000$ mV, $I_{\text{t}} = 100$ pA, 5 K).

3.3. Heptahelicene on Ultra-Thin Fe Films on W(110)

Ultra-thin, epitaxially grown Fe films on W(110) also represent a well-established magnetic substrate system that has been studied in detail [41–45]. The deposition of slightly less than 2 ML Fe on W(110) followed by post-annealing results in sample regions covered with 1 or 2 ML Fe. The BL regions often extend from step edges of the W crystal across the lower-lying terraces. This can be seen in Figure 5a, which presents a constant-current topographic image of a 1.7 ML thick Fe film on W(110) measured with a Fe-functionalized W tip. Regions covered by 1 or 2 ML Fe are marked with 'ML' and 'BL', respectively. The dashed lines signify monatomic step edges of the W(110) crystal surface underneath. Bright lines occurring exclusively on BL regions and running along the [001] direction (red arrows) are due to characteristic dislocation lines. They arise from the relatively big lattice mismatch of 9.4% between Fe and W [41]. The simultaneously recorded dI/dV map at 50 mV in Figure 5b probes the spin-polarized d_{z^2} orbitals and reveals a rich magnetic domain structure, similar to previous reports [29,42–44]. The dark brown-bluish and bright yellow colors in the BL regions represent oppositely magnetized out-of-plane domains separated by mostly horizontal dark blue domain walls. The in-plane magnetized ML regions [42,45] and the dislocation lines also appear in dark blue. Detailed analysis of domain wall profiles, which is beyond the scope of this work, reveals contrasts due to spin-polarized tunneling from the tip with an out-of-plane magnetization component as well as due to tunneling anisotropic magnetoresistance [46,47]. Thus, the Fe/W substrate system provides in the BL regions oppositely out-of-plane magnetized domains that extend across dislocation lines. Unperturbed areas of the domains suitable for molecular adsorption studies range in size from about 20 to 40 nm and are bounded by either 8 nm wide domain walls or dislocation lines.

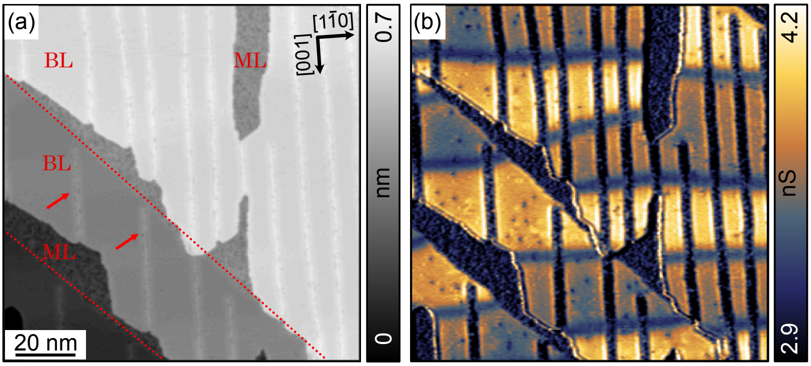

Figure 5. (**a**) Constant-current topographic image of a 1.7 ML thick Fe film on W(110). ML and BL regions are labeled, and arrows point to dislocation lines. (**b**) Simultaneously recorded dI/dV map ($V_{\mathrm{bias}} = 50$ mV, $I_{\mathrm{t}} = 300$ pA, $V_{\mathrm{mod}} = 10$ mV, $f_{\mathrm{mod}} = 875$ Hz, 5 K, Fe-functionalized W tip).

Figure 6a shows the successful deposition of [7]H molecules on the Fe surface. Bright spots visible on both ML and BL regions are single [7]H molecules. In BL regions, [7]H preferentially adsorbs on the dislocation lines that are known to be more reactive than the unperturbed Fe BL surface between the dislocation lines [29,48]. This indicates that the molecules are mobile in the BL regions immediately after the adsorption at RT. However, in ML regions, the [7]H molecules are more randomly distributed and do not preferentially adsorb at step edges, which is probably due to the lower surface mobility. The simultaneously measured dI/dV map in Figure 6b displays the typical domain structure of pristine, out-of-plane magnetized BL regions with domain walls running along $[1\bar{1}0]$, even in the presence of [7]H molecules. This observation proves a clean molecule deposition process, since any absorbed contamination on the highly reactive surface of ultra-thin Fe film would impair the magnetic properties [29].

Figure 6c shows a high-resolution topographic image of [7]H molecules on an unperturbed Fe BL region after applying Gaussian high-pass filtering. The submolecular resolution allows determining the handedness and the absorption orientation of the molecules, similar to [7]H on Cu(111) (Section 3.1) or Co BL nanoislands (Section 3.2). Examples are shown in the inset. Only two adsorption orientations are observed, and the position of the molecule's highest apparent height is located in the $[\bar{1}10]$ or $[001]$ direction from the molecule center. Interestingly and in contrast to [7]H on Cu(111) (Figure 2f) or Co BL nanoislands (Figure 4c), we observe a correlation between absorption orientation and handedness: left-handed molecules (red circular arrow) absorb in the $[\bar{1}10]$ orientation and right-hand molecules absorb in the $[001]$ orientation, respectively. The analysis of 100 molecules in Figure 6c yields 43 molecules with $[\bar{1}10]$ orientation and 44 molecules with $[001]$ orientation (see 4th row of Table 1), while the orientations of 13 molecules remained unknown.

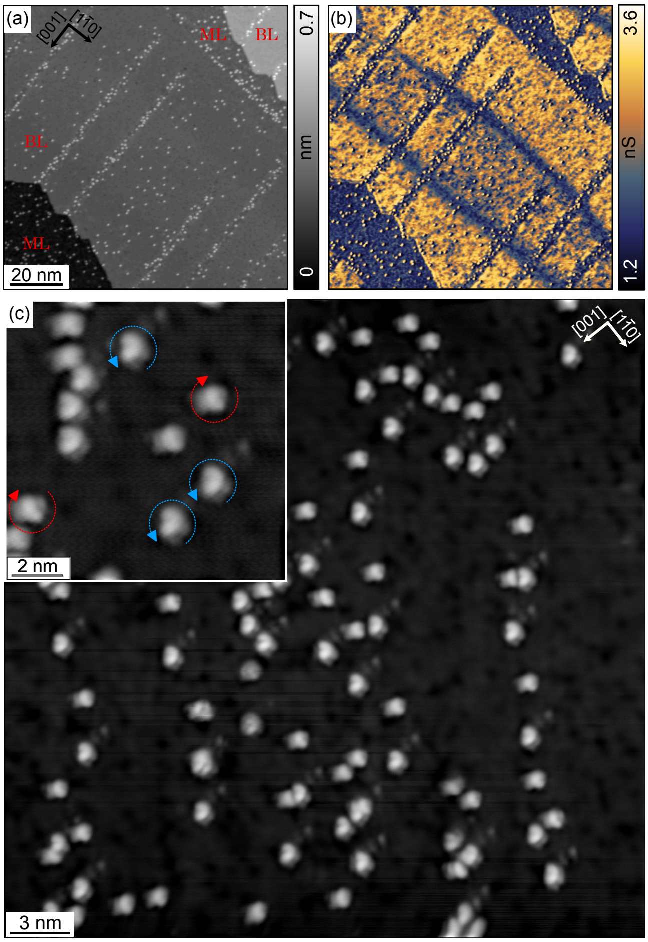

Figure 6. (**a**) Constant-current topographic image of [7]H molecules on Fe/W(110). (**b**) The dI/dV map measured simultaneously with (**a**) reveals that out-of-plane magnetized domains occur in BL regions also in the presence of [7]H molecules, similar to the pristine case in Figure 5. (**c**) High-resolution topographic image of [7]H molecules on an unperturbed Fe BL region after applying Gaussian high-pass filtering. From these data, the molecular handedness and adsorption orientation can be determined, as exemplified by dashed blue and red circular arrows in the inset. Data have been measured at $V_{\text{bias}} = 50$ mV, $I_{\text{t}} = 300$ pA, $V_{\text{mod}} = 10$ mV, $f_{\text{mod}} = 875$ Hz, 5 K, and by means of a Fe-functionalized W tip for (**a**,**b**) and a non-magnetic W tip for (**c**).

In summary, [7]H molecules adsorb on Fe BL regions on W(110) in a configuration with the helix axis perpendicular to the surface and occur in the sub-ML regime as monomers with a strong preference to occupy dislocation lines. In unperturbed areas between dislocation lines, the molecules adsorb at a well-defined site in only two in-plane orientations with respect to the non-uniformly strained Fe lattice. Each of the two orientations is occupied by molecules with a particular handedness, and their overall equal abundance reflects the racemicity of the molecular sample. The symmetry of an fcc (110) surface suggests a larger number of possible absorption orientations than actually observed, indicating a chirality dependence of the adsorption energy. Sub-ML coverage with [7]H molecules does not affect the magnetism of the Fe BL regions, which remain out-of-plane magnetized and exhibit a domain structure similar to pristine Fe BL regions.

3.4. Spectroscopy of Molecules on Different Substrates

To gain more information about the interaction of the [7]H molecules with the different substrates, we recorded by STS local dI/dV spectra over [7]H molecules adsorbed on Cu(111), Co/Cu(111), and Fe/W(110).

In general, the results of STS measurements are highly dependent on the characteristics of the tip, and different tip conditions may cause different spectral features. The wider range of bias voltages applied in STS measurements makes structural and electronic changes of the tip more likely than during STM imaging with fixed V_{bias}. Therefore, we follow a procedure that includes reference measurements to ensure that the tip has not changed during an STS measurement. We start by recording an STS spectrum at a position above the bare substrate (labeled 'substrate before') and compare the result with the STS spectra from the literature, i.e., [49] for Cu(111) and Co BL islands on Cu(111) and [50] for Fe BL regions on W(110). If the spectra are similar, we perform STS on nearby adsorbed [7]H molecules. Finally, we return to the initial position above the bare substrate and record another spectrum (labeled 'substrate after') to ensure that the tip condition has not been changed during the sequence of the measurements. We also repeat each STS measurement five times to improve the signal-to-noise ratio of the STS spectra.

Figure 7a presents STS curves of molecules on the Cu(111) surface. The relatively flat STS spectra of the bare Cu substrate (red and black) result from delocalized s and p states near E_{F}. The spectrum of the molecule (blue) also exhibits a similarly flat, featureless curve within ± 1 eV around E_{F}. The inset shows the spectra in a wider energy range from -2.5 to 2.5 eV. The shoulder at about 1.5 eV and the signal increases at ± 2.5 eV arise from the molecular states, since the substrate contribution is structureless at these energies. The approximately 2.5 to 3.0 eV wide gap between the onsets of the highest occupied molecular orbital (HOMO) at -2.0 eV and the lowest unoccupied molecular orbital (LUMO) at 0.5–1.0 eV is in good agreement with the calculated HOMO–LUMO gap of the [7]H molecule in the gas phase [10]. This observation supports our expectation that [7]H physisorbes on the rather inert Cu(111) surface, which causes only minor changes in the molecular orbitals of the free molecule. The low adsorption energy of the physisorbed molecules renders the monomer unstable and causes dimer formation even at low coverages, which is in agreement with the observation in Figure 2.

STS spectra of the heptahelicene molecules on Co BL nanoislands are shown in Figure 7b. The red and black spectra taken above the bare Co island are dominated by the d-like Co surface state at approximately -0.3 eV. The spectrum taken above the molecule (blue) does not exhibit similarly sharp states but rather a broad, gapless intensity distribution that indicates the hybridization of the molecular orbitals with the Co(111) substrate, which is more reactive compared to Cu(111) [40]. Hence, [7]H chemisorbs on Co(111) and occurs as a monomer (Figure 4).

A qualitatively similar situation is seen in Figure 7c for [7]H adsorbed on Fe BL regions on W(110). The red and black spectra of the bare Fe BL region exhibit the expected sharp peaks at -0.08 and +0.75 eV, which are due to the characteristic d_{z^2} orbitals of BL Fe/W(110). The spectrum taken above the molecule (blue) has neither a gap nor sharp features. The broad peak at approximately 0.85 eV indicates the strong hybridization of molecular orbitals with Fe d_{z^2} orbitals of the substrate, similar to the increasing intensity in the [7]H/Co/Cu(111) spectrum in Figure 7b below -0.25 eV. The strong modification of the molecular LDOS upon adsorption reveals that [7]H monomers also chemisorb on BL Fe on W(110). The expected larger binding energy on Fe(110) compared to Co(111) [40] cannot be inferred from the spectra in Figure 7b,c.

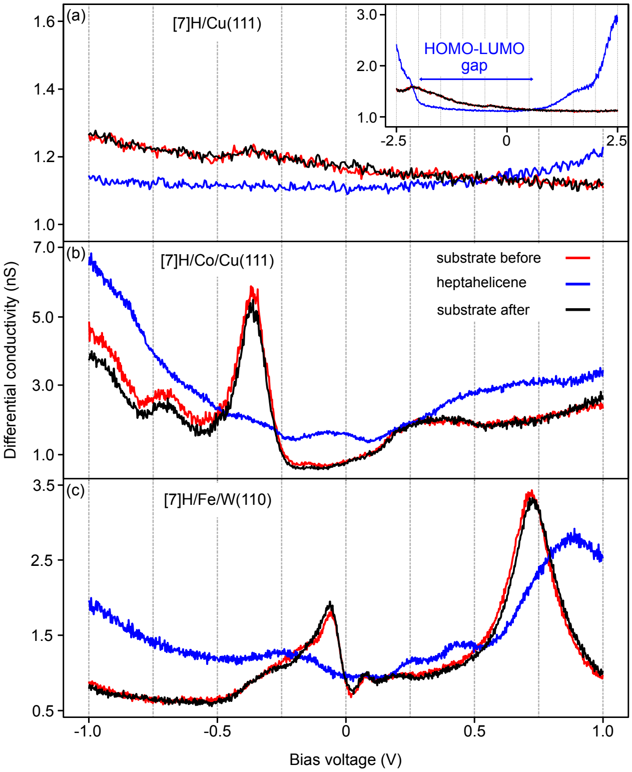

Figure 7. STS spectra of [7]H molecules on (**a**) Cu(111), (**b**) Co BL nanoislands on Cu(111), and (**c**) Fe BL regions on W(110). The inset in (**a**) shows a wider bias voltage range. Red and black curves are reference spectra of the bare substrate taken before and after acquiring the blue spectrum over an adsorbed [7]H molecule. The tip position has been stabilized during the STS measurements at $V_{\mathrm{bias}} = 1$ V and $I_{\mathrm{t}} = 1$ nA. $V_{\mathrm{mod}} = 20$ mV [10 mV for [7]H/Cu(111)], $f_{\mathrm{mod}} = 752$ Hz [875 Hz for [7]H/Cu(111)], 5 K.

4. Discussion

We have demonstrated the deposition of heptahelicene molecules by sublimation under UHV conditions onto structurally and magnetically well-defined substrates, namely Co(111) BL nanoislands on Cu(111), Fe(110) BL films on W(110) and, for reference, Cu(111). On all three substrates, the molecules adsorb in the sub-ML regime in a configuration with the helical axis perpendicular to the surface plane. In this configuration, the electron propagation direction in transport experiments using an STM is colinear to the helical axis of the chiral molecule, which is required for observing the CISS effect. Statistic analyses of the in-plane adsorption orientations evidence that the [7]H molecules adsorb at unique and well-defined sites of the substrate lattices. On Cu(111) and Co(111), there are three equally occupied and therefore degenerate adsorption orientations with intermediate angles of 120°, corresponding to a single adsorption configuration that occurs in three symmetry-equivalent orientations with respect to the atomic Cu or Co substrate lattices. For Fe(110), only two in-plane orientations of [7]H are observed, each occupied by only one particular enantiomer. This correlation between the absorption orientation and handedness of the molecule as well as the lower number of orientations than expected based on the symmetry of the substrate lattice suggest a chirality dependence of the adsorption of [7]H on Fe(110), but this is beyond the scope of the present work. The observation of unique adsorption sites results from the sufficiently high surface mobility of the [7]H molecules after deposition at RT not only for physisorption on the noble metal Cu but also for chemisorption on the more reactive ferromagnets Fe and Co. The preferred adsorption at edges of Co nanoislands and dislocation lines on Fe confirm the high surface mobility, which allows the molecules to reach energetically favorable sites. This knowledge is of utmost importance for the correct atomic modeling of the adsorption configurations in theoretical simulations of the CISS effect.

High-resolution topographic STM images enable determining of the molecular handedness in a similar (and here reproduced) manner as previously reported for [7]H physisorbed on Cu(111) [25], but it is now extended to [7]H chemisorbed on ferromagnetic Co(111) and Fe(110) surfaces. The discrimination of discretely adsorbed enantiomers opens the door for the observation and investigation of the CISS effect at the single-molecule level. The ferromagnetic substrate systems employed here offer two advantages for STM/STS experiments on the CISS effect: First, the out-of-plane magnetization provides electrons with the spins aligned parallel or antiparallel to the tunneling direction, which maximizes the CISS-derived interaction that can be phenomenologically described as the scalar product of the molecule and electron helicities. Second, their well-known magnetic domain structure can be used to confirm and calibrate the spin-resolving capability of STM tips in SP-STM/STS measurements, without which a contrast difference (e.g., between two adsorbed molecules) cannot be unambiguously assigned to a magnetic origin. To this end, we have confirmed that magnetic contrast revealing the domain structure can be achieved on both Co(111) nanoislands and Fe BL regions, which is also in the presence of sub-ML coverage with [7]H molecules.

In conclusion, the presented capabilities for the deposition control and STM/STS imaging of [7]H molecules on Co/Cu(111) and Fe/W(110) substrate systems lay the foundation for studying the CISS effect under well-defined vacuum conditions and on the microscopic level of single molecules in controlled atomic configurations. In particular, enantiospecific adsorption in ferromagnetic surfaces and chirality-induced spin polarization can be addressed by SP-STM/STM. The microscopic structural, electronic, and magnetic characterization of the molecule–substrate systems will make the results readily accessible to theoretical analysis and modeling and shed light on the microscopic origin of the CISS effect.

Author Contributions: Conceptualization, F.M. and D.E.B.; methodology, M.R.S., F.M., D.E.B. and K.-H.E.; formal analysis, M.R.S., F.M. and D.E.B.; investigation, M.R.S., F.M. and K.-H.E.; writing—original draft preparation, M.R.S. and D.E.B.; writing—review and editing, M.R.S., D.E.B., F.M., K.-H.E. and C.M.S; supervision, D.E.B.; funding acquisition, C.M.S. All authors have read and agreed to the published version of the manuscript.

Funding: This research received no external funding.

Institutional Review Board Statement: Not applicable.

Informed Consent Statement: Not applicable.

Data Availability Statement: We can provide original data on request.

Conflicts of Interest: The authors declare no conflict of interest.

Appendix A. Gaussian High-Pass Filter

On all surfaces investigated in this work, the adsorbed [7]H molecules appear in the STM images as compact roundish protrusions with an apparent height of about 250 pm and a width at the base of about 2 nm. High-resolution images reveal a submolecular fine structure, which we attribute mainly to the topographic shape of the flat adsorbed molecules and which contains information about the handedness and adsorption orientation of the molecules. Figure A1a shows the example of a [7]H molecule on the Fe/W(110) substrate system, for which the fine structure is weakest and the determination of handedness and orientation (Figure A1b) is most difficult compared to Cu(111) and Co/Cu(111) substrates.

The fine structure becomes more clearly visible when line sections are taken in different directions through the image of a molecule. The directions of the line-sections are indicated by colored lines in Figure A1b,c and displayed in respective colors in Figure A1d. The topmost C ring of [7]H gives rise to an off-centered maximum and the helix to shoulders of different height and lateral position. To enhance the contrast of the fine structure versus the low-frequency, bell-shaped main apparent height profile of the molecules, we apply two-dimensional Gaussian high-pass filtering.

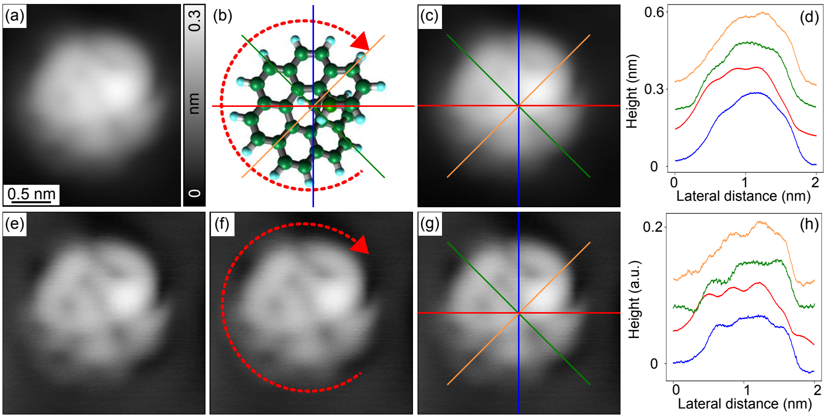

Figure A1. (**a**) High-resolution topographic image of a [7]H molecule on 2 ML Fe on W(110) ($V_{\mathrm{bias}} = 50$ mV, $I_t = 290$ pA). (**b**) Schematic representation of the (*M*)-[7]H molecule in (**a**) in the orientation derived from the fine structure. (**c**,**d**) Differently oriented line-sections through the apparent height image of the molecule show small peaks and shoulders on a bell-shaped background. (**e**,**f**) The enhanced fine structure after applying the Gaussian high-pass filter to the image in (**a**) confirms the assignment of handedness and orientation in (**b**). (**g**,**h**) Differently oriented line sections through the filtered image of the molecule demonstrate the significance of the enhanced features of the fine structure. For clarity, the line sections in (**d**,**h**) are vertically offset.

The Gaussian high-pass filter is defined as

$$\hat{I}(x,y) = I(x,y) - \alpha(I \circledast G)(x,y), \tag{A1}$$

where $I(x,y)$ is the original and $\hat{I}(x,y)$ is the filtered image. $(I \circledast G)(x,y)$ denotes the convolution of $I(x,y)$ with the Gaussian kernel $G(x,y)$, which is a $(2N+1) \times (2N+1)$ matrix with the elements

$$G_{\mathrm{i,j}} = G_0 \exp\left(-\frac{(i\Delta)^2 + (j\Delta)^2}{2\sigma^2}\right) \quad \text{with} \quad i,j = -N,\ldots,+N, \tag{A2}$$

where Δ is the scan step size of $I(x,y)$. A typical value is $\Delta \approx 50$ pm (see Appendix B). The full width at half maximum (FWHM) of the Gaussian profile is given by $2\sqrt{2\ln 2}\sigma$. We use an FWHM of 300 pm, which is of the order of the widths of the fine structure peaks and shoulders and thus much smaller than the width of the bell-shaped overall apparent height profile of a [7]H molecule. The prefactor G_0 is given by the normalization condition

$$\sum_{i,j=-N}^{N} G_{\mathrm{i,j}} = 1. \tag{A3}$$

The size of the kernel matrix $2N+1$ is chosen large enough that the matrix elements at the edges are negligible. $(I \circledast G)(x,y)$ is the low-pass filtered image, so the prefactor α determines the strength of the high-pass filtering. We choose α in the range from 0.6 to 0.8.

The effect of the Gaussian high-pass filter on the original image in Figure A1a can be seen in Figure A1e, which shows the fine structure with more contrast, allowing an easier and clearer assignment of molecular handedness and adsorption orientation (Figure A1f). Line sections through the filtered image, as marked in Figure A1g and shown in Figure A1h, demonstrate the significance of the enhanced fine structure and its clear distinction from noise.

Appendix B. Mosaic Measurements

Acquisition of high-resolution topographic data revealing submolecular features suitable for successful determination of the molecules' handedness and adsorption orientation using Gaussian high-pass filtering requires a scan step size $\Delta \leq 50\,\mathrm{pm}$ per pixel. Together with the technical limitation of the number of pixels per image, this results in a maximum field of view that contains only several dozen isolated monomers or dimers at a molecular coverage typical for this study. In order to achieve good statistics, we perform so-called mosaic measurements as shown in Figure A2. First, we use low-resolution imaging to find a sufficiently large area with a low step density suitable for statistical analysis, such as in Figure A2a. We then divide the area into a regular array of smaller segments, which we can image sequentially at a sufficiently high resolution. For example, the high-resolution image of the red marked segment ($26 \times 26\,\mathrm{nm}^2$) in Figure A2a and taken with a scan step size $\Delta = 50\,\mathrm{pm}$ per pixel is shown in Figure A2b after applying the Gaussian high-pass filter. Based on images such as this, the handedness and adsorption orientation of the molecules can be clearly determined, and it becomes part of the overall mosaic in Figure A2c (red frame). Overlapping of the segments enables precise assembly of the mosaic. The acquisition of an entire mosaic takes up to 10 hours. The result of the analysis of the adsorption orientation of 593 [7]H molecules in the whole mosaic image is listed in the 2nd row of Table 1.

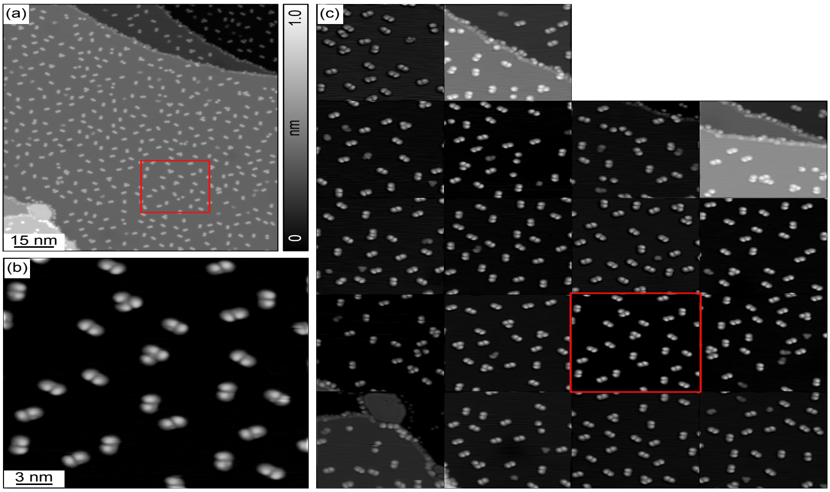

Figure A2. (**a**) Constant-current topographic overview image of a Cu(111) surface covered with more than 600 [7]H molecules taken with a scan step size $\Delta = 290\,\mathrm{pm}$ per pixel ($V_{\mathrm{bias}} = 1000\,\mathrm{mV}$, $I_{\mathrm{t}} = 20\,\mathrm{pA}$). (**b**) High-resolution topographic image of the red marked area in (**a**) taken with a scan step size $\Delta = 51\,\mathrm{pm}$ per pixel after subsequent Gaussian high-pass filtering ($V_{\mathrm{bias}} = 1000\,\mathrm{mV}$, $I_{\mathrm{t}} = 20\,\mathrm{pA}$). (**c**) Reconstructed high-resolution mosaic image of the sample area in (**a**) obtained by merging 18 high-resolution and high-pass filtered segment images such as that in (**b**). All data were measured at 5 K with a W tip.

References

1. Ray, K.; Ananthavel, S.P.; Waldeck, D.H.; Naaman, R. Asymmetric Scattering of Polarized Electrons by Organized Organic Films of Chiral Molecules. *Science* **1999**, *283*, 814–816. [CrossRef] [PubMed]
2. Naaman, R.; Waldeck, D.H. Chiral-induced spin selectivity effect. *J. Phys. Chem. Lett.* **2012**, *3*, 2178–2187. [CrossRef] [PubMed]
3. Naaman, R.; Waldeck, D.H. Spintronics and Chirality: Spin Selectivity in Electron Transport Through Chiral Molecules. *Annu. Rev. Phys. Chem.* **2015**, *66*, 263–281. [CrossRef] [PubMed]
4. Naaman, R.; Paltiel, Y.; Waldeck, D.H. Chiral molecules and the electron spin. *Nat. Rev. Chem.* **2019**, *3*, 250–260. [CrossRef]
5. Aiello, C.D.; Abendroth, J.M.; Abbas, M.; Afanasev, A.; Agarwal, S.; Banerjee, A.S.; Beratan, D.N.; Belling, J.N.; Berche, B.; Botana, A.; et al. A Chirality-Based Quantum Leap. *ACS Nano* **2022**, *16*, 4989–5035. [CrossRef]
6. Al-Bustami, H.; Bloom, B.P.; Ziv, A.; Goldring, S.; Yochelis, S.; Naaman, R.; Waldeck, D.H.; Paltiel, Y. Optical Multilevel Spin Bit Device Using Chiral Quantum Dots. *Nano Lett.* **2020**, *20*, 8675–8681. [CrossRef]
7. Naaman, R.; Waldeck, D.H.; Paltiel, Y. Chiral molecules-ferromagnetic interfaces, an approach towards spin controlled interactions. *Appl. Phys. Lett.* **2019**, *115*, 133701. [CrossRef]
8. Ray, S.G.; Daube, S.S.; Leitus, G.; Vager, Z.; Naaman, R. Chirality-induced spin-selective properties of self-assembled monolayers of DNA on gold. *Phys. Rev. Lett.* **2006**, *96*, 036101. [CrossRef]
9. Mishra, S.; Mondal, A.K.; Smolinsky, E.Z.; Naaman, R.; Maeda, K.; Nishimura, T.; Taniguchi, T.; Yoshida, T.; Takayama, K.; Yashima, E. Spin Filtering Along Chiral Polymers. *Angew. Chem. Int. Ed.* **2020**, *59*, 14671–14676. [CrossRef]
10. Kettner, M.; Maslyuk, V.V.; Nürenberg, D.; Seibel, J.; Gutierrez, R.; Cuniberti, G.; Ernst, K.H.; Zacharias, H. Chirality-Dependent Electron Spin Filtering by Molecular Monolayers of Helicenes. *J. Phys. Chem. Lett.* **2018**, *9*, 2025–2030. [CrossRef]
11. Göhler, B.; Hamelbeck, V.; Markus, T.Z.; Kettner, M.; Hanne, G.F.; Vager, Z.; Naaman, R.; Zacharias, H. Spin selectivity in electron transmission through self-assembled monolayers of double-stranded DNA. *Science* **2011**, *331*, 894–897. [CrossRef] [PubMed]
12. Kim, Y.H.; Zhai, Y.; Lu, H.; Pan, X.; Xiao, C.; Gaulding, E.A.; Harvey, S.P.; Berry, J.J.; Vardeny, Z.V.; Luther, J.M.; et al. Chiral-induced spin selectivity enables a room-temperature spin light-emitting diode. *Science* **2021**, *371*, 1129–1133. [CrossRef] [PubMed]
13. Banerjee-Ghosh, K.; Dor, O.B.; Tassinari, F.; Capua, E.; Yochelis, S.; Capua, A.; Yang, S.H.; Parkin, S.S.; Sarkar, S.; Kronik, L.; et al. Separation of enantiomers by their enantiospecific interaction with achiral magnetic substrates. *Science* **2018**, *360*, 1331–1334. [CrossRef] [PubMed]
14. Ben Dor, O.; Yochelis, S.; Radko, A.; Vankayala, K.; Capua, E.; Capua, A.; Yang, S.H.; Baczewski, L.T.; Parkin, S.S.P.; Naaman, R.; et al. Magnetization switching in ferromagnets by adsorbed chiral molecules without current or external magnetic field. *Nat. Commun.* **2017**, *8*, 14567. [CrossRef]
15. Fransson, J. Chirality-Induced Spin Selectivity: The Role of Electron Correlations. *J. Phys. Chem. Lett.* **2019**, *10*, 7126–7132. [CrossRef]
16. Michaeli, K.; Naaman, R. Origin of Spin-Dependent Tunneling Through Chiral Molecules. *J. Phys. Chem. C* **2019**, *123*, 17043–17048. [CrossRef]
17. Ghazaryan, A.; Paltiel, Y.; Lemeshko, M. Analytic Model of Chiral-Induced Spin Selectivity. *J. Phys. Chem. C* **2020**, *124*, 11716–11721. [CrossRef]
18. Yeganeh, S.; Ratner, M.A.; Medina, E.; Mujica, V. Chiral electron transport: Scattering through helical potentials. *J. Chem. Phys.* **2009**, *131*, 014707. [CrossRef]
19. Geyer, M.; Gutierrez, R.; Mujica, V.; Cuniberti, G. Chirality-Induced Spin Selectivity in a Coarse-Grained Tight-Binding Model for Helicene. *J. Phys. Chem. C* **2019**, *123*, 27230–27241. [CrossRef]
20. Huisman, K.H.; Thijssen, J.M. CISS Effect: A Magnetoresistance through Inelastic Scattering. *J. Phys. Chem. C* **2021**, *125*, 23364–23369. [CrossRef]
21. Kiran, V.; Mathew, S.P.; Cohen, S.R.; Hernández Delgado, I.; Lacour, J.; Naaman, R. Helicenes—A New Class of Organic Spin Filter. *Adv. Mater.* **2016**, *28*, 1957–1962. [CrossRef] [PubMed]
22. Pan, T.R.; Guo, A.M.; Sun, Q.F. Spin-polarized electron transport through helicene molecular junctions. *Phys. Rev. B* **2016**, *94*, 235448. [CrossRef]
23. Fasel, R.; Cossy, A.; Ernst, K.H.; Baumberger, F.; Greber, T.; Osterwalder, J. Orientation of chiral heptahelicene C30H18 on copper surfaces: An x-ray photoelectron diffraction study. *J. Chem. Phys.* **2001**, *115*, 1020–1027. [CrossRef]
24. Seibel, J.; Parschau, M.; Ernst, K.H. From Homochiral Clusters to Racemate Crystals: Viable Nuclei in 2D Chiral Crystallization. *J. Am. Chem. Soc.* **2015**, *137*, 7970–7973. [CrossRef]
25. Ernst, K.H.; Baumann, S.; Lutz, C.P.; Seibel, J.; Zoppi, L.; Heinrich, A.J. Pasteurs Experiment Performed at the Nanoscale: Manual Separation of Chiral Molecules, One by One. *Nano Lett.* **2015**, *15*, 5388–5392. [CrossRef]
26. Ernst, K.H. Stereochemical Recognition of Helicenes on Metal Surfaces. *Acc. Chem. Res.* **2016**, *49*, 1182–1190. [CrossRef]
27. Fasel, R.; Parschau, M.; Ernst, K.H. Amplification of chirality in two-dimensional enantiomorphous lattices. *Nature* **2006**, *439*, 449–452. [CrossRef]
28. Ernst, K.H.; Kuster, Y.; Fasel, R.; McFadden, C.F.; Ellerbeck, U. Adsorption of helical aromatic molecules: Heptahelicene on Ni(111). *Surf. Sci.* **2003**, *530*, 195–202. [CrossRef]

29. Fahrendorf, S.; Matthes, F.; Bürgler, D.E.; Schneider, C.M.; Atodiresei, N.; Caciuc, V.; Blügel, S.; Besson, C.; Kögerler, P. Structural integrity of single bis(phthalocyaninato)-neodymium(iii) molecules on metal surfaces with different reactivity. *Spin* **2014**, *4*, 144007. [CrossRef]
30. Schleicher, S.; Borca, B.; Rawson, J.; Matthes, F.; Bürgler, D.E.; Kögerler, P.; Schneider, C.M. Ultra-High Vacuum Deposition of Pyrene Molecules on Metal Surfaces. *Phys. Stat. Sol. B* **2018**, *255*, 1800235. [CrossRef]
31. De La Figuera, J.; Prieto, J.E.; Ocal, C.; Miranda, R. Scanning-tunneling-microscopy study of the growth of cobalt on Cu(111). *Phys. Rev. B* **1993**, *47*, 13043–13046. [CrossRef] [PubMed]
32. Bode, M.; Krause, S.; Berbil-Bautista, L.; Heinze, S.; Wiesendanger, R. On the preparation and electronic properties of clean W(110) surfaces. *Surf. Sci.* **2007**, *601*, 3308–3314. [CrossRef]
33. Pietzsch, O.; Kubetzka, A.; Bode, M.; Wiesendanger, R. Spin-Polarized Scanning Tunneling Spectroscopy of Nanoscale Cobalt Islands on Cu(111). *Phys. Rev. Lett.* **2004**, *92*, 057202. [CrossRef] [PubMed]
34. Pietzsch, O.; Okatov, S.; Kubetzka, A.; Bode, M.; Heinze, S.; Lichtenstein, A.; Wiesendanger, R. Spin-Resolved Electronic Structure of Nanoscale Cobalt Islands on Cu(111). *Phys. Rev. Lett.* **2006**, *96*, 237203. [CrossRef]
35. Negulyaev, N.N.; Stepanyuk, V.S.; Bruno, P.; Diekhöner, L.; Wahl, P.; Kern, K. Bilayer growth of nanoscale Co islands on Cu(111). *Phys. Rev. B* **2008**, *77*, 125437. [CrossRef]
36. Oka, H.; Ignatiev, P.A.; Wedekind, S.; Rodary, G.; Niebergall, L.; Stepanyuk, V.S.; Sander, D.; Kirschner, J. Spin-Dependent Quantum Interference Within a Single Magnetic Nanostructure. *Science* **2010**, *327*, 843–846. [CrossRef] [PubMed]
37. Esat, T.; Friedrich, R.; Matthes, F.; Caciuc, V.; Atodiresei, N.; Blügel, S.; Bürgler, D.E.; Tautz, F.S.; Schneider, C.M. Quantum interference effects in molecular spin hybrids. *Phys. Rev. B* **2017**, *95*, 094409. [CrossRef]
38. Alkemper, U.; Carbone, C.; Vescovo, E.; Eberhardt, W.; Rader, O.; Gudat, W. Exchange-split electronic states of ultrathin Co layers on Cu(111). *Phys. Rev. B* **1994**, *50*, 17496–17501. [CrossRef]
39. Metzelaars, M.; Schleicher, S.; Hattori, T.; Borca, B.; Matthes, F.; Sanz, S.; Bürgler, D.E.; Rawson, J.; Schneider, C.M.; Kögerler, P. Cyclophane with eclipsed pyrene units enables construction of spin interfaces with chemical accuracy. *Chem. Sci.* **2021**, *12*, 8430–8437. [CrossRef]
40. Jia, X.; An, W. Adsorption of Monocyclic Aromatics on Transition Metal Surfaces: Insight into Variation of Binding Strength from First-Principles. *J. Phys. Chem. C* **2018**, *122*, 21897–21909. [CrossRef]
41. Bethge, H.; Heuer, D.; Jensen, C.; Reshöft, K.; Köhler, U. Misfit-related effects in the epitaxial growth of iron on W(110). *Surf. Sci.* **1995**, *331-333*, 878–884. [CrossRef]
42. Pietzsch, O.; Kubetzka, A.; Bode, M.; Wiesendanger, R. Real-Space Observation of Dipolar Antiferromagnetism in Magnetic Nanowires by Spin-Polarized Scanning Tunneling Spectroscopy. *Phys. Rev. Lett.* **2000**, *84*, 5212–5215. [CrossRef] [PubMed]
43. Kubetzka, A.; Pietzsch, O.; Bode, M.; Wiesendanger, R. Magnetism of nanoscale Fe islands studied by spin-polarized scanning tunneling spectroscopy. *Phys. Rev. B* **2001**, *63*, 140407. [CrossRef]
44. Kubetzka, A.; Bode, M.; Pietzsch, O.; Wiesendanger, R. Spin-Polarized Scanning Tunneling Microscopy with Antiferromagnetic Probe Tips. *Phys. Rev. Lett.* **2002**, *88*, 4. [CrossRef]
45. Pratzer, M.; Elmers, H.J.; Bode, M.; Pietzsch, O.; Kubetzka, A.; Wiesendanger, R. Atomic-Scale Magnetic Domain Walls in Quasi-One-Dimensional Fe Nanostripes. *Phys. Rev. Lett.* **2001**, *87*, 127201–127204. [CrossRef]
46. Bode, M.; Heinze, S.; Kubetzka, A.; Pietzsch, O.; Nie, X.; Bihlmayer, G.; Blügel, S.; Wiesendanger, R. Magnetization-Direction-Dependent Local Electronic Structure Probed by Scanning Tunneling Spectroscopy. *Phys. Rev. Lett.* **2002**, *89*, 237205. [CrossRef]
47. Von Bergmann, K.; Menzel, M.; Serrate, D.; Schröder, Y.Y.; Ferriani, P.; Kubetzka, A.; Wiesendanger, R.; Heinze, S. Tunneling anisotropic magnetoresistance on the atomic scale. *Phys. Rev. B* **2012**, *86*, 134422. [CrossRef]
48. Heß, V.; Friedrich, R.; Matthes, F.; Caciuc, V.; Atodiresei, N.; Bürgler, D.E.; Blügel, S.; Schneider, C.M. Magnetic subunits within a single molecule-surface hybrid. *New J. Phys.* **2017**, *19*. [CrossRef]
49. Sicot, M.; Kurnosikov, O.; Swagten, H.J.; Koopmans, B. Hydrogen superstructures on Co nanoislands and Cu(111). *Surf. Sci.* **2008**, *602*, 3667–3673. [CrossRef]
50. Schlenhoff, A.; Krause, S.; Herzog, G.; Wiesendanger, R. Bulk Cr tips with full spatial magnetic sensitivity for spin-polarized scanning tunneling microscopy. *Appl. Phys. Lett.* **2010**, *97*, 083104. [CrossRef]

3.2 Manuscript 2: Enantioselective adsorption on magnetic surfaces

This section consists entirely of the above-named manuscript and its supplementary information. This manuscript focuses on the single-molecule-level magneto-enantioselective interactions between a racemic mixture of chiral [7]H molecules and an OOP magnetized bilayer of Co nanoislands on Cu(111). The atomic-scale experiments were systematically carried out within precisely defined and controlled surface science conditions, including molecular sublimation in an ultrahigh vacuum environment onto well-defined and clean substrates.

This approach offers the distinct advantage of enabling the direct chemisorption of chiral molecules onto magnetic surfaces at specific adsorption sites, which rules out ensemble or cooperative effects and the necessity for an intermediate oxidation protection layer, as opposed to the previously discussed studies in Section 1.3.4.

The statistical analysis conducted on over 700 molecules across 107 islands revealed a significant difference in the absolute handedness of adsorbed [7]H molecules depending on the OOP magnetization direction of the substrate. This specific adsorption behavior is due to variations in adsorption rates associated with different combinations of molecular handedness and magnetization direction.

The well-established adsorption configuration and experimental conditions enabled us to carry out one-to-one DFT simulations of [7]H molecules adsorbed on OOP magnetized Co nanoislands. Our combination of quantitative measurements of the energy differences associated with enantioselectivity, along with the DFT simulations presented in this manuscript, suggests that enantioselective separation occurs in a transiently occupied physisorption precursor state before the final chemisorption step. The manuscript highlights that the enantiospecific adsorption is kinetically controlled, with varying barrier heights for the transition from the precursor state to the final chemisorption state. The manuscript is published in *Advanced Materials* and available as [128].

Mohammad Reza Safari and Frank Matthes conducted the sample preparations and the STM experiments. Karl-Heinz Ernst synthesized and provided the molecules. Mohammad Reza Safari, Frank Matthes and Daniel E. Bürgler conducted the data analysis. Vasile Caciuc and Nicolae Atodiresei performed the DFT simulations. Mohammad Reza Safari wrote the manuscript in close collaboration with Daniel E. Bürgler and Frank Matthes and with contributions from Vasile Caciuc, Nicolae Atodiresei, Karl-Heinz Ernst and Claus M. Schneider.

RESEARCH ARTICLE

ADVANCED MATERIALS
www.advmat.de

Enantioselective Adsorption on Magnetic Surfaces

Mohammad Reza Safari, Frank Matthes, Vasile Caciuc, Nicolae Atodiresei, Claus M. Schneider, Karl-Heinz Ernst,* and Daniel E. Bürgler**

From the beginning of molecular theory, the interplay of chirality and magnetism has intrigued scientists. There is still the question if enantiospecific adsorption of chiral molecules occurs on magnetic surfaces. Enantiomer discrimination was conjectured to arise from chirality-induced spin separation within the molecules and exchange interaction with the substrate's magnetization. Here, it is shown that single helical aromatic hydrocarbons undergo enantioselective adsorption on ferromagnetic cobalt surfaces. Spin and chirality sensitive scanning tunneling microscopy reveals that molecules of opposite handedness prefer adsorption onto cobalt islands with opposite out-of-plane magnetization. As mobility ceases in the final chemisorbed state, it is concluded that enantioselection must occur in a physisorbed transient precursor state. State-of-the-art spin-resolved ab initio simulations support this scenario by refuting enantio-dependent chemisorption energies. These findings demonstrate that van der Waals interaction should also include spin-fluctuations which are crucial for molecular magnetochiral processes.

1. Introduction

Soon after his seminal discovery of molecular chirality[1] and its common occurrence in organic matter Pasteur conjectured physical fields as its origin.[2] As natural optical activity and Faraday rotation are both manifested by rotating the plane of polarization of light, Pasteur assumed that magnetic fields must be the source of chirality in the universe.[3] However, Kelvin made clear that magnetic rotation (i.e., Faraday rotation) has no chirality.[4] In 1894, Pierre Curie proposed that parallel and antiparallel alignments of electric and magnetic fields will induce chirality,[5] but as Barron pointed out, such chiral influence will vanish under conditions of thermodynamic equilibrium.[6] However, it was shown later that collinear aligned light and magnetic field are a truly chiral influence.[7,8]

Recent experiments have demonstrated an interaction between electron spin and molecular chirality, coined as chirality-induced spin selectivity (CISS).[9–11] The characteristic feature of CISS is the spin-dependent propagation of electrons in chiral molecules, as evidenced by photoemission[9,12,13] and electric transport[14–18] experiments. However, profound understanding of CISS including a suitable theory framework is still lacking.[19]

M. R. Safari, F. Matthes, C. M. Schneider, D. E. Bürgler
Peter Grünberg Institute, Electronic Properties (PGI-6)
Forschungszentrum Jülich
52425 Jülich, Germany
E-mail: m.safari@fz-juelich.de; d.buergler@fz-juelich.de
M. R. Safari, F. Matthes, C. M. Schneider, D. E. Bürgler
Jülich Aachen Research Alliance (JARA-FIT), Fundamentals of Future Information Technology
Forschungszentrum Jülich
52425 Jülich, Germany
V. Caciuc, N. Atodiresei
Peter Grünberg Institute and Institute for Advanced Simulation, Quantum Theory of Materials (PGI-1/IAS-1)
Forschungszentrum Jülich
52425 Jülich, Germany
C. M. Schneider
Fakultät für Physik
Universität Duisburg-Essen
47057 Duisburg, Germany
K.-H. Ernst
Molecular Surface Science Group, Empa
Swiss Federal Laboratories for Materials Science and Technology
8600 Dübendorf, Switzerland
E-mail: karl-heinz.ernst@empa.ch
K.-H. Ernst
Nanosurf Laboratory, Institute of Physics
The Czech Academy of Sciences
16200 Prague, Czech Republic
K.-H. Ernst
Institut für Chemie
Universität Zürich
8057 Zürich, Switzerland

The ORCID identification number(s) for the author(s) of this article can be found under https://doi.org/10.1002/adma.202308666

DOI: 10.1002/adma.202308666

Interestingly, recent reports of enantioselective adsorption on magnetized substrates were also considered a manifestation of CISS.[20–23] In all cases, evidence of enantiospecificity was provided indirectly, either by temporal separation under flow conditions from solution onto ferromagnetic substrates coated with 5–10 nm Au for oxidation protection or integrally over large ensembles. However, no direct evidence of lateral separation depending on absolute handedness and magnetization has been provided so far. In particular, no detailed information on the structure and orientation of the adsorbate were provided, which makes theoretical approaches extremely difficult, if not impossible. In recent studies of chiral molecules on ferromagnetic Ni(100), neither enantiomeric separation nor differences in adsorption kinetics between magnetic domains were observed.[24,25]

Here, we report enantiospecific adsorption of heptahelicene, a chiral helical polyaromatic molecule, on ferromagnetic single-crystal cobalt surfaces in ultrahigh vacuum by means of spin-polarized scanning tunneling microscopy (SP-STM). Lateral enantioselection onto domains of opposite out-of-plane magnetization occurs in a transient physisorbed precursor state before final chemisorption. Density functional theory (DFT) calculations show degenerated ground states in the chemisorbed state of the enantiomers on the ferromagnetic surface, suggesting that enantiospecificity arises from spin-dependent van der Waals (vdW) interactions.

2. Results

2.1. Determination of Molecular Handedness and Substrate Magnetization

Bilayer Co nanoislands are created on a Cu(111) single-crystal surface by evaporation of metallic cobalt.[26,27] Such islands are known to exhibit out-of-plane magnetization.[28–33] The magnetization directions of the islands are probed by spin-polarized scanning tunneling microscopy and spectroscopy (SP-STM/STS). That is, the tungsten tip of the STM is modified with Co prior to imaging (for details, see Experimental Section). A contrast in differential conductance (dI/dV) arises from different spin-polarized tunneling probabilities between the oppositely magnetized Co nanoislands and the magnetic STM tip[28–33] (**Figure** 1a–c). With the absolute magnetization direction of the STM tip unknown, there is no unique assignment of higher or lower dI/dV signal to the absolute direction of the island magnetization $\boldsymbol{M}$. For the sake of analysis, a higher dI/dV signal (yellow contrast) is arbitrarily assigned as up magnetization ($\boldsymbol{M}$ pointing to the vacuum; $\boldsymbol{M} = \uparrow$) and a lower dI/dV signal (blue contrast) as down magnetization ($\boldsymbol{M}$ pointing to the copper substrate; $\boldsymbol{M} = \downarrow$).

Sub-monolayer coverages of chiral heptahelicene $C_{30}H_{18}$ molecules ([7]H) are deposited in ultrahigh vacuum by sublimation of racemic powder onto these ferromagnetic islands. The handedness of the molecules is then determined for each adsorbate one-by-one using STM (Figure 1d). As the [7]H molecules are adsorbed with their proximal phenanthrene group parallel to the surface (see Section S7, Supporting Information), their helical axis is oriented perpendicular to the surface. The absolute handedness is therefore clearly distinguishable from a clockwise or counterclockwise increase in apparent height in constant-current STM images (Figure 1e and Figure S9c-f, Supporting Information). For each island, the ratio of left- to right-handed molecules adsorbed on it is then determined in order to analyze any enantiospecific interaction (Figure 1f).

2.2. Magneto-Enantiospecific [7]H Adsorption on Co

In principle, the adsorption of [7]H occurs in four possible combinations of substrate magnetization direction ($\boldsymbol{M} = \uparrow$ or $\boldsymbol{M} = \downarrow$) and enantiomer handedness [*(P)* or *(M)*]. Enantiospecific adsorption of [7]H molecules on Co islands is evidenced by directly counting the occurrence of the four combinations in topographic STM images measured on Co nanoisland with magnetization directions determined from spin-polarized differential conductance maps. **Figure** 2 presents results of such a chirality counting procedure in one STM frame. A constant-current topographic STM image shows [7]H molecules on Co/Cu(111) at 5 K after deposition at room temperature (RT), see Figure 2a. At the low coverages investigated here, the triangular Co nanoislands are decorated with molecules, while the Cu substrate remains bare. Hence, the surface mobility of the [7]H molecules during deposition allows them to travel to the Co nanoislands, where they accumulate as a result of stronger binding.[34] The preferential adsorption of the molecules at the rims of the islands is analyzed and discussed in Section S8 (Supporting Information). The dI/dV map reveals magnetic contrast of the Co nanoislands (Figure 2b), demonstrating Co island ferromagnetism also in the presence of chemisorbed [7]H molecules.[27] Figure 2c,d presents high-resolution topographic images of the dashed and dotted framed areas in Figure 2a,b. The two islands chosen have opposite magnetization, i.e., $\boldsymbol{M} = \downarrow$ and $\boldsymbol{M} = \uparrow$. The absolute handedness of the helicene molecules is indicated by red and green circular arrows for *(M)*-[7]H and *(P)*-[7]H molecules, respectively. The arrows spiral upward from the proximal to the distal end of the molecular helix. The enantiomer count on both islands yields opposite enantiomeric imbalances, i.e., *(M)*/*(P)* ratios of 5/10 (Figure 2c) and 9/4 (Figure 2d), which suggests indeed magneto-enantiospecific adsorption of [7]H on ferromagnetic Co islands (for more examples of STM images resolving the molecular handedness, see Figure S4, Supporting Information).

To support this observation with better statistics, two independent data sets were measured using separately prepared Co/Cu(111) substrate systems, different runs of [7]H deposition, and newly Co-functionalized STM tips (see Section S2, Supporting Information). For the sake of further statistical analyses, the enantiomer handedness is expressed here as “pitch vector” $\boldsymbol{h}$. $\boldsymbol{h} = \uparrow$ represents the *(P)*-[7]H enantiomer and $\boldsymbol{h} = \downarrow$ the *(M)*-[7]H enantiomer (**Figure** 3). A more detailed definition of $\boldsymbol{h}$ is given in Section S1 (Supporting Information). The number of occupation for each of the four possible adsorption configurations are denoted by N_{Mh}, with $\boldsymbol{M} = \uparrow$ or $\boldsymbol{M} = \downarrow$ and $\boldsymbol{h} = \uparrow$ or $\boldsymbol{h} = \downarrow$. Hence, $\boldsymbol{M}$ and $\boldsymbol{h}$ can be parallel ($N_{\uparrow\uparrow}$ and $N_{\downarrow\downarrow}$) or antiparallel ($N_{\uparrow\downarrow}$ and $N_{\downarrow\uparrow}$), see Figure 3.

Statistical analysis of more than 740 molecules on 107 islands revealed a pronounced imbalance of the handedness of adsorbed [7]H molecules with respect to the direction of the out-of-plane substrate magnetization. **Table** 1 summarizes the statistical counts of two different data sets. Dividing the adsorbed molecules into these two classes ($\boldsymbol{M}$ and $\boldsymbol{h}$ parallel or antiparallel,

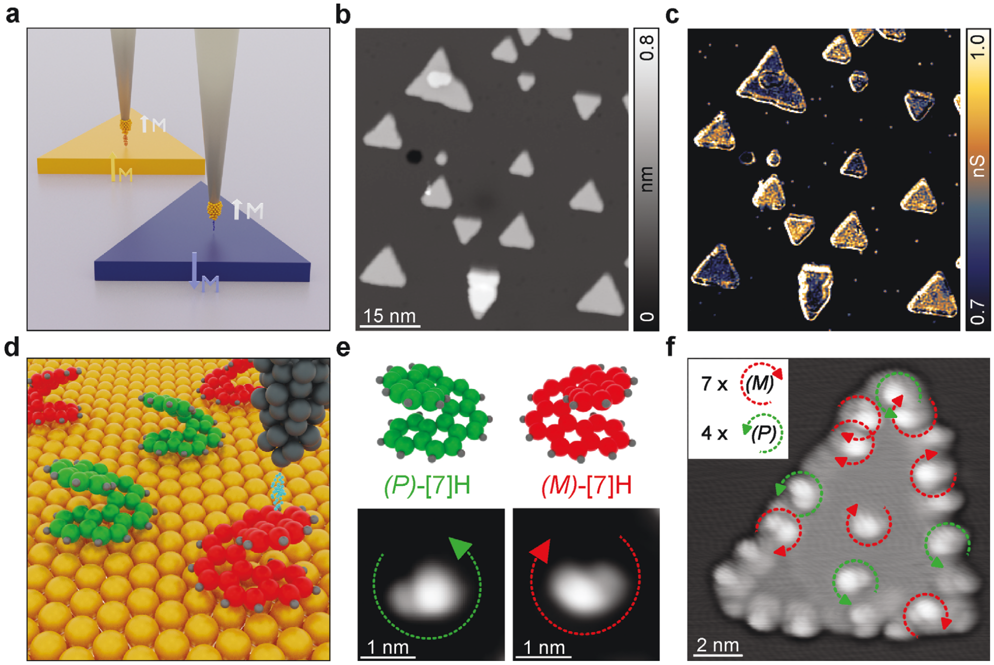

Figure 1. Principles of spin-polarized and enantio-resolved STM. a) Sketch of two oppositely out-of-plane magnetized Co nanoislands probed with a magnetic Co-functionalized STM tip. b) Constant-current topographic STM image of triangular Co nanoislands on Cu(111). The two triangle orientations are due to different stacking sequences of the Co layers on the Cu surface. c) dI/dV map at $V_{\text{bias}} = -600$ mV measured with a magnetic Co-functionalized STM tip simultaneously with the topographic image in (b). d) Sketch of STM imaging of single molecules. e) Ball-and-stick model of [7]H enantiomers and assignment of their absolute handedness from topographic STM contrast. Counterclockwise increase of brightness denotes a *(P)*-enantiomer (left), while clockwise increase of brightness denotes an *(M)*-enantiomer (right). f) Example for "chirality counting" of [7]H molecules on a single Co nanoisland. Indicated by circular arrows, 4 *(P)*- and 7 *(M)*-enantiomers are identified. STM parameters: b,c) $V_{\text{bias}} = -600$ mV, $I_t = 1$ nA, $V_{\text{mod}} = 10$ mV, $f_{\text{mod}} = 875$ Hz, 5 K, Co-functionalized W tip, e) $V_{\text{bias}} = 1$ V, $I_t = 50$ pA, 5 K, W tip, f) $V_{\text{bias}} = 1$ V, $I_t = 50$ pA, 5 K, Gaussian high-pass filtered.

respectively) plus taking the different island areas by a weighting factor ($\alpha = A_{M_\uparrow}/A_{M_\downarrow}$) into account gives: $N_1 = N_{\uparrow\uparrow} + \alpha N_{\downarrow\downarrow}$ and $N_2 = N_{\uparrow\downarrow} + \alpha N_{\downarrow\uparrow}$. For both data sets, the antiparallel $\boldsymbol{M}$-$\boldsymbol{h}$ alignment outnumbers the parallel alignment ($N_1 < N_2$). Magneto-enantiospecific adsorption is identified if the ratio of $r = N_1/N_2$ deviates from unity, i.e. $r \neq 1$. The statistical analysis of our data in the framework of a trinomial distribution (see Section S3, Supporting Information) yields for the combined data sets an magneto-enantiospecific ratio $r = 0.68 \pm 0.06$, i.e., r is about five standard deviations lower than one (**Table 2**). Hence, the adsorption probability of [7]H enantiomers on a ferromagnetic Co(111) islands clearly depends on the molecular handedness and the substrate magnetization, meaning that the *(M)*-[7]H enantiomer is preferably found on Co islands with one magnetization direc-

Table 1. Enantioselective counting of [7]H on Co nanoislands.

Data sets	$N_{\uparrow\uparrow}$	$N_{\uparrow\downarrow}$	$N_{\downarrow\uparrow}$	$N_{\downarrow\downarrow}$	Indeterminable handedness	Analyzed molecules
Set 1	39	61	98	78	15	291
Set 2	63	94	172	114	14	457
Total	102	155	270	192	29	748

Occupation numbers N_{Mh} of the four combinations of $\boldsymbol{M}$ and $\boldsymbol{h}$ in the data presented in Figure 2 and Section S2 (Supporting Information). The number of molecules for which the handedness could not be determined and the total number of analyzed molecules are also listed.

Table 2. Statistics of [7]H adsorption on Co nanoislands.

Data sets	$\alpha = A_{M_\uparrow}/A_{M_\downarrow}$	$N_1 = N_{\uparrow\uparrow} + \alpha N_{\downarrow\downarrow}$	$N_2 = N_{\uparrow\downarrow} + \alpha N_{\downarrow\uparrow}$	N_3	$r = N_1/N_2$	ΔE (meV)
Set 1	0.62	88	122	15	0.72 ± 0.10	8 ± 4
Set 2	0.49	119	178	14	0.67 ± 0.08	10 ± 3
Total	0.55	207	303	29	0.68 ± 0.06	10 ± 2

$\alpha = A_{M_\uparrow}/A_{M_\downarrow}$ is the ratio of the total areas of islands with $\boldsymbol{M} = \uparrow$ and $\boldsymbol{M} = \downarrow$, respectively. $N_1 = N_{\uparrow\uparrow} + \alpha N_{\downarrow\downarrow}$ and $N_2 = N_{\uparrow\downarrow} + \alpha N_{\downarrow\uparrow}$ are the number of molecules in classes 1 and 2. N_3 is the number of molecules with indeterminable handedness. The error bar of r is calculated according to Equation (S1) in Section S3 (Supporting Information). ΔE is the energy difference of the two molecule classes, which is derived from r using Equation (1).

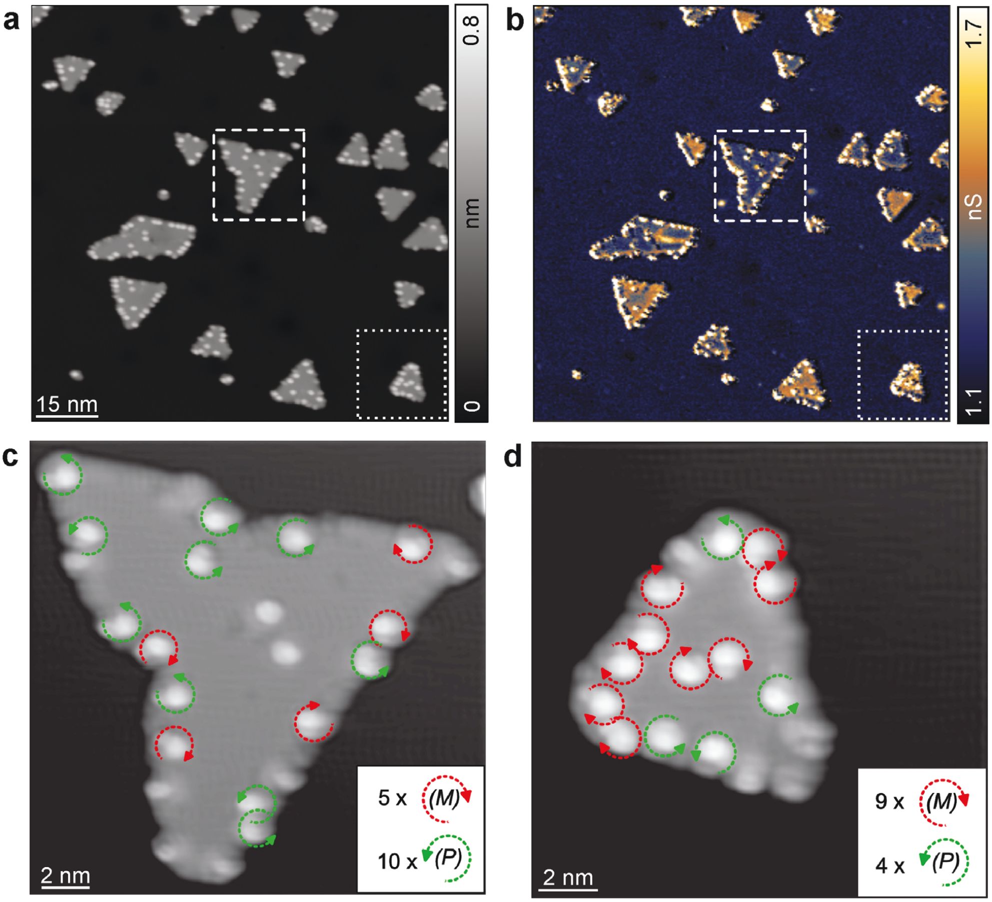

Figure 2. Enantiospecific adsorption of [7]H on ferromagnetic Co nanoislands. Topographic images reveal the handedness of each molecule and the spectroscopic maps allow to distinguish between the opposite magnetization directions of the Co islands. Both quantities are determined individually for each molecule. a) Constant-current topographic image showing [7]H molecules attached only to Co nanoislands. b) Simultaneously with (a) measured differential conductance (dI/dV) map scaled in nS revealing magnetic contrast (blue versus yellowish) between Co nanoislands with opposite out-of-plane magnetization ($V_{\mathrm{bias}} = -600$ mV, $I_{\mathrm{t}} = 950$ pA, $V_{\mathrm{mod}} = 20$ mV, $f_{\mathrm{mod}} = 752$ Hz, 5 K, Co-functionalized W tip). c,d) High-resolution topographic STM images of the areas framed in (a) and (b) by dashed and dotted lines, respectively ($V_{\mathrm{bias}} = 1$ V, $I_{\mathrm{t}} = 50$ pA, 5 K, Gaussian high-pass filtered). Green and red circular arrows indicate the handedness of the respective [7]H molecules. The insets represent the number of right-handed *(P)* and left-handed *(M)* molecules adsorbed on the corresponding island.

tion (e.g., $\boldsymbol{M} = \uparrow$), whereas the *(P)*-[7]H enantiomer preferably adsorbs on nanoislands with the opposite magnetization direction (e.g., $\boldsymbol{M} = \downarrow$).

2.3. Precursor-Mediated Chemisorption at RT

[7]H molecules sublimed from a racemate arrive on the sample surface at random positions and with uniformly distributed handedness. Hence, the observed adsorption preference based on island magnetization and molecular handedness reflects a process in which the molecules can travel across the surface in order to choose islands with preferred magnetization. However, STM imaging at RT, at which deposition is performed, shows clearly that molecules have very limited mobility once chemisorbed on an island, thus leaving the Cu regions between the Co islands free of molecules and suppressing exchange of molecules between islands (**Figure** 4a,b and Section S4, Supporting Information).

The finding that the magnetization-dependent enantiomeric excess on the Co nanoislands develops during deposition at RT requires that the superparamagnetic blocking temperature of

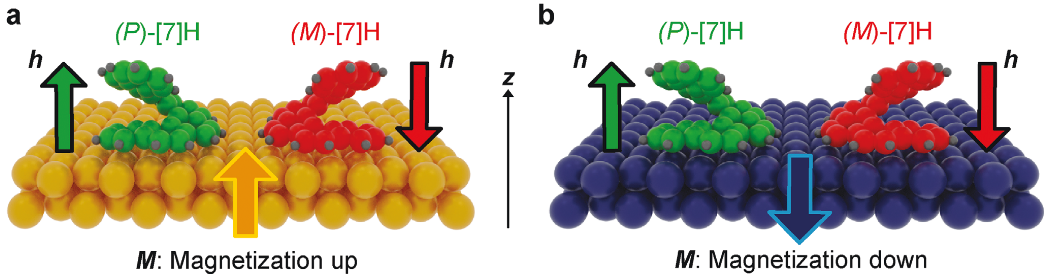

Figure 3. Adsorption configurations of [7]H on Co nanoislands. Both enantiomers, *(P)*-[7]H and *(M)*-[7]H, can adsorb on Co nanoislands with both a) magnetization up ($\boldsymbol{M} = \uparrow$) or b) magnetization down ($\boldsymbol{M} = \downarrow$). The pitch vectors of the molecular helices $\boldsymbol{h} = \uparrow$ (green) and $\boldsymbol{h} = \downarrow$ (red) represent *(P)*-[7]H and *(M)*-[7]H enantiomers, respectively (see Section S1, Supporting Information).

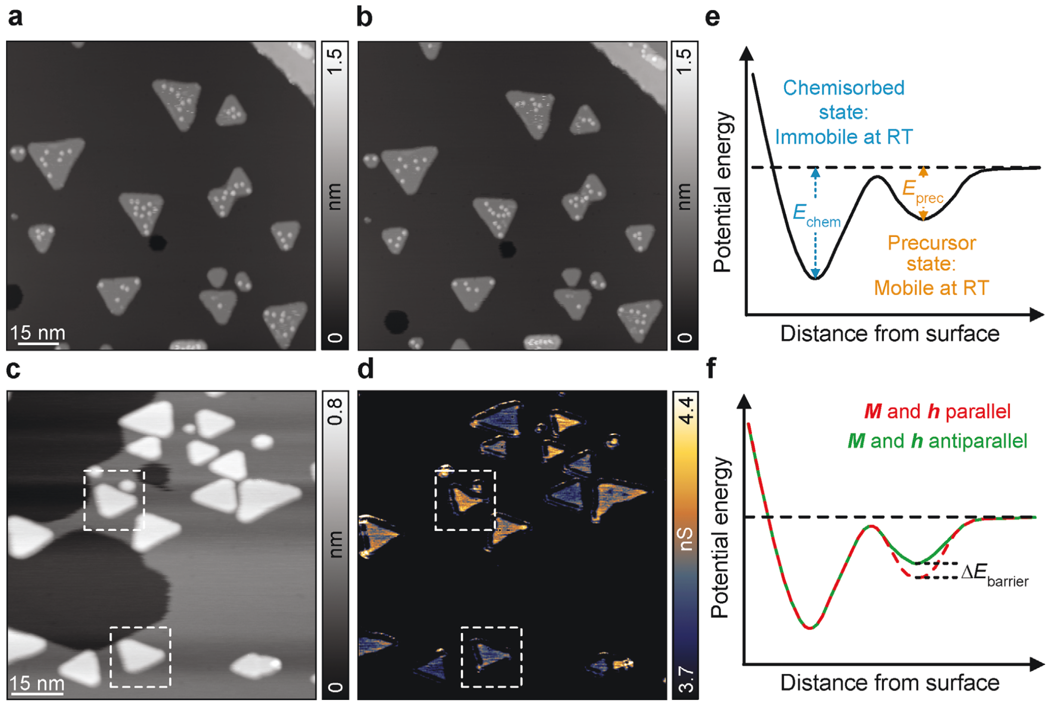

Figure 4. Magneto-enantiospecific [7]H adsorption at RT. a) Constant-current STM images of [7]H molecules deposited on Co nanoislands on Cu(111) at RT and imaged at 296 K after right after deposition. b) STM image of same area under same conditions as in (a) imaged after 329 min. Only small lateral movement of molecules is observed, and all molecules remained on their island ($V_{\text{bias}} = 500$ mV, $I_{\text{t}} = 20$ pA, 296 K, W tip). c) Constant-current topographic image of Co nanoislands on Cu(111) deposited and measured at RT. Dashed squares indicate two islands of approximately equal size and identical stacking. d) Simultaneously measured dI/dV map of the same area as in (c). The different contrast of quasi-identical islands (dashed squares) is assigned to ferromagnetism ($V_{\text{bias}} = -600$ mV, $I_{\text{t}} = 250$ pA, $V_{\text{mod}} = 20$ mV, $f_{\text{mod}} = 752$ Hz, 296 K, Co-functionalized W tip). e) Sketch of the potential energy curve of adsorption. Prior to reaching a strongly bound chemisorbed state, the molecule can travel laterally long distances in a physisorbed precursor state. f) Sketch of magnetochiral binding differences in the physisorbed precursor state.

the Co bilayer nanoislands is above RT on the time scale of the precursor-mediated adsorption process. Otherwise, the island magnetizations ***M*** would fluctuate thermally and could not cause the enantiomeric excess on the islands. Such a conclusion is experimentally verified by performing spin-polarized measurements at RT (for details see Section S5, Supporting Information), which revealed clear and stable magnetic contrast of the Co nanoislands (Figure 4c,d).

We also examined our data to determine whether the observed enantiospecificity could be due to other properties of the Co nanoislands. Separate evaluation of the enantiomeric ratio for [7]H molecules at the rim and center of the islands revealed stronger enantioselectivity at the center than at the rim. This allows us to rule out scenarios in which specific electronic properties of the rim area[29] or the diffusion barrier of the molecules to overcome the step at the island edge, e.g., at chiral kink sites, play a role in enantiospecific adsorption (for details see Section S8, Supporting Information). Similarly, testing the relationship between the enantiomeric excess of the islands and their stacking type (unfaulted or faulted)[35] rather than magnetization direction revealed no significant effect (for details see Section S9, Supporting Information). This finding is corroborated by the experimental observations that i) magneto-enantiospecific adsorption due to the magnetization direction occurs for both stacking types with equal selectivity and ii) there is no statistically significant correlation between island stacking and island magnetization direction, see Sections S9 and S10 (Supporting Information).

2.4. DFT Results

Important additional insight is provided by spin-polarized first-principles calculations of the [7]H – 2 ML Co/Cu(111) system in the framework of dispersion-corrected DFT (see Experimental Section). As already mentioned, the [7]H molecule adsorbs with the proximal phenanthrene group aligned basically parallel to the Co surface (see Figure S9a, Supporting Information). Twelve carbon atoms of that group are at distances between 210 and 240 pm to Co atoms. The adsorption energy evaluated from these calculations amounts to 3.51 eV per molecule, which, together with the short C–Co distances, indicates that the molecule strongly chemisorbs to the ferromagnetic Co substrate. Such strong chemisorption explains in part the low mobility of [7]H at RT. Moreover, no differences in binding energy (within the error of these ab initio calculations) are obtained in non-collinear spin-polarized calculations when the Co magnetization points up or down (for details see Section S7, Supporting Information). Molecular handedness and magnetically induced asymmetric spin-orbit interactions do not play a role once the molecule reaches the final chemisorption state.

3. Discussion

As no interisland exchange of molecules is possible in the chemisorbed state, magnetochiral selection must occur in a transient precursor state. Such an adsorption precursor state is a physisorbed state that is transiently occupied when molecules approach the surface before reaching the ground state of chemisorption (Figure 4e). Precursor states were originally introduced in order to explain deviations from Langmuirian adsorption and desorption kinetics,[36,37] and have been directly observed via STM for aromatic compounds.[38] The larger distance from the surface and a much weaker adsorption energy of molecules in a precursor state result in enhanced lateral mobility and allow molecules to seek out preferred adsorption sites over a large distance.[37] Therefore, molecules in the physisorbed precursor state can probe the magnetization direction of several Co islands before they are selectively chemisorbed. Hence, molecules undergo enantioselection while transiently occupying the precursor state. When finally chemisorbed, the molecules are tightly bound, and inter-island mobility and island selection are stopped.

In general, adsorption may occur under thermodynamic or kinetic control. The ratio of the magnetochiral occupation numbers N_1 and N_2 can be related via Boltzmann factors to an energy difference ΔE by

$$r = \frac{N_1}{N_2} = \exp\left(-\frac{\Delta E}{k_B T}\right) \tag{1}$$

see Section S6 (Supporting Information). The statistics in Table 2 yields $\Delta E = (10 \pm 2)$ meV for $T = 296$ K. However, as diffusion or desorption from the strongly bound chemisorbed state can be safely excluded, thermodynamic equilibrium is not achieved. Furthermore, our DFT calculations did not yield different chemisorption energies for the enantiomers that could lead to enantiomeric excess in the ground state. The energy difference is therefore based on different transition rates between precursor and chemisorbed state, due to magneto-enantiospecific binding in the precursor state (Figure 4f and Figure S8, Supporting Information). Physisorption in the precursor state is based on dispersive forces and enantioselection in that state points to an electron spin-selective process at the vdW level. Our results seem therefore to support the controversial picture of vdW interactions that go beyond spin averaging but include a spin-dependence in dispersive forces.[39,40] The well-defined [7]H – 2 ML Co/Cu(111) system holds the potential to become the drosophila for the development and improvement of novel spin-dependent vdW functionals.

4. Conclusion

In summary, a pronounced magnetochiral selectivity during adsorption of a helical hydrocarbon on ferromagnetic Co nanoislands has been observed under well-defined conditions in ultrahigh vacuum at the single-molecule level by spin-polarized STM. An influence of collective or ensemble effects on the adsorption behavior can therefore be clearly excluded. The selection occurs in a van der Waals-bound precursor state, allowing the molecules to sample several Co islands prior to final chemisorption. Our report shines new light onto magnetochiral phenomena in molecule-surface interactions and provides a well-defined adsorbate system for theoretical studies.

5. Experimental Section

Measurements were performed in an ultrahigh vacuum (UHV, $<10^{-8}$ Pa) cluster tool equipped with a preparation chamber for substrate preparation and analysis, a separate molecule deposition chamber, and a LT-STM (Omicron Scienta) operating down to 5 K.

Molecule Synthesis: Racemic mixtures of heptahelicene were synthesized from a stilbene precursor by photocyclyzation as described previously.[41]

Sample Preparation: Co bilayer nanoislands were grown on an atomically clean Cu(111) surface by in situ deposition at RT from a 99.99% pure Co rod using e-beam evaporation. The deposition rate was 0.2 ML min^{-1} and the pressure during deposition was $<2 \times 10^{-8}$ Pa. After deposition, cooling of the sample was initiated within a few minutes to avoid surface diffusion of Cu atoms onto the Co islands.[42] The cleaning procedure of the Cu(111) single crystal consisted of repeated cycles of Ar^+ sputtering followed by annealing. Further details about the Co deposition can be found in Ref. [27]. After Co deposition, the shape and density of the Co bilayer islands as well as the cleanness of the deposition were checked by means of topographic STM images. Simultaneously, spin-polarized STM measurements were performed to confirm the presence of a well-defined magnetization of the islands perpendicular to the surface. Due to their typical size of 10–15 nm, the nanoislands are in a magnetic single-domain state.[43] Then, the Co/Cu(111) substrate was transferred at RT to the molecule chamber and exposed to the molecular vapor sublimed from a carefully heated glass crucible. The crucible temperature was about 400 K, the exposure time typically less than one minute, and the pressure during sublimation less than 10^{-7} Pa.[27] Finally, the sample was transferred to the STM chamber within a few minutes and immediately cooled for the STM experiments, which were performed at a pressure in the mid 10^{-9} Pa range and at 5 K unless otherwise specified. Higher measurement temperatures T_{meas} were achieved by cooling with liquid N_2 instead of liquid He ($T_{\text{meas}} = 78$ K), during the slow warming of the system to RT ($T_{\text{meas}} = 285$ K), or by measuring immediately after [7]H deposition at RT without any cooling ($T_{\text{meas}} = 296$ K).

STM Measurements: Electrochemically etched W tips (polycrystalline W wire in 5 M NaOH solution) were used for all STM measurements. Co-functionalized W tips providing magnetic contrast were obtained by intentionally bringing the tip in near mechanical contact with a remote ferromagnetic Co nanoisland and by applying short bias voltage pulses to transfer Co atoms from the island to the tip. The functionalization procedure was repeated until successful acquisition of a spin-polarized dI/dV map from Co nanoislands confirmed the sensitivity of the tip to the out-of-plane magnetization component.

Two types of STM data were presented: i) Topographic STM images were taken in constant-current mode. The bias voltage V_{bias} was applied to the sample, and I_t denotes the setpoint current of the STM feedback loop. ii) Differential conductance (dI/dV) maps that were taken simultaneously with constant-current topographic images, i.e. with the STM feedback loop closed. dI/dV maps represent, to a good approximation, the local density of states as a function of the lateral position and at the energy eV_{bias}, where $V_{\text{bias}} = 0$ corresponds to the Fermi energy. The dI/dV signal for the conductance maps was obtained by modulating V_{bias} with a small sinusoidal signal (rms amplitude $V_{\text{mod}} = 20$ mV; frequency $f_{\text{mod}} = 752$ Hz) and detecting the resulting modulation of the tunneling current at f_{mod} using a lock-in amplifier.

The high-resolution topographic STM images in Figures 1e,f and 2c,d as well as Figures S4 and S9c,e (Supporting Information) were processed with a Gaussian high-pass filter to enhance the contrast of intramolecular fine structure as described in Ref. [27].

DFT Calculations: Spin-polarized first-principles calculations in the framework of density functional theory (DFT) were performed by employing the generalized gradient approximation (PBE)[44] and the optB86b non-local van der Waals exchange-correlation functional[45] in a projector augmented plane-wave formulation[46] as implemented in the VASP code.[47,48]

The [7]H – 2 ML Co/Cu(111) system was modeled within the supercell approach [(8 × 8) in-plane surface unit cells and 1.45 nm vacuum above the molecule, i.e., $2.056 \times 2.056 \times 3.100\ \text{nm}^3$] containing five atomic layers (2 Co and 3 Cu) with the adsorbed molecule on one side of the slab.[49] Using a plane-wave energy cutoff of 500 eV in the ab initio calculations, the two Co layers and the molecule atoms were allowed to relax until the atomic forces were lower than 0.05 eV nm^{-1}.

Supporting Information

Supporting Information is available from the Wiley Online Library or from the author.

Acknowledgements

The authors are grateful for stimulating discussions with G. Bihlmayer. N.A. acknowledges Deutsche Forschungsgemeinschaft (DFG) support through the Collaborative Research Center SFB 1238 Project No. 277146847 (subproject C01). The authors gratefully acknowledge the computing time granted by the JARA Vergabegremium and provided on the JARA Partition part of the supercomputer JURECA at Forschungszentrum Jülich.

Open access funding enabled and organized by Projekt DEAL.

Conflict of Interest

The authors declare no conflict of interest.

Data Availability Statement

The data that support the findings of this study are available from the corresponding author upon reasonable request.

Keywords

chirality, CISS, enantiospecific adsorption, magnetic surfaces, van der Waals interactions

Received: August 25, 2023
Revised: November 29, 2023

---

[1] L. Pasteur, *Annales Chimie Phys.* **1848**, *24*, 442.
[2] L. Pasteur, Œuvres de Pasteur Vol. 1, Masson et Cie, Paris, **1922**, p. 329.
[3] L. Pasteur, *Rev. Sci. Paris* **1884**, *7*, 2.
[4] W. Thomson, *Proc. Roy. Soc.* **1894**, *54*, 59.
[5] P. M. Curie, *J. Phys. Theor. Appl.* **1894**, *3*, 393.
[6] L. D. Barron, *Science* **1994**, *266*, 1491.
[7] G. Wagnière, A. Meier, *Chem. Phys. Lett.* **1982**, *93*, 78.
[8] G. L. J. A. Rikken, E. Raupach, *Nature* **2000**, *405*, 932.
[9] K. Ray, S. P. Ananthavel, D. H. Waldeck, R. Naaman, *Science* **1999**, *283*, 814.
[10] R. A. Rosenberg, *Electronic and Magnetic Properties of Chiral Molecules and Supramolecular Architectures*, Springer, Berlin, Heidelberg, **2011**, pp. 279–306.
[11] R. Naaman, D. H. Waldeck, *J. Phys. Chem. Lett.* **2012**, *3*, 2178.
[12] B. Göhler, V. Hamelbeck, T. Z. Markus, M. Kettner, G. F. Hanne, Z. Vager, R. Naaman, H. Zacharias, *Science* **2011**, *331*, 894.

[13] M. Kettner, V. V. Maslyuk, D. Nürenberg, J. Seibel, R. Gutierrez, G. Cuniberti, K. H. Ernst, H. Zacharias, *J. Phys. Chem. Lett.* **2018**, *9*, 2025.
[14] Z. Xie, T. Z. Markus, S. R. Cohen, Z. Vager, R. Gutierrez, R. Naaman, *Nano Lett.* **2011**, *11*, 4652.
[15] V. Kiran, S. P. Mathew, S. R. Cohen, I. Hernández Delgado, J. Lacour, R. Naaman, *Adv. Mater.* **2016**, *28*, 1957.
[16] A. C. Aragonès, E. Medina, M. Ferrer-Huerta, N. Gimeno, M. Teixidó, J. L. Palma, N. Tao, J. M. Ugalde, E. Giralt, I. Díez-Pérez, V. Mujica, *small* **2017**, *13*, 1602519.
[17] H. Al-Bustami, B. P. Bloom, A. Ziv, S. Goldring, S. Yochelis, R. Naaman, D. H. Waldeck, Y. Paltiel, *Nano Lett.* **2020**, *20*, 8675.
[18] S. Mishra, A. K. Mondal, E. Z. Smolinsky, R. Naaman, K. Maeda, T. Nishimura, T. Taniguchi, T. Yoshida, K. Takayama, E. Yashima, *Angew. Chemie - Int. Ed.* **2020**, *59*, 14671.
[19] F. Evers, A. Aharony, N. Bar-Gill, O. Entin-Wohlman, P. Hedegård, O. Hod, P. Jelinek, G. Kamieniarz, M. Lemeshko, K. Michaeli, V. Mujica, R. Naaman, Y. Paltiel, S. Refaely-Abramson, O. Tal, J. Thijssen, M. Thoss, J. M. van Ruitenbeek, L. Venkataraman, B. Y. D. H. Waldeck, L. Kronik, *Adv. Mater.* **2022**, *34*, 2106629.
[20] K. Banerjee-Ghosh, O. B. Dor, F. Tassinari, E. Capua, S. Yochelis, A. Capua, S. H. Yang, S. S. Parkin, S. Sarkar, L. Kronik, L. T. Baczewski, R. Naaman, Y. Paltiel, *Science* **2018**, *360*, 1331.
[21] F. Tassinari, J. Steidel, S. Paltiel, C. Fontanesi, M. Lahav, Y. Paltiel, R. Naaman, *Chem. Sci.* **2019**, *10*, 5246.
[22] Y. Lu, B. P. Bloom, S. Qian, D. H. Waldeck, *J. Phys. Chem. Lett.* **2021**, *12*, 7854.
[23] T. N. H. Nguyen, L. Rasabathina, O. Hellwig, A. Sharma, G. Salvan, S. Yochelis, Y. Paltiel, L. T. Baczewski, C. Tegenkamp, *ACS Appl. Mater. Interfaces* **2022**, *14*, 38013.
[24] M. Radetic, A. J. Gellman, *Isr. J. Chem.* **2022**, *62*, 202200028.
[25] M. Baljozović, A. L. Fernandes Cauduro, J. Seibel, A. Mairena, S. Grass, J. Lacour, A. K. Schmid, K. H. Ernst, *Phys. Status Solidi B* **2021**, *258*, 2100263.
[26] J. De La Figuera, J. E. Prieto, C. Ocal, R. Miranda, *Phys. Rev. B* **1993**, *47*, 13043.
[27] M. R. Safari, F. Matthes, K.-H. Ernst, D. E. Bürgler, C. M. Schneider, *Nanomaterials* **2022**, *12*, 3281.
[28] O. Pietzsch, A. Kubetzka, M. Bode, R. Wiesendanger, *Phys. Rev. Lett.* **2004**, *92*, 057202.
[29] O. Pietzsch, S. Okatov, A. Kubetzka, M. Bode, S. Heinze, A. Lichtenstein, R. Wiesendanger, *Phys. Rev. Lett.* **2006**, *96*, 237203.
[30] H. Oka, P. A. Ignatiev, S. Wedekind, G. Rodary, L. Niebergall, V. S. Stepanyuk, D. Sander, J. Kirschner, *Science* **2010**, *327*, 843.
[31] J. Park, C. Park, M. Yoon, A.-P. Li, *Nano Lett.* **2017**, *17*, 292.
[32] T. Esat, R. Friedrich, F. Matthes, V. Caciuc, N. Atodiresei, S. Blügel, D. E. Bürgler, F. S. Tautz, C. M. Schneider, *Phys. Rev. B* **2017**, *95*, 094409.
[33] M. Metzelaars, S. Schleicher, T. Hattori, B. Borca, F. Matthes, S. Sanz, D. E. Bürgler, J. Rawson, C. M. Schneider, P. Kögerler, *Chem. Sci.* **2021**, *12*, 8430.
[34] X. Jia, W. An, *J. Phys. Chem. C* **2018**, *122*, 21897.
[35] N. N. Negulyaev, V. S. Stepanyuk, P. Bruno, L. Diekhöner, P. Wahl, K. Kern, *Phys. Rev. B* **2008**, *77*, 125437.
[36] W. H. Weinberg, *Kinetics of Intrface Reactions*, Springer Series in Surface Science, vol. *8*, Springer-Verlag, Berlin Heidelberg **1987**, pp. 94–124.
[37] M. Bowker, *Top. Catal.* **2016**, *59*, 663.
[38] D. E. Brown, D. J. Moffatt, R. A. Wolkow, *Science* **1998**, *279*, 542.
[39] O. A. Vydrov, T. V. Voorhis, *Phys. Rev. Lett.* **2009**, *103*, 063004.
[40] D. C. Langreth, B. I. Lundqvist, *Phys. Rev. Lett.* **2010**, *104*, 0999303.
[41] A. Sudhakar, T. J. Katz, *Tetrahedron Lett.* **1986**, *27*, 2231.
[42] A. Rabe, N. Memmel, A. Steltenpohl, T. Fauster, *Phys. Rev. Lett.* **1994**, *73*, 2728.
[43] S. Ouazi, S. Wedekind, G. Rodary, H. Oka, D. Sander, J. Kirschner, *Phys. Rev. Lett.* **2012**, *108*, 107206.
[44] J. P. Perdew, K. Burke, M. Ernzerhof, *Phys. Rev. Lett.* **1996**, *77*, 3865.
[45] I. Hamada, *Phys. Rev. B* **2014**, *89*, 121103.
[46] P. E. Blöchl, *Phys. Rev. B* **1994**, *50*, 17953.
[47] G. Kresse, J. Hafner, *Phys. Rev. B* **1994**, *49*, 14251.
[48] G. Kresse, J. Furthmüller, *Phys. Rev. B* **1996**, *54*, 11169.
[49] G. Makov, M. C. Payne, *Phys. Rev. B* **1995**, *51*, 4014.

ADVANCED
MATERIALS

Supporting Information

for *Adv. Mater.*, DOI 10.1002/adma.202308666

Enantioselective Adsorption on Magnetic Surfaces

Mohammad Reza Safari, Frank Matthes, Vasile Caciuc, Nicolae Atodiresei, Claus M. Schneider, Karl-Heinz Ernst* and Daniel E. Bürgler**

Supporting Information

Enantioselective Adsorption on Magnetic Surfaces

Mohammad Reza Safari[1,2*], Frank Matthes[1,2], Vasile Caciuc[3], Nicolae Atodiresei[3], Claus M. Schneider[1,2,4], Karl-Heinz Ernst[5,6,7*] and Daniel E. Bürgler[1,2*]

[1]Peter Grünberg Institute, Electronic Properties (PGI-6), Forschungszentrum Jülich, 52425, Jülich, Germany.
[2]Jülich Aachen Research Alliance (JARA-FIT), Fundamentals of Future Information Technology, Forschungszentrum Jülich, 52425, Jülich, Germany.
[3]Peter Grünberg Institute and Institute for Advanced Simulation, Quantum Theory of Materials (PGI-1/IAS-1), Forschungszentrum Jülich, 52425, Jülich, Germany.
[4]Fakultät für Physik, Universität Duisburg-Essen, 47057, Duisburg, Germany.
[5]Molecular Surface Science Group, Empa, Swiss Federal Laboratories for Materials Science and Technology, 8600, Dübendorf, Switzerland.
[6]Nanosurf Laboratory, Institute of Physics, The Czech Academy of Sciences, 16200, Prague, Czech Republic.
[7]Institut für Chemie, Universität Zürich, 8057, Zürich, Switzerland.

*Corresponding author(s). E-mail(s): m.safari@fz-juelich.de; karl-heinz.ernst@empa.ch; d.buergler@fz-juelich.de;
Contributing authors: f.matthes@fz-juelich.de; v.caciuc@fz-juelich.de; n.atodiresei@fz-juelich.de; c.m.schneider@fz-juelich.de;

S1 Definition of the pitch vector of a helix

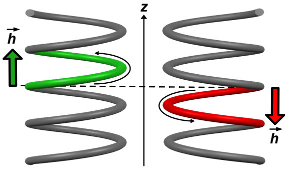

Suppl. Fig. S1 Pitch vector of a helix. The pitch vector $\boldsymbol{h}$ of a helix points from the start to the end point of a complete counterclockwise helix winding (increasing parameter $s \to s+1$). For a right-handed helix the pitch vector $\boldsymbol{h}$ points in $+z$-direction and for a left-handed helix in $-z$-direction.

A helical curve with the helix axis aligned in z-direction is defined by the following parametrization in Cartesian coordinates

$$\begin{aligned} x(s) &= R\cos(2\pi s), \\ y(s) &= R\sin(2\pi s), \\ z(s) &= hs, \end{aligned}$$

where R is the helix radius and h the helix pitch, i.e. the height of one complete helix winding measured parallel to the helix axis. $h > 0$ describes a right-handed helix and $h < 0$ a left-handed one. The pitch vector is defined as $\boldsymbol{h} = h\boldsymbol{e}_z$, where $\boldsymbol{e}_z$ the unit vector in $+z$-direction (Supplementary Fig. S1). Since heptahelicene molecules adsorb on Co nanoislands with their helix axis perpendicular to the surface, right-handed *(P)*-[7]H molecules are characterized by a pitch vector $\boldsymbol{h}$ pointing into the vacuum ($+z$-direction) and left-handed *(M)*-[7]H molecules by a pitch vector $\boldsymbol{h}$ pointing into the substrate ($-z$-direction).

S2 Data sets 1 and 2 on magneto-enantiospecific [7]H adsorption on Co

Data on the magneto-enantiospecific adsorption of [7]H on ferromagnetic Co nanoislands is obtained from two independent data sets measured using separately prepared Co/Cu(111) substrate systems, different runs of [7]H deposition, and newly Co-functionalized STM tips.

Supplementary Fig. S2 shows two topographic overview images (Supplementary Figs. S2a and c) containing all Co bilayer islands analysed in data set 1, together with the corresponding simultaneously recorded dI/dV maps (Supplementary Figs. S2b and d). The dI/dV maps reveal islands with $\boldsymbol{M} = \uparrow$ and $\boldsymbol{M} = \downarrow$. The topography image and dI/dV map in Supplementary Figs. S2c and d were acquired following Supplementary Figs. S2a and b after shifting the

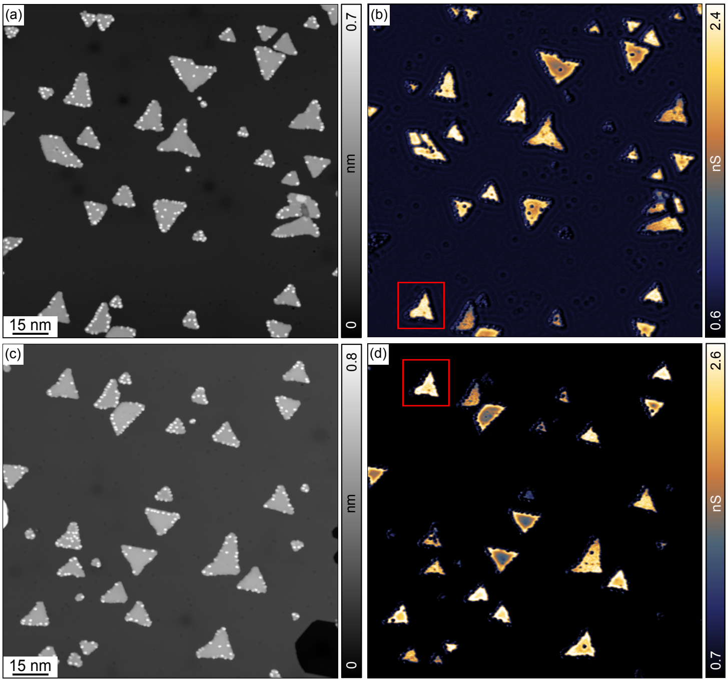

Suppl. Fig. S2 Data set 1 on enantiospecific adsorption of [7]H on ferromagnetic Co nanoislands. **a** and **c**, Constant-current topographic image of [7]H molecules on Co nanoislands on Cu(111). **b** and **d**, Simultaneously with **a** and **c** measured dI/dV maps. The scan area of **c** and **d** is vertically shifted relative to that of **a** and **b** to enlarge the data set. The red frames in **b** and **d** indicate a common island in the two consecutive scans showing the same magnetic contrast ($V_{\mathrm{bias}} = -350\,\mathrm{mV}$, $I_{\mathrm{t}} = 340\,\mathrm{pA}$, $V_{\mathrm{mod}} = 20\,\mathrm{mV}$, $f_{\mathrm{mod}} = 752\,\mathrm{Hz}$, 5 K, Co-functionalized W tip).

scan area downward. This is to increase the number of islands and molecules examined. The shift is chosen so that at least one island is visible in both images (red frames) to detect a possible unintentional change of the tip magnetization between the two consecutive scans, but this is not the case in this data set. Therefore, the enantiomer counts obtained from high-resolution topographic images of all 48 islands visible in Supplementary Figs. S2c and d can be added. The occupation numbers $N_{\boldsymbol{Mh}}$ for 291 analyzed [7]H molecules are listed in the first row of Tables 1 and 2 in the main text.

The topographic overview images and the simultaneously recorded dI/dV maps for the even larger data set 2 are presented in Supplementary Fig. S3. The amount of deposited Co was increased by about 20% and also the sublimation time for the molecules was slightly increased. This is to obtain more

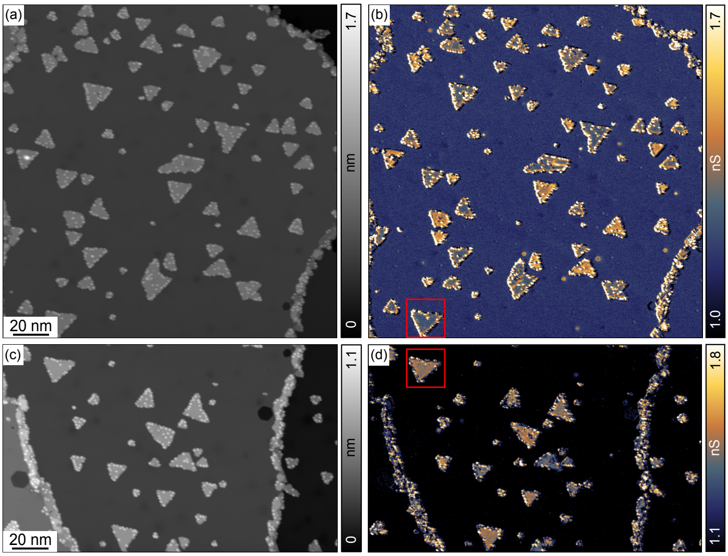

Suppl. Fig. S3 Data set 2 on enantiospecific adsorption of [7]H on ferromagnetic Co nanoislands. **a** and **c**, Constant-current topographic image of [7]H molecules on Co nanoislands on Cu(111). **b** and **d**, Simultaneously with **a** and **c** measured dI/dV maps. The scan area of **c** and **d** is vertically shifted relative to **a** and **b** to enlarge the data set. The red frames in **b** and **d** indicate a common island in the two consecutive scans with opposite magnetic contrast due to a reversal of the tip magnetization between the two scans ($V_{\mathrm{bias}} = -600\,\mathrm{mV}$, $I_{\mathrm{t}} = 950\,\mathrm{pA}$, $V_{\mathrm{mod}} = 20\,\mathrm{mV}$, $f_{\mathrm{mod}} = 752\,\mathrm{Hz}$, 5 K, Co-functionalized W tip).

islands that can accommodate correspondingly more molecules without causing molecular aggregation. As a consequence, the number of analysed molecules in data set 2 is larger than in data set 1. In this data set, the island in the red frame shows in Suppl. Fig. S3b dark and in Suppl. Fig. S3d bright magnetic contrast. The change in the relative magnetization of the tip and island that gives rise to this contrast inversion can only be explained by the reversal of tip magnetization that occasionally occurs due to interaction with the surface. Structural as well as magnetic changes of the tip during the acquisition of an image can easily be recognized by an abrupt contrast change within a horizontal scan line. Areas of STM images or dI/dV maps with such artifacts are discarded and not considered for data analysis. Tip changes that occur between scans are much more difficult to detect and require cross-checking, such as the overlap of scan areas with an island common to the preceding and subsequent scans used here. For the statistical analysis, the reversal of the tip magnetization can be accounted for by assigning and adding the enantiomer counts of the bright (dark) islands of Suppl. Fig. S3d to the enantiomer counts of dark (bright) islands of Suppl. Fig. S3b. The statistical evaluation for data

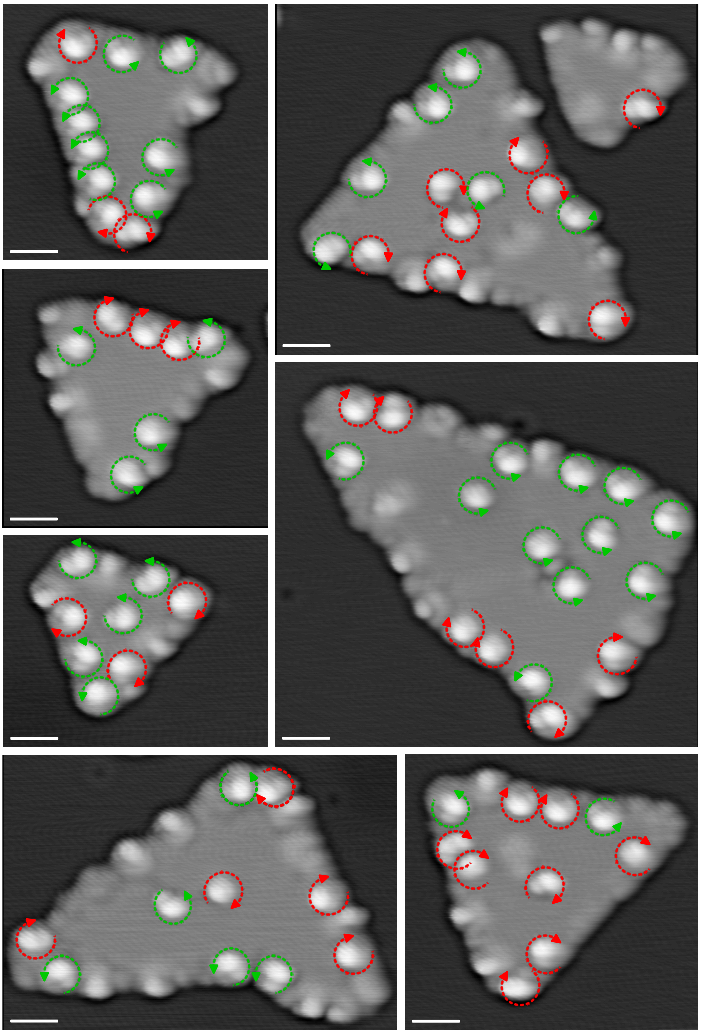

Suppl. Fig. S4 High-resolution topographic STM images revealing the molecules' handedness. Green and red circular arrows indicate *(P)*-[7]H and *(M)*-[7]H enantiomers, respectively ($V_{\text{bias}} = 1\,\text{V}$, $I_{\text{t}} = 50\,\text{pA}$, 5 K, Co-functionalized W tip, Gaussian high-pass filtered). All scale bars indicate 2 nm.

set 2, which includes 457 analyzed [7]H molecules on 62 islands, is reported in the second row of Tables 1 and 2 in the main text.

Supplementary Fig. S4 shows seven representative examples of more than 100 of high-resolution topographic STM images used to determine the handedness of individual [7]H molecules. Only features with proper diameter and apparent height were consider as [7]H molecules. The STM images were processed with a Gaussian high-pass filter to enhance the contrast of intramolecular fine structure and to facilitate the determination of the molecular handedness, as described in detail in Ref. [1].

S3 Error calculation

The deposition of a racemic mixture of [7]H molecules on perpendicularly magnetized Co nanoislands can be considered as dicing with three possible outcomes: The pitch vector $\boldsymbol{h}$ of the molecular helix can be (i) parallel or (ii) antiparallel to the island magnetization $\boldsymbol{M}$, or (iii) the handedness of the molecule cannot be determined, e.g. because the molecule is adsorbed on a defect in the substrate. When depositing N molecules, the three outcomes occur N_i ($i = 1, 2, 3$) times, and $N_1 + N_2 + N_3 = N$. The probability for observing the outcome combination $[N_1, N_2, N_3]$ is given by the trinomial distribution function [2]

$$P([N_1, N_2, N_3], N, [p_1, p_2, p_3]) = \frac{N!}{N_1!N_2!N_3!}\, p_1^{N_1} p_2^{N_2} p_3^{N_3} \quad \text{for} \quad N = \sum_{i=1}^{3} N_i,$$

where p_i are the probabilities of the individual outcomes i, $N_i = Np_i$. The variance $(\Delta N_i)^2$ of N_i and the covariance $\mathrm{covar}(N_i, N_j)$ for $i \neq j$ are

$$\begin{aligned} (\Delta N_i)^2 &= Np_i(1-p_i) = N_i\left(1 - \frac{N_i}{N}\right), \\ \mathrm{covar}(N_i, N_j) &= -Np_ip_j = \frac{-N_iN_j}{N}. \end{aligned}$$

The error Δr of functions $r(N_1, N_2, N_3)$ is given by error propagation taking covariances into account

$$(\Delta r)^2 = \sum_{i=1}^{3}\left(\frac{dr}{dN_i}\right)^2 (\Delta N_i)^2 + \sum_{i \neq j} 2\frac{dr}{dN_i}\frac{dr}{dN_j}\mathrm{covar}(N_i, N_j).$$

For the function of interest, the enantiospecific ratio $r = \frac{N_1}{N_2}$, the relative error becomes

$$\frac{\Delta r}{r} = \sqrt{\frac{N_1 + N_2}{N_1N_2}} = \sqrt{\frac{N - N_3}{N_1N_2}}. \tag{S1}$$

S4 Suppressed [7]H exchange between Co bilayer nanoislands on Cu(111)

The STM experiments to detect the enantiospecific adsorption of [7]H molecules on Co nanoislands were performed at 5 K to enable the high-resolution and time-consuming measurements at all. Low thermal drift and strongly suppressed atomic diffusion provide the mechanical and electronic stability of the tip-sample tunnel junction to obtain topographic images and dI/dV conductance maps of sufficiently high quality. However, the surface diffusion, which plays a major role for the [7]H molecules to reach and preferentially chemisorb on the energetically favored enantiospecific sites (i.e., a Co nanoisland with suitable magnetization direction), is also frozen at 5 K. Therefore, the low-temperature STM/STS data represent a snapshot of a state that was formed at a higher temperature.

To determine this temperature, we performed time series of topographic STM measurements at elevated temperatures of 78, 285, and 296 K, the latter corresponding to RT in our laboratory. Each time series shows the positions of [7]H molecules adsorbed at RT on Co nanoislands during a time interval of 4 to 5 hours at the corresponding measurements temperature of 78, 285, and 296 K,

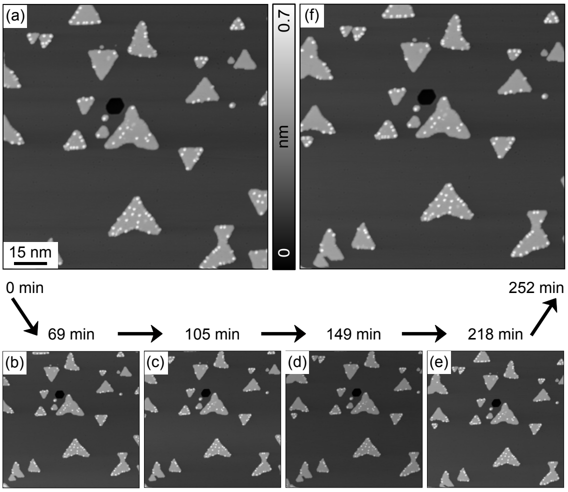

Suppl. Fig. S5 Time series at 78 K of [7]H molecules on Co nanoislands. **a-f**, Time series of constant-current topographic images of [7]H molecules deposited on Co nanoislands on Cu(111) at RT and imaged at 78 K. **a**, The first measurement of the series (0 min) and **f** the last after 252 min. **b-e**, Intermediate images of approximately the same area after 69, 105, 149, and 218 min, respectively. No molecular motion is observed. Slight shifts of the field of view are due to thermal drift, which was compensated for as best as possible by manually tracking the sample ($V_{\mathrm{bias}} = 500\,\mathrm{mV}$, $I_{\mathrm{t}} = 100\,\mathrm{pA}$, 78 K, W tip).

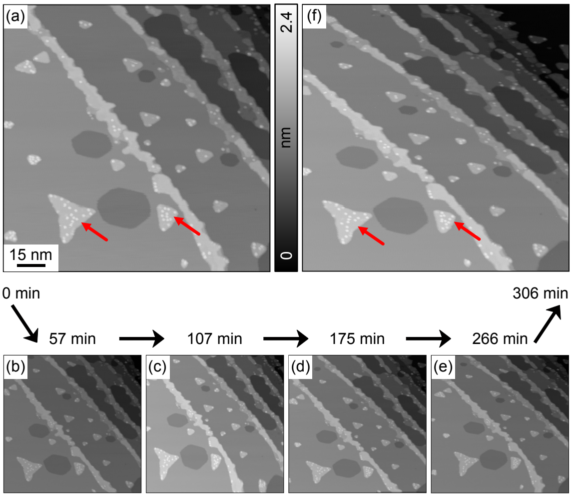

Suppl. Fig. S6 Time series at 285 K of [7]H molecules on Co nanoislands. a-f, Time series of constant-current topographic images of [7]H molecules deposited on Co nanoislands on Cu(111) at RT and imaged at 285 K. **a**, The first measurement of the series (0 min) and **f** the last after 306 min. **b-e**, Intermediate images of approximately the same area after 57, 107, 175, and 266 min, respectively. Few molecules move on the nanoisland they are adsorbed on (e.g., red arrows), but the number of molecules on each island is constant. Slight shifts of the field of view and distortions at the bottom edge of the images are due to enhanced thermal drift and piezo creep, which was compensated for as best as possible by manually tracking the sample ($V_{\text{bias}} = 500\,\text{mV}$, $I_{\text{t}} = 50\,\text{pA}$, 285 K, W tip).

see Suppl. Figs. S5, S6, and S7. These time intervals are longer than the time we needed to cool the samples for the low-temperature STM/STS experiments after the molecules were deposited. Between acquiring the individual images, we manually compensated for thermal drift to have the same surface area with the same nanoislands and molecules in the field of view over the whole duration of each time series. The first two time series were measured with the same sample, first cooled to 78 K with liquid nitrogen (Supplementary Fig. S5) and then during the slow warming of the system to RT at about 285 K (Supplementary Fig. S5). The third time series at 296 K was measured with a freshly prepared sample immediately after depositing the [7]H molecules at RT, i.e. without intermediate cooling. For each time series, we show in panel (a) the start image labeled '0 min' and in panel (f) the end image labeled with the total duration of the time series (e.g. '329 min') in large format to allow easy comparison. Intermediate snapshots of approximately the same sample area are displayed in smaller format in panels (b) to (e) and labeled with the elapsed time.

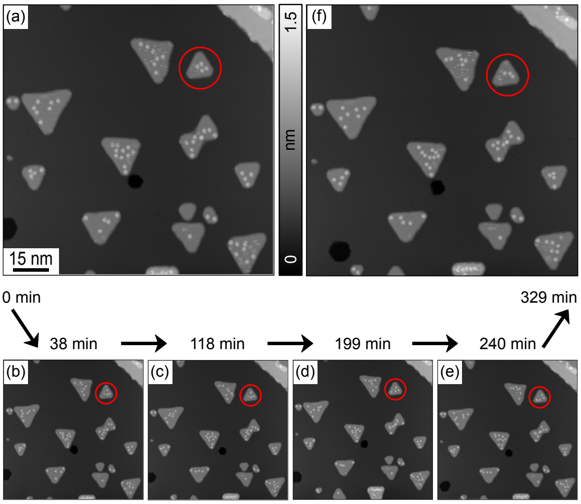

Suppl. Fig. S7 Time series at 296 K of [7]H molecules on Co nanoislands. a-f, Time series of constant-current topographic images of [7]H molecules deposited on Co nanoislands on Cu(111) at RT and imaged at 296 K. **a**, The first measurement of the series (0 min) and **f** the last after 329 min. **b-e**, Intermediate images of approximately the same area after 38, 118, 199, and 240 min, respectively. The number of molecules on the island marked in red appears to fluctuate between 3 and 4. Slight shifts of the field of view are due to enhanced thermal drift, which was compensated for as best as possible by manually tracking the sample ($V_{\mathrm{bias}} = 500\,\mathrm{mV}$, $I_{\mathrm{t}} = 20\,\mathrm{pA}$, 296 K, W tip).

In the time series at 78 K shown in Suppl. Fig. S5, all [7]H molecules on the nanoislands remain at the same position for more than 4 hours. There is no indication of molecular surface diffusion, neither on the island surfaces nor between the islands.

In the time series at 285 K shown in Suppl. Fig. S6, few molecules move to another adsorption site on the same nanoisland (e.g. red arrows), but the number of molecules on each island remains constant for the whole duration of about 5 hours. Therefore, molecular surface diffusion on the Co nanoislands starts slightly below RT, while exchange of [7]H molecules between Co islands is still not observed, most likely due to Ehrlich-Schwoebel barriers for diffusion across the island edges [3–5].

The third time series at 296 K, measured independently with a different sample and shown in Suppl. Fig. S7, reveals similar behavior as at 285 K: Molecules diffuse on the island surfaces, but not between the islands. The number of molecules on the island marked in red appears to fluctuate between 3 and 4. However, the horizontal streaks visible on several islands indicate molecules diffusing on the time scale of the measurement. Tip-induced motion of molecules may also play a role. Note that Suppl. Figs. S7a and f are also shown in Figs. 4a and b of the main text.

The preferred positions of the molecules gradually shift with increasing measurement temperature from the island rims to the centers. We attribute this behavior to the thermodynamic instability inherent in the Co/Cu(111) system [6]: When the sample is exposed to temperatures close to room temperature for a prolonged period of time during STM measurements, surface diffusion of Cu atoms occurs, which eventually leads to decoration of the Co island rims with Cu atoms, thereby reducing the local adsorption energy of the [7]H molecules.

The substrate is not significantly heated by the adsorption process and basically remains at RT because the molecular coverage in our experiments is very low and the Co/Cu substrate system has a large heat capacity. Therefore, our observations demonstrate that the magnetization-dependent enantiomeric excess on the Co nanoislands observed by STM at 5 K develops during deposition at RT.

S5 Ferromagnetism of Co nanoislands at RT

The formation of the magnetization-dependent enantiomeric excess on the Co islands occurs during deposition at RT. This requires that the superparamagnetic blocking temperature of the nanoislands is above RT on the time scale of the precursor-mediated adsorption process. To verify this premise, we performed spin-polarized measurements at RT. Figures 4c and d of the main text show the topographic image and the simultaneously acquired dI/dV map, respectively, measured at RT immediately after depositing Co nanoislands at RT, i.e. without intermediate cooling. Islands with clearly different contrast are visible in the dI/dV map. Contributions to the contrast due the different island stacking (i.e. triangular islands pointing to the left or right) can be excluded as the dI/dV map was measured at $V_{\text{bias}} = -600\,\text{mV}$ [7]. Contrast resulting from weak size-dependent shifts of the dI/dV peak near -600 meV [8] can be excluded by comparing islands of similar size. The two islands marked by dashed frames in Figs. 4c and d of the main text have the same stacking and almost equal size, but still exhibit different dI/dV contrast, which can only arise from different magnetization directions. The acquisition time for Figs. 4c and d of the main text was about 6 hours. Therefore, the imaging of an island took about 1 hour, during which the magnetization direction of the island is stable. This time interval is much longer than the duration of the precursor-mediated adsorption process discussed in the main text. We conclude that the Co nanoislands exhibit at RT ferromagnetism with stable magnetization directions on the time scale relevant for the enantiospecific adsorption of [7]H molecules.

S6 Precursor-mediated chemisorption

The schematic potential energy landscape for precursor-mediated chemisorption is shown in Suppl. Fig. S8a [9]. When molecules approach the substrate from vacuum, they are transiently trapped in the metastable, weakly bound precursor state with adsorption energy E_{prec} before overcoming the energy barrier to the strongly bound chemisorbed state ($E_{\text{chem}} > E_{\text{prec}}$). Due to the larger distance to the substrate and weaker binding, molecules in the precursor state have high lateral mobility, allowing them to seek out suitable adsorption sites within a wider radius of the landing site. For [7]H on Co, chemisorption is so strong ($E_{\text{chem}} = 3.5\,\text{eV}$) that the lateral mobility is suppressed in the chemisorbed state up to RT (see Supplementary Section S4).

Supplementary Figs. S8b-d show different scenarios for enantiospecific chemisorption via a precursor state. The two molecule classes with parallel and antiparallel alignment of substrate magnetization $\boldsymbol{M}$ and molecular pitch vector $\boldsymbol{h}$ then exhibit different potential curves shown in red and green.

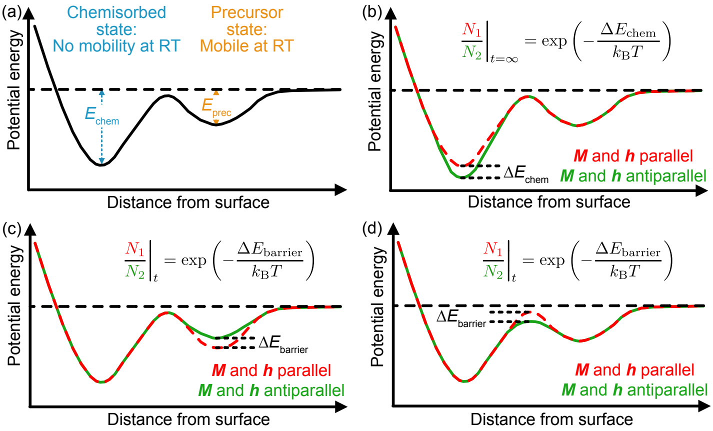

Suppl. Fig. S8 Precursor-mediated chemisorption. a, Schematic potential energy diagram showing the strongly bound chemisorption state (E_{chem}) at short distance to the substrate as well as the weaker van der Waals (vdW) bound precursor state (E_{prec}) at a larger distance from the substrate. **b**, Scenario for thermodynamic control where the enantiomeric excess is due to chemisorption energies for classes 1 and 2 (red and green curves, respectively) that differ by $\Delta E = \Delta E_{\text{chem}}$. **c** and **d**, Scenarios for kinetic control in which the enantiomeric excess is due to different energy barriers for the transition from the precursor to the chemisorption state, $\Delta E = \Delta E_{\text{barrier}}$. The difference in barrier height can arise from both different depths of the precursor adsorption potential E_{prec} (**c**) or different heights of the potential maximum between the two states (**d**).

In Suppl. Fig. S8b, it is assumed that the two classes have different chemisorption energies $E_{\mathrm{chem}}^{(1),(2)}$. When the thermodynamic equilibrium at temperature T is reached, which in principle is always the case after infinite waiting time, the occupation numbers of the chemisorption states for the two classes are different, $N_{1,2} \propto \exp(-E_{\mathrm{chem}}^{(1),(2)}/k_{\mathrm{B}}T)$ and the ratio r becomes

$$r = \frac{N_1}{N_2} = \exp\left(-\frac{E_{\mathrm{chem}}^{(1)} - E_{\mathrm{chem}}^{(2)}}{k_{\mathrm{B}}T}\right) = \exp\left(-\frac{\Delta E_{\mathrm{chem}}}{k_{\mathrm{B}}T}\right).$$

Taking into account that the occupation number distribution measured at 5 K is the one established at $T = 296\,\mathrm{K}$, this corresponds to Equation (1) of the main text with $\Delta E = \Delta E_{\mathrm{chem}}$. In this scenario based on thermodynamic equilibrium, enantiospecificity would – in contrast to our DFT calculations – arise from handedness- and magnetization-dependent chemical bonding. Furthermore, as surface mobility and desorption of the strongly bound, chemisorbed [7]H molecules are suppressed at RT (see Supplementary Section S4), reaching a thermodynamic equilibrium reflecting ΔE_{chem} can be ruled out.

If thermodynamic equilibrium is not reached, the kinetically controlled occupation number distribution is given by the rates of transition from the precursor to the chemisorption state, which depend on the height of the energy barrier between the two states. Enantiospecificity may then arise from different adsorption energies of the precursor state $E_{\mathrm{prec}}^{(1),(2)}$ for the two molecule classes (Supplementary Figs. S8c) or from different maxima of the barrier (Supplementary Figs. S8d). In both cases, the transition rates are proportional to $\exp(-E_{\mathrm{barrier}}^{(1),(2)}/k_{\mathrm{B}}T)$ and the ratio r becomes

$$r = \frac{N_1}{N_2} = \exp\left(-\frac{\Delta E_{\mathrm{barrier}}}{k_{\mathrm{B}}T}\right),$$

which again corresponds to Equation (1) of the main text with $\Delta E = \Delta E_{\mathrm{barrier}}$ and $T = 296\,\mathrm{K}$. The latter two scenarios are based on kinetic control of the adsorption process, and enantiospecificity arises from chirality- and spin-dependent interaction in the precursor state at the van der Waals level.

S7 Density functional theory calculations

Results of spin-polarized first-principles calculations of the [7]H – 2 ML Co/Cu(111) system performed in the framework of DFT including vdW interaction (see Methods) are presented in Suppl. Fig. S9. The adsorption geometry after relaxation of all Co and molecule atoms is shown in Suppl. Fig. S9a. The 3 six-membered rings closest to the Co surface are aligned nearly parallel to the surface plane resulting for 12 C atoms in short distances to the nearest Co atoms between 210 and 240 pm (blue-green sticks). The 3D isosurface of the charge density difference due to molecule-surface interaction in Suppl. Fig. S9b show charge accumulation (yellow) on the axis between neighboring C and

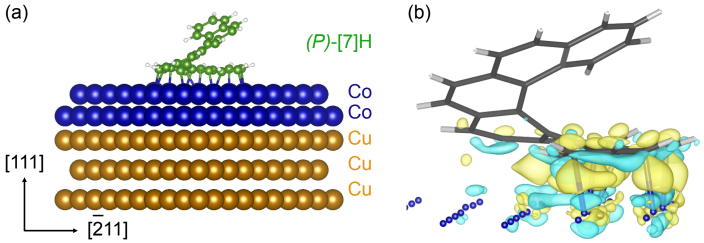

(c) Experiment V_{bias} = +1 V (d) DFT: V_{bias} = +1 V (e) Experiment V_{bias} = −1 V (f) DFT: V_{bias} = −1 V

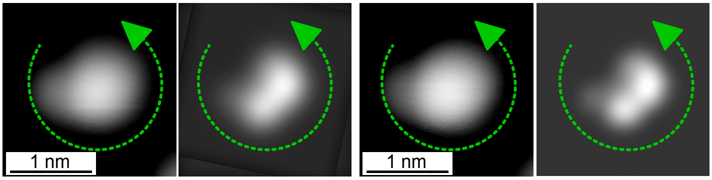

Suppl. Fig. S9 Results of DFT calculations. **a**, Calculated schematic adsorption geometry of a *(P)*-[7]H molecule on 2 ML Co on Cu(111). The 12 shortest Co-C distances in the range from 210 to 240 pm are indicated by blue-green sticks. **b**, 3D isosurface of the charge density difference due to molecule-surface interaction. Yellow and light blue volumes indicate charge accumulation and depletion, respectively. Small dark blue balls mark to positions of the Co surface atoms. **c**, High-resolution constant-current topographic STM image of a *(P)*-[7]H molecule on a Co bilayer island ($V_{\text{bias}} = 1\,\text{V}$, $I_{\text{t}} = 500\,\text{pA}$, 5 K, W tip, Gaussian high-pass filtered). **d**, Simulated topographic STM image at $V_{\text{bias}} = 1\,\text{V}$ of a *(P)*-[7]H molecule on 2 ML Co on Cu(111). **e** and **f**, Same as (**c**) and (**d**), but for $V_{\text{bias}} = -1\,\text{V}$.

Co atoms and charge depletion (light blue) in d orbitals of Co and π orbitals of the molecule. Hence, C-C bonds in the proximal phenantrene are slightly weakened upon chemisorption, and weak covalent C-Co bonds (compared to C-C bonds) are formed. The charge accumulation, which also contains charge density originating from Co d-orbitals, is slightly shifted towards the C atoms, meaning that the C-Co bonds are of polar covalent nature. The admixture of sp^3 character due to the additional weak C-Co bonds causes a slight upward bending of the C-H bonds for the involved C-rings, which is not the case for the distal C-rings pointing to the vacuum.

Including spin-orbit coupling interaction, we performed non-collinear spin-polarized calculations in which the Co magnetization axis is oriented perpendicular to the substrate and thus coincides with the helical axis of the molecule. To investigate enantiospecific adsorption, we considered for a given enantiomer two configurations in which the Co magnetization points either into the vacuum or vice versa into the substrate. We find that the energy difference between these configurations is only a few μeV, which is within the error bar of our ab initio calculations.

Supplementary Figs. S9c and d show the comparison between an experimental and a simulated topographic STM image of a *(P)*-[7]H molecule on a Co(111). The experimental image was measured at a bias voltage of $V_{\text{bias}} = +1\,\text{V}$, and the simulated image is an isosurface of the partial density of states (DOS) integrated from 0 to $eV_{\text{bias}} = +1\,\text{eV}$, where 0 corresponds to the Fermi energy. The isosurface was additionally convoluted with a 2D Gauss kernel with a full width at half maximum of 220 pm, representing the geometric shape of the STM tip. A similar comparison for $V_{\text{bias}} = -1\,\text{V}$, i.e., for the occupied states, is shown in Suppl. Figs. S9e and f. Both comparisons show qualitative agreement and confirm that the spiral increase in contrast (apparent height in the experiment and integrated DOS in the calculations, respectively) from dark via gray to white (see circular arrows) reflects the handedness of the adsorbed [7]H molecule.

As a consequence of the strong hybridization between the atomic-like p_z orbitals of carbon with the exchange-split d states of Co, the magnetic moment of Co atoms directly binding to C atoms is reduced ($1.425\,\mu_{\text{B}}$) compared to the magnetic moment ($1.785\,\mu_{\text{B}}$) of Co atoms located farther from the molecule, which is practically identical to the magnetic moment of the clean surface [10, 11]. Inversely, the spin-dependent hybridization leads to a small magnetic moment in the chemisorbed molecule of $0.089\,\mu_{\text{B}}$, which is antiferromagnetically aligned to that of the ferromagnetic Co surface.

S8 Island rims and diffusion barriers at island edges do not cause enantiospecific adsorption

Our low-temperature STM data indicate that a majority of the [7]H molecules are located at the rim of the Co islands (e.g. Fig. 2 of the main text or Fig. S4). The rim region with a width of about 1.7 nm [12] occupies about 50% of the area of an island with an edge length of 20 nm, but about 90% of the molecules are adsorbed in this region. This enhanced adsorption probability can be attributed to different electronic properties in the rim region compared to the island center, the so-called rim state [12]. This observation raises the question of whether specific properties at the rim or the diffusion barrier for molecules to overcome the island edges play a role in enantiospecific adsorption. To rule out such scenarios, we determined the enantiomeric ratio r (as introduced in Section 2.2 of the main text) for the island centers and the island rims separately, r_{center} and r_{rim}. The results for the total data set comprising 719 [7]H molecules on 107 islands are complied in Table S1.

The rim areas A_{rim} and center areas A_{center} determining in the weighting factors α are calculated for each island from its measured total area A.

Assuming an equilateral triangular island, the side length l is

$$l = \sqrt{\frac{4A}{\sqrt{3}}}. \tag{S2}$$

The side length of the triangle inside the rim is

$$l_{\text{center}} = l - \frac{2w}{\tan(30°)}, \tag{S3}$$

where $w = 1.7\,\text{nm}$ is the width of the rim [12]. Hence,

$$A_{\text{center}} = \frac{\sqrt{3}}{4} l_{\text{center}}^2 \quad \text{and} \quad A_{\text{rim}} = A - A_{\text{center}}. \tag{S4}$$

We note that the values of r are rather insensitive to the details of the weighting procedure, e.g. doubling or halving w does not significantly change r and its error.

The main results in Table S1 are (i) that enantioselectivity occurs at the island rims as well as in the centers and (ii) that it is significantly higher in the island centers ($r_{\text{center}} < r_{\text{rim}}$). If the observed enantioselective adsorption were solely due to the diffusion barrier at the island edges, then the enantioselectivity at the island centers should be lower than at the rims, i.e. $r_{\text{center}} > r_{\text{rim}}$. Still assuming that the precursor state does not play a role, this is because the molecules that directly land and chemisorb on top of islands are racemic and cannot leave the islands (see Section S4). Therefore, any scenario in which the enantiospecificity is due to the diffusion barrier of the [7]H molecules to overcome the edges of Co islands or due to specific local properties of the islands rims can be excluded as the origin of the observed enantiospecificity. Whether another, secondary mechanism based on a magnetization- and handedness-dependent barrier for diffusion across the island edges, which only affects r_{rim}, contributes to the difference between r_{rim} and r_{center} cannot be conclusively clarified with the available data.

The low-energy step edges bounding the triangular islands are achiral, but kinks sites in the step edges are chiral. Note that two kinks on the same island edge, one kinking toward the center of the island and the other kinking in

Suppl. Table S1 Enantiospecific adsorption of [7]H at rims and centers of Co nanoislands. $\alpha = A_{M_\uparrow}/A_{M_\downarrow}$ is the ratio of the total areas of considered islands with $\boldsymbol{M} = \uparrow$ and $\boldsymbol{M} = \downarrow$, respectively. $N_1 = N_{\uparrow\uparrow} + \alpha N_{\downarrow\downarrow}$ and $N_2 = N_{\uparrow\downarrow} + \alpha N_{\downarrow\uparrow}$ are the number of molecules in classes 1 and 2. The error bar of r is calculated according to Equation (S1) in Section S3.

Location of molecule	$\alpha = A_{M_\uparrow}/A_{M_\downarrow}$	$N_1 = N_{\uparrow\uparrow} + \alpha N_{\downarrow\downarrow}$	$N_2 = N_{\uparrow\downarrow} + \alpha N_{\downarrow\uparrow}$	$r = N_1/N_2$
Rim	0.63	207	289	0.72 ± 0.07
Center	0.41	13	29	0.45 ± 0.15
Both	0.55	207	303	0.68 ± 0.06

the opposite direction, have opposite handedness. Therefore, in principle, only islands with an unequal number of right- and left-handed kinks could exhibit enantiospecific diffusion across the island edges. However, the analysis on the enantiomeric ratios for the island centers r_{center} and the island rims r_{rim} given above also rules out this mechanism.

S9 Different island stacking does not cause enantiospecific adsorption

To rule out further alternative mechanisms, we tested whether the two stacking types of Co nanoislands can also lead to enantiospecific adsorption. To this end, we counted the number of *(M)*- and *(P)*-[7]H enantiomers on unfaulted and faulted islands, respectively, and calculated the enantiospecific ratio r_{stacking} analogous to the procedure in Section 2.2 of the main text. For five irregularly shaped islands, the stacking type could not be unambiguously determined, resulting in an analysis of 663 molecules on 102 islands. We count $N_{\triangle\uparrow} = 190$, $N_{\triangle\downarrow} = 189$, $N_{\triangledown\uparrow} = 147$, and $N_{\triangledown\downarrow} = 137$, where the first index denotes the stacking type ($\triangle$=unfaulted and $\triangledown$=faulted) and the second the molecular handedness ($\uparrow$ = *(P)*-[7]H) and ($\downarrow$ = *(M)*-[7]H). As in Section 2.2 of the main text, the four combinations of island stacking and molecular handedness of the adsorbed molecules are divided into two classes $N_1 = N_{\triangledown\downarrow} + \beta N_{\triangle\uparrow}$ and $N_2 = N_{\triangledown\uparrow} + \beta N_{\triangle\downarrow}$. $\beta = A_{\triangledown}/A_{\triangle}$ is again a weighting factor that accounts for the different total areas of unfaulted ($A_{\triangle}$) and faulted ($A_{\triangledown}$) islands. The measured value $\beta = 0.61$ is in fair agreement with the ratio of the relative probabilities for the formation of faulted and unfaulted Co bilayer nanoislands on Cu(111) obtained from kinetic Monte Carlo and molecular static simulations, $\beta_{\mathrm{simulation}} = 0.54$ [13]. We define the enantioselective ratio due to islands stacking as $r_{\mathrm{stacking}} = N_1/N_2$. Enantiospecific adsorption due to stacking would be demonstrated if r_{stacking} were significantly different from unity, and is disproved if it is close to unity, i.e. $r_{\mathrm{stacking}} \approx 1$. Our data yield $r_{\mathrm{stacking}} = 0.96 \pm 0.08$, which clearly rules out the possibility that differences between faulted and unfaulted Co bilayer nanoislands cause enantiospecific adsorption of [7]H molecules on Co islands.

In addition, we separately calculated the magneto-enantiospecific ratio r (as introduced in Section 2.2 of the main text) for the unfaulted and faulted islands. The results are compiled in Table S2. Magneto-enantiospecific adsorption occurs for both stacking types, and the selectivity is within error bars the same. Consequently, island stacking does not play a role for the observed enantiospecific adsorption.

S10 Island stacking and direction of island magnetization are uncorrelated

Some dI/dV maps (e.g. Fig. 4d of the main text) give the impression that most triangular islands with the same in-plane orientation also share a common

Suppl. Table S2 Statistics of [7]H adsorption on unfaulted and faulted Co nanoislands. $\alpha = A_{M_\uparrow}/A_{M_\downarrow}$ is the ratio of the total areas of the considered islands with $\boldsymbol{M} = \uparrow$ and $\boldsymbol{M} = \downarrow$, respectively. $N_1 = N_{\uparrow\uparrow} + \alpha N_{\downarrow\downarrow}$ and $N_2 = N_{\uparrow\downarrow} + \alpha N_{\downarrow\uparrow}$ are the number of molecules in classes 1 and 2. The error bar of r is calculated according to Equation (S1) in Section S3.

Stacking type	$\alpha = A_{M_\uparrow}/A_{M_\downarrow}$	$N_1 = N_{\uparrow\uparrow} + \alpha N_{\downarrow\downarrow}$	$N_2 = N_{\uparrow\downarrow} + \alpha N_{\downarrow\uparrow}$	$r = N_1/N_2$
Unfaulted	0.71	120	191	0.63 ± 0.07
Faulted	0.35	72	91	0.78 ± 0.12
Both	0.55	193	281	0.69 ± 0.06

magnetization direction. The two in-plane orientations reflect the different stacking of the islands. In order to investigate this issue systematically, we performed an analysis of the correlation between island stacking (faulted or unfaulted) and island magnetization direction (up or down). $I_{\triangle(\triangledown)\uparrow(\downarrow)}$ denotes the number of unfaulted (faulted) islands with up (down) magnetization. For the total data set comprising 102 islands, we count $I_{\triangle\uparrow} = 29$, $I_{\triangle\downarrow} = 31$, $I_{\triangledown\uparrow} = 15$, and $I_{\triangledown\downarrow} = 27$. The correlation factor is defined as

$$c = \frac{1}{2}\left[\frac{I_{\triangle\uparrow} - I_{\triangle\downarrow}}{I_{\triangle\uparrow} + I_{\triangle\downarrow}} - \frac{I_{\triangledown\uparrow} - I_{\triangledown\downarrow}}{I_{\triangledown\uparrow} + I_{\triangledown\downarrow}}\right]. \tag{S5}$$

$c = \pm 1$ corresponds to perfect correlation, that means all unfaulted islands are up magnetized and all faulted islands are down magnetized or vice versa, and $c = 0$ indicates the absence of any correlation. Our analysis yields $c = 0.13 \pm 0.20$. Obviously and as expected, the investigated islands show within error bars no significant correlation between stacking and magnetization. Therefore, the observed magneto-enantioselective adsorption is unequivocally a magnetization-dependent effect and cannot be traced back to the different stacking of the islands. This is in full agreement with the conclusions in Section S9.

References

[1] Safari, M.R., Matthes, F., Ernst, K.-H., Bürgler, D.E., Schneider, C.M.: Deposition of Chiral Heptahelicene Molecules on Ferromagnetic Co and Fe Thin-Film Substrates. Nanomaterials **12**, 3281 (2022). https://doi.org/10.3390/nano12193281

[2] Berendsen, H.J.C.: A Student's Guide to Data and Error Analysis. Cambridge University Press, Cambridge (2011). https://doi.org/10.1017/CBO9780511921247

[3] Ehrlich, G., Hudda, F.G.: Atomic View of Surface Self-Diffusion: Tungsten on Tungsten. J. Chem. Phys. **44**, 1039–1049 (1966). https://doi.org/10.1063/1.1726787

[4] Schwoebel, R.L., Shipsey, E.J.: Step Motion on Crystal Surfaces. J. Appl. Phys. **37**, 3682–3686 (1966). https://doi.org/10.1063/1.1707904

[5] Fendrich, M., Krug, J.: Ehrlich-Schwoebel effect for organic molecules: Direct calculation of the step-edge barrier using empirical potentials. Phys. Rev. B **76**, 121302 (2007). https://doi.org/10.1103/PhysRevB.76.121302

[6] Rabe, A., Memmel, N., Steltenpohl, A., Fauster, T.: Room–Temperature Instability of Co/Cu(111). Phys. Rev. Lett. **73**, 2728–2731 (1994). https://doi.org/10.1103/PhysRevLett.73.2728

[7] Pietzsch, O., Kubetzka, A., Bode, M., Wiesendanger, R.: Spin-Polarized Scanning Tunneling Spectroscopy of Nanoscale Cobalt Islands on Cu(111). Phys. Rev. Lett. **92**, 057202 (2004). https://doi.org/10.1103/PhysRevLett.92.057202

[8] Rastei, M.V., Heinrich, B., Limot, L., Ignatiev, P.A., Stepanyuk, V.S., Bruno, P., Bucher, J.P.: Size-Dependent Surface States of Strained Cobalt Nanoislands on Cu(111). Phys. Rev. Lett. **99**, 246102 (2007). https://doi.org/10.1103/PhysRevLett.99.246102

[9] Weinberg, W.H.: Precursor Intermediates and Precursor-Mediated Surface Reactions: General Concepts, Direct Observations and Indirect Manifestations. In: Grunze, M., Kreuzer, H.J. (eds.) Kinetics of Intrface Reactions. Springer Series in Surface Science, vol. 8, pp. 94–124. Springer, Berlin Heidelberg (1987). https://doi.org/10.1007/978-3-642-72675-0

[10] Atodiresei, N., Brede, J., Lazić, P., Caciuc, V., Hoffmann, G., Wiesendanger, R., Blügel, S.: Design of the local spin polarization at the organic-ferromagnetic interface. Phys. Rev. Lett. **105**, 066601 (2010). https://doi.org/10.1103/PhysRevLett.105.066601

[11] Callsen, M., Caciuc, V., Kiselev, N., Atodiresei, N., Blügel, S.: Magnetic hardening induced by nonmagnetic organic molecules. Phys. Rev. Lett. **111**, 106805 (2013). https://doi.org/10.1103/PhysRevLett.111.106805

[12] Pietzsch, O., Okatov, S., Kubetzka, A., Bode, M., Heinze, S., Lichtenstein, A., Wiesendanger, R.: Spin-Resolved Electronic Structure of Nanoscale Cobalt Islands on Cu(111). Phys. Rev. Lett. **96**, 237203 (2006). https://doi.org/10.1103/PhysRevLett.96.237203

[13] Negulyaev, N.N., Stepanyuk, V.S., Bruno, P., Diekhöner, L., Wahl, P., Kern, K.: Bilayer growth of nanoscale Co islands on Cu(111). Phys. Rev. B **77**, 125437 (2008). https://doi.org/10.1103/PhysRevB.77.125437

3.3 Enantioselective adsorption of enantiopure *(M)*-[7]H molecules on magnetic Co nanoislands

This section represents a follow-up investigation that builds upon the research presented in the previous manuscript in Section 3.2. Two notable challenges in the previous work, served as motivations for the current experiment.

The first challenge emerged from determining the handedness of chiral molecules in racemic mixtures, as it demands tedious high-resolution STM topographic imaging for each molecule. This process is not only time-consuming but also involves the difficult task of modifying and achieving an atomically sharp STM tip, crucial for high-resolution topographic data. Furthermore, despite using high-resolution STM topography, our previous manuscript highlighted that for about 4% (29 out of 748) of the molecules, we were unable to ascertain their handedness.

The second challenge centred around the higher adsorption probability of molecules at the rim area of Co islands compared to the island interior. This issue was extensively discussed in Supplementary Information Section S8 of the aforementioned manuscript. In practice, nearly 90% of the total molecule population adhered to the island rim. Consequently, when examining the enantiospecific adsorption ratio of molecules located in the island interior, we were limited to only 71 molecules, thereby constraining the statistical significance of our findings.

To overcome these challenges, we conducted experiments using enantiopure *(M)*-[7]H molecules. This approach did not require the need for time-consuming single-molecule STM topography and subsequent analysis. As a result, it significantly improved our dataset's statistical power, enabling the measurement and analysis of a substantially larger number of molecules. Consequently, even after subtracting the molecules attached to the island rims, there are still a significant number of molecules on the interior of the islands, which allowed us to conduct a more thorough statistical analysis with substantially reduced error values compared to the data presented in Table S1 of the manuscript in Section 3.2.

Figure 3.1a shows a constant-current topographic STM image of *(M)*-[7]H molecules on the Co/Cu(111) substrate at a low temperature of 5 K, following their deposition at room temperature. The deposition of molecules at low coverage results in the decoration of triangular Co nanoislands with molecules. In contrast, the Cu substrate between the nanoislands remains bare. This aligns with the findings observed when depositing a

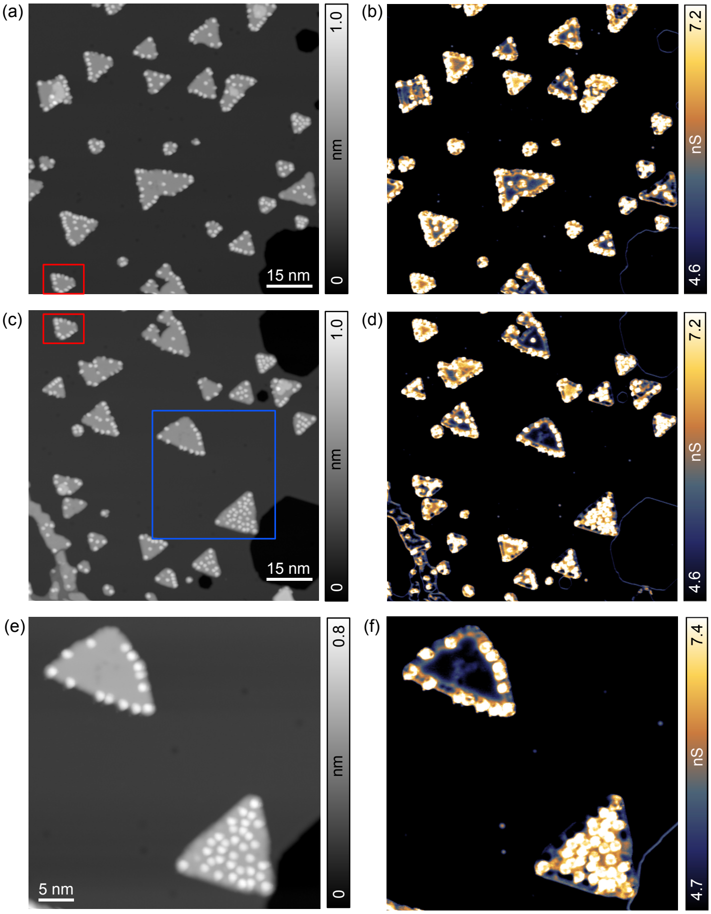

Figure 3.1: (a) and (c), constant-current topographic image of *(M)*-[7]H molecules on Co nanoislands on Cu(111). (b) and (d), Simultaneously with (a) and (c) measured dI/dV maps. The scan area of (c) and (d) is vertically shifted relative to (a) and (b) to enlarge the data set. The red frames in (a) and (c) indicate a common island in the two consecutive scans while a consistent dI/dV contrast of these islands in Figures (b) and (d) demonstrates that the tip's magnetization remained unchanged between these scans ($V_{\mathrm{bias}} = -620\,\mathrm{mV}$, $I_{\mathrm{t}} = 300\,\mathrm{pA}$, $V_{\mathrm{mod}} = 20\,\mathrm{mV}$, $f_{\mathrm{mod}} = 752\,\mathrm{Hz}$, 5 K, Co-functionalized W tip).

racemic mixture of molecules [127–129]. The simultaneously recorded dI/dV map of Figure 3.1a, depicted in Figure 3.1b, reveals magnetic contrast of the Co nanoislands.
In order to expand our examination to include a larger number of islands and molecules, the scan area has been shifted downward (as illustrated in Figure 3.1c). The shift was

selected so that at least one island is common to both images (highlighted by red frames). This procedure enables us to closely monitor and detect any unintentional alterations in tip magnetization alignment between the two consecutive scans. However, the comparison of the island's magnetization in the two subsequent dI/dV maps (Figures 3.1b and d) confirmed the absence of any such changes within this dataset. In this manner, proper magnetization alignment is confidently assigned to the islands within both scan areas, and consequently, the data from these islands can be aggregated, enabling a more extensive analysis.

Figure 3.1e presents high-resolution topographic images of the region outlined by the blue frame in Figure 3.1c. Two islands have been selected that have opposite magnetization directions, i.e., $M_{\downarrow}$ and $M_{\uparrow}$[1]. Notably, there is a significant difference in the number of adsorbed molecules on the two islands, with 14 and 33 adsorbed molecules for islands with $M_{\downarrow}$ and $M_{\uparrow}$, respectively. This indicates a preference for the adsorption of *(M)*-[7]H on islands with $M_{\uparrow}$. To support this observation with better statistics, a series of STM data has been obtained, which is shown as a reconstructed mosaic image in Figure 3.2. To generate this comprehensive overview image, we initially conducted 15 individual STM scans, each comprising both topographical data and the corresponding dI/dV maps. These scans were performed with particular attention to the scan area shifting conditions explained earlier. Throughout the entire data acquisition process, the magnetization alignment of the STM tip remained constant. As a result, the assigned magnetization alignment of the Co nanoislands remains consistent across all the acquired data sets. This consistency enables us to integrate information from all individual scans, significantly enriching our statistical dataset.

In Figure 3.2, each scan area is labeled with a number corresponding to the scan number used to construct this mosaic overview image. Notably, mosaic 1 and mosaic 2 correspond to the STM images shown earlier in Figures 3.1c and a, respectively. The individual topography and corresponding dI/dV maps for mosaic images 3 to 15 are provided in Appendix A.

After thorough analysis of these mosaic images, we determined that the reconstructed overview image comprises a total of 225 islands and 2178 molecules. To conduct a comprehensive analysis, similar to what was previously reported in Table S1 of the manuscript

---

[1] Since the absolute magnetization direction of the STM tip is unknown, a higher or lower dI/dV signal cannot be assigned to the absolute direction of island magnetization M. In order to facilitate analysis, we have adopted an arbitrary assignment: a higher dI/dV signal (indicated by yellow contrast) is designated as representing up magnetization (M pointing to the vacuum; $M_{\uparrow}$), and a lower dI/dV signal (blue contrast) as down magnetization (M pointing to the copper substrate; $M_{\downarrow}$).

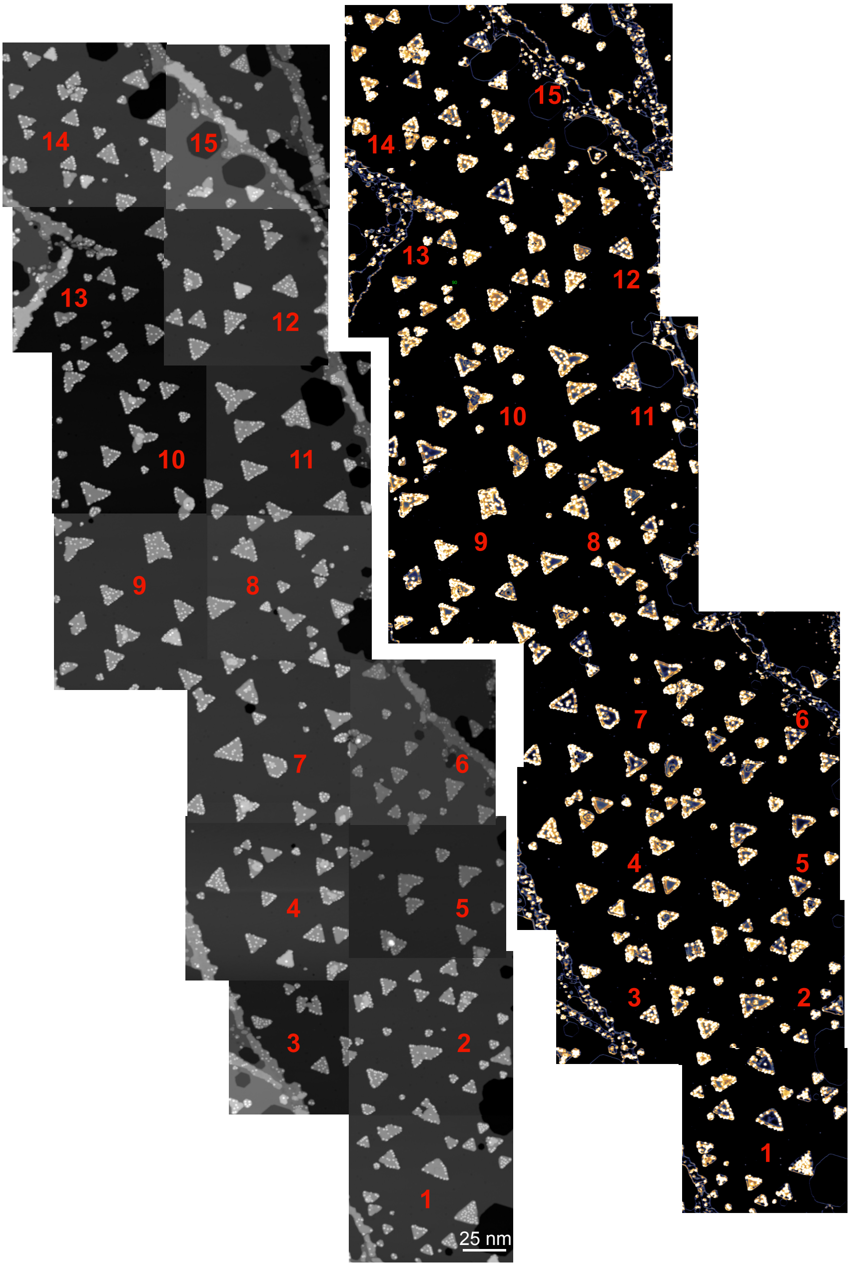

Figure 3.2: Reconstructed overview mosaic image of constant current topographies accompanied by simultaneously recorded dI/dV maps, derived from merging 15 individual scan areas. All the STM data were measured with the following parameters: $V_{\text{bias}} = -620\,\text{mV}$, $I_{\text{t}} = 300\,\text{pA}$, $V_{\text{mod}} = 20\,\text{mV}$, $f_{\text{mod}} = 752\,\text{Hz}$, at a temperature of $5\,\text{K}$, using a Co-functionalized W tip.

presented in Section 3.2, we initially categorized our molecules into two distinct groups. Specifically, N_1 and N_2 represent the number of *(M)*-[7]H molecules on islands with $M_\downarrow$ and $M_\uparrow$ magnetization, respectively. To normalize the molecular population on islands relative to their corresponding areas, we introduced the parameter $\alpha = A(M_\uparrow)/A(M_\downarrow)$, which represents the ratio of the total areas of islands with $M_\uparrow$ and $M_\downarrow$. Subsequently, we calculated the enantiospecific adsorption ratio as $r = \alpha N_1/N_2$, which is presented in the third row of Table 3.1.

Additionally, for each class of molecules, we differentiated between those adhered to the rim of the islands and those located within the bulk area of the islands. We employed appropriate normalization factors based on the calculated areas of the island rim and the island bulk area [2]. Consequently, the first row of Table 3.1 represents the enantiospecific ratio of *(M)*-[7]H molecules, specifically focusing on those attached to the rim of the islands and the second row corresponds to the molecules found within the bulk area of the islands.

Additionally, to accurately assess the energy differences arising from the enantiospecific adsorption of molecules on ferromagnetic OOP Co nanoislands, we have calculated these values using the equation presented below. These calculated energy differences (ΔE)[3] are detailed in the last column of Table 3.1:

$$r = \frac{N_1}{N_2} = \exp\left(-\frac{\Delta E}{k_B T}\right), \tag{3.1}$$

in this equation, k_B represents the Boltzmann constant, and the temperature T is set at 296 K.

In this step, to facilitate an easier comparison of the enantiospecific adsorption ratios and the associated magnetoenantiospecific energy of two samples of molecules (i.e. racemic mixture and enantiopure) adsorbed on Co nanoislands, data similar to that presented in Table 3.1 has been extracted from the manuscript in Section 3.2. The extracted data is now displayed in Table 3.2.

In general, the comparison reveals a close agreement between the total enantiospecific adsorption ratios (r) for enantiopure *(M)*-[7]H molecules on Co nanoislands and those obtained in prior experiments using racemic mixtures. Notably, both sets of experiments

---

[2] For detailed information on how the area of the island bulk and rim are calculated, please refer to Section S8 of the supplementary information provided in the manuscript presented in Section 3.2.

[3] A detailed explanation of the associated energy differences between the two molecular classes, as well as the underlying mechanisms, including the different transition rates between precursor and chemisorbed states due to magnetoenantiospecific binding in the precursor state, has been discussed previously in Section S6 of the manuscript presented in Section 3.2.

Table 3.1: Enantiospecific adsorption of *(M)*-[7]H at rims and centers of Co nanoislands. $\alpha = A_{M_\uparrow}/A_{M_\downarrow}$ is the ratio of the total areas of considered islands with $M_\uparrow$ and $M_\downarrow$, respectively. N_1 and N_2 are the number of molecules adsorbed on islands with $M_\uparrow$ and $M_\downarrow$ magnetization, respectively. The error value of r is calculated according to equation presented in Section S3 of the supplementary information provided in the manuscript presented in Section 3.2.

Location of molecule	$\alpha =$ $A_{M_\uparrow}/A_{M_\downarrow}$	N_1	N_2	$r =$ $\alpha N_1/N_2$	ΔE (meV)
Rim	0.78	956	797	0.93 ± 0.04	1.7 ± 1
Center	0.42	147	278	0.22 ± 0.02	38.6 ± 2
Both	0.66	1103	1075	0.68 ± 0.03	10.0 ± 1

Table 3.2: Enantiospecific adsorption of racemic mixture of [7]H at rims and centers of Co nanoislands. $\alpha = A_{M_\uparrow}/A_{M_\downarrow}$ is the ratio of the total areas of considered islands with $M_\uparrow$ and $M_\downarrow$, respectively. $N_1 = N_{\uparrow\uparrow} + \alpha N_{\downarrow\downarrow}$ and $N_2 = N_{\uparrow\downarrow} + \alpha N_{\downarrow\uparrow}$ are the number of molecules in classes 1 and 2. The error value of r is calculated according to equation presented in Section S3 of the supplementary information provided in the manuscript presented in Section 3.2.

Location of molecule	$\alpha =$ $A_{M_\uparrow}/A_{M_\downarrow}$	$N_1 =$ $N_{\uparrow\uparrow} + \alpha N_{\downarrow\downarrow}$	$N_2 =$ $N_{\uparrow\downarrow} + \alpha N_{\downarrow\uparrow}$	$r =$ N_1/N_2	ΔE (meV)
Rim	0.63	207	289	0.72 ± 0.07	8.4 ± 2
Center	0.41	13	29	0.45 ± 0.15	20.5 ± 8
Both	0.55	207	303	0.68 ± 0.06	10.0 ± 2

yielded consistent r values of 0.68. The follow-up experiment with enantiopure molecules, however, achieved a reduced error margin in r (decreasing from 0.68 ± 0.06 to 0.68 ± 0.03). This enhanced accuracy can be attributed to the nearly threefold increase in the number of molecules assessed during the error calculation for enantiopure molecules.

Interestingly, a closer examination of the enantiomeric excess for molecules at the rim and center (bulk) reveals that the increased statistical sample of enantiopure molecules led to a more distinct differentiation between the two enantiomeric excess values r_{rim} and r_{bulk}. For enantiopure molecules, a significantly stronger r_{bulk} was observed, decreasing from 0.45 ± 0.15 to 0.22 ± 0.02, resulting in an associated energy difference of 38 meV for the adsorption of two *(M)*-[7]H molecules on oppositely magnetized OOP Co nanoislands. Moreover, the value of r_{rim} for enantiopure molecules increased from 0.72 ± 0.07 to 0.93 ± 0.04, approaching unity. This significant increase suggests that enantiospecific adsorption at the rim is considerably weaker compared to the bulk, with the associated magnetoenantiospecific energy difference for two *(M)*-[7]H molecules adsorbed on the rim of oppositely magnetized OOP Co nanoislands being only about 2 meV.

In conclusion, the newly acquired experimental data, in conjunction with the comprehensive analysis detailed in Sections S9 and S10 of the manuscript presented in Section 3.2 , effectively rule out any significant impact of island edges on the observed enantiospecific adsorption of chiral [7]H molecules on the OOP magnetized Co nanoislands. This conclusion is of crucial importance in confirming our understanding of adsorption dynamics and can establish a solid foundation for subsequent theoretical investigations aimed at understanding the underlying mechanisms of the CISS effect, particularly in relation to the enantiomeric separation of chiral molecules interacting with magnetic substrates.

3.4 Manuscript 3: Spin-selective electron transport through single chiral molecules

This section contains the above-named manuscript and its supplementary information. The primary focus of this manuscript is to tackle a fundamental question: Is the CISS effect a result of collective behavior, or can it be attributed to individual molecules?

To address this issue, we have performed single-molecule-level experiments employing the STM technique. This approach enables us to quantitatively measure and compare spin-selective electron transport through distinct chiral molecules, deposited under UHV conditions, directly onto clean and uncoated OOP magnetized ferromagnetic bilayer Co nanoislands on Cu(111).

Our experimental approach incorporates a racemic mixture of chiral molecules, the presence of two opposing OOP substrate magnetizations, and the capability to manipulate the OOP magnetization sensitivity of the STM tip. This strategic arrangement allows us to systematically investigate the impact of the substrate or STM tip magnetization and the chirality of the adsorbed molecules, all at the atomic scale.

Comparing single-molecule spectra obtained from laterally separated enantiomer pairs under consistent conditions and utilizing identical microscopic electrodes (STM tip and Co nanoisland), reveals remarkable magnetochiral conductance asymmetries of up to 50%, even at a low temperature of 5 K. These findings rule out ensemble or cooperative effects, as well as the primary role of electron-phonon coupling (associated with thermal vibrations), which were previously discussed in Section 1.4, to explain the effectiveness of the CISS effect. This experimental evidence obtained through precisely defined molecule and electrode configurations can serve as a crucial benchmark for theoretical simulations and modeling. The manuscript is published in *Small* and available in [129].

Mohammad Reza Safari and Frank Matthes conducted the sample preparations and the STM experiments. Karl-Heinz Ernst synthesized and provided the molecules. Mohammad Reza Safari, Frank Matthes and Daniel E. Bürgler conducted the data analysis. Mohammad Reza Safari wrote the manuscript in close collaboration with Daniel E. Bürgler and Frank Matthes and with contributions from Karl-Heinz Ernst and Claus M. Schneider.

RESEARCH ARTICLE

NANO · MICRO
small
www.small-journal.com

Spin-Selective Electron Transport Through Single Chiral Molecules

Mohammad Reza Safari, Frank Matthes, Claus M. Schneider, Karl-Heinz Ernst,* and Daniel E. Bürgler**

The interplay between chirality and magnetism is a source of fascination among scientists for over a century. In recent years, chirality-induced spin selectivity (CISS) has attracted renewed interest. It is observed that electron transport through layers of homochiral molecules leads to a significant spin polarization of several tens of percent. Despite the abundant experimental evidence gathered through mesoscopic transport measurements, the exact mechanism behind CISS remains elusive. This study reports spin-selective electron transport through single helical aromatic hydrocarbons that are sublimed in vacuo onto ferromagnetic cobalt surfaces and examined with spin-polarized scanning tunneling microscopy (SP-STM) at a temperature of 5 K. Direct comparison of two enantiomers under otherwise identical conditions revealed magnetochiral conductance asymmetries of up to 50% when either the molecular handedness is exchanged or the magnetization direction of the STM tip or Co substrate is reversed. Importantly, the results rule out electron–phonon coupling and ensemble effects as primary mechanisms responsible for CISS.

1. Introduction

A characteristic hallmark of life is the mirror asymmetry at the biomolecular level, the so-called homochirality of its building blocks such as amino acids and sugars. As the origin of this asymmetry of life remains elusive, attempts have been made to relate this observation to fundamental forces in the universe.[1,2] Because electrons from radioactive β-decay are spin-polarized due to parity violation of the weak nuclear force, Vester and Ulbricht pointed out that this fact should cause either direct asymmetric interaction of electrons with chiral matter or asymmetric radiolysis by their bremsstrahlung.[3] While Farago and Kessler have indeed observed spin-polarized electron scattering from chiral molecules in the vapor phase, the observed asymmetries were only of the order of 10^{-4}.[4,5] However, Blum and coworkers calculated enantio-differential scattering of spin-polarized electrons of up to 80% for oriented molecules and proposed experiments with surface-aligned chiral molecules.[6] More recently, asymmetric crystallization induced by polarized electrons and positrons emanating from radioactive sources have been reported.[7]

For ordered helical systems aligned on surfaces, large asymmetries in photo current depending on the sense of circular light polarization have been reported.[8] Spin-selective detection was then used to associate this so-called chirality-induced spin selectivity (CISS) with the state of electron polarization.[9] Opposite spin polarization effects of similar magnitude were also found for molecular monolayers of enantiomers of helical hydrocarbons, so-called helicenes.[10] Among the various methods employed previously to study the CISS effect, spin-dependent electron transport measurements through chiral molecules have

---

M. R. Safari, F. Matthes, C. M. Schneider, D. E. Bürgler
Peter Grünberg Institute
Electronic Properties (PGI-6)
Forschungszentrum Jülich
52425 Jülich, Germany
E-mail: m.safari@fz-juelich.de; d.buergler@fz-juelich.de

M. R. Safari, F. Matthes, C. M. Schneider, D. E. Bürgler
Jülich Aachen Research Alliance (JARA-FIT)
Fundamentals of Future Information Technology, Forschungszentrum Jülich
52425 Jülich, Germany

The ORCID identification number(s) for the author(s) of this article can be found under https://doi.org/10.1002/smll.202308233

DOI: 10.1002/smll.202308233

C. M. Schneider
Fakultät für Physik
Universität Duisburg-Essen
47057 Duisburg, Germany

K.-H. Ernst
Molecular Surface Science Group, Empa
Swiss Federal Laboratories for Materials Science and Technology
8600 Dübendorf, Switzerland
E-mail: karl-heinz.ernst@empa.ch

K.-H. Ernst
Nanosurf Laboratory, Institute of Physics
The Czech Academy of Sciences
16200 Prague, Czech Republic

K.-H. Ernst
Institut für Chemie
Universität Zürich
8057 Zürich, Switzerland

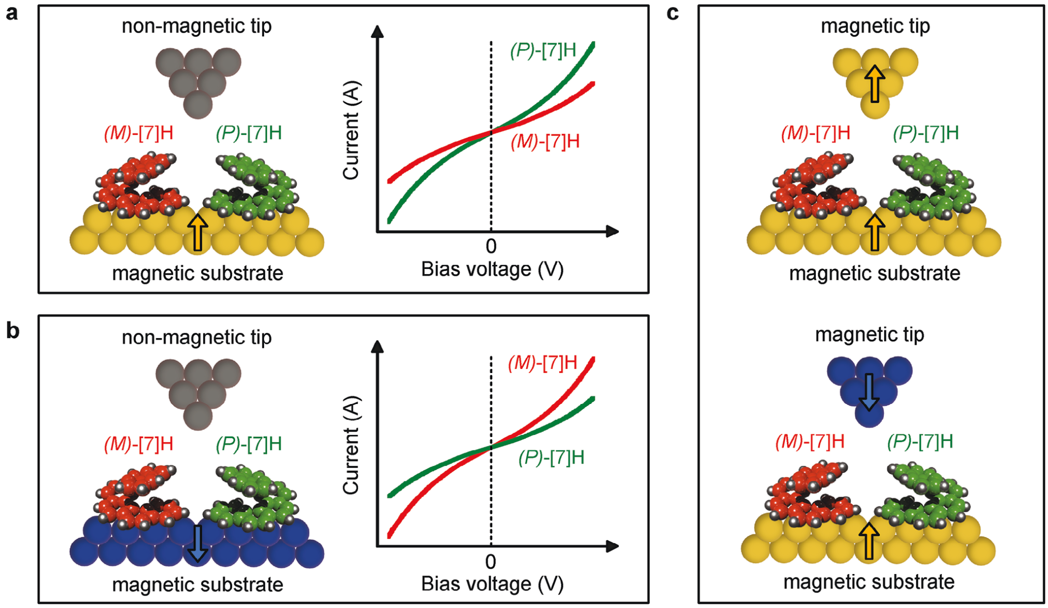

Figure 1. Evaluation of magnetochiral electron tunneling asymmetries with SP-STM. a) On a ferromagnetic surface with out-of-plane magnetization, magnetochiral tunneling will show different conductance for the enantiomers, here *(M)*-[7]H and *(P)*-[7]H. b) The effect will reverse on a surface with opposite out-of-plane magnetization direction. c) For STM conductance measurements on a ferromagnetic surface with a magnetic STM tip, the conductance of the enantiomers will switch when the tip magnetization is reversed.

often been applied. In magnetoresistance devices, the magnetic reference electrode is thereby replaced by a monolayer of homochiral molecules in order to measure the spin-dependent molecular conductance (resistance).[11–22] In many cases, such devices have been realized with the tips of scanning probe microscopes (STM and AFM), still contacting an ensemble of molecules with the uncertainty of a defined contact. In addition, break junctions have been employed.[23–25] However, all contact-based transport studies suffer from poor reproducibility in forming identical single-molecule junctions. Another limitation of these experimental approaches is the inability to study both enantiomers in direct comparison, as separate fabrication of the junctions is required, leading to non-identical experimental conditions. Finally, molecular deposition under ambient conditions leaves the exact adsorption geometry unknown, but it is imperative for theoretical modeling and simulation of the experimental results.

In this study, the aforementioned shortcomings are circumvented by performing spin-polarized scanning tunneling microscopy and spectroscopy (SP-STM/STS) measurements on single chiral heptahelicene ([7]H) molecules sublimed in vacuo from a racemic mixture onto single-crystalline cobalt bilayer nanoislands on a Cu(111) surface. Submolecular resolution of SP-STM/STS allows examination of spin selectivity of individual enantiomers under well-defined conditions. This single-molecule approach represents a major advance over previous studies, as it allows to distinguish the handedness of molecules adsorbed on a substrate with a given magnetization. Hence, the conductance of enantiomers can be compared while the electrodes (same Co island and same STM tip) remain unchanged. The direct measurement of the tunneling current through single enantiomer molecules on the same Co nanoisland yields magnetochiral conductance asymmetries of up to 50%.

2. Results and Discussion

Magnetochiral asymmetries in electron tunneling are expected, for example for enantiomers on a surface with uniform out-of-plane magnetization. **Figure 1** presents principle approaches for identifying magnetochiral asymmetries with SP-STM/STS. Using a non-magnetic STM tip, enantiomers will show different conductances on an out-of-plane magnetized ferromagnetic surface (Figure 1a). In order to quantify differences between the current-voltage ($I - V$) curves of different enantiomers, the so-called magnetochiral conductance asymmetry (MChA) is here defined as

$$\mathrm{MChA} = \frac{I_{(\mathrm{P})} - I_{(\mathrm{M})}}{I_{(\mathrm{P})} + I_{(\mathrm{M})}} \tag{1}$$

where $I_{(\mathrm{P})}$ and $I_{(\mathrm{M})}$ represent the tunneling current passing through the *(P)*- and *(M)*-[7]H molecule, respectively. If the measurement is repeated on a surface with opposite out-of-plane magnetization direction, the $I - V$ curves of the enantiomers

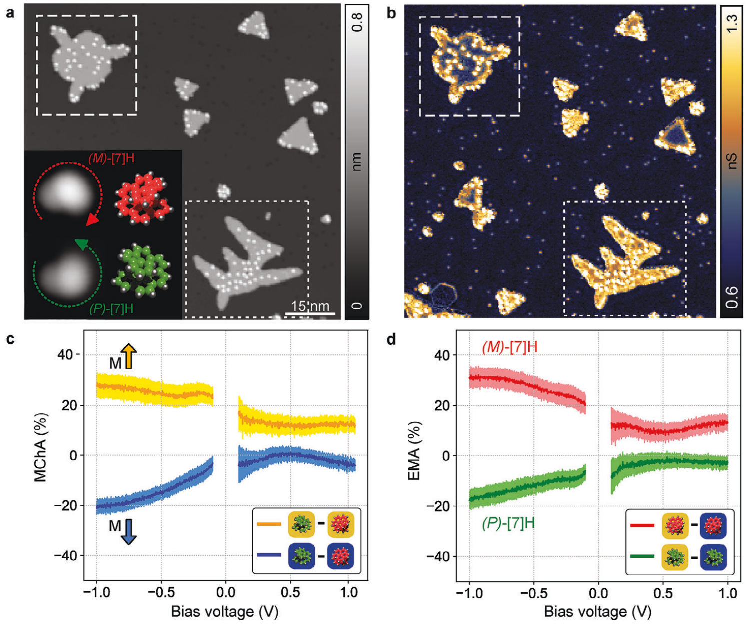

Figure 2. Magnetochiral tunneling conductance asymmetries. a) Constant-current topographic STM image showing adsorbed [7]H molecules that are exclusively attached to the Co nanoislands. The inset shows high-resolution topographic images of the enantiomers. The determined handedness of the *(P)*- and *(M)*-[7]H enantiomer is indicated by a green and red circular arrow, respectively. b) The dI/dV map recorded simultaneously with (a) reveals magnetic contrast between Co nanoislands with opposite out-of-plane magnetization directions, here displayed by blue and yellowish false colors ($V_{\mathrm{bias}} = -600$ mV, $I_t = 550$ pA, $V_{\mathrm{mod}} = 20$ mV, $f_{\mathrm{mod}} = 752$ Hz, 5 K, Co-functionalized W tip). c,d) Magnetochiral asymmetry MChA and enantiospecific magnetic asymmetry EMA curves of [7]H enantiomers calculated according to Equations (1) and (2), respectively, from $I - V$ curves measured with a non-magnetic tip. The dark lines display the calculated values, and the light colored areas represent the standard error resulting from averaging the $I - V$ curves of five molecules. The values near $V_{\mathrm{bias}} = 0$ diverge due to division by small values and have been masked out.

will interchange (Figure 1b). In order to quantify the differences between the $I - V$ curves measured on oppositely magnetized surfaces, the enantiospecific magnetic conductance asymmetry (EMA) is here defined as

$$\mathrm{EMA} = \frac{I_{\mathrm{up}} - I_{\mathrm{down}}}{I_{\mathrm{up}} + I_{\mathrm{down}}} \tag{2}$$

where I_{up} and I_{down} correspond to the measured tunneling current through molecules of identical absolute handedness but adsorbed on surfaces with opposite out-of-plane magnetization. Another way of identifying magnetochiral asymmetries is using oppositely magnetized ferromagnetic STM tips plus evaluating $I - V$ curves of enantiomeric pairs on a surface with fixed magnetization direction (Figure 1c). This method does not require measurements on different surfaces and avoids averaging of $I - V$ curves of different molecules. Again, the two enantiomers on a single magnetic domain should show different conductances solely based on exchanging the absolute handedness of adsorbed molecules.

An ideal ferromagnetic surface system for such studies is the Co/Cu(111) surface. Triangular Co bilayer nanoislands are formed by in situ sublimation of a sub-monolayer of Co onto a pre-cleaned (111) surface of a Cu single crystal. The formation process, atomic structure, electronic properties, and magnetic characteristics are well established.[26–30] It has been previously reported that the controlled deposition of organic molecules on the surface of these highly reactive ferromagnetic nanoislands does not impair the magnetization of the underlying substrate.[31–33] By using a Co-functionalized tip, the different out-of-plane magnetization directions of the Co-nanoislands (i.e., pointing into vacuum or substrate) can be determined.

Figure 2a shows a constant-current topographic STM image of [7]H chiral molecules taken with a Co-functionalized STM tip (see Section S1, Supporting Information). The molecules were sublimed at 400 K from a racemic mixture under ultra-high vacuum (UHV) conditions onto a Cu(111) crystal covered by about 10% with previously formed Co nanoislands. During [7]H deposition, the substrate was at room temperature (RT), and the deposited amount of [7]H molecules corresponds to less than 2% of a close-packed monolayer (ML) on Cu(111). The Co nanoislands are decorated with [7]H molecules, while the Cu surface in between the islands remains bare. This is due to a high surface mobility of the molecules upon adsorption at RT and the stronger binding of [7]H to Co than to Cu.[32,33] The preferential adsorption of molecules at the island rims is due to electronic rim states[28] and was discussed in detail in a previous report.[33] In the present work, all single-molecule transport measurements (e.g., $I-V$ curves) were performed on [7]H molecules that are chemisorbed in the central region of the Co nanoislands and are not affected by island edges and rim states. Moreover, all investigated molecules exhibited one of the three symmetry-equivalent and degenerate in-plane adsorption orientations, reflecting adsorption in a unique and well-defined binding configuration to the Co(111) lattice.[32]

Figure 2b shows the differential conductance (dI/dV) map recorded simultaneously with the topographic image in Figure 2a (see Section S1, Supporting Information). The different dI/dV signal of the islands arises from opposite magnetization directions of the out-of-plane magnetized islands[28,30] and hence confirms that the islands are ferromagnetic even in the presence of chemisorbed [7]H molecules.[31,33,34] The dashed and dotted framed areas in Figures 2a,b indicate two Co islands that are oppositely magnetized. High-resolution constant-current topography images of each selected island reveal the chirality of the adsorbed molecules. The inset in Figure 2a illustrates an example of two adsorbed enantiomers on the island with dark dI/dV contrast. The resolved submolecular structure can be attributed to the topographic profile of the [7]H molecules, which adsorb with their helical axis basically perpendicular to the surface. The handedness of the molecules is reflected in the sense of rotation of the screw-like increasing height variations, as indicated by red and green circular arrows for *(M)*-[7]H and *(P)*-[7]H enantiomers, respectively.[32,33]

After identification of islands with opposite out-of-plane magnetization with a Co-functionalized tip, the tip was remodified with copper such that no longer any magnetic contrast has been observed (see Section S2, Supporting Information). With this non-magnetic tip, $I-V$ curves from ten molecules (five *(P)*- and five *(M)*-[7]H enantiomers) on each of the framed islands in Figure 2a were measured (for measurement procedure see Section S1, Supporting Information). $I-V$ curves of single molecules and averaged $I-V$ curves are shown in Section S3 (Supporting Information). The magnetochiral conductance asymmetries (MChA, as defined in Equation (1)) between enantiomers on identical islands (i.e., with identical magnetization) is plotted in Figure 2c as a function of applied bias voltage. The enantiospecific magnetic conductance asymmetries (EMA, as defined in Equation (2)) for *(P)*- and *(M)*-[7]H molecules on oppositely magnetized Co island (i.e., islands with bright and dark magnetic dI/dV contrast) are plotted in Figure 2d. For both evaluation methods clear asymmetries are observed. Both pairs of curves are significantly separated from each other by more than the standard errors, which clearly confirms the CISS effect at the single-molecule level. Previous conclusions based on ensemble effects at work in CISS are therefore questionable.[22,35] Interestingly, the qualitative similarities between MChA and EMA curves suggest that exchanging the chirality of the molecules (Figure 2c) or reversing the magnetization of the substrate (Figure 2d) produce similar effects on the conductance measurements.

To avoid the required averaging of $I-V$ curves over different molecules and in order to reveal true single-molecular properties, $I-V$ curves of a single pair of enantiomers adsorbed on a single Co nanoisland with a fixed magnetization direction have been acquired. **Figure 3**a shows the $I-V$ curves for two enantiomers recorded with a magnetized tip. The dark red and green lines represent here the $I-V$ curves of one enantiomer each, and the light colored areas indicate the standard error of the single-molecule $I-V$ curves (see Section S1, Supporting Information). Under these conditions, the *(M)*-[7]H enantiomer (red curve) shows the larger conductance. In particular for negative bias voltages, meaning that electrons tunnel from the occupied states of the sample into the unoccupied states of the tip, a distinct difference is observed. Such $I-V$ asymmetry for the enantiomers switches if the tip magnetization is reversed (Figure 3b). The reversal of the tip magnetization upon re-functionalization above a remote Co island is verified by the dI/dV maps presented in Section S4 (Supporting Information), which show opposite magnetic contrast.

The respective magnetochiral asymmetry MChA and enantiospecific magnetic asymmetry EMA curves evaluated from the $I-V$ curves are displayed in Figure 3c,d. Here, I_{up} and I_{down} in Equation (2) refer to the current measured for the different directions of the tip magnetization of the first and second tip configuration, respectively. The different shapes and magnitudes of the MChA and EMA curves are most likely due to structural and electronic differences of the STM tip induced by the re-functionalization. Such changes strongly affect the EMA curves, for which $I-V$ curves taken with different tip configurations are subtracted from each other (Equation (2)). The MChA curves, on the contrary, are each calculated from two single-molecule $I-V$ curves taken with the same tip configuration (Equation (1)), so the structural and electronic changes of the tip do not play a role. Remarkably, both pairs of curves are separated by more than the standard errors, clearly demonstrating CISS as a property of a single molecule. As expected for CISS, experiments in which either surface (Figure 2) or tip (Figure 3) magnetization was reversed lead to an effect similar to that of changing molecular handedness.

A final proof of single-molecule magnetochiral asymmetry comes from an experimental procedure in which the constant-height STM mode of operation (see Section S1, Supporting Information) is used to map current variations directly across a single pair of enantiomers, while all other conditions (tip structure, tip height, tip and island magnetization directions, etc.) are kept identical. A topographic constant-current STM image of the pair of enantiomers adsorbed on a Co nanoisland is shown in **Figure 4**a. The absolute handedness of the molecules, as identified by their intramolecular topographic STM contrast profiles, is indicated. The corresponding single-molecule $I-V$ curves are displayed in Figure 4b. For the given magnetization direction of this Co island, the *(P)*-[7]H enantiomer exhibits a larger conductance than the *(M)*-[7]H enantiomer under such identical experimental conditions. Figure 4c,d show constant-height STM images at +1 V and -1 V bias voltage, respectively, with the current intensity displayed by brightness. The STM tip is scanned across the sample with deactivated feedback loop at a constant distance from the Co surface, and the tunneling current is recorded as a function of lateral position (see Section S1, Supporting Information). From the brightness contrast for both enantiomers in both images, it becomes clear that the enantiomers

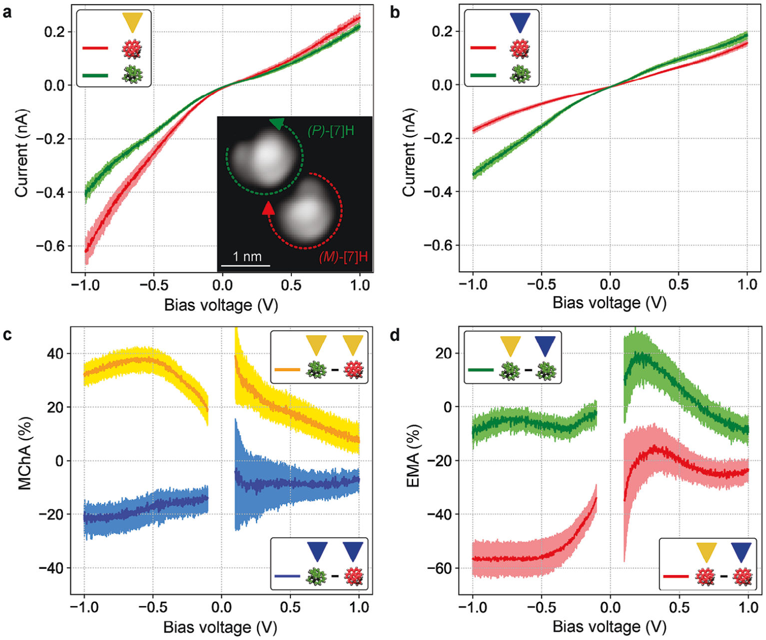

Figure 3. Magnetochiral asymmetries with a magnetic STM tip. a) $I - V$ curves acquired for both [7]H enantiomers using a first magnetization direction of the STM tip ($V_{\mathrm{stab}} = 2$ V and $I_{\mathrm{stab}} = 800$ pA). The inset shows a high-resolution topographic image of the [7]H enantiomer pair with the determined handedness of the molecules indicated by green and red circular arrows, respectively ($V_{\mathrm{bias}} = 100$ mV, $I_{\mathrm{t}} = 100$ pA, 5 K, Co-functionalized W tip). b) Same as (a), but utilizing a second magnetic tip configuration with reversed magnetization direction. c,d) Magnetochiral asymmetry (MChA) and magnetic asymmetry (EMA) curves of the [7]H enantiomers according to Equations (1) and (2), respectively. The dark lines display the calculated values in percent, and the light colored areas represent the propagated error resulting from the standard errors of the two involved single-molecule $I - V$ curves.

exhibit different conductance, regardless of the exact lateral tip position on the molecules. In order to quantitatively compare the current through the two enantiomers, line profiles across the molecules (along red and green dashed lines in Figure 4c,d) are plotted in Figure 4e,f. The larger amplitudes of the tunneling currents above the *(P)*-[7]H give unequivocal evidence that this enantiomer exhibits a larger conductance than the *(M)*-[7]H enantiomer. The MChA (Equation (1)) in the current peaks in Figure 4e,f amounts to 9% and 48%, respectively.

The presented experimental results are based on individual enantiomers that are laterally separated by a few nanometers. The observed magnetochiral asymmetries are thus unequivocal evidence that CISS is a single-molecule property. Previously proposed mechanisms based on intermolecular interactions[35] or cooperative effects[22] are not needed for explaining CISS effects. All $I - V$ measurements are carried out in the tunneling mode with a vacuum gap between tip and molecule that guarantees small perturbation of the molecule-substrate system by the tip. This was multiply confirmed by the good agreement between experimental STM images and theoretical simulations in the framework of the Tersoff-Hamann approximation,[36] in particular also for the here studied [7]H – 2 ML Co/Cu(111) system.[33] Furthermore, the size of the measurement spot is given by the overlap of the tip and sample wave functions, which decreases exponentially in the lateral direction on a length scale of Angstroms, resulting also in the high lateral resolution of STM. Thus, in contrast to contact-based transport studies, uncertainties of contact formation, averaging over large contact areas, and molecular deformation due to force interaction with the tip do not play a role.

We emphasize that here the CISS effect was observed at 5 K. The asymmetry values of up to about 50% are similar those measured at RT for cationic [4]helicenes on HOPG by conducting-probe AFM and using a magnetic Ni tip.[16] In contrast, only 6 to 8% spin polarization of photoelectrons was observed after transmission through a ML of enantiopure [7]H molecules on Cu(332), Ag(110), and Au(111).[10] However, these experiments employed photoelectrons travelling 1.18 eV above the vacuum level, whereas the $I - V$ measurements presented here cover electronic states within ±1 eV around the Fermi energy. Despite the challenge in comparing conductance asymmetry and polarization values of different molecule-substrate systems and complementary measurement techniques, our low-temperature data suggest that thermal enhancement mechanisms[37] are not essential ingredients for CISS.

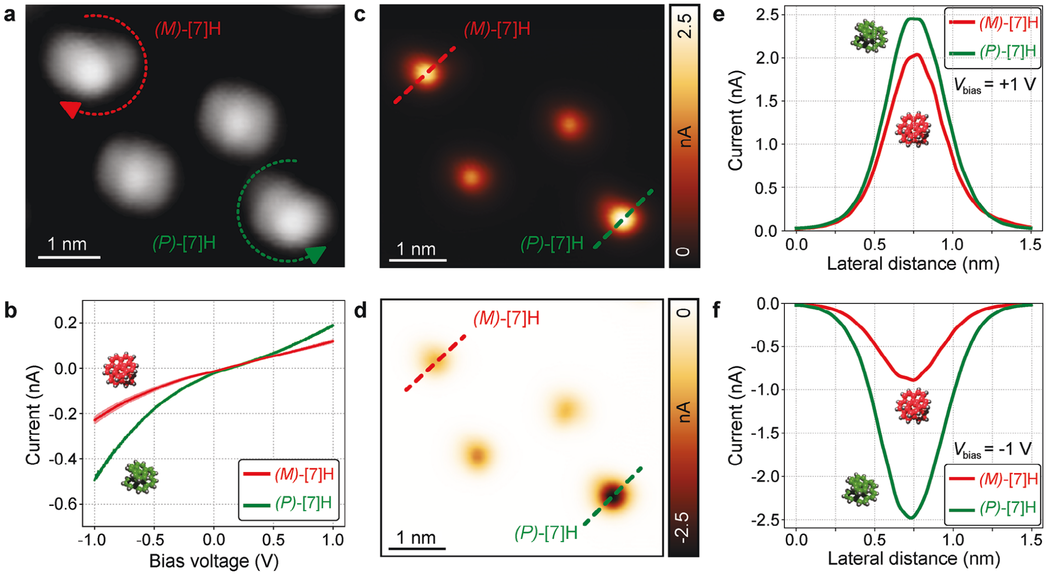

Figure 4. CISS for a single pair of [7]H enantiomers. a) High-resolution topographic image of a pair of enantiomers with the handedness indicated by circular arrows. The handedness of the two molecules in the middle could not be determined ($V_{bias} = -1$ V, $I_t = 1$ nA, 5 K). b) $I - V$ curves of two the [7]H enantiomers in a) ($V_{stab} = 2$ V and $I_{stab} = 500$ pA). The light green and red colored areas indicate the standard error of the single-molecule $I - V$ curves. c,d) Constant-height STM images (5 K, Co-functionalized W tip) acquired in the same area as shown in (a) with $V_{bias} = 1$ V ($\Delta z_0 = 0.20$ nm) and $V_{bias} = -1$ V ($\Delta z_0 = 0.15$ nm), respectively. Dashed lines indicate the positions of the line profiles across the two enantiomers shown in (e,f).

3. Conclusion

Sizable CISS effects in electron transport through helical hydrocarbon molecules chemisorbed to ferromagnetic Co nanoislands have been observed microscopically under well-defined conditions in ultrahigh vacuum at the single-molecule level by spin-polarized STM. The minimum setup for detecting these CISS effects comprises a single pair of enantiomers adsorbed on an out-of-plane magnetized Co nanoisland and imaged quasi-simultaneously with the same STM tip. Even at 5 K, magnetochiral asymmetries in electrical conductance are of the order of 50%. Therefore, coupling of electrons to phonons (thermal vibrations) and ensemble effects due to intermolecular interaction can be ruled out as primary mechanisms of CISS. The well-defined experimental conditions, including the specific adsorption geometry and weak coupling to the STM tip render the presented experiments amenable to theoretical modeling and simulation.

Supporting Information

Supporting Information is available from the Wiley Online Library or from the author.

Acknowledgements

Open access funding enabled and organized by Projekt DEAL.

Conflict of Interest

The authors declare no conflict of interest.

Data Availability Statement

The data that support the findings of this study are available from the corresponding author upon reasonable request.

Keywords

chirality, CISS effect, ferromagnetic substrate, scanning probe microscopy, single-molecule studies

Received: September 19, 2023
Revised: October 30, 2023

---

[1] L. Pasteur, *Œuvres de Pasteur*, Vol. *1*, Recherches sur la dissymétrie moléculaire des produits organiques naturels, Masson et Cie, Paris **1922**, pp. 329.
[2] W. A. Bonner, *Origins Life Evol. Biosphere* **1995**, *25*, 175.
[3] T. Ulbricht, F. Vester, *Tetrahedron* **1962**, *18*, 629.
[4] D. Campbell, P. Farago, *Nature* **1985**, *318*, 52.
[5] S. Mayer, C. Nolting, J. Kessler, *J. Phys. B: At. Mol. Opt. Phys.* **1996**, *29*, 3497.
[6] A. Busalla, M. Musigmann, K. Blum, D. Thompson, *Complete Scattering Experiments*, Differential Cross Section and Spin Asymmetries

for Collisions Between Electrons and Oriented Chiral Molecules, Springer, Boston, MA **2002**, pp. 93–109.
[7] S. Mahurin, M. McGinnis, J. S. Bogard, L. D. Hulett, R. M. Pagni, R. N. Compton, *Chirality* **2001**, *13*, 636.
[8] K. Ray, S. P. Ananthavel, D. H. Waldeck, R. Naaman, *Science* **1999**, *283*, 814.
[9] B. Göhler, V. Hamelbeck, T. Z. Markus, M. Kettner, G. F. Hanne, Z. Vager, R. Naaman, H. Zacharias, *Science* **2011**, *331*, 894.
[10] M. Kettner, V. V. Maslyuk, D. Nürenberg, J. Seibel, R. Gutierrez, G. Cuniberti, K. H. Ernst, H. Zacharias, *J. Phys. Chem. Lett.* **2018**, *9*, 2025.
[11] Z. Xie, T. Z. Markus, S. R. Cohen, Z. Vager, R. Gutierrez, R. Naaman, *Nano Lett.* **2011**, *11*, 4652.
[12] S. P. Mathew, P. C. Mondal, H. Moshe, Y. Mastai, R. Naaman, *Appl. Phys. Lett.* **2014**, *105*, 242408.
[13] M. Kettner, B. Göhler, H. Zacharias, D. Mishra, V. Kiran, R. Naaman, C. Fontanesi, D. H. Waldeck, S. Sek, J. Pawowski, J. Juhaniewicz, *J. Phys. Chem. C* **2015**, *119*, 14542.
[14] P. C. Mondal, N. Kantor-Uriel, S. P. Mathew, F. Tassinari, C. Fontanesi, R. Naaman, *Adv. Mater.* **2015**, *27*, 1924.
[15] B. P. Bloom, V. Kiran, V. Varade, R. Naaman, D. H. Waldeck, *Nano Lett.* **2016**, *16*, 4583.
[16] V. Kiran, S. P. Mathew, S. R. Cohen, I. H. Delgado, J. Lacour, R. Naaman, *Adv. Mater.* **2016**, *28*, 1957.
[17] V. Kiran, S. R. Cohen, R. Naaman, *J. Chem. Phys.* **2017**, *146*, 092302.
[18] V. Varade, T. Markus, K. Vankayala, N. Friedman, M. Sheves, D. H. Waldeck, R. Naaman, *Phys. Chem. Chem. Phys.* **2018**, *20*, 1091.
[19] F. Tassinari, D. R. Jayarathna, N. Kantor-Uriel, K. L. Davis, V. Varade, C. Achim, R. Naaman, *Adv. Mater.* **2018**, *30*, 1706423.
[20] G. Bullard, F. Tassinari, C. H. Ko, A. K. Mondal, R. Wang, S. Mishra, R. Naaman, M. J. Therien, *J. Am. Chem. Soc.* **2019**, *141*, 14707.
[21] C. Kulkarni, A. K. Mondal, T. K. Das, G. Grinbom, F. Tassinari, M. F. Mabesoone, E. Meijer, R. Naaman, *Adv. Mater.* **2020**, *32*, 1904965.
[22] T. N. H. Nguyen, L. Rasabathina, O. Hellwig, A. Sharma, G. Salvan, S. Yochelis, Y. Paltiel, L. T. Baczewski, C. Tegenkamp, *ACS Appl. Mater. Interfaces* **2022**, *14*, 38013.
[23] A. C. Aragonès, E. Medina, M. Ferrer-Huerta, N. Gimeno, M. Teixidó, J. L. Palma, N. Tao, J. M. Ugalde, E. Giralt, I. Díez-Pérez, V. Mujica, *Small* **2017**, *13*, 1602519.
[24] D. Slawig, T. N. H. Nguyen, S. Yochelis, Y. Paltiel, C. Tegenkamp, *Phys. Rev. B* **2020**, *102*, 115425.
[25] C. Yang, Y. Li, S. Zhou, Y. Guo, C. Jia, Z. Liu, K. N. Houk, Y. Dubi, X. Guo, *Nat. Chem.* **2023**, *15*, 972.
[26] J. De La Figuera, J. E. Prieto, C. Ocal, R. Miranda, *Phys. Rev. B* **1993**, *47*, 13043.
[27] O. Pietzsch, A. Kubetzka, M. Bode, R. Wiesendanger, *Phys. Rev. Lett.* **2004**, *92*, 057202.
[28] O. Pietzsch, S. Okatov, A. Kubetzka, M. Bode, S. Heinze, A. Lichtenstein, R. Wiesendanger, *Phys. Rev. Lett.* **2006**, *96*, 237203.
[29] N. N. Negulyaev, V. S. Stepanyuk, P. Bruno, L. Diekhöner, P. Wahl, K. Kern, *Phys. Rev. B* **2008**, *77*, 125437.
[30] H. Oka, P. A. Ignatiev, S. Wedekind, G. Rodary, L. Niebergall, V. S. Stepanyuk, D. Sander, J. Kirschner, *Science* **2010**, *327*, 843.
[31] T. Esat, R. Friedrich, F. Matthes, V. Caciuc, N. Atodiresei, S. Blügel, D. E. Bürgler, F. S. Tautz, C. M. Schneider, *Phys. Rev. B* **2017**, *95*, 094409.
[32] M. R. Safari, F. Matthes, K.-H. Ernst, D. E. Bürgler, C. M. Schneider, *Nanomaterials* **2022**, *12*, 3281.
[33] M. R. Safari, F. Matthes, V. Caciuc, N. Atodiresei, C. M. Schneider, K.-H. Ernst, D. E. Bürgler, *Adv. Mater.* **2023**, 202308666, https://doi.org/10.1002/adma.202308666.
[34] M. Metzelaars, S. Schleicher, T. Hattori, B. Borca, F. Matthes, S. Sanz, D. E. Bürgler, J. Rawson, C. M. Schneider, P. Kögerler, *Chem. Sci.* **2021**, *12*, 8430.
[35] A. Dianat, R. Gutierrez, H. Alpern, V. Mujica, A. Ziv, S. Yochelis, O. Millo, Y. Paltiel, G. Cuniberti, *Nano Lett.* **2020**, *20*, 7077.
[36] J. Tersoff, D. R. Hamann, *Phys. Rev. Lett.* **1983**, *50*, 1998.
[37] T. K. Das, F. Tassinari, R. Naaman, J. Fransson, *J. Phys. Chem. C* **2022**, *126*, 3257.

NANO · MICRO
small

Supporting Information

for *Small*, DOI 10.1002/smll.202308233

Spin-Selective Electron Transport Through Single Chiral Molecules

Mohammad Reza Safari, Frank Matthes, Claus M. Schneider, Karl-Heinz Ernst* and Daniel E. Bürgler**

Supporting Information

Spin-Selective Electron Transport Through Single Chiral Molecules

M.R. Safari, F. Matthes, C.M. Schneider, K.-H. Ernst*, D.E. Bürgler**

CONTENTS

S1. Experimental Procedures S3
  A. Molecule Synthesis S3
  B. Sample Preparation S3
  C. STM/STS Measurements S3

S2. Magnetic Sensitivity of the STM Tip S6

S3. Single-Molecule $I-V$ Curves S7

S4. Reversing the Magnetization Direction of the STM Tip S9

References S10

S1. EXPERIMENTAL PROCEDURES

All measurements were carried out in a multi-chamber UHV system with a base pressure of $< 10^{-8}$ Pa comprising a substrate preparation and analysis chamber, a distinct chamber for the controlled deposition of molecules, and a low-temperature scanning tunneling microscope (LT-STM from Omicron Scienta) operating at a temperature of 5 K.

A. Molecule Synthesis

The synthesis of racemic mixtures of heptahelicene molecules was performed using a stilbene precursor through the process of photocyclization as described previously [1].

B. Sample Preparation

The fabrication of the Co/Cu(111) substrate involved several steps. The surface of the Cu crystal was first cleaned by repeated cycles of Ar^+ sputtering ($p_{\mathrm{Ar}} = 5 \times 10^{-4}$ Pa, 30 min) followed by annealing (850 K, 60 min) to ensure an atomically clean surface. Co bilayer nanoislands were then grown on the surface by in-situ Co deposition at RT using e-beam evaporation from a 99.99% pure Co rod. The deposition rate was 0.2 ML/min and the pressure during deposition was less than 2×10^{-8} Pa. The characteristics of the Co bilayer islands, including their shape, density, and cleanliness, were verified by means of topographic STM images. In addition, spin-polarized STM measurements were conducted to confirm the presence of well-defined out-of-plane magnetization of the islands. The substrate was subsequently transferred to a separate chamber for molecular deposition. A racemic powder of [7]H molecules was sublimed from a glass crucible heated to a temperature of 400 K, and the substrate was exposed to the molecular vapor for a duration of less than one minute [2]. The sample was then immediately transferred to the STM chamber without vacuum break and cooled to 5 K for subsequent STM measurements under a pressure of 10^{-9} Pa.

C. STM/STS Measurements

For STM/STS measurements, electrochemically etched polycrystalline tungsten (W) tips were used. If needed, short bias pulses were applied to achieve high spatial resolution. To obtain magnetic contrast, the W tip is functionalized by bringing it into and out of mechanical contact with a remote Co nanoisland at enhanced bias voltage to transfer Co atoms from the island to the tip apex. This functionalization procedure was performed repeatedly until a dI/dV map was obtained that showed magnetic contrast on Co nanoislands, which served as confirmation of the tip's capability to detect spin polarization of the tunneling current in the direction perpendicular to the substrate.

Four different modes of STM operation are used to address structural, electronic, magnetic, and transport properties of the samples: (i) In constant-current mode, the tip follows an isosurface of the integrated local density of states (LDOS) above the surface. A bias voltage V_{bias} was applied to the sample, and the height corrections made by the STM feedback loop to regulate the tunneling current to the constant setpoint current I_{t} were recorded while scanning the surface point-by-point. The recorded data can be interpreted as the topography of the sample. (ii) Differential conductance (dI/dV) maps were obtained simultaneously with a constant-current topographic image, i.e., with the feedback loop closed. To extract the dI/dV signal, the DC bias voltage V_{bias} is superimposed with a small sinusoidal modulation with an rms amplitude of $V_{\text{mod}} = 20\,\text{mV}$ and a frequency of $f_{\text{mod}} = 752\,\text{Hz}$. The resulting modulation of the tunneling current at f_{mod} is detected with a lock-in amplifier and recorded as a function of the lateral tip position during a scan in a second data channel. dI/dV maps represent to a good approximation the spatial variations of the LDOS above the sample at the energy given by eV_{bias}, where $V_{\text{bias}} = 0$ corresponds to the Fermi energy. (iii) For constant-height STM images, the feedback loop was deactivated and the STM tip was scanned over the sample surface at a fixed height z_{Co} above the Co surface. The tunneling current flowing due to the applied bias voltage V_{bias} is recorded as a function of lateral tip position. Setting and keeping constant z_{Co} with the feedback loop disabled is critical for this type of measurement, since a change of the tip-surface distance by one Ångström leads to a variation of the tunneling current by about one order of magnitude [3]. Therefore, the inclination of the Co surface is first determined from a constant-current image and then used to align the scanning plane of the constant-height measurement coplanar with the Co surface. The height z_{Co} for a constant-height measurement is set by the bias voltage V_{bias} and setpoint current I_{t} applied before switching off the feedback loop and the subsequent retraction of the tip by Δz_0. The latter is needed to keep the current amplitude within the range of the pre-amplifier (1 pA to 3.3 nA) throughout the constant-height scan.

(iv) For current-voltage ($I - V$) curves, the tip is moved to the sample spot of interest and the vertical position is stabilized by applying $V_{\mathrm{stab}} = 2\,\mathrm{V}$ with the activated feedback loop regulating the tunneling current to the setpoint current $I_{\mathrm{stab}} = 800\,\mathrm{pA}$ for Figures 2 and 3 of the main text and $I_{\mathrm{stab}} = 500\,\mathrm{pA}$ for Figure 4 of the main text. Then, the feedback loop is deactivated, i.e., the tip height is fixed, and the V_{bias} is swept in the range from -1 to $+1\,V$ and the resulting tunneling current is recorded. The bias sweep is repeated five times to improve the signal-to-noise ratio. The standard error of this averaging is displayed as light colored area in Figures 3a,b and 4b of the main text and is used to calculate the errors of the asymmetries MChA and EMA in Figures 3c and d of the main text. An $I - V$ curve obtained in this manner represents, to a good approximation, the energy-dependent integrated LDOS at the fixed position of the tip above the sample surface, where $V_{\mathrm{bias}} = 0$ corresponds to the Fermi energy.

S2. MAGNETIC SENSITIVITY OF THE STM TIP

Supporting Figure S1a shows a dI/dV map with an extended scanning area that includes the scan area shown in Figures 2b. This dI/dV map was obtained using a Co-functionalized STM tip, which has out-of-plane magnetic sensitivity. This sensitivity is highlighted by the different dI/dV contrast of the two Co islands framed by dashed and dotted rectangles, which is due to their opposite out-of-plane magnetizations. To eliminate the out-of-plane magnetic sensitivity of the tip, it was re-functionalized over a remote bare Cu area by removing the Co atoms from the apex of the W tip. A subsequent dI/dV map measured with the newly Cu-functionalized tip but otherwise identical scanning parameters as in Supporting Figure S1a is displayed in Supporting Figure S1b. The absence of contrast between the islands, including that between the dashed and dotted framed islands, confirms that the tip is no longer sensitive to the magnetization of the out-of-plane magnetized Co islands.

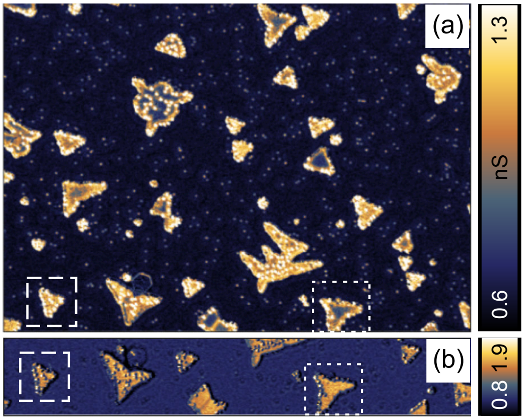

FIG. S1. dI/dV maps with magnetic and non-magnetic tip. (a) The dI/dV map obtained using a Co-functionalized (magnetic) tip demonstrates magnetic contrast between Co nanoislands with opposite perpendicular magnetization, e.g., the islands framed by dashed and dotted rectangles. (b) The same scan area as in (a) was again imaged with the newly functionalized (nonmagnetic) W tip, and no contrast is seen between the two selected islands. This confirms that the tip is no longer sensitive to the out-of-plane magnetization of the Co islands ($V_{\mathrm{bias}} = -600\,\mathrm{mV}$, $I_{\mathrm{t}} = 550\,\mathrm{pA}$, $V_{\mathrm{mod}} = 20\,\mathrm{mV}$, $f_{\mathrm{mod}} = 752\,\mathrm{Hz}$, $5\,\mathrm{K}$).

S3. SINGLE-MOLECULE $I-V$ CURVES

Supporting Figures S2a and c present the single-molecule $I-V$ curves of five *(M)*-[7]H and *(P)*-[7]H molecules each, located on the dotted framed Co island exhibiting dark dI/dV contrast in Figure 2b of the main text or in Supporting Figure S1a. Similarly, Supporting Figures S2b and d show single-molecule $I-V$ curves of five other *(M)*-[7]H and *(P)*-[7]H molecules each, located on the Co island exhibiting bright dI/dV contrast in Figure 2b of the main text or in Supporting Figure S1a. After detecting the island magnetization directions using dI/dV maps and before recording the the singe-molecule $I-V$ curves, the STM tip was re-functionalized in a remote Cu area to obtain a non-magnetic tip insensitive to the spin polarization of the tunneling current (see Supporting Section S2). For each molecule, the tip was positioned above the highest part of the molecule, and after stabilizing the vertical tip position at $V_{\mathrm{stab}} = 2\,\mathrm{V}$ and $I_{\mathrm{stab}} = 800\,\mathrm{pA}$, five consecutive bias sweeps were acquired to enhance signal-to-noise ratios (see Supporting Section S1). The average $I-V$ curve for each individual molecule is plotted as dark red or green line, while the light colored area around the averaged $I-V$ curve indicates the standard error associated with the spread of the repeated bias sweeps. In a next step, the five single-molecule $I-V$ curves for each combination of handedness and island magnetization direction were averaged and plotted in Supporting Figures S2e and f. In these plots, the light colored areas indicate the standard errors due to the averaging over five individual molecules.

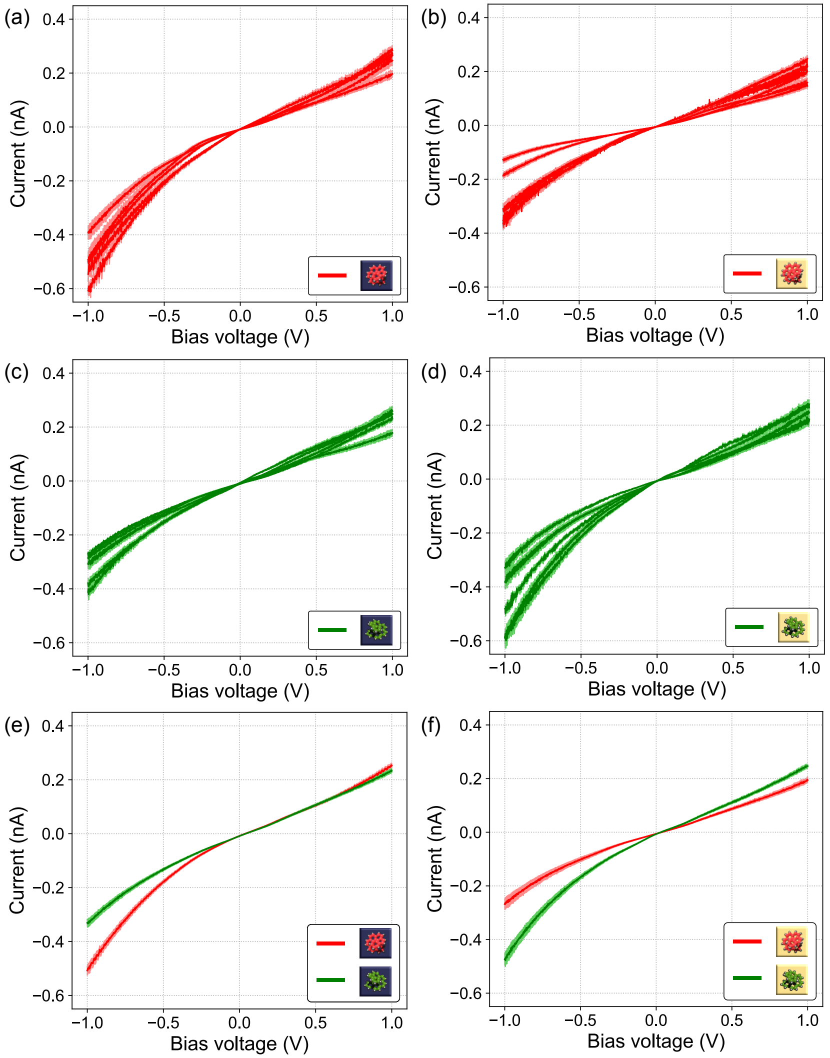

FIG. S2. $I-V$ curves of molecules adsorbed on two oppositely magnetized Co islands. (a) and (c) Five single-molecule $I-V$ curves of individual *(M)*-[7]H and *(P)*-[7]H molecules on the dark island, respectively. (b) and (d) Five single-molecule $I-V$ curves of individual *(M)*-[7]H and *(P)*-[7]H molecules on the bright island, respectively. (e) and (f) Averaged $I-V$ curves of the five molecules each with the same handedness on dark and bright islands, respectively. All $I-V$ curves were obtained with a non-magnetic STM tip ($V_{\mathrm{stab}} = 2\,\mathrm{V}$ and $I_{\mathrm{stab}} = 800\,\mathrm{pA}$). The dark lines represent the averaged $I-V$ curves, while the light-colored regions indicate the calculated standard errors.

S4. REVERSING THE MAGNETIZATION DIRECTION OF THE STM TIP

Supporting Figure S3a shows a dI/dV map featuring [7]H-decorated Co nanoislands on Cu(111). The island framed by the dashed rectangle hosts the molecules shown in the inset of Figure 3a of the main text. The area in the dotted frame is displayed at higher resolution in Supporting Figure S3b. This data was recorded using a Co-functionalized STM tip, referred to in the main text as the first magnetic tip configuration. As observed in Supporting Figure S3b, the islands in the upper left corner of the image exhibit dark dI/dV contrast, whereas the islands in the lower right show bright dI/dV contrast due to their different perpendicular magnetization directions.

After acquiring this data, the tip was moved to a remote Co island and re-functionalized

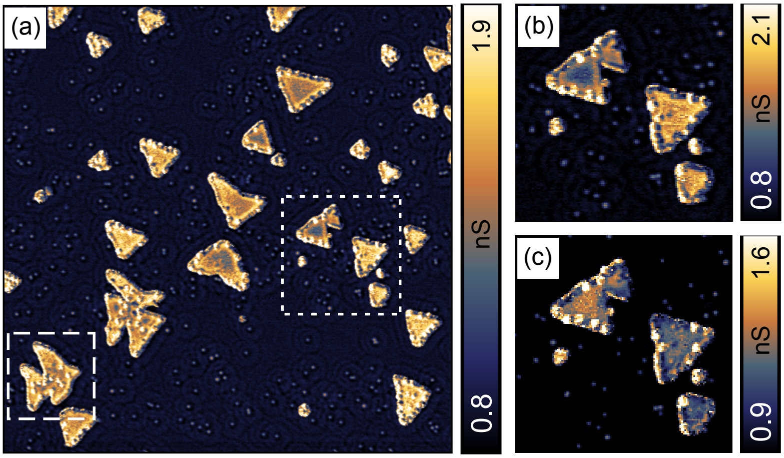

FIG. S3. Reversing the magnetization direction of the STM tip. (a) The dI/dV map, measured with the first magnetic tip configuration, displays magnetic contrast between Co nanoislands with opposite perpendicular magnetization. The island framed by the dashed rectangle contains the molecules depicted in the inset of Figure 3a in the main text. (b) Presents the area indicated by the dotted frame in (a) at a higher resolution. (c) shows the same scan area as in (b) measured with the same scanning parameters, but using a re-functionalized tip referred to as the second magnetic tip configuration. This configuration demonstrates a reversal in the magnetic contrast of the Co nanoislands. ($V_{\mathrm{bias}} = -600\,\mathrm{mV}$, $I_{\mathrm{t}} = 550\,\mathrm{pA}$, $V_{\mathrm{mod}} = 20\,\mathrm{mV}$, $f_{\mathrm{mod}} = 752\,\mathrm{Hz}$, 5 K, Co-functionalized W tip).

to alter the magnetization direction of the tip apex (see Supporting Section S1). After returning to the scan area of Supporting Figure S3b, another dI/dV measurement was performed to assess the magnetic sensitivity of the newly modified tip. This procedure was repeated until the Co nanoislands in Supporting Figure S3b exhibited reversed magnetic dI/dV contrast, as shown in Supporting Figure S3c. In this dI/dV map, the previously dark islands in the upper left corner now appear bright, while the islands in the lower right exhibit dark contrast. This outcome verifies that the tip's out-of-plane magnetic sensitivity is still present, but the magnetization direction of the tip apex has reversed, which is referred to in the main text as the second magnetic tip configuration.

[1] A. Sudhakar and T. J. Katz, Directive effect of bromine on stilbene photocyclizations. An improved synthesis of [7]helicene, Tetrahedron Lett. **27**, 2231 (1986).

[2] M. R. Safari, F. Matthes, K.-H. Ernst, D. E. Bürgler, and C. M. Schneider, Deposition of Chiral Heptahelicene Molecules on Ferromagnetic Co and Fe Thin-Film Substrates, Nanomaterials **12**, 3281 (2022).

[3] B. Voigtländer, *Scanning probe microscopy: Atomic force microscopy and scanning tunneling microscopy* (Springer, Berlin, 2015).

3.5 Enantiospecific magnetic conductance asymmetries through single chiral molecules

This section extends our previous investigation (described in Section 3.4) on spin-selective electron transport through single chiral molecules. In this continuation, enantiopure *(M)*-[7]H molecules are used instead of a racemic mixture, and the substrate has been changed to epitaxially grown Fe bilayers on W(110), which exhibit OOP magnetization. These modifications are aimed at enhancing the experimental methodologies described in the manuscript, in the context of Figure 4, where we have used a constant-height STM measurement technique.

Switching to the Fe/W(110) substrate offers a distinct advantage: it presents significantly larger magnetic domain areas compared to the previously used Co nanoislands on Cu(111). This not only facilitates constant-height measurements across a larger statistical set of molecules, but also allows us to select scanning areas that include both magnetic domains. By doing so, we can perform constant-height STM measurements over regions where two oppositely magnetic domains coexist, thereby allowing us to measure current maps directly across chiral molecules deposited on two oppositely OOP magnetized domains.

Furthermore, the use of enantiopure molecules circumvents the complexities involved in determining the handedness of deposited molecules, a task that proved to be particularly challenging on the reactive Fe substrate as previously described in Section 3.1, where the handedness of 13 out of 100 analyzed molecules on the bilayer Fe/W(110) remained indeterminable. By substituting for enantiopure molecules, we significantly reduce the uncertainty in evaluating molecule handedness, thereby enhancing the reliability of our experimental results.

Figure 3.3a displays a constant-current topographic image of *(M)*-[7]H molecules deposited on 1.7 ML thick Fe film on a W(110) surface, measured using a Fe functionalized W tip. Areas covered by 1 ML and 2 ML of Fe are labeled as 'ML' and 'BL', respectively. The corresponding dI/dV map, shown in Figure 3.3b, reveals the magnetic domain structures. In this map, the dark blue and bright yellow colours within the bilayer areas signify magnetic domains with opposite out-of-plane magnetization [4]. The high-resolution dI/dV maps and constant current topography data of the region outlined in the red frames in Figures 3.3a and b are presented in Figure 3.3c to e. The yellow and blue arrows in Figure 3.3c represent two oppositely magnetized OOP domains that are separated by a domain

---

[4] Detailed insights into the topographical features and magnetic properties of these domains have been previously discussed in the manuscript presented in Section 3.1.

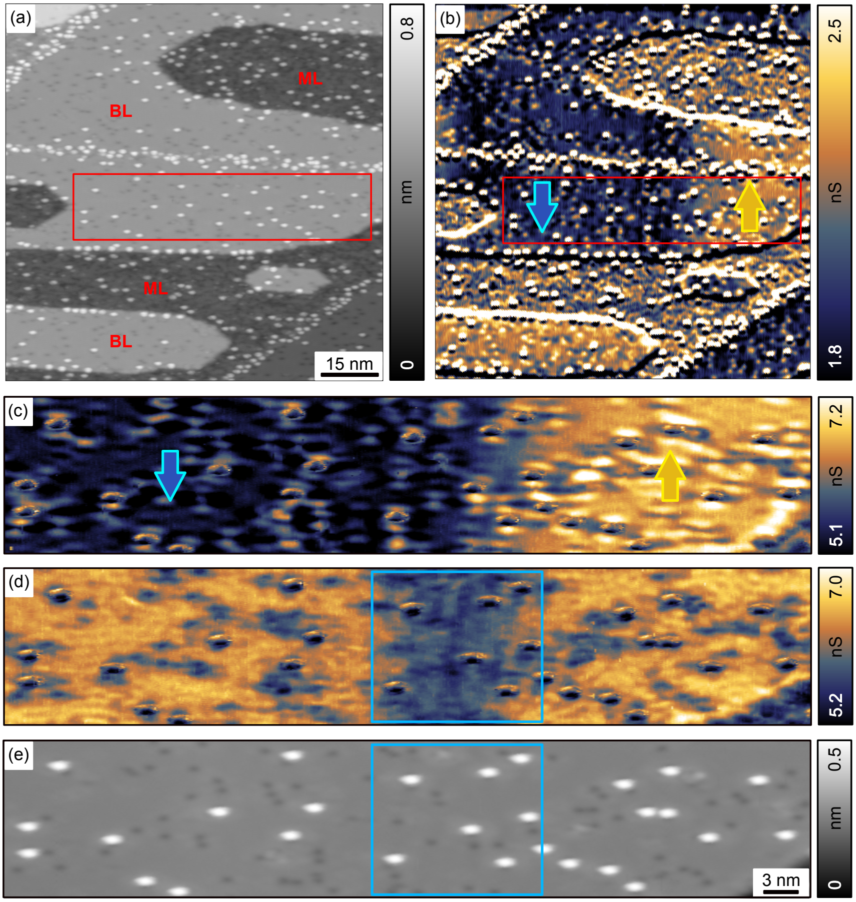

Figure 3.3: (a) Constant-current STM topography of *(M)*-[7]H molecules on a substrate of 1.7 ML of Fe on W(110), where BL and ML denote the first and second ML of Fe, respectively. (b) dI/dV map acquired simultaneously with (a), displaying opposite alignments of the OOP magnetized domains in the BL region, indicated by blue and yellow arrows ($V_{\text{bias}} = -100\,\text{mV}$ and $I_{\text{t}} = 150\,\text{pA}$, $V_{\text{mod}} = 20\,\text{mV}$, $f_{\text{mod}} = 752\,\text{Hz}$). (c) and (d) High-resolution dI/dV maps of the area marked by a red frame in (b), measured at $V_{\text{bias}} = -100\,\text{mV}$ and $I_{\text{t}} = 450\,\text{pA}$ and $V_{\text{bias}} = 50\,\text{mV}$ and $I_{\text{t}} = 250\,\text{pA}$, respectively. The blue frame in (d) marks the approximate location of the magnetic domain wall. (e) High-resolution constant-current topography of the region outlined in red frame in (a) and (b), with a blue frame indicating the molecules deposited on the domain wall ($V_{\text{bias}} = 50\,\text{mV}$, $I_{\text{t}} = 250\,\text{pA}$). All STM data were obtained at 5 K using a Fe-functionalized W tip.

wall. As discussed in Section 2.2.3, the contrast in spin-polarized tunneling is proportional to the product of the sample's ($\mathbf{P}_{\text{sample}}$) and the tip's ($\mathbf{P}_{\text{tip}}$) spin polarization. Considering our sample's pronounced OOP magnetization, we needed a tip that was also sensitive to OOP magnetization direction, to accurately map the magnetic properties of the sample. Figure 3.3c shows measurement conducted with such a magnetic tip, set at a bias voltage of $-100\,\mathrm{mV}$. This specific voltage corresponds to an energy range where there is a notable imbalance in the density of states between spin-up and spin-down electrons at the tip, enabling the effective extraction of the OOP magnetization characteristics of the Fe substrate. For improved information on the domain wall area, we adjusted the bias voltage to $+50\,\mathrm{mV}$ for the subsequent dI/dV measurement. At this bias voltage, the imbalance in the density of states for spin-up and spin-down electrons at the tip diminishes, leading to the disappearance of the spin-polarized contrast. However, due to the presence of spin-orbit coupling effects, particularly pronounced when using a heavy metal tungsten (W) tip, the sense of rotation of the spin alignment of the Fe atoms in the Bloch-type domain wall is still clearly visible as a distinct vertical dark blue region in Figure 3.3d [130].

In Figure 3.3d, the blue frame indicates the region of the domain wall. This frame, when superimposed onto the constant current topographical image in Figure 3.3e, enables us to identify and exclude the molecules within the domain wall. Consequently, we are left with a total of 20 molecules, evenly distributed into 10 molecules in each magnetic domain. This count offers a statistically significant sample for analyzing the current transported through single chiral *(M)*-[7]H molecules located on oppositely magnetized OOP domains. Such a procedure strengthens our statement that the comparison is made under controlled experimental conditions. These conditions include identical *(M)*-[7]H molecules, constant tip properties, and identical STM parameters, with the only variable being the substrate's magnetization.

By increasing the sample size from the single-molecule pair discussed previously in Section 3.4 to 20 molecules, we further minimize experimental factors beyond our control, such as the potential adsorption of molecules on substrate defects. This statistical enhancement allows for a more robust and reliable comparison, strengthening the validity of our observations regarding measuring enantiospecific magnetic conductance asymmetries through single chiral molecules under identical experimental conditions.

In the subsequent step, we conducted constant-height STM measurements at various bias voltages. To acquire constant-height STM images, we employed a methodology similar to that detailed in the Supplementary Section 1C of the manuscript described in 3.4. The accuracy of our constant-height measurement begins with the determination of the Fe surface's inclination, using a constant-current image. This crucial step allows us to precisely adjust the scanning plane for the constant-height measurement, ensuring it is perfectly aligned coplanar with the Fe surface. The specific height for these constant-height scans, denoted as z_{Fe}, is set based on the bias voltage V_{bias} and the setpoint current I_{t}, established prior to disabling the feedback loop. Subsequently, the STM tip is retracted by a distance of Δz_0. This retraction is necessary to ensure that the tunneling current remains within the operational range of the pre-amplifier (1 pA to 3.3 nA).

Figure 3.4 presents a sequence of five constant height STM images from the area indicated in Figure 3.3e. These images depict the effects of varying bias voltages on tunneling currents through chiral molecules, captured at bias voltages of -1 V, -100 mV, 50 mV, 100 mV, and 1 V. This range allowed for the measurement of both negative and positive tunneling currents. The images correspond sequentially from Figures a to e, in ascending order, to these bias voltages, each representing the molecular response at that voltage.

The variations in brightness contrast observed between molecules in each data set can be attributed to different conductance levels in identical molecules under constant experimental conditions. The enhanced brightness of molecules positioned above the magnetic domain with $M_{\downarrow}$ suggests a more conductive scenario. In this context, the substrate magnetization in association with the chirality of the left-handed molecules leads to an increased conductance compared to molecules positioned over the domain with $M_{\uparrow}$. Furthermore, the comprehensive statistics of discrete molecules in these magnetic domains, together with the data presented in Figure 4 of the manuscript in Section 3.4, support our observation that the CISS effect is apparent at the single-molecule level. This observation eliminates the need for intermolecular interactions or an ensemble effect to demonstrate the CISS effect.

To quantitatively examine the conductance through the molecules, line profiles were extracted across the molecules from each data set. An illustrative example of these line profiles, marked by a red dashed line along the molecule, is shown in Figure 3.4a. These profiles are further detailed in Figure 3.5.

Figure 3.5a1 shows the line profiles representing the tunneling current (in nA) measured through ten molecules located on a magnetic domain with $M_{\downarrow}$ shown in Figure 3.4a. Each line profile corresponds to the measured current through a particular molecule. Similarly, Figure 3.5a2 shows the extracted line profiles for molecules placed on a domain with $M_{\uparrow}$ magnetization, also referred to Figure 3.4a. The average tunneling current was then calculated for the ten molecules within each magnetic domain. Figure 3.5a3 shows these averages (dark blue and red curves) with their respective standard errors (light blue and red shading) for comparative analysis. The methodology for extracting and plotting the

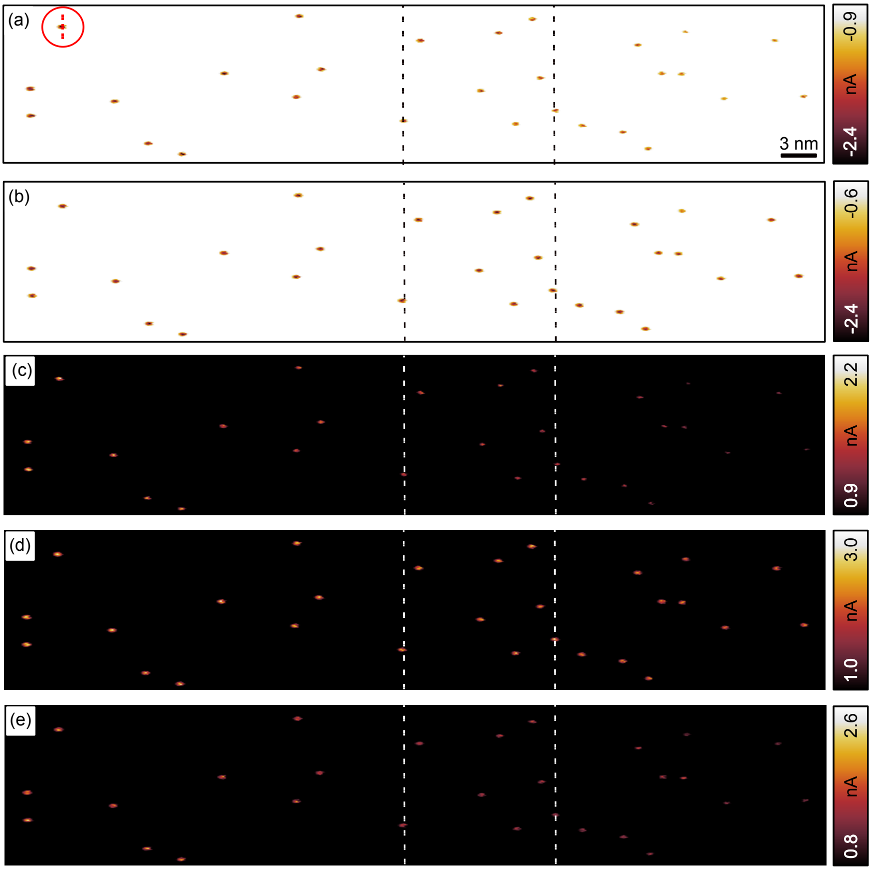

Figure 3.4: Constant-height STM images from the same area depicted in Figure 3.3e, captured using an Fe-functionalized W-tip at 5 K. The bias voltage and corresponding changes in tip height are as follows: (a) $V_{\text{bias}} = -1\,\text{V}$ ($\Delta z_0 = 0.13\,\text{nm}$), (b) $V_{\text{bias}} = -0.1\,\text{V}$ ($\Delta z_0 = 0.2\,\text{nm}$), (c) $V_{\text{bias}} = 0.05\,\text{V}$ ($\Delta z_0 = 0.23\,\text{nm}$), (d) $V_{\text{bias}} = 0.1\,\text{V}$ ($\Delta z_0 = 0.2\,\text{nm}$), and (e) $V_{\text{bias}} = 1\,\text{V}$ ($\Delta z_0 = 0.12\,\text{nm}$).

tunneling current line profiles as applied to the data in Figure 3.4a has been consistently applied to the data sets in Figures 3.4b through 3.4e. The larger amplitude of the blue curves in Figures 3.5a3 to e3 relative to the red curves clearly shows that left-handed *(M)*-[7]H molecules have higher conductance on the domain with $M_{\downarrow}$ magnetization alignment, a trend that persists across all applied bias voltages. An evaluation of the enantiospecific magnetic conductance asymmetry (EMA) is then performed using the average conductance values derived from each magnetic domain. For the sake of brevity, we have included

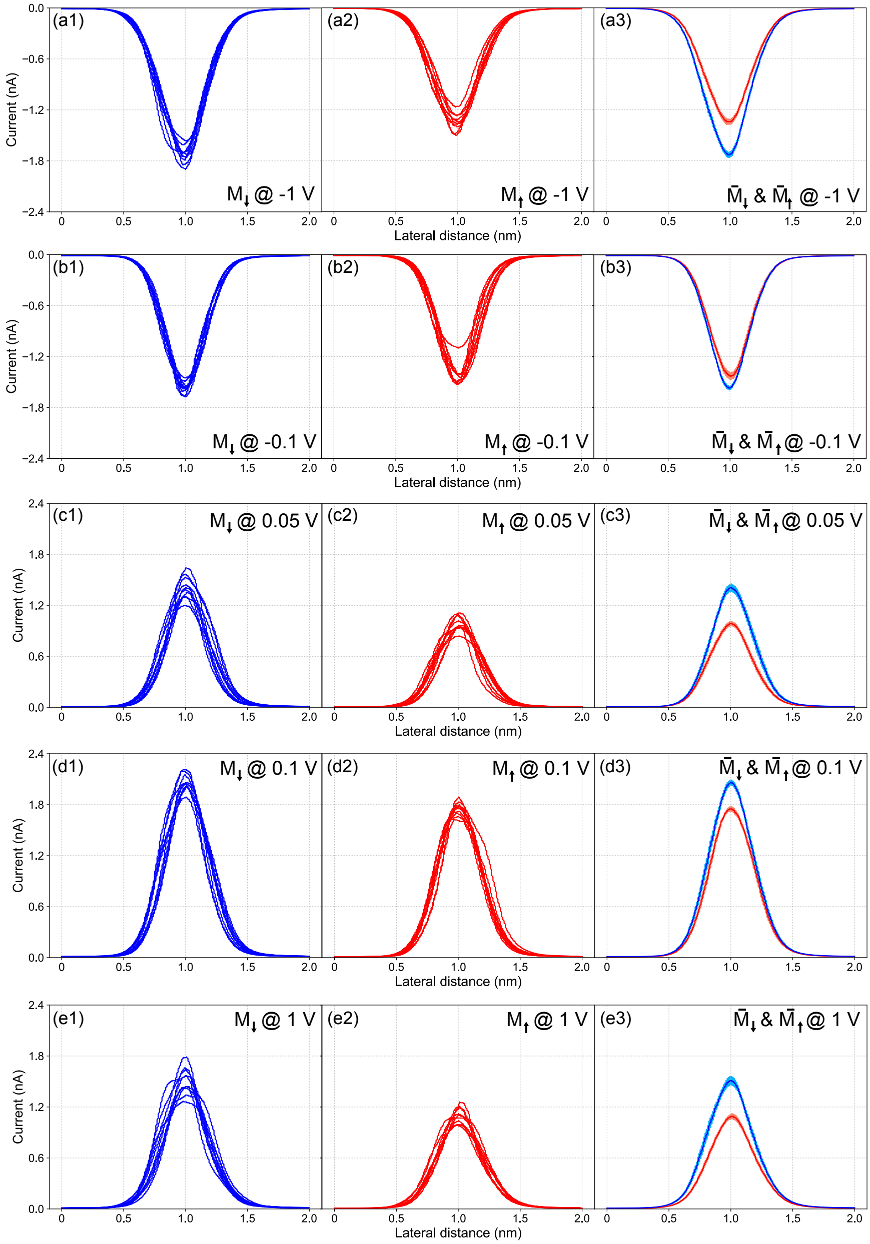

Figure 3.5: (a1) to (e1), (a2) to (e2): Individual line profiles of single *(M)*-[7]H molecules extracted from Figure 3.5 (a-e), situated on domains with $M_\downarrow$ and $M_\uparrow$ magnetization, respectively. (a3) to (e3): Averaged line profiles derived from 10 molecules in the respective individual profiles in (a1)-(e1) and (a2)-(e2). The solid lines indicate the average line profiles, while the shaded areas represent the standard error margins. Each sub-figure specifies the applied bias voltage and the magnetization direction of the substrate.

only the magnitude of the peak current values in the equation below to determine the EMA values, and the results are shown in Figure 3.6.

$$\mathrm{EMA} = \frac{I_{\mathrm{up}} - I_{\mathrm{down}}}{I_{\mathrm{up}} + I_{\mathrm{down}}}. \tag{3.2}$$

This data underlines the complex relationship between molecular conductance, electron spin properties, and the spin sensitivity of the STM tip, as well as the polarity of electron flow. Notably, the data reveal a minimum EMA value of 4.6% at -100 mV bias voltage, which is the condition where pronounced magnetic contrast was observed in our dI/dV maps. This implies that the magnetization of the tip might counteract the electron spin as they tunnel from the tip to the molecules, reducing the tunneling current. Conversely, at 50 mV bias voltage, where we previously noted a diminished spin-polarized sensitivity of the tip, we observe a peak EMA value of 17.7%. The absence of spin-polarized tip sensitivity could correspond to this elevated EMA value. An intriguing consideration for future work would be to intentionally alter the magnetic alignment of the STM tip and reassess the measurements—a possibility not explored in this dataset. However, such an experiment would be a valuable addition to future research projects.

In conclusion, the newly acquired experimental data, along with the comprehensive analysis presented in this section, demonstrate a pronounced CISS effect in simple and small *(M)*-[7]H molecules chemisorbed directly onto a highly reactive, OOP magnetized Fe substrate. The modifications considered in this experiment—including the selection of several discrete molecules spaced a few nanometers apart and switching the substrate from discrete Co nanoislands to more extended Fe magnetic domains—allowed for the inclusion of a larger number of molecules in our analysis. This change excluded uncontrolled variables, such as molecule deposition on potential substrate defects, and facilitated a more detailed investigation of the CISS effect at the single-molecule level. These modifications ensured the reproducibility of controlled single-molecule experiments and served as a supplementary experiment to reinforce our previously reported results in Section 3.4. Additionally, they provided a more extensive dataset that can be used to lay the groundwork for future theoretical studies.

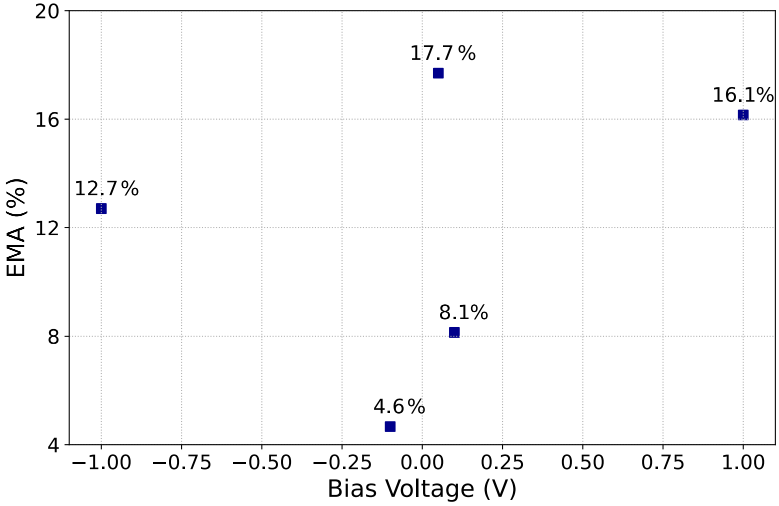

Figure 3.6: The calculated EMA values for *(M)*-[7]H molecules deposited on the oppositely magnetized OOP Fe substrate as a function of the applied bias voltage.

CHAPTER 4

Summary and Outlook

In this thesis, the spin selectivity of chiral heptahelicene molecules deposited on single-crystalline ferromagnetic surfaces was investigated. Utilizing low-temperature and spin-polarized scanning tunneling microscopy and spectroscopy, the goal was to study the complex interaction between chirality and magnetism on the single-molecule scale.

The experimental procedure began with a thorough examination of substrate preparation and the sublimation of racemic mixtures of chiral 7[H] molecules onto various crystalline surfaces under UHV conditions. These surfaces ranged from the noble metal Cu(111) to the more reactive ferromagnetic Co bilayer nanoislands on Cu(111) and Fe bilayers on W(110). High-resolution SP-STM/STS conducted at low temperatures demonstrated that in all cases, the molecules remain structurally intact and align with the proximal phenanthrene group parallel to the surface. This study revealed three degenerate in-plane orientations on Cu(111) and Co(111), aligned with the symmetry of these substrates, and only two on Fe(110), suggesting distinct and specific adsorption sites according to each substrate type. While 7[H] physisorbs on Cu(111), it chemisorbs on Co(111) and Fe(110) bilayers, which maintain their ferromagnetic characteristics and out-of-plane magnetization.

Furthermore, topographic STM images enabled the precise identification of the molecular handedness of individual molecules adsorbed on these crystalline substrates. These foundational data were crucial for advancing our investigations into the CISS effect, by providing a framework for subsequent experiments. Building on these observations, our research delved deeper into the complex interplay between electron spin and molecular handedness by focusing on the interactions between chiral molecules and magnetic substrates.

We first explored the deposition of racemic mixtures of chiral heptahelicene molecules onto ferromagnetic cobalt nanoislands. Using spin- and chirality-sensitive scanning tunneling microscopy, we determined the handedness of each adsorbed molecule and the magnetization alignment of the underlying substrates. This method enabled precise counting of left- and right-handed molecules on both islands type with opposite OOP magnetization alignments. An opposite enantiomeric imbalance was observed: on one island type, the number of left-handed molecules was higher than that of right-handed molecules, while on the second island type with opposite magnetic alignment, the number of right-handed molecules was higher.

To strengthen these observations with more robust statistics, the analysis was extended to 107 islands and over 740 molecules. The outcomes indicated a pronounced imbalance in the handedness of adsorbed [7]H molecules that depended on the OOP magnetization direction of the substrate.

The observed enantiomeric excess on each island highlighted the effect of both molecular chirality and the island's magnetization on the magneto-enantiospecific adsorption of molecules. This effect indicates an energy difference of approximately $10 \pm 2\,\mathrm{meV}$ between the two enantiomers, which is attributed to different transition rates between the precursor and chemisorbed states due to magneto-enantiospecific binding in the precursor state. Further measurements revealed that molecular mobility decreased significantly upon achieving a chemisorbed state on the cobalt islands. This indicates that we observe a kinetically controlled enantiomer distribution resulting from enantioselection that mainly occurs in an earlier, physisorbed state. Advanced spin-resolved *ab initio* simulations supported this by showing no significant differences in enantio-dependent chemisorption energies. Instead, enantioselection is likely to take place in a van der Waals-bound precursor state, enabling molecules to probe multiple cobalt islands before final chemisorption. These findings suggest that we need to consider the influence of spin fluctuations in van der Waals interactions, as these interactions play a crucial role in molecular magnetochiral processes.

Additionally, other properties of the Co nanoislands that may contribute to the observed enantiospecificity were discussed. According to the obtained STM data, a significant majority of the molecules were found preferentially adhering to the island rims. This led us to explore whether the enantiospecific adsorption correlated with the electronic properties of the rim or the molecular diffusion barriers at the island edges. A detailed examination of the enantiomeric ratios of [7]H molecules at both the rim and the center of the islands revealed more pronounced enantioselectivity in the center. However, the the statistical significance of this analysis was limited by the small fraction of molecules evaluated from the island centers—less than 10% of our total molecule.

To overcome this limitation, we deposited enantiopure left-handed [7]H molecules onto the Co islands, instead of the previously used racemic mixture. This change streamlined the process by removing the need for time-consuming high-resolution STM topography to determine each molecule's chirality. Consequently, we were able to examine a larger number of molecules, greatly expanding our analytical capabilities. The expanded study included 225 islands and 2178 molecules. Detailed analysis of this larger dataset confirmed the initial findings, demonstrating a pronounced enantiomeric ratio for chiral molecules in the center of the islands. Quantitatively, this translated to an energy difference of $38.6 \pm 2\,\mathrm{meV}$ for molecules in the center compared to $1.7 \pm 1\,\mathrm{meV}$ for molecules at the rim. As described above, this difference arises from varying transition rates between the precursor and chemisorbed states, driven by magneto-enantiospecific binding in the precursor state.

In the following, we used a detailed single-molecule approach to investigate spin-selective electron transport. Initially, a racemic mixture of [7]H molecules was deposited on single-crystalline ferromagnetic cobalt islands under UHV conditions. These molecules were then probed with the help of a spin-sensitive STM tip at a low temperature of 5 K. This technique enabled precise measurement of tunneling currents through individual molecules while keeping all experimental conditions identical, except for controlled variations in molecular handedness or the magnetization direction of the STM tip or cobalt substrate. By selectively adjusting these variables, we were able to accurately determine the magnetochiral conductance asymmetry when two enantiomers were located on the same magnetic domain (Co island) and the enantiospecific magnetic conductance asymmetry when comparing two molecules of the same handedness on two islands with opposite OOP magnetization.

To begin with, we considered 20 molecules, with equal numbers of both enantiomers, deposited on two cobalt islands with opposite OOP magnetization. Each island contained 10 molecules: five *(M)*-[7]H and *(P)*-[7]H molecules. We obtained individual I-V curves for each molecule and then averaged the I-V curves for combination of handedness and island magnetization direction. This allowed us to calculate the MChA and EMA values for each configuration.

Striving for a minimal experimental setup without averaging over several molecules, we then focused on pairs of enantiomers with opposite handedness deposited on a single cobalt island with a specific OOP magnetization. By comparing the I-V curves obtained from these two molecules, we were able to calculate the MChA values. In the next step, we reversed the magnetization direction of the STM tip. This reversal enabled us to compare the I-V curves measured from the molecules before and after changing the tip's magnetization direction. By examining these conductance asymmetries with the STM tip in both magnetization alignments, we were able to calculate the EMA values for an isolated pair of chiral molecules.

A final proof of single-molecule magnetochiral asymmetry involved performing constant-height STM measurements directly above pairs of molecules deposited on the same cobalt island. This method maintained all experimental conditions (e.g., tip structure, tip height, magnetization directions of both tip and substrate) identical, providing high-resolution current maps at specific bias voltages. These measurements confirmed the different conductance between enantiomers under fixed experimental conditions, offering unequivocal evidence of the CISS effect at the single-molecule level and revealing conductance asymmetries of up to 50%.

Importantly, these findings effectively ruled out electron-phonon coupling and ensemble effects as primary mechanisms responsible for CISS. However, the small size of the cobalt islands posed challenges in the latter measurements with constant-height. Selecting a measurement area large enough to accommodate multiple molecules of both enantiomers is essential for increasing the statistical depth of our investigation.

To overcome these limitations, we switched to an epitaxially grown bilayer Fe on W(110) substrate, which features significantly larger magnetic domains with OOP magnetization compared to cobalt islands. This change allowed us to perform constant-height STM measurements on a larger scale, accommodating more molecules and enhancing the statistical robustness of our findings. Additionally, we switched to enantiopure *(M)*-[7]H molecules, simplifying the process by eliminating the need for high-resolution STM data to determine the chirality of individual molecules, a task that proved particularly challenging on Fe substrates.

Subsequently, we collected constant-height STM data over an area of the Fe bilayer that included both OOP magnetic domains, accommodating 20 molecules—ten per domain. By maintaining consistent conditions such as tip structure, height, and magnetization directions, we acquired current maps across these 20 molecules. This data enabled us to determine the EMA values for molecules on iron substrates, which reached up to 17% at a low temperature of 5 K, providing solid statistical evidence of conductance asymmetry.

As a conclusion, the findings of this research provide a clearer picture of the interaction between chirality and magnetism proofing the existence of CISS effects on the single-molecule level. The well-defined and ideal experimental conditions created a framework which will hopefully inspire theorists to develop concrete models that also enable a quantitative comparison with our results.

Building on the insights gained from this research, which validated the observation of the CISS effect at the single-molecule scale, future studies could explore various parameters that can be modified at this scale. For instance, investigating a series of different chiral molecules designed to systematically vary their spin-orbit coupling and magnetic moments, e.g. by isoelectronic substitution of the metal center causing chirality, would provide a deeper understanding of these factors on the interaction with magnetic substrates. Additionally, modifying substrates to develop ferromagnetic surfaces that interact more weakly with deposited molecules could offer a novel approach to study the role of the substrate and the adsoprption kinetics for the CISS effects.

The combination of these proposals and advanced simulations incorporating the mentioned modifications can substantially advance our understanding of the interaction of chiral molecules with magnetic substrates and the electron spin in particular, a topic that has drawn the interest of scientists already for decades.

APPENDIX A

Individual STM images used to construct the mosaic representation presented in Figure 3.2

This appendix presents the individual topographic data and corresponding dI/dV maps that are used to construct the assembled mosaic image in Figure 3.2. As described in Section 3.3, consistent STM parameters were used for all scans. In addition, strategic overlapping with at least one Co island in common between subsequent scans ensured uniform tip magnetization throughout the entire imaging process.

The integrated image (Figure 3.2) is a product of fifteen individual STM images (both topography and dI/dV maps). Figure 3.1a-d already showed detailed views of the first two images. The remaining thirteen images are presented in this appendix. Each shows both its topographic and corresponding dI/dV maps. These individual scans are essential for demonstrating the extensive scan area that was systematically covered to gather data on a significant number of Co islands and the molecules attached to them. These detailed scans underpin the analysis of over 220 islands and 2100 molecules.

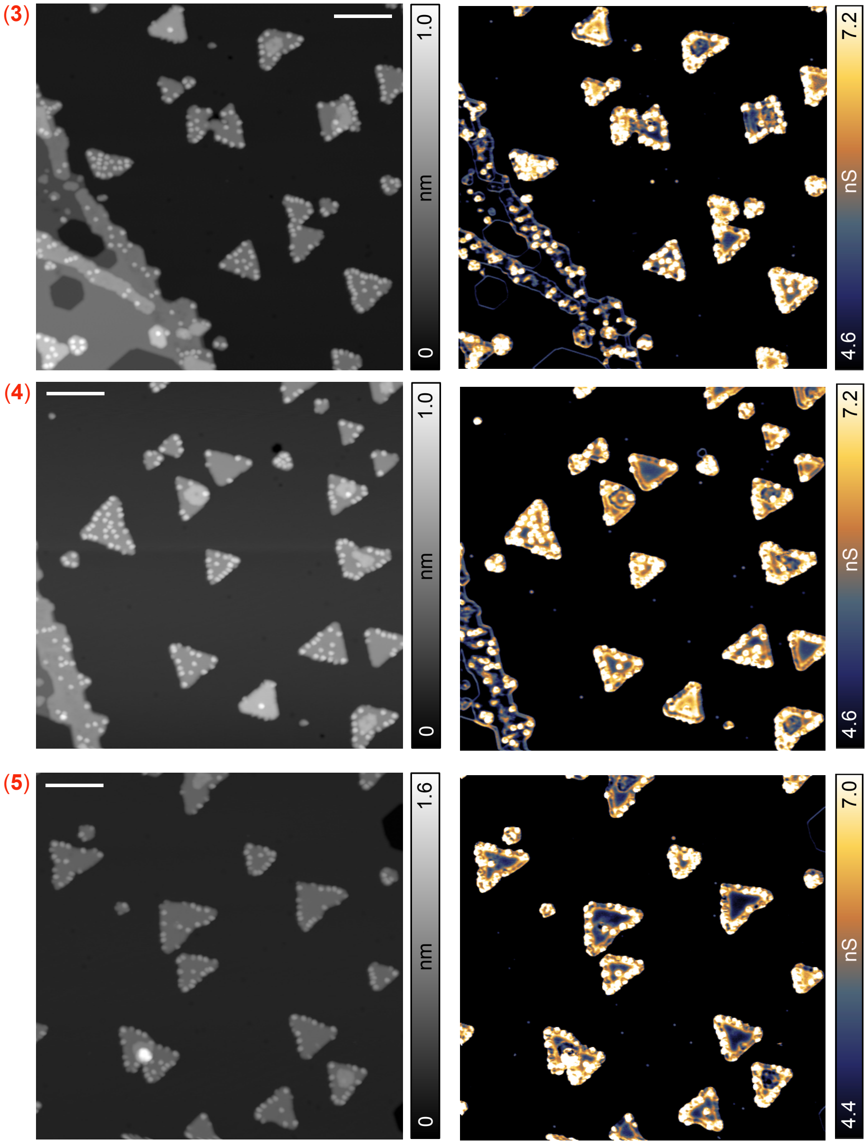

Figure A.1: Constant current topographies and corresponding dI/dV maps of scan number 3 to 5 in mosaic image presented in Figure 3.2. Data were obtained with the following parameters: $V_{\text{bias}} = -620\,\text{mV}$, $I_{\text{t}} = 300\,\text{pA}$, $V_{\text{mod}} = 20\,\text{mV}$, $f_{\text{mod}} = 752\,\text{Hz}$, at a temperature of 5 K, using a Co-functionalized W tip. The scale bars represent 20 nm.

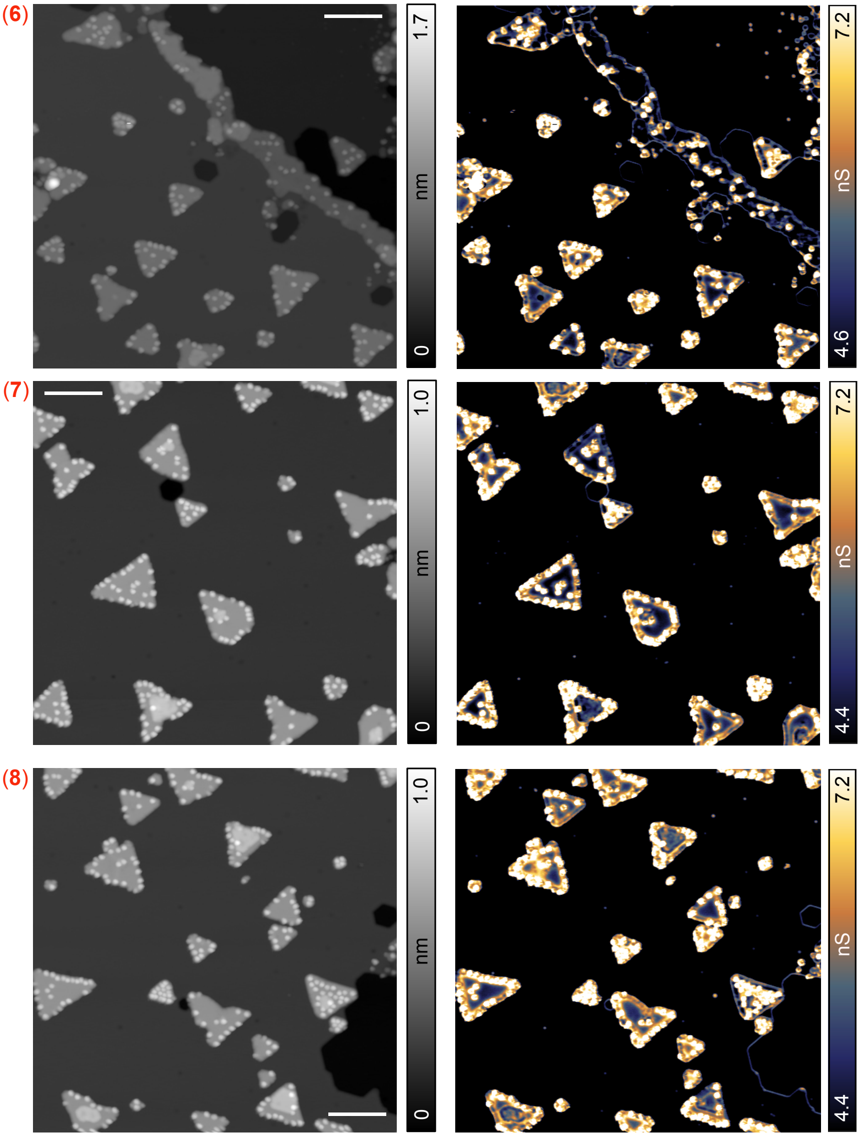

Figure A.2: Constant current topographies and corresponding dI/dV maps of scan number 6 to 8 in mosaic image presented in Figure 3.2. Data were obtained with the following parameters: $V_{\mathrm{bias}} = -620\,\mathrm{mV}$, $I_{\mathrm{t}} = 300\,\mathrm{pA}$, $V_{\mathrm{mod}} = 20\,\mathrm{mV}$, $f_{\mathrm{mod}} = 752\,\mathrm{Hz}$, at a temperature of 5 K, using a Co-functionalized W tip. The scale bars represent 20 nm.

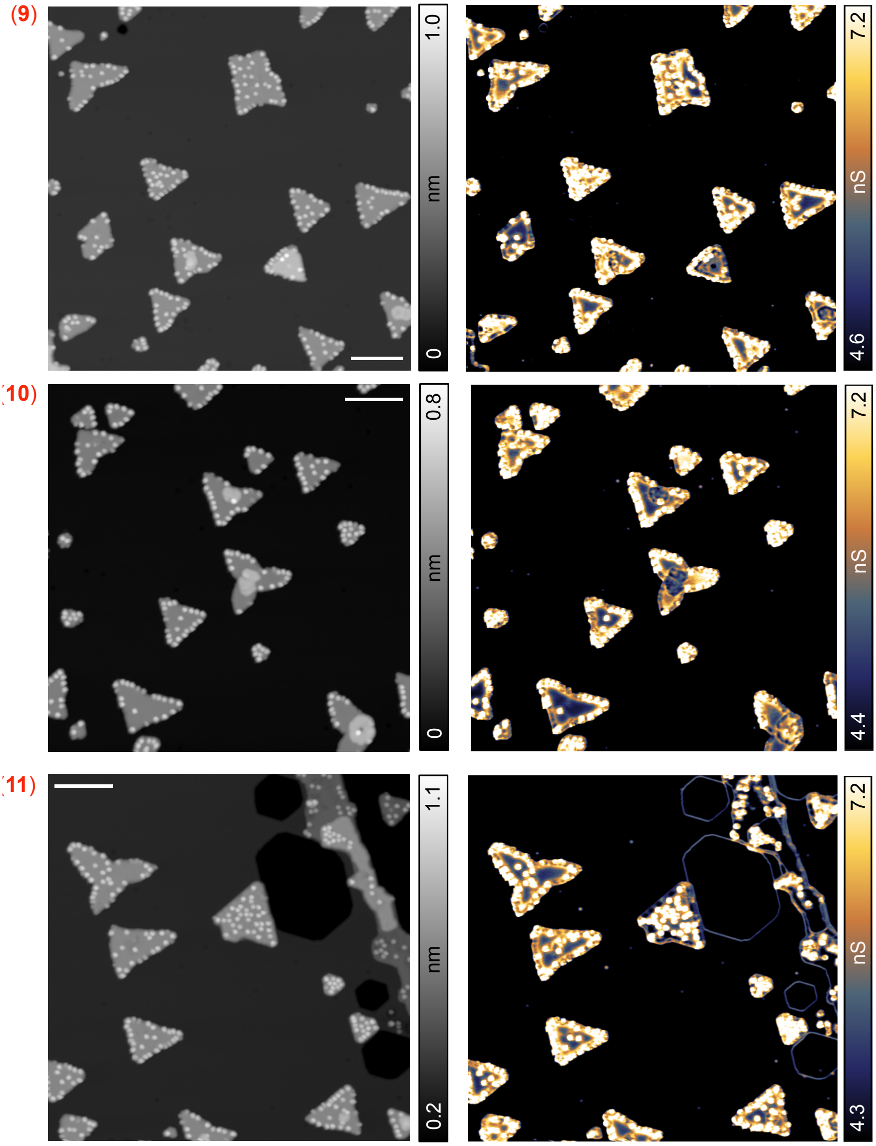

Figure A.3: Constant current topographies and corresponding dI/dV maps of scan number 9 to 11 in mosaic image presented in Figure 3.2. Data were obtained with the following parameters: $V_{\mathrm{bias}} = -620\,\mathrm{mV}$, $I_{\mathrm{t}} = 300\,\mathrm{pA}$, $V_{\mathrm{mod}} = 20\,\mathrm{mV}$, $f_{\mathrm{mod}} = 752\,\mathrm{Hz}$, at a temperature of 5 K, using a Co-functionalized W tip. The scale bars represent 20 nm.

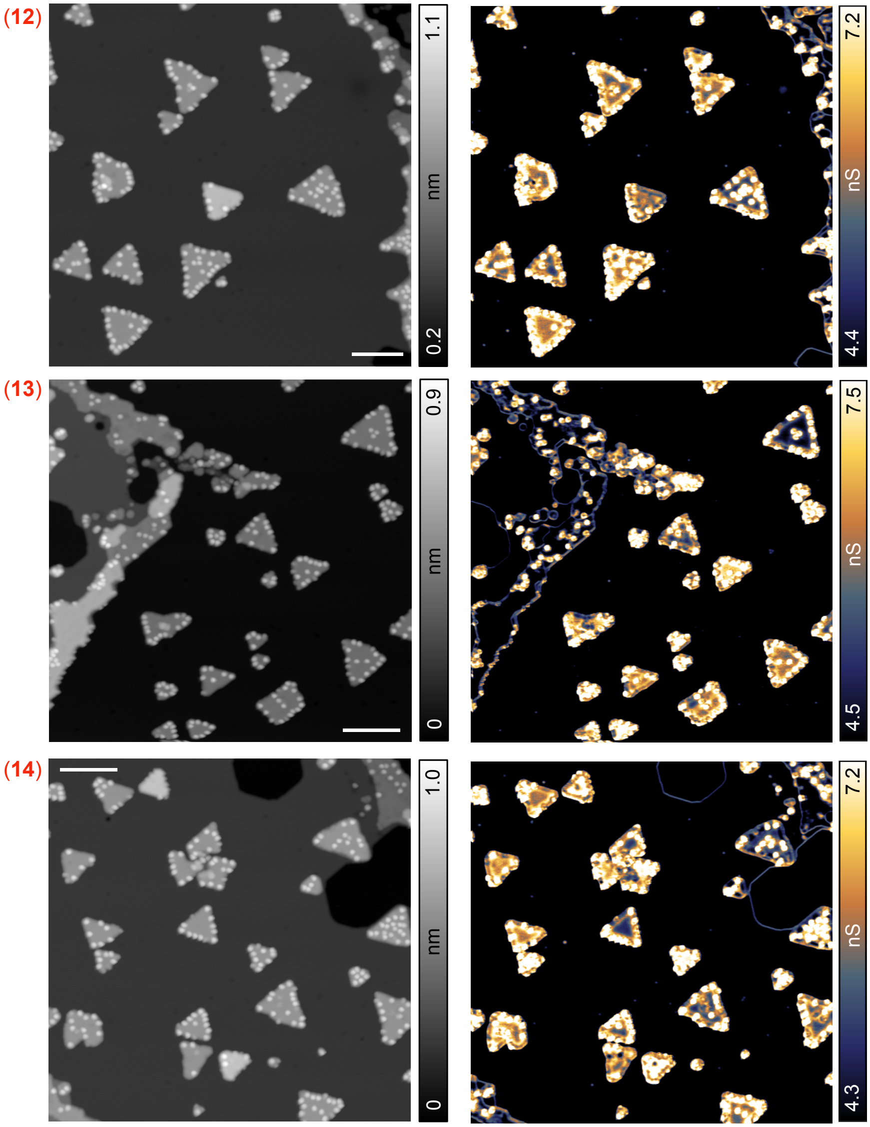

Figure A.4: Constant current topographies and corresponding dI/dV maps of scan number 12 to 14 in mosaic image presented in Figure 3.2. Data were obtained with the following parameters: $V_{\mathrm{bias}} = -620\,\mathrm{mV}$, $I_{\mathrm{t}} = 300\,\mathrm{pA}$, $V_{\mathrm{mod}} = 20\,\mathrm{mV}$, $f_{\mathrm{mod}} = 752\,\mathrm{Hz}$, at a temperature of 5 K, using a Co-functionalized W tip. The scale bars represent 20 nm.

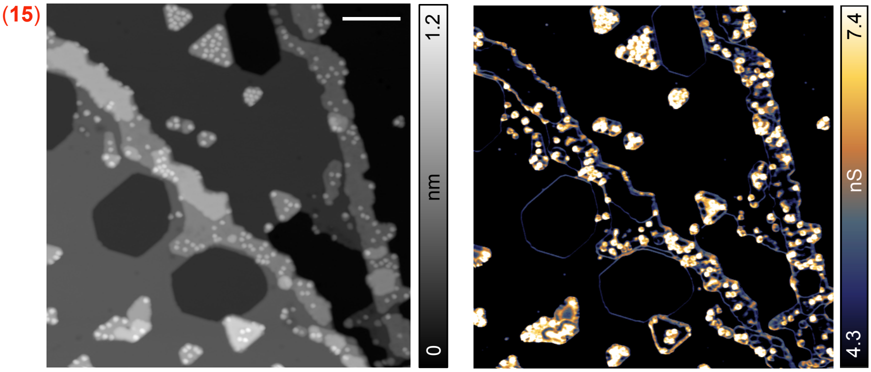

Figure A.5: Constant current topography and corresponding dI/dV map of scan number 15 in mosaic image presented in Figure 3.2. Data were obtained with the following parameters: $V_{\text{bias}} = -620\,\text{mV}$, $I_{\text{t}} = 300\,\text{pA}$, $V_{\text{mod}} = 20\,\text{mV}$, $f_{\text{mod}} = 752\,\text{Hz}$, at a temperature of $5\,\text{K}$, using a Co-functionalized W tip. The scale bars represent $20\,\text{nm}$.

APPENDIX B

List of Publications

Part of the results presented in this thesis can be found in the following publications:

[127] **Mohammad Reza Safari**, Frank Matthes, Karl-Heinz Ernst, Daniel E. Bürgler, Claus M. Schneider
Deposition of Chiral Heptahelicene Molecules on Ferromagnetic Co and Fe Thin-Film Substrates
Nanomaterials 2022, **12(19)**, 3281.

[128] **Mohammad Reza Safari**, Frank Matthes, Vasile Caciuc, Nicolae Atodiresei, Claus M. Schneider, Karl-Heinz Ernst, Daniel E. Bürgler
Enantioselective Adsorption on Magnetic Surfaces
Advanced Materials 2024, **36(14)**, 2308666.

[129] **Mohammad Reza Safari**, Frank Matthes, Claus M. Schneider, Karl-Heinz Ernst, Daniel E. Bürgler
Spin-Selective Electron Transport Through Single Chiral Molecules
Small 2024, **20(22)**, 2308233.

Conference contributions as presenting author:

2021 Virtual ICMM conference, the 17th international conference on molecule-based magnets, Manchester (GB), *Towards single-molecule-scale studies of enantioselective adsorption of chiral molecules on ferromagnetic surfaces.* Poster

2022 DPG spring meeting, Dresden (DE), *Growth of chiral heptahelicene molecules on ferromagnetic Co and Fe thin-film substrates* . Talk

2022 WE-Heraeus-Seminar, Bad Honnef (DE), *Enantiospecific adsorption on a ferromagnetic surface at the single-molecule scale.* Poster

2023 EMPA weekly seminar, Dübendorf (CH), *Enantiospecific Adsorption of chiral [7]H molecules on a Ferromagnetic Surfaces.* Talk

2023 WE-Heraeus-Seminar, Bad Honnef (DE), *Enantiospecific adsorption on a ferromagnetic surface at the single-molecule scale.* Poster

2023 DPG spring meeting, Dresden (DE), *Enantiospecific adsorption on a ferromagnetic surface at the single-molecule scale.* Talk

Bibliography

[1] W. Thomson, Baron Kelvin, 'ON THE MOLECULAR TACTICS OF A CRYSTAL. In Baltimore Lectures on Molecular Dynamics and the Wave Theory of Light' (Cambridge University Press., 2010). Cited on page(s) 1

[2] J. Gal and P. Cintas, in 'Biochirality: Origins, Evolution and Molecular Recognition', edited by P. Cintas (Springer Berlin Heidelberg, 2013), Pages 1–40. Cited on page(s) 1

[3] F. N. Memon and S. Memon, 'Differential Recognition of D and L-Alanine by Calix[4]Arene Amino Derivative', *Journal of Inclusion Phenomena and Macrocyclic Chemistry* **77**, 413 (2013). Cited on page(s) 2

[4] V. Böhmer, D. Kraft and M. Tabatabai, 'Inherently chiral calixarenes.', *Journal of Inclusion Phenomena and Molecular Recognition in Chemistry* **19**, 17 (1994). Cited on page(s) 2

[5] K. Ray, S. P. Ananthavel, D. H. Waldeck and R. Naaman, 'Asymmetric Scattering of Polarized Electrons by Organized Organic Films of Chiral Molecules', *Science* **283**, 814 (1999). Cited on page(s) 3 and 5

[6] S. Mayer and J. Kessler, 'Experimental verification of electron optic dichroism', *Physical Review Letters* **74**, 4803 (1995). Cited on page(s) 3

[7] C. Nolting, S. Mayer and J. Kessler, 'Electron dichroism-new data and an experimental cross-check', *Journal of Physics B: Atomic, Molecular and Optical Physics* **30**, 5491 (1997). Cited on page(s) 3

[8] B. Göhler, V. Hamelbeck, T. Z. Markus, M. Kettner, G. F. Hanne, Z. Vager, R. Naaman and H. Zacharias, 'Spin selectivity in electron transmission through self-assembled monolayers of double-stranded DNA', *Science* **331**, 894 (2011). Cited on page(s) 3, 4, 5, 6, 7, and 8

[9] R. Naaman and D. H. Waldeck, 'Chiral-induced spin selectivity effect', *The Journal of Physical Chemistry Letters* **3**, 2178 (2012). Cited on page(s) 3, 4, and 25

[10] H. Al-Bustami, S. Khaldi, O. Shoseyov, S. Yochelis, K. Killi, I. Berg, E. Gross, Y. Paltiel and R. Yerushalmi, 'Atomic and Molecular Layer Deposition of Chiral Thin Films Showing up to 99% Spin Selective Transport', *Nano Letters* **22**, 5022 (2022). Cited on page(s) 4

[11] R. Naaman, Y. Paltiel and D. H. Waldeck, 'Chiral induced spin selectivity gives a new twist on spin-control in chemistry', *Accounts of Chemical Research* **53**, 2659 (2020). Cited on page(s) 4

[12] H. Al-Bustami, B. Bloom, A. Ziv, S. Goldring, S. Yochelis, R. Naaman, D. Waldeck and Y. Paltiel, ‘Optical multilevel spin bit device using chiral quantum dots’, *Nano Letters* **20**, 8675 (2020). Cited on page(s) 4

[13] R. Naaman, Y. Paltiel and D. H. Waldeck, ‘Chiral induced spin selectivity and its implications for biological functions’, *Annual Review of Biophysics* **51**, 99 (2022). Cited on page(s) 4

[14] S.-H. Yang, R. Naaman, Y. Paltiel and S. S. Parkin, ‘Chiral spintronics’, *Nature Reviews Physics* **3**, 328 (2021). Cited on page(s) 4

[15] J. Wang, H. Lu, X. Pan, J. Xu, H. Liu, X. Liu, D. R. Khanal, M. F. Toney, M. C. Beard and Z. V. Vardeny, ‘Spin-dependent photovoltaic and photogalvanic responses of optoelectronic devices based on chiral two-dimensional hybrid organic–inorganic perovskites’, *ACS Nano* **15**, 588 (2020). Cited on page(s) 4

[16] Y. Liang *et al.*, ‘Enhancement of electrocatalytic oxygen evolution by chiral molecular functionalization of hybrid 2D electrodes’, *Nature Communications* **13**, 3356 (2022). Cited on page(s) 4

[17] C. D. Aiello *et al.*, ‘A Chirality-Based Quantum Leap’, *ACS Nano* **16**, 4989 (2022). Cited on page(s) 4

[18] R. Naaman and D. H. Waldeck, ‘Spintronics and Chirality: Spin Selectivity in Electron Transport Through Chiral Molecules’, *Annual Review of Physical Chemistry* **66**, 263 (2015). Cited on page(s) 4, 10, and 12

[19] R. Naaman, Y. Paltiel and D. H. Waldeck, ‘Chiral molecules and the electron spin’, *Nature Reviews Chemistry* **3**, 250 (2019). Cited on page(s) 4, 24, and 25

[20] S. G. Ray, S. S. Daube, G. Leitus, Z. Vager and R. Naaman, ‘Chirality-induced spin-selective properties of self-assembled monolayers of DNA on gold’, *Physical Review Letters* **96**, (2006). Cited on page(s) 4, 5, and 6

[21] I. Carmeli, V. Skakalova, R. Naaman and Z. Vager, ‘Magnetization of Chiral Monolayers of Polypeptide: A Possible Source of Magnetism in Some Biological Membranes’, *Angewandte Chemie International Edition* **41**, 761 (2002). Cited on page(s) 5

[22] I. Carmeli, Z. Gefen, Z. Vager and R. Naaman, ‘Alternation between modes of electron transmission through organized organic layers’, *Physical Review B* **68**, 115418 (2003). Cited on page(s) 5

[23] T. J. Gay and F. Dunning, ‘Mott electron polarimetry’, *Review of Scientific Instruments* **63**, 1635 (1992). Cited on page(s) 5

[24] `https://www.cancer.gov/publications/dictionaries/genetics-dictionary/def/base-pair`, 2023, genetics dictionary ,National Cancer Institute. Cited on page(s) 7

[25] M. Kettner, B. Göhler, H. Zacharias, D. Mishra, V. Kiran, R. Naaman, C. Fontanesi, D. H. Waldeck, S. Sek, J. Pawowski and J. Juhaniewicz, ‘Spin Filtering in Electron Transport Through Chiral Oligopeptides’, *Journal of Physical Chemistry C* **119**, 14542 (2015). Cited on page(s) 8, 12, and 15

[26] D. Mishra, T. Z. Markus, R. Naaman, M. Kettner, B. Göhler, H. Zacharias, N. Friedman, M. Sheves and C. Fontanesi, 'Spin-dependent electron transmission through bacteriorhodopsin embedded in purple membrane', *Proceedings of the National Academy of Sciences of the United States of America* **110**, 14872 (2013). Cited on page(s) 8

[27] M. Ángel Niño, I. A. Kowalik, F. J. Luque, D. Arvanitis, R. Miranda and J. J. D. Miguel, 'Enantiospecific spin polarization of electrons photoemitted through layers of homochiral organic molecules', *Advanced Materials* **26**, 7474 (2014). Cited on page(s) 9

[28] M. Kettner, V. V. Maslyuk, D. Nürenberg, J. Seibel, R. Gutierrez, G. Cuniberti, K. H. Ernst and H. Zacharias, 'Chirality-Dependent Electron Spin Filtering by Molecular Monolayers of Helicenes', *Journal of Physical Chemistry Letters* **9**, 2025 (2018). Cited on page(s) 9, 31, and 50

[29] S. Dalum and P. Hedegård, 'Theory of chiral induced spin selectivity', *Nano letters* **19**, 5253 (2019). Cited on page(s) 9 and 30

[30] J. Fransson, 'Chirality-induced spin selectivity: The role of electron correlations', *The Journal of Physical Chemistry Letters* **10**, 7126 (2019). Cited on page(s) 9 and 30

[31] J. Fransson, 'Vibrational origin of exchange splitting and" chiral-induced spin selectivity', *Physical Review B* **102**, 235416 (2020). Cited on page(s) 9 and 30

[32] J. Gersten, K. Kaasbjerg and A. Nitzan, 'Induced spin filtering in electron transmission through chiral molecular layers adsorbed on metals with strong spin-orbit coupling', *The Journal of Chemical Physics* **139**, (2013). Cited on page(s) 10 and 28

[33] S. Alwan and Y. Dubi, 'Spinterface origin for the chirality-induced spin-selectivity effect', *Journal of the American Chemical Society* **143**, 14235 (2021). Cited on page(s) 10 and 28

[34] F. Evers, A. Aharony, N. Bar-Gill, O. Entin-Wohlman, P. Hedegård, O. Hod, P. Jelinek, G. Kamieniarz, M. Lemeshko, K. Michaeli, V. Mujica, R. Naaman, Y. Paltiel, S. Refaely-Abramson, O. Tal, J. Thijssen, M. Thoss, J. M. van Ruitenbeek, L. Venkataraman, D. H. Waldeck, B. Yan and L. Kronik, 'Theory of Chirality Induced Spin Selectivity: Progress and Challenges', *Advanced Materials* **34**, 2106629 (2022). Cited on page(s) 10 and 31

[35] C. Nogues, S. R. Cohen, S. S. Daube and R. Naaman, 'Electrical properties of short DNA oligomers characterized by conducting atomic force microscopy', *Physical Chemistry Chemical Physics* **6**, 4459 (2004). Cited on page(s) 10

[36] Z. Xie, T. Z. Markus, S. R. Cohen, Z. Vager, R. Gutierrez and R. Naaman, 'Spin Specific Electron Conduction through DNA Oligomers', *Nano Letters* **11**, 4652 (2011). Cited on page(s) 10, 11, 12, 15, and 27

[37] K. Michaeli, N. Kantor-Uriel, R. Naaman and D. H. Waldeck, 'The electron's spin and molecular chirality – how are they related and how do they affect life processes?', *Chemical Society Reviews* **45**, 6478 (2016). Cited on page(s) 12

[38] B. P. Bloom, V. Kiran, V. Varade, R. Naaman and D. H. Waldeck, 'Spin selective charge transport through cysteine capped CdSe quantum dots', *Nano Letters* **16**, 4583 (2016). Cited on page(s) 12, 15, and 18

[39] V. Kiran, S. P. Mathew, S. R. Cohen, I. H. Delgado, J. Lacour and R. Naaman, 'Helicenes - A New Class of Organic Spin Filter', *Advanced Materials* **28**, 1957 (2016). Cited on page(s) 12, 13, 14, 15, 18, 31, and 50

[40] V. Kiran, S. R. Cohen and R. Naaman, 'Structure dependent spin selectivity in electron transport through oligopeptides', *Journal of Chemical Physics* **146**, (2017). Cited on page(s) 12 and 15

[41] F. Tassinari, D. R. Jayarathna, N. Kantor-Uriel, K. L. Davis, V. Varade, C. Achim and R. Naaman, 'Chirality Dependent Charge Transfer Rate in Oligopeptides', *Advanced Materials* **30**, (2018). Cited on page(s) 12 and 15

[42] G. Bullard, F. Tassinari, C. H. Ko, A. K. Mondal, R. Wang, S. Mishra, R. Naaman and M. J. Therien, 'Low-Resistance Molecular Wires Propagate Spin-Polarized Currents', *Journal of the American Chemical Society* **141**, 14707 (2019). Cited on page(s) 12 and 15

[43] H. Al-Bustami, G. Koplovitz, D. Primc, S. Yochelis, E. Capua, D. Porath, R. Naaman and Y. Paltiel, 'Single Nanoparticle Magnetic Spin Memristor', *Small* **14**, (2018). Cited on page(s) 14 and 15

[44] A. C. Aragonès, E. Medina, M. Ferrer-Huerta, N. Gimeno, M. Teixidó, J. L. Palma, N. Tao, J. M. Ugalde, E. Giralt, I. Díez-Pérez and V. Mujica, 'Measuring the Spin-Polarization Power of a Single Chiral Molecule', *Small* **13**, (2017). Cited on page(s) 15

[45] T. N. H. Nguyen, L. Rasabathina, O. Hellwig, A. Sharma, G. Salvan, S. Yochelis, Y. Paltiel, L. T. Baczewski and C. Tegenkamp, 'Cooperative Effect of Electron Spin Polarization in Chiral Molecules Studied with Non-Spin-Polarized Scanning Tunneling Microscopy', *ACS Applied Materials and Interfaces* **14**, 38013 (2022). Cited on page(s) 15, 19, and 23

[46] G. Binasch, P. Grünberg, F. Saurenbach and W. Zinn, 'Enhanced magnetoresistance in layered magnetic structures with antiferromagnetic interlayer exchange', *Physical Review B* **39**, 4828 (1989). Cited on page(s) 15

[47] M. N. Baibich, J. M. Broto, A. Fert, F. N. Van Dau, F. Petroff, P. Etienne, G. Creuzet, A. Friederich and J. Chazelas, 'Giant magnetoresistance of (001) Fe/(001) Cr magnetic superlattices', *Physical Review Letters* **61**, 2472 (1988). Cited on page(s) 15

[48] J. S. Moodera, L. R. Kinder, T. M. Wong and R. Meservey, 'Large magnetoresistance at room temperature in ferromagnetic thin film tunnel junctions', *Physical Review Letters* **74**, 3273 (1995). Cited on page(s) 15

[49] W. Butler, X.-G. Zhang, T. Schulthess and J. MacLaren, 'Spin-dependent tunneling conductance of Fe| MgO| Fe sandwiches', *Physical Review B* **63**, 054416 (2001). Cited on page(s) 15

[50] V. Varade, T. Markus, K. Vankayala, N. Friedman, M. Sheves, D. H. Waldeck and R. Naaman, 'Bacteriorhodopsin based non-magnetic spin filters for biomolecular spintronics', *Physical Chemistry Chemical Physics* **20**, 1091 (2018). Cited on page(s) 16 and 18

[51] S. P. Mathew, P. C. Mondal, H. Moshe, Y. Mastai and R. Naaman, 'Non-magnetic organic/inorganic spin injector at room temperature', *Applied Physics Letters* **105**, 242408 (2014). Cited on page(s) 17

[52] H. Moshe, G. Levi, D. Sharon and Y. Mastai, ‘Atomic layer deposition of enantioselective thin film of alumina on chiral self-assembled-monolayer’, *Surface Science* **629**, 88 (2014). Cited on page(s) 17

[53] P. C. Mondal, N. Kantor-Uriel, S. P. Mathew, F. Tassinari, C. Fontanesi and R. Naaman, ‘Chiral conductive polymers as spin filters’, *Advanced Materials* **27**, 1924 (2015). Cited on page(s) 18

[54] C. Kulkarni, A. K. Mondal, T. K. Das, G. Grinbom, F. Tassinari, M. F. Mabesoone, E. Meijer and R. Naaman, ‘Highly Efficient and Tunable Filtering of Electrons’ Spin by Supramolecular Chirality of Nanofiber-Based Materials’, *Advanced Materials* **32**, 1904965 (2020). Cited on page(s) 18

[55] D. Stevenson and I. D. Wilson, ‘Chiral separations’ (Plenum Press, 1988). Cited on page(s) 19

[56] B. G. Katzung and T. W. Vanderah, ‘Basic & Clinical Pharmacology, 15e’ (McGraw-Hill, 2021). Cited on page(s) 19

[57] L. Pasteur, ‘Researches on the Molecular Asymmetry of Natural Organic Products, Alembic Club Reprints, 14, Edinburgh, 1948.’, *Review Science Paris (Ser. 3)* **7**, 2 (1884). Cited on page(s) 19

[58] S. F. Mason, ‘Origins of biomolecular handedness’, *Nature* **311**, 19 (1984). Cited on page(s) 19

[59] B. L. Feringa and R. A. Van Delden, ‘Absolute asymmetric synthesis: the origin, control, and amplification of chirality’, *Angewandte Chemie International Edition* **38**, 3418 (1999). Cited on page(s) 19

[60] T. J. Ward and K. D. Ward, ‘Chiral Separations: A Review of Current Topics and Trends’, *Analytical Chemistry* **84**, 626 (2012). Cited on page(s) 19

[61] K. Banerjee-Ghosh *et al.*, ‘Separation of enantiomers by their enantiospecific interaction with achiral magnetic substrates’, *Science* **360**, 1331 (2018). Cited on page(s) 19 and 20

[62] F. Tassinari, J. Steidel, S. Paltiel, C. Fontanesi, M. Lahav, Y. Paltiel and R. Naaman, ‘Enantioseparation by crystallization using magnetic substrates’, *Chemical Science* **10**, 5246 (2019). Cited on page(s) 19 and 21

[63] Y. Lu, B. P. Bloom, S. Qian and D. H. Waldeck, ‘Enantiospecificity of Cysteine Adsorption on a Ferromagnetic Surface: Is It Kinetically or Thermodynamically Controlled?’, *The Journal of Physical Chemistry Letters* **12**, 7854 (2021). Cited on page(s) 19, 21, and 22

[64] S. Yeganeh, M. A. Ratner, E. Medina and V. Mujica, ‘Chiral electron transport: Scattering through helical potentials’, *The Journal of Chemical Physics* **131**, 014707 (2009). Cited on page(s) 23, 26, and 27

[65] A.-M. Guo and Q.-f. Sun, ‘Spin-selective transport of electrons in DNA double helix’, *Physical Review Letters* **108**, 218102 (2012). Cited on page(s) 23, 26, and 28

[66] R. Gutierrez, E. Díaz, R. Naaman and G. Cuniberti, ‘Spin-selective transport through helical molecular systems’, *Physical Review B* **85**, 081404 (2012). Cited on page(s) 23, 26, and 28

[67] E. Medina, F. López, M. A. Ratner and V. Mujica, ‘Chiral molecular films as electron polarizers and polarization modulators’, *Europhysics Letters* **99**, 17006 (2012). Cited on page(s) 23, 26, and 27

[68] D. J. Griffiths, ‘Introduction to quantum mechanics’ (Cambridge university press, 2005). Cited on page(s) 24

[69] J. M. Coey, ‘Magnetism and magnetic materials’ (Cambridge university press, 2010). Cited on page(s) 24

[70] S. Varela, E. Medina, F. Lopez and V. Mujica, ‘Inelastic electron scattering from a helical potential: transverse polarization and the structure factor in the single scattering approximation’, *Journal of Physics: Condensed Matter* **26**, 015008 (2013). Cited on page(s) 27

[71] S. Varela, V. Mujica and E. Medina, ‘Effective spin-orbit couplings in an analytical tight-binding model of DNA: Spin filtering and chiral spin transport’, *Physical Review B* **93**, 155436 (2016). Cited on page(s) 27

[72] R. A. Rosenberg, J. M. Symonds, V. Kalyanaraman, T. Markus, T. M. Orlando, R. Naaman, E. A. Medina, F. A. lopez and V. Mujica, ‘Kinetic energy dependence of spin filtering of electrons transmitted through organized layers of DNA’, *The Journal of Physical Chemistry C* **117**, 22307 (2013). Cited on page(s) 27

[73] A.-M. Guo and Q.-f. Sun, ‘Sequence-dependent spin-selective tunneling along double-stranded DNA’, *Physical Review B* **86**, 115441 (2012). Cited on page(s) 28

[74] A.-M. Guo, E. Díaz, C. Gaul, R. Gutierrez, F. Domínguez-Adame, G. Cuniberti and Q.-f. Sun, ‘Contact effects in spin transport along double-helical molecules’, *Physical Review B* **89**, 205434 (2014). Cited on page(s) 28

[75] A.-M. Guo and Q.-F. Sun, ‘Spin-dependent electron transport in protein-like single-helical molecules’, *Proceedings of the National Academy of Sciences* **111**, 11658 (2014). Cited on page(s) 28

[76] T.-R. Pan, A.-M. Guo and Q.-F. Sun, ‘Spin-polarized electron transport through helicene molecular junctions’, *Physical Review B* **94**, 235448 (2016). Cited on page(s) 28 and 31

[77] R. Gutierrez, E. Díaz, C. Gaul, T. Brumme, F. Domínguez-Adame and G. Cuniberti, ‘Modeling spin transport in helical fields: derivation of an effective low-dimensional Hamiltonian’, *The Journal of Physical Chemistry C* **117**, 22276 (2013). Cited on page(s) 28

[78] A. Ghazaryan, Y. Paltiel and M. Lemeshko, ‘Analytic model of chiral-induced spin selectivity’, *The Journal of Physical Chemistry C* **124**, 11716 (2020). Cited on page(s) 28

[79] K. Michaeli and R. Naaman, ‘Origin of spin-dependent tunneling through chiral molecules’, *The Journal of Physical Chemistry C* **123**, 17043 (2019). Cited on page(s) 28

[80] S. Ghosh, S. Mishra, E. Avigad, B. P. Bloom, L. Baczewski, S. Yochelis, Y. Paltiel, R. Naaman and D. H. Waldeck, ‘Effect of chiral molecules on the electron’s spin wavefunction at interfaces’, *The Journal of Physical Chemistry Letters* **11**, 1550 (2020). Cited on page(s) 28, 29, and 30

[81] T. K. Das, F. Tassinari, R. Naaman and J. Fransson, ‘Temperature-dependent chiral-induced spin selectivity effect: Experiments and theory’, *The Journal of Physical Chemistry C* **126**, 3257 (2022). Cited on page(s) 30

[82] Y. Liu, J. Xiao, J. Koo and B. Yan, ‘Chirality-driven topological electronic structure of DNA-like materials’, *Nature materials* **20**, 638 (2021). Cited on page(s) 30

[83] K. H. Huisman and J. M. Thijssen, ‘CISS Effect: A Magnetoresistance Through Inelastic Scattering’, *The Journal of Physical Chemistry C* **125**, 23364 (2021). Cited on page(s) 31

[84] M. Geyer, R. Gutierrez, V. Mujica and G. Cuniberti, ‘Chirality-induced spin selectivity in a coarse-grained tight-binding model for helicene’, *The Journal of Physical Chemistry C* **123**, 27230 (2019). Cited on page(s) 31

[85] V. Heß, Doctoral Thesis, ‘Scanning tunneling microscopy of single-molecule magnets and hybrid-molecular magnets: two approaches to molecular spintronics’, 2016. Cited on page(s) 34

[86] S. Fahrendorf, Doctoral Thesis, ‘Single $NdPc_2$ Molecules on Surfaces: Adsorption, Interaction, and Molecular Magnetism’, 2012. Cited on page(s) 35

[87] X. Zhou, Doctoral Thesis, ‘Temperature-Induced Metamagnetic Transition and Domain Structures of Single-Crystalline FeRh Thin Films on MgO(100)’, 2013. Cited on page(s) 35

[88] G. Binnig, H. Rohrer, C. Gerber and E. Weibel, ‘Tunneling through a controllable vacuum gap’, *Applied Physics Letters* **40**, 178 (1982). Cited on page(s) 35

[89] G. Binnig, H. Rohrer, C. Gerber and E. Weibel, ‘Surface studies by scanning tunneling microscopy’, *Physical Review Letters* **49**, 57 (1982). Cited on page(s) 35

[90] G. Binnig and H. Rohrer, ‘Scanning tunneling microscopy’, *Surface Science* **126**, 236 (1983). Cited on page(s) 35

[91] G. Binnig, H. Rohrer, C. Gerber and E. Weibel, ‘7× 7 reconstruction on Si (111) resolved in real space’, *Physical Review Letters* **50**, 120 (1983). Cited on page(s) 35

[92] D. M. Eigler and E. K. Schweizer, ‘Positioning single atoms with a scanning tunnelling microscope’, *Nature* **344**, 524 (1990). Cited on page(s) 35

[93] J. Foster, J. Frommer and P. Arnett, ‘Molecular manipulation using a tunnelling microscope’, *Nature* **331**, 324 (1988). Cited on page(s) 35

[94] C. Bai, ‘Scanning tunneling microscopy and its application’ (Springer Science & Business Media, 2000). Cited on page(s) 36

[95] C. J. Chen, ‘Introduction to Scanning Tunneling Microscopy Third Edition’ (Oxford University Press, USA, 2021). Cited on page(s) 36 and 48

[96] S. Gasiorowicz, ‘Quantum Physics, Third Edition’ (John Wiley and Sons, New York, 2003). Cited on page(s) 37

[97] J. Bardeen, ‘Tunnelling from a many-particle point of view’, *Physical Review Letters* **6**, 57 (1961). Cited on page(s) 38

[98] J. Tersoff and D. R. Hamann, ‘Theory and application for the scanning tunneling microscope’, *Physical Review Letters* **50**, 1998 (1983). Cited on page(s) 39

[99] J. Tersoff and D. R. Hamann, ‘Theory of the scanning tunneling microscope’, *Physical Review B* **31**, 805 (1985). Cited on page(s) 39

[100] R. Wiesendanger, ‘Spin mapping at the nanoscale and atomic scale’, *Reviews of Modern Physics* **81**, 1495 (2009). Cited on page(s) 40

[101] T. Esat, Doctoral Thesis, ‘Tailoring Molecular Magnetism’, 2017. Cited on page(s) 43 and 44

[102] M. Julliere, ‘Tunneling between ferromagnetic films’, *Physics Letters A* **54**, 225 (1975). Cited on page(s) 43

[103] S. Maekawa and U. Gafvert, ‘Electron tunneling between ferromagnetic films’, *IEEE Transactions on Magnetics* **18**, 707 (1982). Cited on page(s) 43

[104] J. C. Slonczewski, ‘Conductance and exchange coupling of two ferromagnets separated by a tunneling barrier’, *Physical Review B* **39**, 6995 (1989). Cited on page(s) 43

[105] D. Wortmann, S. Heinze, P. Kurz, G. Bihlmayer and S. Blügel, ‘Resolving complex atomic-scale spin structures by spin-polarized scanning tunneling microscopy’, *Physical Review Letters* **86**, 4132 (2001). Cited on page(s) 44

[106] B. Voigtländer, ‘Scanning probe microscopy: Atomic force microscopy and scanning tunneling microscopy’ (Springer, 2015). Cited on page(s) 46, 47, and 49

[107] V. A. Ukraintsev, ‘Data evaluation technique for electron-tunneling spectroscopy’, *Physical Review B* **53**, 11176 (1996). Cited on page(s) 48

[108] R. Hamers, ‘Atomic-resolution surface spectroscopy with the scanning tunneling microscope’, *Annual Review of Physical Chemistry* **40**, 531 (1989). Cited on page(s) 49

[109] K. H. Ernst, S. Baumann, C. P. Lutz, J. Seibel, L. Zoppi and A. J. Heinrich, ‘Pasteurs Experiment Performed at the Nanoscale: Manual Separation of Chiral Molecules, One by One’, *Nano Letters* **15**, 5388 (2015). Cited on page(s) 50

[110] K. H. Ernst, ‘Stereochemical Recognition of Helicenes on Metal Surfaces’, *Accounts of Chemical Research* **49**, 1182 (2016). Cited on page(s) 50

[111] K.-H. Ernst, Y. Kuster, R. Fasel, C. F. McFadden and U. Ellerbeck, ‘Adsorption of helical aromatic molecules: heptahelicene on Ni(111)’, *Surface Science* **530**, 195 (2003). Cited on page(s) 50

[112] J. Seibel, M. Parschau and K.-H. Ernst, ‘From Homochiral Clusters to Racemate Crystals: Viable Nuclei in 2D Chiral Crystallization’, *Journal of the American Chemical Society* **137**, 7970 (2015). Cited on page(s) 50

[113] R. Fasel, A. Cossy, K. H. Ernst, F. Baumberger, T. Greber and J. Osterwalder, ‘Orientation of chiral heptahelicene C30H18 on copper surfaces: An x-ray photoelectron diffraction study’, *The Journal of Chemical Physics* **115**, 1020 (2001). Cited on page(s) 50

[114] R. Fasel, M. Parschau and K.-H. Ernst, ‘Amplification of chirality in two-dimensional enantiomorphous lattices’, *Nature* **439**, 449 (2006). Cited on page(s) 50

[115] H. Bethge, D. Heuer, C. Jensen, K. Reshöft and U. Köhler, ‘Misfit-related effects in the epitaxial growth of iron on W(110)’, *Surface Science* **331-333**, 878 (1995). Cited on page(s) 51

[116] O. Pietzsch, A. Kubetzka, M. Bode and R. Wiesendanger, ‘Real-Space Observation of Dipolar Antiferromagnetism in Magnetic Nanowires by Spin-Polarized Scanning Tunneling Spectroscopy’, *Physical Review Letter* **84**, 5212 (2000). Cited on page(s) 51

[117] M. Pratzer, H. J. Elmers, M. Bode, O. Pietzsch, A. Kubetzka and R. Wiesendanger, ‘Atomic-Scale Magnetic Domain Walls in Quasi-One-Dimensional Fe Nanostripes’, *Physical Review Letters* **87**, 127201 (2001). Cited on page(s) 51

[118] A. Kubetzka, O. Pietzsch, M. Bode and R. Wiesendanger, ‘Magnetism of nanoscale Fe islands studied by spin-polarized scanning tunneling spectroscopy’, *Physical Review B - Condensed Matter and Materials Physics* **63**, 1 (2001). Cited on page(s) 51

[119] A. Kubetzka, M. Bode, O. Pietzsch and R. Wiesendanger, ‘Spin-Polarized Scanning Tunneling Microscopy with Antiferromagnetic Probe Tips’, *Physical Review Letters* **88**, 4 (2002). Cited on page(s) 51

[120] O. Pietzsch, A. Kubetzka, M. Bode and R. Wiesendanger, ‘Spin-Polarized Scanning Tunneling Spectroscopy of Nanoscale Cobalt Islands on Cu(111)’, *Physical Review Letter* **92**, 057202 (2004). Cited on page(s) 51

[121] O. Pietzsch, S. Okatov, A. Kubetzka, M. Bode, S. Heinze, A. Lichtenstein and R. Wiesendanger, ‘Spin-Resolved Electronic Structure of Nanoscale Cobalt Islands on Cu(111)’, *Physical Review Letter* **96**, 237203 (2006). Cited on page(s) 51

[122] J. Park, C. Park, M. Yoon and A.-P. Li, ‘Surface Magnetism of Cobalt Nanoislands Controlled by Atomic Hydrogen’, *Nano Letters* **17**, 292 (2017). Cited on page(s) 51

[123] H. Oka, P. A. Ignatiev, S. Wedekind, G. Rodary, L. Niebergall, V. S. Stepanyuk, D. Sander and J. Kirschner, ‘Spin-Dependent Quantum Interference Within a Single Magnetic Nanostructure’, *Science* **327**, 843 (2010). Cited on page(s) 51

[124] N. N. Negulyaev, V. S. Stepanyuk, P. Bruno, L. Diekhöner, P. Wahl and K. Kern, ‘Bilayer growth of nanoscale Co islands on Cu(111)’, *Physical Review B* **77**, 125437 (2008). Cited on page(s) 51

[125] M. Metzelaars, S. Schleicher, T. Hattori, B. Borca, F. Matthes, S. Sanz, D. E. Bürgler, J. Rawson, C. M. Schneider and P. Kögerler, ‘Cyclophane with eclipsed pyrene units enables construction of spin interfaces with chemical accuracy’, *Chemical Science* **12**, 8430 (2021). Cited on page(s) 51

[126] T. Esat, R. Friedrich, F. Matthes, V. Caciuc, N. Atodiresei, S. Blügel, D. E. Bürgler, F. S. Tautz and C. M. Schneider, ‘Quantum interference effects in molecular spin hybrids’, *Physical Review B* **95**, 1 (2017). Cited on page(s) 51

[127] M. R. Safari, F. Matthes, K.-H. Ernst, D. E. Bürgler and C. M. Schneider, ‘Deposition of Chiral Heptahelicene Molecules on Ferromagnetic Co and Fe Thin-Film Substrates’, *Nanomaterials* **12**, (2022). Cited on page(s) 54, 103, 148, and 163

[128] M. R. Safari, F. Matthes, V. Caciuc, N. Atodiresei, C. M. Schneider, K.-H. Ernst and D. E. Bürgler, ‘Enantioselective adsorption on magnetic surfaces’, *Advanced Materials* **36**, 2308666 (2024). Cited on page(s) 73, 103, 148, and 163

[129] M. R. Safari, F. Matthes, C. M. Schneider, K.-H. Ernst and D. E. Bürgler, ‘Spin-Selective Electron Transport Through Single Chiral Molecules’, *Small* **20**, 2308233 (2024). Cited on page(s) 103, 109, 148, and 164

[130] M. Bode, A. Kubetzka, S. Heinze, O. Pietzsch, R. Wiesendanger, M. Heide, X. Nie, G. Bihlmayer and S. Blügel, ‘Spin–orbit induced local band structure variations revealed by scanning tunnelling spectroscopy’, *Journal of Physics: Condensed Matter* **15**, S679 (2003). Cited on page(s) 130

Acknowledgements

This dissertation was developed during my Ph.D. at the institute of Prof. Dr. Claus M. Schneider at the Peter Grünberg Institute (PGI-6) of the Forschungszentrum Jülich. I would like to take this opportunity to express my heartfelt gratitude to all those who supported me during this fascinating journey.

First and foremost, my deepest gratitude belongs to my supervisor, PD Dr. Daniel Bürgler, who always kept his office door open, found time for my questions, and valued my ideas. He supported and encouraged me and believed in my abilities even during challenging times. I truly appreciate the trust he placed in me, allowing me to pursue my ideas and conduct experiments in my own way. Our numerous discussions were invaluable, not only for the scientific knowledge I gained but also for teaching me how to be a better person in life.

I am also thankful to Prof. Dr. Claus M. Schneider for giving me the opportunity to carry out my research at his institute. His advice and encouragement during our weekly meetings, as well as his support, were crucial to the success of this work. I also deeply appreciate the fruitful discussions we had during the coffee lectures and breaks.

I extend my gratitude to Prof. Dr. Thomas Michely for undertaking the second review of my thesis, and to Prof. Dr. Helmut Zacharias for his contributions as the third examiner.

I also wish to thank Prof. Karl-Heinz Ernst, not only for providing the molecules used in our experiments but also for his insightful discussions, creative ideas, and support throughout our collaboration. His generosity in hosting and inviting me to seminars in Zurich and Prague offered enriching experiences that broadened my academic perspective.

My heartfelt thanks belong to my lab supervisor, Dr. Frank Matthes (my old friend with a selective memory), who tirelessly assisted me with lab work and data analysis. His continual encouragement and belief in my abilities was a great source of motivation during challenging times.

Additionally, I am grateful to Dr. Nicolae Atodiresei and Dr. Vasile Caciuc for their excellent work in providing simulations that complement my experimental results. Special thanks to Nico for his readiness to answer my questions and his active participation in discussions throughout the manuscript preparation process.

It has been a true pleasure working with my colleagues and friends at PGI-6. Over the past three years, the opportunity to work and share ideas with this talented group has been one of the most enriching aspects of my Ph.D. journey. In particular, I would like to highlight the technical support provided by Thomas Jansen, Heinz Pfeifer, Norbert Schnitzler, and Arnd Bremen. Their hard work, dedication, and passion for science have been instrumental in the success of our experiments, reflecting the collaborative spirit of our lab.

Additionally, I am grateful to my mother, father, and brothers for their constant support and love throughout my life. It has been their ongoing encouragement that has enabled me to achieve my professional and personal goals.

Finally, I must express my profound thanks to Faranak, my best friend and wife. She has selflessly inspired me, supporting me through every challenge and celebrating every success. I am eternally grateful for her presence in my life, and I look forward to our journey together in the future. Her unconditional support has not only shaped my personal life but also been fundamental to my professional success.

Erklärung zur Dissertation

gemäß der Promotionsordnung vom 12. März 2020

Hiermit versichere ich an Eides statt, dass ich die vorliegende Dissertation selbstständig und ohne die Benutzung anderer als der angegebenen Hilfsmittel und Literatur angefertigt habe. Alle Stellen, die wörtlich oder sinngemäß aus veröffentlichten und nicht veröffentlichten Werken dem Wortlaut oder dem Sinn nach entnommen wurden, sind als solche kenntlich gemacht. Ich versichere an Eides statt, dass diese Dissertation noch keiner anderen Fakultät oder Universität zur Prüfung vorgelegen hat; dass sie - abgesehen von unten angegebenen Teilpublikationen und eingebundenen Artikeln und Manuskripten - noch nicht veröffentlicht worden ist sowie, dass ich eine Veröffentlichung der Dissertation vor Abschluss der Promotion nicht ohne Genehmigung des Promotionsausschusses vornehmen werde. Die Bestimmungen dieser Ordnung sind mir bekannt. Darüber hinaus erkläre ich hiermit, dass ich die Ordnung zur Sicherung guter wissenschaftlicher Praxis und zum Umgang mit wissenschaftlichem Fehlverhalten der Universität zu Köln gelesen und sie bei der Durchführung der Dissertation zugrundeliegenden Arbeiten und der schriftlich verfassten Dissertation beachtet habe und verpflichte mich hiermit, die dort genannten Vorgaben bei allen wissenschaftlichen Tätigkeiten zu beachten und umzusetzen. Ich versichere, dass die eingereichte elektronische Fassung der eingereichten Druckfassung vollständig entspricht.

Teilpublikationen:

[127] **Mohammad Reza Safari**, Frank Matthes, Karl-Heinz Ernst, Daniel E. Bürgler, Claus M. Schneider
Deposition of Chiral Heptahelicene Molecules on Ferromagnetic Co and Fe Thin-Film Substrates
Nanomaterials 2022, **12(19)**, 3281.

[128] **Mohammad Reza Safari**, Frank Matthes, Vasile Caciuc, Nicolae Atodiresei, Claus M. Schneider, Karl-Heinz Ernst, Daniel E. Bürgler

Enantioselective Adsorption on Magnetic Surfaces
Advanced Materials 2024, **36(14)**, 2308666.

[129] **Mohammad Reza Safari**, Frank Matthes, Claus M. Schneider, Karl-Heinz Ernst, Daniel E. Bürgler
Spin-Selective Electron Transport Through Single Chiral Molecules
Small 2024, **20(22)**, 2308233.

Villingen-Schwenningen , den 06.10.2024 Mohammad Reza Safari

Datenverfügbarkeit

Die in dieser Dissertation gezeigten Primärdaten sind bei der Arbeitsgruppe von Priv.-Doz. Dr. Daniel Bürgler am Peter Grünberg Institut, Elektronische Eigenschaften (PGI-6) hinterlegt.

Lebenslauf *(Curriculum Vitae)*

Persönliche Daten

Name	Safari
Vorname	Mohammad Reza
Geburtstag	05.04.1990
Geburtsort	Karaj
Staatsangehörigkeit	Iranisch

Ausbildung

03/2020 – 08/2023	Promotionsstudium Forschungszentrum Jülich, Peter Grünberg Institut (PGI-6) und Universität zu Köln, Deutschland Arbeitsgruppe Priv.-Doz. Dr. Daniel Bürgler
04/2018 – 10/2019	Master of Science in Physics Heinrich-Heine-Universität Düsseldorf, Deutschland Durchschnittsnote: gut (1.7) Masterarbeit “Practical guidelines towards hyperthermic manipulation of magnetic nanoparticles in nanomedicine” (Note: gut 1.7) Experimentelle Medizinphysik, Heinrich-Heine-Universität Düsseldorf Arbeitsgruppe Prof. Dr. Cornelia Monzel
09/2008 – 09/2012	Bachelor of Science in Solid State Physics Semnan Universität, Iran Durchschnittsnote: 16.82 von 20
07/2008	Voruniversitärer Abschluss Sheikh Koleini Boarding High school, Teheran, Iran Durchschnittsnote: 17.48 von 20
06/2007	Hochschulreife, Sheikh Koleini Boarding High school, Teheran, Iran Durchschnittsnote: 18.12 von 20

Band / Volume 94
HAXPES study of interface and bulk chemistry of ferroelectric HfO_2 capacitors
T. Szyjka (2023), viii, 120 pp
ISBN: 978-3-95806-692-2

Band / Volume 95
A brain inspired sequence learning algorithm and foundations of a memristive hardware implementation
Y. Bouhadjar (2023), xii, 149 pp
ISBN: 978-3-95806-693-9

Band / Volume 96
Characterization and modeling of primate cortical anatomy and activity
A. Morales-Gregorio (2023), ca. 260 pp.
ISBN: 978-3-95806-698-4

Band / Volume 97
Hafnium oxide based memristive devices as functional elements of neuromorphic circuits
F. J. Cüppers (2023), vi, ii, 214 pp
ISBN: 978-3-95806-702-8

Band / Volume 98
Simulation and theory of large - scale cortical networks
A. van Meegen (2023), ca. 250 pp
ISBN: 978-3-95806-708-0

Band / Volume 99
Structure of two-dimensional multilayers and topological superconductors: surfactant mediated growth, intercalation, and dopingY.-R. Lin (2023), x, 111 pp
ISBN: 978-3-95806-716-5

Band / Volume 100
Frequency mixing magnetic detection for characterization and multiplex detection of superparamagnetic nanoparticles
A. M. Pourshahidi (2023), X, 149 pp
ISBN: 978-3-95806-727-1

Band / Volume 101
Unveiling the relaxation dynamics of Ag/HfO2 based diffusive memristors for use in neuromorphic computing
S. A. Chekol (2023), x, 185 pp
ISBN: 978-3-95806-729-5

Schriften des Forschungszentrums Jülich
Reihe Information

Band / Volume 102
Analysis and quantitative comparison of neural network dynamics on a neuron-wise and population level
R. Gutzen (2024), xii, 252 pp
ISBN: 978-3-95806-738-7

Band / Volume 103
3D Scaffolds with Integrated Electrodes for Neuronal Cell Culture
J. Abu Shihada (2024), vii, 163 pp
ISBN: 978-3-95806-756-1

Band / Volume 104
Advances in Photoemission Orbital Tomography
A. Haags (2024), ix, 254 pp
ISBN: 978-3-95806-766-0

Band / Volume 105
Quantitative investigation of point defects and their dynamics in focused ion beam-prepared group III-nitride lamellas by off-axis electron holography
K. Ji (2024), 164 pp
ISBN: 978-3-95806-782-0

Band / Volume 106
NeuCoNS and Stacked-Net: Facilitating the Communication for Accelerated Neuroscientific Simulations
R. Kleijnen (2024), xx, 110, xxi-xxxiv pp
ISBN: 978-3-95806-788-2

Band / Volume 107
Construction of a Spiking Network Model of Macaque Primary Visual Cortex: Towards Digital Twins
A. Kurth (2024), xvi, 207 pp
ISBN: 978-3-95806-800-1

Band / Volume 108
Spin selectivity of chiral molecules on surfaces
M.R. Safari (2025), xiv, 165 pp
ISBN: 978-3-95806-810-0

Weitere ***Schriften des Verlags im Forschungszentrum Jülich*** unter
http://wwwzb1.fz-juelich.de/verlagextern1/index.asp

Information
Band / Volume 108
ISBN 978-3-95806-810-0

Mitglied der Helmholtz-Gemeinschaft

JÜLICH
Forschungszentrum